Denitrification and ozone loss in the Arctic stratosphere

by

David Stewart Davies

Submitted in accordance with the requirements for the degree of Doctor of Philosophy.

The University of Leeds

School of the Environment

May 2003.

The candidate confirms that the work submitted is his own and that appropriate credit has been given where reference has been made to the work of others.

Acknowledgements

Abstract

This thesis investigates the mechanism of denitrification of the Arctic lower stratosphere and the impact of denitrification on ozone loss using the SLIMCAT chemical transport model. The development of a new microphysical model for the simulation of growth and sedimentation of large nitric acid trihydrate particles is also described.

Model simulations of Arctic denitrification were carried out using thermodynamic equilibrium schemes based on the sedimentation of either nitric acid trihydrate or ice using different meteorological analyses. The severity and extent of denitrification in ice-based model runs was found to be highly sensitive to the meteorological analyses used whereas nitric acid trihydrate denitrification schemes exhibited considerably less sensitivity.

The response of thermodynamic equilibrium and microphysical NAT-based denitrification to meteorological conditions has been studied in a series of short idealised simulations. It was found that microphysical denitrification was considerably more sensitive to the relative orientation of the polar vortex flow and the region of cold temperatures. A concentric vortex and cold region are required to promote the long particle growth times required for strong denitrification in the microphysical model. Reduced rates of denitrification were evident in the microphysical model at the highest altitudes.

Results from the microphyical denitrification scheme were compared with in-situ and remote observations of denitrification for two recent cold Arctic winters. There was remarkable agreement between model and observations of both the magnitude and location of denitrification despite the simple volume-averaged nucleation rate used in the model. The limited range of observations did not allow further constraints to be placed on the microphysical model.

Denitrification was found to enhance Arctic ozone loss by up to 30% during 1999/2000. Sensitivity studies of the impact of denitrification on Arctic ozone loss were performed using thermodynamic nitric acid trihydrate denitrification schemes. Cumulative ozone depletion was found to increase non-linearly with increasing denitrification. Enhanced recovery of chlorine radicals to hydrogen chloride in strongly denitrified model runs offset reduced recovery to chlorine nitrate, limiting the impact of denitrification to the equivalent of 20 days additional ozone loss.

Contents

List of Figures

List of Tables

List of Acronyms

AAOE	Airborne Antarctic Ozone Experiment
AASE	Airborne Arctic Stratospheric Experiment
ADEOS	Advanced Earth Observing Satellite
ALIAS	Aircraft Laser Infrared Absorption Spectrometer
ASUR	Airborne Submillimeter Radiometer
BADC	British Antarctic Data Centre
CLAES	Cryogenic Linb Array Etalton Spectromoter
CLaMS	Chemical Lagrangian Model of the Stratosphere
DLAPSE	Denitrification by LAgrangian Particle SEdimentation model
DNA	Deoxyribonucleic acid
DU	Dobson units
ECMWF	European Centre for Meduim-range Weather Forcasts
EOS	Earth Observing System
GCM	Global circulation model
GHG	Greenhouse gas
GISS	Goddard Institute for Space Studies
IPCC	Intergovernmental Panel for Climate Change
ILAS	Improved Limb Atmospheric Spectromoter
JPL	Jet Propulsion Laboratory, Pasadena, California
MASP	Multiple Aerosol Scattering Probe
MIDRAD	Middle Atmosphere Radiation Scheme
MIPAS	Michelsen Passive
MLS	Microwave Limb Sounder
MMS	Meteorological Measurement System
MPV	Modified potential vorticity
NAD	Nitric acid dihydrate
NASA	National Aeronautics and Space Administration
NAT	Nitric acid trihydrate

NCEP	National Centers for Environmental Prediction
NERC	Natural Environment Research Council
NOAA	National Oceanographic and Atmospheric Administration
OMS	Observations of the Middle Stratosphere balloon
PSC	Polar stratospheric cloud
PV	Potential vorticity
PVU	Potential vorticity unit
QBO	Quasi-biennial Oscillation
SAGE	Stratospheric Aerosol and Gas Experiment
SOLVE	SAGE III Aerosol and Gas Experiment
STRAT	Stratospheric Tracers of Arctic Transport
THESEO-2000	Third European Experiment on Ozone
UARS	Upper Atmosphere Research Satellite
UGAMP	United Kindom Universities' Global Atmospheric Modelling Project
UM	Unified model
UNEP	United Nations Environment Programme
WMO	World Meteorological Organisation

List of Symbols

$\mathbf{a}$	inertial acceleration	ms^{-2}
$\mathbf{a}_c$	Coriolis acceleration	ms^{-2}
$\mathbf{a}_l$	local acceleration	ms^{-2}
$\mathbf{a}_r$	centripetal acceleration	ms^{-2}
A	pre-exponential factor	$-$
$\bar{A}$	available surface area	cm^2
A_{NAT}	area of NAT supersaturation	km^2
c	concentration	molec cm^{-3}
c_p	specific heat capacity of dry air at constant pressure	$\text{J kg}^{-1} \text{ K}^{-1}$
$\bar{c}_\text{X}$	mean molecular velocity	ms^{-1}
C_c	Cunningham slip-flow correction factor	$-$
D_g	diffusivity in air	$\text{cm}^2 \text{ s}^1$
D_m	modified diffusion coefficient	$\text{cm}^2 \text{ s}^1$
E_a	activation energy	kJ mol^{-1}
$\mathbf{F}$	resultant force	N
F_drag	drag force	N
$\mathbf{F}_g^*$	gravitational force	N
$\mathbf{F}_g$	effective gravitational force	N
$\mathbf{F}_p$	pressure-gradient force	N
$\mathbf{F}_v$	viscous force	N
g	gravitational constant	m s^{-2}
h	Planck's Constant	Js
H^*	Efective Henry's Law constant	$\text{mol kg}^{-1} \text{ s}^{-1}$
H_NNb^*	Efective Henry's Law constant (binary nitric acid solution)	$\text{mol kg}^{-1} \text{ s}^{-1}$
H_NSb^*	Efective Henry's Law constant (binary sulphuric acid solution)	$\text{mol kg}^{-1} \text{ s}^{-1}$
I_{abs}	intensity of light absorption	$\text{photons cm}^{-2} \text{ s}^{-1}$
I_0	intensity of incident light	$\text{photons cm}^{-2} \text{ s}^{-1}$

J	Photodissociation constant	s^{-1}
$J(\lambda)$	total irradiance at a wavelength (λ)	photons cm^{-2} s^{-1}
J_c	total molar flux to particle in continuum regime	mol s^{-1}
J_k	total molar flux to particle in kinetic regime	mol s^{-1}
$\bar{J}_{X,r}$	molar flux of X at any distance r	mol s^{-1}
k	Boltzmann constant	J K^{-1}
K	Kelvin factor	–
k_x	reaction rate constant for reaction x	variable
k'_x	equivalent first order rate constant for reaction x	s^{-1}
Kn	Knudsen number	–
L	photochemical loss rate	molec cm^{-3} s^{-1}
l	path length	m
m	mass	kg
M	inert molecule	–
M_N	molality of nitric acid in liquid ternary droplet	mol kg^{-1} H_2O
M_S	molality of sulphuric acid in liquid ternary droplet	mol kg^{-1} H_2O
M_{Nb}	molality of nitric acid in liquid binary droplet	mol kg^{-1} H_2O
M_{Sb}	molality of sulphuric acid in liquid binary droplet	mol kg^{-1} H_2O
n_s	concentration of sulphuric acid	mol m_{-3}
N	number of molecules per unit volume	m^{-3}
p	pressure	Pa
p_{H_2O}	vapour pressure of water over ice	Pa
$p_{H_2O}^0$	saturation vapour pressure of water over ice	Pa
p_{HNO_3}	vapour pressure of nitric acid over NAT	Pa
$p_{HNO_3}^0$	saturation vapour pressure of nitric acid over NAT	Pa
p_N	vapour pressure of nitric acid over liquid aerosol	Pa
p_s^*	saturation vapour pressure over curved surface	Pa
p_s	saturation vapour pressure over plane surface	Pa
P	photochemical production rate	s^{-1}
Q	total energy of a system	J
r	radial distance	m
r_p	particle radius	m
R	dry air gas constant	J kg^{-1} K^{-1}
R_e	Earth's radius	km
t	time	s
T	temperature	K
T_{ice}	ice frost point	K
T_{min}	minimum temperature	K
T_{NAT}	NAT-supersaturation temperature	K
u, v, w	3-D wind components	m s^{-1}
U	internal energy of a system	J

$\mathbf{v}$	absolute velocity	m s^{-1}
W	work done on (by) system	J
x, y	horizontal coordinates	m
z	vertical coordinate	m
Z_N	molecular flux per unit area	s^{-1}
α	molecular accommodation constant	–
γ_x	reaction probability for reaction x	–
η	kinematic viscosity of air	kg m^{-1}s^{-1}
ρ	density	kg m^{-3}
ν	frequency	Hz
$\bar{\nu}$	mean molecular speed	ms^{-1}
θ	potential temperature	K
λ	wavelength	m
$\bar{\lambda}$	mean free path	m
ϕ	quantum yield	–
π	universal constant	
σ	surface viscosity	Pa s
σ_c	absorption cross section	cm^2 molecule^{-1}
χ	volume mixing ratio	–
ϕ	latitude	radians
Ω	angular velocity of the earth	radians s^{-1}

Chapter 1

Introduction

1.1 Overview

Chemical depletion of stratospheric ozone (O_3) by halogens released from synthetic chlorofluorocarbons (CFCs) and bromocarbons has undoubtedly become one of the most scientifically studied environmental issues. Ozone plays a vital role in ensuring the survival of life on Earth through the attenuation of solar ultraviolet (UV) radiation and is important for the regulation of climate as a radiatively active "greenhouse" gas. Understanding how changes in the concentration and distribution of stratospheric ozone may impact upon the future climate of the Earth is of considerable importance to mankind. Satellite and ground-based observations of mid-latitude and polar surface UV-B irradiance have shown increases consistent with decreased ozone columns [for example, *Herman et al., 1996*; *Bodhaine et al.*, 1997; *Fioletov et al.*, 1997; *Frederick et al., 1998*].

Increased levels of surface UV-B radiation are associated with a number of socio-economic problems. Human health may be directly affected as increased UV radiation is associated with impaired immune system function, DNA-mutation and ocular damage [*Longstreth et al.*, 1998]. *Moan et al.* [1989] demonstrated an association between UV-B exposure and the incidence of non-melanoma skin cancer. Potential indirect health effects of increased surface UV radiation include increased rates of pathogen mutation and alterations to agricultural production [for example, *Sinha and Hader*,

1998; *Caldwell et al.*, 1998]. Changes in terrestrial and oceanic biodiversity as well as material damage by photo-degradation may also contribute to the economic consequences of increased terrestrial UV radiation [for example, *UNEP*, 1995; *Andrady et al.*, 1998].

Ozone also plays a significant role in regulating the climate of the Earth as a radiatively active greenhouse gas. Changes in the concentration and distribution of stratospheric ozone may impact upon the future climate of the Earth and increased penetration of the troposphere by UV radiation may alter the complex photochemistry of this region. Coupled ocean-atmosphere general circulation model (GCM) calculations indicate that stratospheric ozone depletion may have offset around one third of the radiative forcing due to the increases in the atmospheric burden of well-mixed greenhouse gases [*WMO*, 1999].

The annual mean Southern Hemisphere mid-latitude ozone column has declined by around 6% per decade since 1975 [*WMO*, 2003]. A smaller decrease in has occurred in the annual mean ozone column over the Northern Hemisphere mid-latitudes during this time. A long-term trend is difficult to establish due to the limited duration of observations combined with effect of the Mount Pinatubo volcanic eruption in 1991 [*WMO*, 2003]. Large seasonal ozone losses in the Antarctic region continue to be reported in all years (except the unusual winter of 2002) with column reductions of up to 70% in October. Ozone loss is almost complete between 12 and 20 km at this time [for example, *Hofmann et al.*, 1997].

Substantial Arctic ozone loss has been reported for seven winter/spring periods between 1988/89 and 2001/02 [for example, *Rex et al.*, 1997, 2002; *Goutail and Pommerau*, 1997; *Newman et al.*, 1997]. Each of these winters of enhanced ozone loss is associated with particularly low stratospheric temperatures [*Pawson and Naujokat*, 1999]. Despite column losses of 30% or more during cold winters, the total ozone column above the Arctic has not fallen below the 220 Dobson Units (DU) threshold for an ozone "hole". For dynamic reasons the Arctic has a background ozone column that is around 40% higher than the Antarctic in early spring [*Bojkov et al.*, 1986].

Many of the fundamental dynamic and chemical processes responsible for the regulation of stratospheric ozone and its anthropogenic destruction are well understood,

however it is still not possible to quantitatively reproduce these effects in numerical models. The Arctic poses a particular challenge to the stratospheric modelling community as the wintertime meteorology exhibits considerable interannual variability. Arctic stratospheric temperatures are frequently at the threshold for the formation of polar stratospheric clouds which catalyse the heterogeneous conversion of halogen reservoirs to more active forms. Studies using general circulation models (GCMs) show that coupling between ozone loss and radiative cooling of the lower stratosphere may lead to significantly increased Arctic ozone losses during the period 2010-2020 [*Shindell et al.*, 1998] although subsequent studies tend to contradict this [for example, *Schnadt et al.*, 2000; *Austin*, 2002].

Major questions that remain to be answered include: How do polar stratospheric clouds (PSCs) form and grow? What is the significance of lee-wave events in PSC formation? Do heterogeneous halogen activation rates on PSC particles agree with laboratory measurements? Is it possible to reconcile observed polar ozone loss rates with measured halogen and nitrogen species? How will climate change impact ozone loss processes? How can observations of denitrification and dehydration in polar regions be explained quantitatively and what is their current and potential future impact on chemical ozone loss? The last of these questions is addressed in this thesis.

1.2 Summary

The essential role played by stratospheric ozone in protecting the biosphere from the harmful effects of solar UV light and its crucial role in the atmospheric radiative budget has been described briefly. In the following chapter, the chemical and dynamic processes regulating the O_3 budget of the stratosphere are described with particular emphasis on the high-latitudes. Chapter 3 describes the physical principles of the SLIMCAT model used as the basis for this study and in Chapter 4, results are presented for the winter of 1999/2000 using two simplified denitrification schemes. The coupling of SLIMCAT to a new Lagrangian microphysical denitrification scheme (hereafter, DLAPSE) is described in detail in Chapter 5. Chapter 6 explores the sensitivity of this denitrification scheme to idealised meteorology, while the subsequent chapter compares in detail the model denitrification for two cold Arctic winters with observations from a variety of platforms.

Chapter 8 discusses the effect of denitrification on ozone depletion during the Arctic winter of 1999/2000 and Chapter 9 explores the sensitivity of O_3 depletion in this winter to changes in denitrification. In the final chapter, conclusions based on the results presented in the preceeding chapters are drawn and some suggestions made for continued work.

Chapter 2

Chemical, dynamical and physical processes in the stratosphere

2.1 Introduction

Ozone is a trace constituent of the atmosphere, comprising a few parts per million by volume in the stratosphere. A full explanation of the observed distribution and trends in the distribution of stratospheric O_3 requires a detailed understanding of the chemical and transport processes affecting O_3 in the stratosphere. Total reactive nitrogen (NO_y) plays a crucial role in regulating the halogen-catalysed loss processes which destroy O_3 in the lower stratosphere. Section 2.2 describes the formation and partitioning of O_3, NO_y and halogens in the lower stratosphere. The dynamics of the stratosphere are discussed in Section 2.3 which focusses on the meteorological factors governing the distribution of trace gases and the formation of the polar vortex. Section 2.4 describes the dominant polar O_3 loss processes and the subsequent section examines the properties of PSCs. The final two sections of this chapter review current understanding of the association between denitrification and O_3 loss and future predictions of the impact of climate change on stratospheric O_3.

2.2 Stratospheric chemistry of ozone and reactive nitrogen

2.2.1 Oxygen-only chemistry

Stratospheric ozone is produced in two steps from molecular oxygen (O_2). The first stage is the photodissociation of O_2 by solar radiation with wavelengths below 242 nm which occurs at altitudes greater than 20 km. The oxygen atoms formed may be either the ground state ($O(^3P)$) or the first excited electronic state ($O(^1D)$). Subsequent reaction of $O(^3P)$ with O_2 and an inert molecule yields O_3 in a three-body reaction. Chapman was the first to describe the photochemistry of O_3 in his seminal publication of 1930 [*Chapman*, 1930a]:

$$O_2 + h\nu \rightarrow O + O \tag{2.1}$$

$$O_2 + O(^3P) + M \rightarrow O_3 + M \tag{2.2}$$

$$O_3 + h\nu \rightarrow O_2 + O \tag{2.3}$$

$$O_3 + O(^3P) \rightarrow 2O_2 \tag{2.4}$$
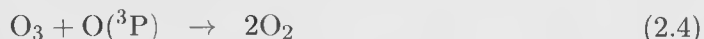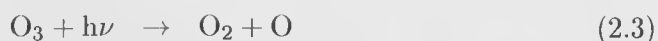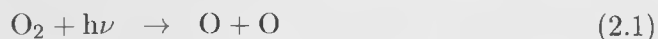
where M represents an inert third molecule.

Photolysis (Reaction 2.4) is the most rapid O_3 loss term whilst reaction with O_2 dominates the loss of O (Reaction 2.3) and leads to a rapid inter-conversion of O and O_3 without loss of odd oxygen ($O_x = O + O_3$). Stratospheric chemical models often integrate O_x as a "family" before steady-state partitioning of O_x into its constituents.

Chapman soon extended this oxygen-only theory of stratospheric ozone to include the exponential decrease of pressure with altitude and spherical geometry [1930b, 1931a, 1931b]. The maximum concentration of O_3 is typically between 4 and 8 parts per million by volume (ppmv) at around 30 km altitude. The peak concentration in molecules per cm^3 is, however, found at around 25 km due to the exponential decrease of pressure with altitude.

2.2.2 Trace Species

Extensions to the oxygen-only theory of stratospheric O_3 recognised apparent discrepancies between the seasonal and latitudinal variations in O_3 columns which had been previously attributed to upper stratospheric circulation [for example, *Craig*, 1950]. Three families of trace species have been identified which catalytically alter the stratospheric abundance of O_3. These families are hydrogen (H), nitrogen (N) and halogens (Cl and Br):

$$X + O_3 \rightarrow XO + O \tag{2.5}$$

$$\underline{XO + O_3 \rightarrow X + 2O_2} \tag{2.6}$$

$$overall: \qquad 2O_3 \rightarrow 3O_2 \tag{2.7}$$
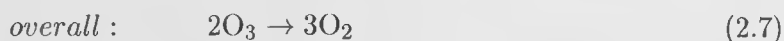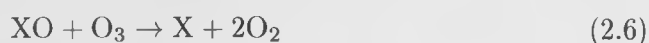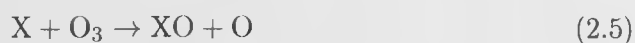
where X = OH, NO, Cl or Br. Several additional stratospheric ozone loss cycles catalysed by halogens have subsequently been identified. Two of the most important halogen-catalysed cycles responsible for the depletion of ozone in the polar lower stratosphere are discussed in more detail in Section 2.4. The first of these cycles involves the formation and subsequent photolysis of the ClO dimer [*Molina and Molina*, 1987]. The rate of dimer formation and the relative importance of this cycle to overall chemical ozone loss is increased at low temperatures. Stratospheric ozone may also significantly depleted by a cycle which involves the coupling of ClO and BrO [*Yung et al.*, 1980]. Although the abundance of bromine in the stratosphere ($\sim$20 pptv) is considerably lower than that of chlorine, bromine reservoirs are more readily photolysed to active forms [*WMO*, 1999].

In the mesosphere the hydrogen family dominates O_3 loss. At lower altitudes, the nitrogen family dominates. Halogen-catalysed losses by the ClO + O cycle are calculated to peak around 40 km. Water (4-5 ppmv) and methane (CH_4, 1.8 ppmv) are the source gases for the hydrogen family; and nitrous oxide (N_2O, 320 ppbv) is the predominant source of stratospheric nitrogen. Emissions of CH_4 and N_2O are predominantly natural in origin although anthropogenic sources are increasing their tropospheric concentrations by approximately 1% per annum [*WMO*, 1999]. The precursors of stratospheric halogens are dominated by anthropogenic sources of both Cl and Br. These are linked to the use of chlorofluorocarbons (CFCs) and other brominated and chlorinated hydrocarbons. These anthropogenic compounds are unreactive in the troposphere and are

transported to the stratosphere where they release halogens. In 1999, the stratospheric chlorine concentration was 3.8 ppbv compared with pre-industrial levels estimated to be 0.6 ppbv [*WMO*, 1999].

Stratospheric reactive nitrogen chemistry

Total reactive nitrogen (NO_y) is the sum of the reactive nitrogen species present in an air parcel ($N + NO + NO_2 + NO_3 + 2N_2O_5 + HNO_3 + ClONO_2 + HO_2NO_2 + BrONO_2$ + minor constituents). In this section, the stratospheric sources of NO_y and its partitioning between long-lived and short-lived forms are described.

N_2O is relatively unreactive in the troposphere and is transported to the stratosphere where it is photolysed. Around 90% of this photochemical loss is due to Reaction 2.10 which does not produce NO_y:

$$N_2O + h\nu \rightarrow O + N_2 \tag{2.8}$$

$$N_2O + O(^1D) \rightarrow O_2 + N_2 \tag{2.9}$$

$$N_2O + O(^1D) \rightarrow 2NO \tag{2.10}$$
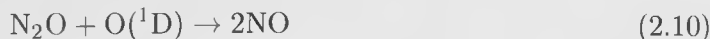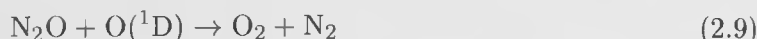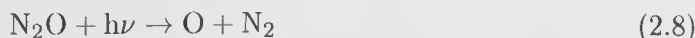
Only Reaction 2.10 (around 6% of N_2O loss) produce NO_y with the former reaction responsible for the majority of stratospheric NO_y. This relationship can be clearly seen in Figure 2.1 in the range 30 ppbv $< [N_2O] <$ 300 ppbv. Other minor stratospheric sources of NO_y include aircraft emissions and transport from the mesosphere (from dissociation of N_2 by photolysis, solar protons, cosmic rays and electron-precipitation).

At higher altitudes in the stratosphere (>30 km) the rate of chemical NO_y loss increases rapidly due to the reaction between N and NO:

$$N + NO \rightarrow N_2 + O. \tag{2.11}$$
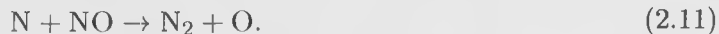
This results in a maximum NO_y concentration around 25-30 km before decreasing rapidly. Figure 2.1 shows a characteristic stratospheric NO_y/N_2O correlation obtained from the NASA Jet Propulsion Laboratory (JPL) Mark IV interferometer aboard an Observations of the Middle Stratosphere (OMS) balloon in early December 1999 with the rapid turnover in NO_y at $[N_2O] <$ 30 ppbv.
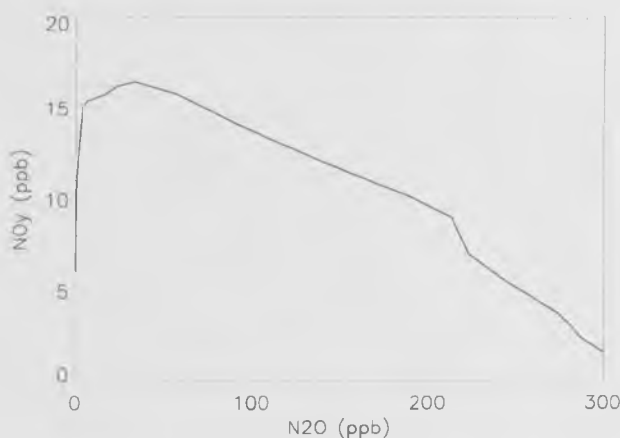
Figure 2.1: NO_y/N_2O from the JPL Mark IV interferometer aboard an OMS balloon on December 3, 1999 from Kiruna, Sweden.

The inter-conversion of NO_y species in the stratosphere and the partitioning between long-lived (reservoir) and short-lived NO_y species plays a crucial role in halogen-catalysed polar ozone loss chemistry as discussed in Section 2.4. The short-lived NO_y constituents $(N + NO + NO_2 + NO_3 = NO_x)$ are participants in ozone destruction cycles as discussed in Section 2.4.

There are 4 long-lived NO_y (reservoir) species of particular relevance to the lower stratosphere.

Dinitrogen pentoxide (N_2O_5) is formed at night by the three-body reaction between NO_2 and NO_3:

$$NO_2 + NO_3 + M \rightarrow N_2O_5 + M. \tag{2.12}$$

Chlorine nitrate $(ClONO_2)$ and bromine nitrate $(BrONO_2)$ are formed in three-body reactions between NO_2 and ClO or BrO respectively:

$$NO_2 + ClO + M \rightarrow ClONO_2 + M. \tag{2.13}$$

$BrONO_2$ has a short lifetime compared to $ClONO_2$ due to more rapid photolysis. Therefore, the impact of NO_y on deactivation of ClO is greater than its effect on BrO due to

more rapid re-activation of the latter. Nitric acid (HNO_3) is formed by the three-body reaction of NO_2 and hydroxyl (OH):

$$NO_2 + HO + M \rightarrow HNO_3 + M. \tag{2.14}$$

N_2O_5 undergoes photolysis and thermal decomposition, although the former is the greater contributor in the lower stratosphere in the absence of heterogeneous chemistry:

$$N_2O_5 + h\nu \rightarrow NO_2 + NO_3 \tag{2.15}$$

$$N_2O_5 + M \rightarrow NO_2 + NO_3 + M. \tag{2.16}$$
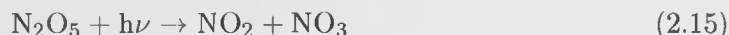
$ClONO_2$ and $BrONO_2$ are re-converted to NO_x by photolysis:

$$ClONO_2 + h\nu \rightarrow NO_3 + Cl. \tag{2.17}$$
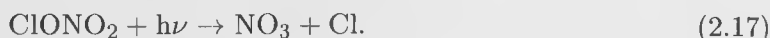
HNO_3 is destroyed by photolysis and oxidation by OH, each of which makes a comparable contribution in the lower stratosphere:

$$HNO_3 + h\nu \rightarrow NO_2 + OH \tag{2.18}$$

$$HNO_3 + OH \rightarrow NO_3 + H_2O. \tag{2.19}$$
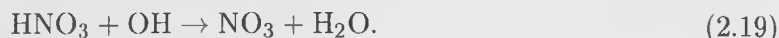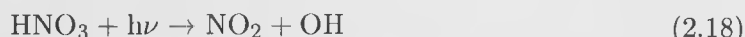
2.2.3 Stratospheric halogen chemistry

Organic halogen compounds are released into the troposphere where they are rapidly mixed. The fully halogenated species e.g. CFC-11 ($CHCl_3$) and CFC-12 (CF_2CCl_2) are totally inert in the troposphere and are transported to the stratosphere. Organic halogens containing hydrogen react with OH in the troposphere and their lifetimes in the lower atmosphere determine the fraction transported to the stratosphere. Emissions of CFCs, Halons, HCFCs and several halogenated solvents are regulated by the Montreal Protocol and subsequent amendments. Emissions peaked in the early 1990s and the timescales involved with their transport from the boundary-layer to the stratosphere are such that stratospheric loadings are now at about their maximum.

The constituents of total organic chlorine ($CCl_y = 3[CCl_3F] + 2[CCl_2F_2] + 3[CCl_2FCClF_2]$ $+ 3[CH_3CCl_3] + 4[CCl_4] + [CH_3Cl] + [CHClF_2]$ + minor constituents) are rapidly mixed in the troposphere and are transported to the stratosphere under the influence

of the residual circulation. CCl_y is transported through the stratosphere by the meridional circulation where they are converted to inorganic forms either by photolysis or reaction with OH. Above 30 km, virtually all stratospheric Cl is in inorganic forms, mostly HCl and ClO. This air is transported to high latitudes by the meridional circulation where it descends. Halogens are eventually transported out of the stratosphere to the troposphere where the soluble components are rained out.

2.3   Dynamics of the stratosphere

The distributions of ozone and other trace species in the atmosphere are determined not only by chemistry but also by transport. The rate of many chemical reactions and the position of thermodynamic equilibrium are temperature-dependent and the thermal structure of the atmosphere is influenced by the distribution of radiatively active trace gases. This section discusses the meteorological factors which govern the transport of mass, momentum and heat in the middle atmosphere. A consideration of these processes is essential in any examination of the distribution of stratospheric components under the influence of the large-scale circulation and quasi-horizontal mixing. These processes are discussed in detail in *Holton*, [1992] and are summarised here.

2.3.1   Atmospheric temperature structure

The stratosphere is the region of the atmosphere between the troposphere (approximately 10-15 km) and the mesosphere (approximately 50 km). Approximately 10% of the mass of the atmosphere resides in the stratosphere. The lower boundary of the stratosphere, the tropopause, is characterised by a temperature minimum and the upper boundary, the stratopause, is defined by a temperature maximum. This negative lapse rate is due primarily to the balance between infrared (IR) radiative cooling and the absorption of solar UV by O_3 and affords the stratosphere a strong static stability. Figure 2.2 shows a schematic representation of a typical high-latitude atmospheric temperature profile.
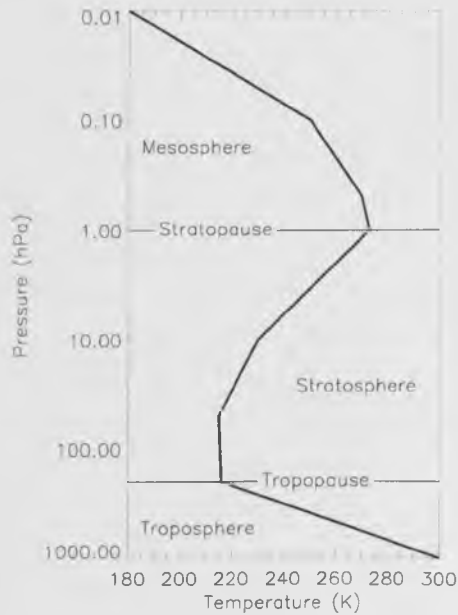
Figure 2.2: Schematic diagram of the vertical temperature profile of the atmosphere at high latitude (adapted from *Guyot*, [1998]).

2.3.2   Meridional stratospheric circulation

The upper stratosphere is considered to be approximately in radiative equilibrium with the temperature decreasing from the warm summer pole to the cold winter pole. In contrast, the lower stratosphere is disrupted by the transfer of heat and momentum by planetary wave propagation from the troposphere. Planetary wave forcing maintains extra-tropical stratospheric temperatures above thermal equilibrium. This results in additional radiative cooling and a residual downward motion. In contrast, tropical lower stratospheric temperatures are displaced below thermal wind balance resulting in radiative heating and large-scale ascent of air.

The transport of mass and energy between the stratosphere and its surrounding regions, the mesosphere above and especially the troposphere below, has been long studied. *Dobson et al.* [1929] speculated that there was a persistent global poleward and downward circulation in the stratosphere based on their measurements of the latitudinal variation in column ozone. Two decades later, following observations of dramatic
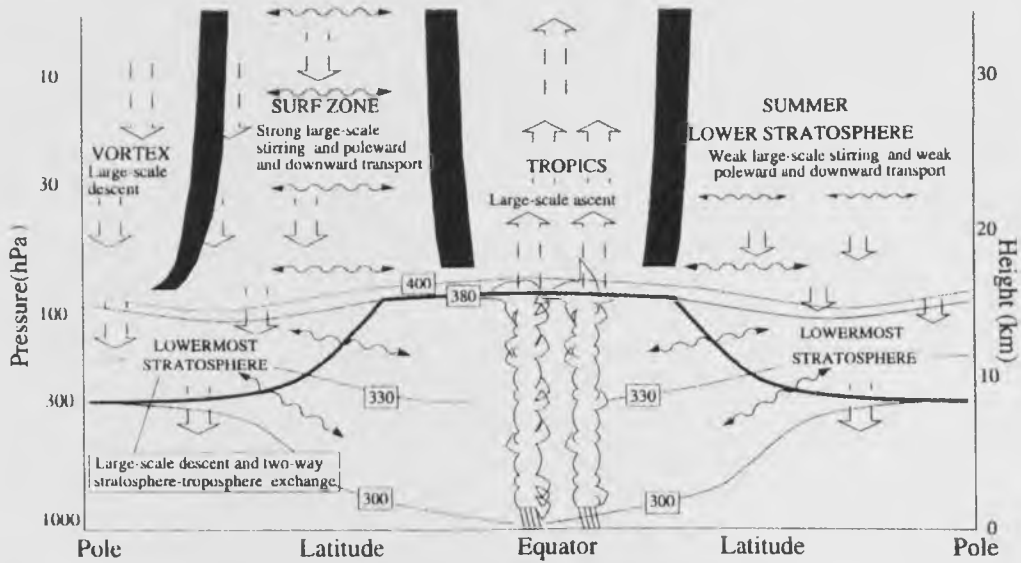
Figure 2.3: Schematic diagram of the Brewer-Dobson circulation. Reproduced from WMO [1999].

decreases in water vapour across the tropical tropopause [*Dobson et al.*, 1946], *Brewer* [1949] proposed that air ascended into the stratosphere across the tropical tropopause and travelled poleward before descending at mid and high latitudes.

Figure 2.3 shows the classical picture of the global mean stratospheric circulation with large-scale ascent in the tropics (due to widespread convection) in addition to the slower wave-induced upwelling. Most recent studies of tropospheric convection suggest that convection rarely penetrates the stratosphere but stops several kilometres short [*WMO*, 2003]. Airmasses subsequently ascend into the stratosphere under the influence of the residual circulation.

The wintertime mid-latitudes are charaterised by a "surf zone" where rapid isentropic transport is combined with slower poleward and downward motion of air. This region is stirred by breaking Rossby waves. Potential temperature surfaces greater than 380 K remain entirely within the stratosphere and no isentropic transport between the stratosphere and troposphere occurs. Below the 300 K potential temperature surface airmasses remain within the troposphere and similarly no direct isentropic stratosphere - troposphere exchange occurs. Direct transport between the mid and high latitude

stratosphere and troposphere may also occur directly on isentropic surfaces between approximately 300 and 380 K. These surfaces lie within the stratosphere at high latitudes but at lower latitudes lie within the troposphere.

2.3.3 The Polar Vortex

The isolation of an airmass for a protracted period is an essential pre-requisite for significant chemical depletion of polar stratospheric O_3. At the autumnal equinox, the polar regions experience increasing darkness and insufficient radiative heating occurs to counterbalance the infrared radiative cooling. Rapid cooling of this region, allied to warm mid-latitudes, results in a large latitudinal pressure gradient which, under the influence of the Coriolis force, results in a strong westerly wind. This polar night jet extends from 100 mb to 1 mb or higher. Air poleward of the night jet is referred to as the *polar vortex* and may evolve to be substantially different in its chemical composition compared to the mid-latitude stratosphere.

The vertical propagation of Rossby planetary waves which disrupt the polar vortex may only occur in the presence of westerly winds below a critical threshold, the *Rossby critical velocity*. The *Rossby critical velocity* is dependent upon the horizontal scale of the waves and, in practice, vertical propogation of planetary waves is limited to waves with wavenumbers 1 – 3.

Juckes and McIntyre [1987] have shown that Rossby wave breaking is responsible for detrainment of air from the edge of the vortex. This process occurs mainly in the form of filaments. The reverse process, injection of air into the vortex, also occurs on occasions although the core of the vortex is generally unaffected [*Plumb et al.*, 1994].

In the Antarctic, the polar night jet has a velocity sufficient to form a strong and persistent barrier to horizontal mixing between the polar vortex and the mid-latitudes. Combination of the mixing barrier with the extremely low temperatures found within the vortex conspire to create the ideal conditions for substantial springtime ozone losses, commonly referred to as the Antarctic ozone hole.

The Arctic polar vortex is both warmer and smaller than the Antarctic vortex, with considerable interannual meteorological variability. These differences may be attributed

to the interhemispheric differences in distribution of landmasses. In the northern hemisphere, orographically enhanced planetary wave activity may transfer energy and momentum to the Arctic stratosphere distorting and warming the polar vortex. This distortion may become large enough to cause a reversal of the mean zonal flow from westerly to easterly and cause the vortex to decay prematurely.

Major warmings occur every 2 - 3 years in the Arctic on average although they have been less frequent the 1990s. Minor warmings, which result in an increase in vortex temperature without a reversal of the mean flow, occur to some extent in all winters. Cold Arctic winter stratospheres are characterised by an absence of planetary wave activity and a stable vortex which, in turn, are coupled to meteorological phenomena such as the periodic reversal of the mean zonal wind in the equatorial stratosphere, the Quasi-biennial Oscillation (QBO).

The concept of an isolated region of the stratosphere in the polar regions during wintertime surrounded by a surf zone does not strictly apply to the lowermost stratosphere (below ~380 K). In this region, the polar night jet is weak and there is no strong barrier to mixing between mid and high latitudes. In addition, isentropic surfaces may intersect the troposphere resulting in significant horizontal transport from midlatitudes to polar regions and the reverse by synoptic-scale waves [*Holton et al.*, 1995].

2.4   Polar ozone depletion

Farman et al. [1985] discovered large springtime column O_3 losses over Antarctica. A persistent feature of this seasonal O_3 loss over the last 20 years has been the almost total loss of O_3 in the lower stratosphere. These losses have been coincident with the dramatic increase in the stratospheric halogen loading. Such large losses could not be explained by chemical models utilising gas-phase halogen chemistry alone. It has become clear that the Antarctic ozone hole is a result of a combination of dynamical and chemical factors unique to the polar regions in winter and spring.

2.4.1 Activation of halogen reservoirs

The chemical reactions responsible for the interconversion of the reservoir species ($ClONO_2$, $BrONO_2$, N_2O_5 and HNO_3) occur on aerosol surfaces. As the temperature drops below a threshold of approximately 195 K in the lower stratosphere, PSCs may form. Lower temperatures increase the rate of heterogeneous conversion of halogen reservoirs to active halogens. Reactions 2.20–2.24 list the five main activation pathways although other activation reactions may occur. The background sulphate aerosol itself may also catalyse the heterogeneous activation of halogens at low temperatures:

$$ClONO_2 + H_2O \rightarrow HNO_3 + HOCl \tag{2.20}$$

$$BrONO_2 + H_2O \rightarrow HNO_3 + HOBr \tag{2.21}$$

$$ClONO_2 + HCl \rightarrow HNO_3 + Cl_2 \tag{2.22}$$

$$N_2O_5 + H_2O \rightarrow 2HNO_3 \tag{2.23}$$

$$HCl + HOCl \rightarrow Cl_2 + H_2O \tag{2.24}$$
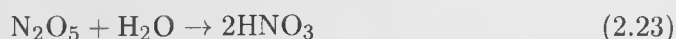
The heterogeneous activation reactions detailed above prime the polar vortex with chlorine gas (Cl_2), bromine gas (Br_2) and bromine chloride (BrCl). These halogen compounds require subsequent photodissociation to initiate the catalytic O_3 loss cycles:

$$Cl_2 + h\nu \rightarrow Cl + Cl. \tag{2.25}$$
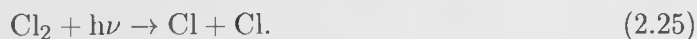
Br_2 and BrCl photolyse similarly.

2.4.2 Catalytic O_3 loss

There are a number of catalytic cycles which destroy O_3 in the polar stratosphere. Two of these cycles (involving Cl and OH) are described in Section 2.2.2. A significant loss cycle under very cold conditions involves the formation and subsequent photolysis of

the ClO dimer, dichlorine dioxide (Cl_2O_2) [*Molina and Molina*, 1987]:

$$2(Cl + O_3 \rightarrow ClO + O_2) \qquad (2.26)$$

$$ClO + ClO + M \rightarrow Cl_2O_2 + M \qquad (2.27)$$

$$Cl_2O_2 + h\nu \rightarrow ClO_2 + Cl \qquad (2.28)$$

$$\underline{ClO_2 + M \rightarrow Cl + O_2 + M} \qquad (2.29)$$

$$overall: \qquad 2O_3 \rightarrow 3O_2 \qquad . \qquad (2.30)$$
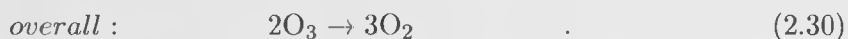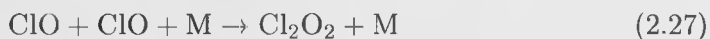
The coupled ClO and BrO cycle [*Yung et al.*, 1980] plays a significant role in polar O_3 depletion, especially in the Arctic where temperatures are generally higher and less favourable to ClO dimer formation:

$$Br + O_3 \rightarrow BrO + O_2 \qquad (2.31)$$

$$Cl + O_3 \rightarrow ClO + O_2 \qquad (2.32)$$

$$ClO + BrO \rightarrow Br + ClO_2 \qquad (2.33)$$

$$\underline{ClO_2 + M \rightarrow Cl + O_2 + M} \qquad (2.34)$$

$$overall: \qquad 2O_3 \rightarrow 3O_2 \qquad . \qquad (2.35)$$
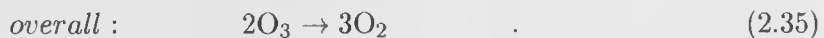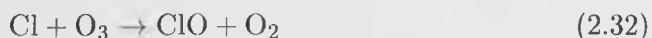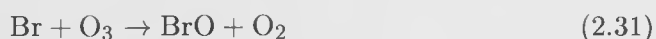
The relative contribution of each of these cycles to the overall O_3 loss in the Arctic for several winters in the late-1990s has been determined by *Millard et al.*, [2002]. Despite considerable interannual variability in the magnitude of O_3 loss associated with dynamical factors, halogen chemistry dominates O_3 loss processes in all years. The ClO-BrO cycle is the major contributor with the dimer cycle making a significant contribution during cold winters. During warmer winters, the HO_2-catalysed cycle may contribute losses comparable to the ClO-BrO cycle although the total loss is generally lower. Other loss cycles contribute only small amounts to the total O_3 loss.

2.4.3 Deactivation of halogens

Within an isolated polar vortex, catalytic ozone destruction can continue until either all the O_3 is removed, as occurs in the Antarctic, or until the ClO_x is deactivated by reconversion to reservoir species. In the Arctic, ClO_x is deactivated predominantly by reaction of ClO with NO_2 to reform $ClONO_2$ (Reaction 2.13). In the Antarctic, the

conditions of very low O_3 and low NO_x cause the ClO_x to be converted directly to HCl [e.g. *Douglass et al.*, 1995]:

$$Cl + CH_4 \rightarrow HCl + CH_3. \qquad (2.36)$$
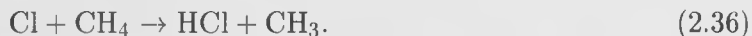
Heterogeneous conversion of N_2O_5 to form HNO_3 (Reaction 2.23) on liquid aerosols and PSCs also contributes to very low NO_2 concentrations in winter [e.g. *Noxon*, 1978; *Fahey et al.*, 1989]. The recovery of NO_2 in the sunlit spring vortex occurs in two ways: through photolysis of HNO_3 (Reaction 2.19) and reaction of HNO_3 with OH and subsequent photolysis of the NO_3 formed (Reactions 2.19 and 2.37) leading to the deactivation of ClO_x:

$$NO_3 + h\nu \quad \rightarrow \quad NO_2 + O. \qquad (2.37)$$
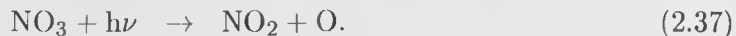
2.5   Polar stratospheric clouds

It is clearly established that under the extremely cold conditions which prevail within both polar lower stratospheric vortices during wintertime that PSCs are able to form through the condensation of trace gases (predominantly H_2O and HNO_3). PSCs play a crucial role in providing a surface to catalyse the heterogeneous chemical reactions which activate halogens from their inert reservoirs and destroy ozone. PSCs can also re-distribute condensed material vertically by gravitational sedimentation [*Solomon*, 1999]. The dynamics of the wintertime polar stratosphere is such that any redistribution of HNO_3 within an airmass is seasonally permanent and only replenished when the vortex breaks down.

2.5.1   The role of PSCs in ozone depletion

PSCs were considered to be a colourful meteorological curiosity during the winter and early springtime in both hemispheres until the discovery of the Antarctic ozone hole [*Farman et al.*, 1985]. A complete understanding of the process of polar ozone loss is dependent on a quantitative description of the chemical and microphysical properties of PSCs due to their crucial role in catalysing halogen activation.

In addition to the direct effect of PSCs as surfaces for heterogeneous halogen activation reactions, PSCs were soon implicated in more indirect effects on gas-phase chemistry. In 1986, PSCs were proposed to sequestrate gas-phase HNO_3, reducing the rate of photolytic formation of NO_x (Reactions 2.19 and 2.19) [*Toon et al.*, 1986; *Crutzen and Arnold*, 1986]. *Salawitch et al.* [1989] suggested that denitrification could contribute to the exacerbated ozone losses reported over the Antarctic. The presence of NO_y in PSCs was confirmed by observations during the 1987 Antarctic Ozone Experiment (AAOE) [*Fahey et al.*, 1989].

2.5.2 Types of PSC

Two basic types of PSC were identified by lidar (light detection and ranging) during AAOE - Type I and Type II [*Browell et al.*, 1990; *Toon et al.*, 1990]. Type II PSCs are rare in the Arctic and believed to be water ice clouds. Type I clouds are more frequently observed and are subdivided into at least two further categories based on their differing properties under lidar observation. Type Ia PSCs exhibit moderate backscatter and high depolarisation of lidar and are assumed to be aspherical solids composed largely of nitric acid hydrates. PSCs which produce moderate backscatter without depolarisation are assumed to be composed of small, spherical particles in the liquid state [*Toon et al.*, 1990]. These Type Ib PSCs are believed to be a solution of sulphuric and nitric acids with a variable composition determined by the ambient temperature [*Carslaw et al.*, 1994; *Tabazadeh et al.*, 1994]. *Peter* [1997] has reviewed the thermodynamic, microphysical and chemical properties of PSCs and the following description of PSC composition is adapted from this work.

Ice

The condensation of stratospheric water vapour to form ice is commonplace in the Antarctic wintertime stratosphere where temperatures can fall as low as 180 K for extended periods [*McCormick et al.*, 1981]. In the Arctic, where synoptic temperatures infrequently drop below the ice frost point, ice clouds may form in lee-waves where rapid adiabatic cooling may produce localised temperatures below T_{ice}. Ice particles have radii in the range 1 - 10 μm and number densities between 10^{-4} – $\sim$1 cm^{-3}. The

thermodynamic properties of ice are described by *Marti and Mauersberger* [1993]:

$$\log(p_{H_2O}) = \frac{-2663.5}{T} + 12.537 \tag{2.38}$$

where $\log(p_{H_2O})$ is the vapour pressure of water over ice in Torr. A similar expression for p_{H_2O} is also described in *Hanson and Mauersberger* [1988] although the differences between these two expressions under typical lower stratospheric conditions is negligible.

Nitric acid trihydrate

Voigt et al. [2000] have identified the existence of nitric acid trihydrate (NAT) by in-situ mass spectrometry in a PSC over Scandinavia in 1999. Laboratory determination of the vapour pressure of NAT under conditions relevant to the stratosphere have been determined by *Hanson and Mauersberger*, [1988]. NAT is thermodynamically the most stable of the HNO_3 hydrates under stratospheric conditions. The saturation vapour pressure of HNO_3 (in Torr) over NAT for the range 200 K < T < 180 K is given by:

$$\log(p_{HNO_3}) = m(T).\log(p_{H_2O}) + b(T) \tag{2.39}$$

where m(T) = -2.7836 - 0.00088T, and b(T) = 38.9855 - 11 397/T + 0.009179T.

Under typical lower stratospheric conditions (50 mb and 6 ppmv H_2O), the saturation vapour pressure of NAT (T_{NAT}) is typically $\sim$7 K higher than T_{ice}. Observations of NAT-containing Type Ia PSCs in the Arctic prior to the SOLVE/THESEO-2000 field campaign indicated that these solid particles were generally smaller than ice particles with maximum radii typically around a few μm and number densities in the range $10^{-4} - 0.1$ cm^{-3}. Vertical redistribution of HNO_3 by the gravitational sedimentation of NAT particles was considered to be insignificant due to their small size. Subsequent in-situ observations by *Fahey et al.*, [2001] have revealed the existence of very large NAT particles with radii up to 20 μm and integrated number densities of $\sim$10^{-4} cm^{-3} which may be capable of efficiently denitrifying the Arctic stratosphere [*Carslaw et al.*, 2002].

In-situ observations of total PSC particle volumes greater than those attributable to either NAT or ternary liquid aerosols [*Dye et al.*, 1990] prompted *Wofsy et al.* [1990] to propose that such particles were composed of ice coated with NAT. An alternative

explanation was provided by *Peter et al.* [1990] where NAT and ice co-condense. Gravitational sedimentation of NAT-coated ice was considered to be the most likely mechanism to account for denitrification of the Arctic stratosphere until observations of very large NAT particles by *Fahey et al.* [2001] forced a re-evaluation of the mechanism of Arctic denitrification [*Tolbert and Middlebrook*, 1990; *Middlebrook et al.*, 1996].

Nitric acid dihydrate

The existence of metastable HNO_3-containing hydrates in the polar stratosphere has been proposed. Only the vapour pressure of nitric acid dihydrate (NAD) has been measured in the laboratory in the range 190 K $<$ T $<$ 230 K:

$$\ln(p_{HNO_3}) = \frac{-22360}{T} + 84.8 - 2\ln(p_{H_2O}) \qquad (2.40)$$

where p_{HNO_3} and p_{H_2O} are the partial pressures of HNO_3 and H_2O in Torr [*Worsnop et al.*, 1993]. This study suggests that NAD is only slightly less stable than NAT under typical lower stratospheric conditions and may form more readily due to its lower free-energy barrier for nucleation.

Liquid PSCs

Thermodynamic models have been used to calculate the composition and condensed volume of liquid ternary PSCs [*Carslaw et al.*, 1994, 1995a, 1997; *Tabazadeh et al.*, 1994]. For use in large-scale models *Carslaw et al.* [1995b] derived an analytical expression for the composition of aqueous ternary $HNO_3/H_2SO_4/H_2O$ solutions under stratospheric conditions using effective Henry's Law constant (H^*):

$$\frac{(p_N^0 - p_N)}{RT} = n_S \frac{M_N}{M_S} \qquad (2.41)$$

where p_N is the equilibrium vapour pressure of HNO_3 over the droplet in atmospheres (atm) and p_N^0 is the total partial pressure of gas phase HNO_3 (atm) assuming no uptake. n_S is the concentration of H_2SO_4 (in mol m^{-3}), M_N is the molality of HNO_3 in the droplet (mol kg^{-1} H_2O), M_S is the molality of H_2SO_4 (mol kg^{-1} H_2O) and R is the gas constant ($= 8.207 \times 10^{-5}$ m^3 atm mol^{-1} K^{-1}). p_N is given by:

$$p_N = \frac{M_N}{H^*} \qquad (2.42)$$

where H^* has units mol kg^{-1} atm^{-1}.

$$H^* = \frac{H^*_{NNb}m_N}{(M_N + M_S)} + \frac{H^*_{NSb}M_S}{(M_N + M_S)} \qquad (2.43)$$

where H^*_{NNb} is the Henry's Law constant of HNO_3 in a binary $H_2O - HNO_3$ solution and H^*_{NSb} is the Henry's Law constant of H_2SO_4 in a binary $H_2O - H_2SO_4$ solution. The concentrations of HNO_3 and H_2SO_4 in the ternary solution may be related to their concentrations in the respective binary solutions:

$$\frac{M_S}{M_{Sb}} + \frac{M_N}{M_{Nb}} = 1 \qquad (2.44)$$

where M_{Nb} and M_{Sb} are the binary solution concentrations of HNO_3 and H_2SO_4.

These equations may be solved to produce analytic solutions for M_N and M_S:

$$M_S = -(A + 2\cos([E + D]/3)(A^2 - 3B)^{1/2})/3 \qquad (2.45)$$

$$M_N = M_{Nb}(1 - \frac{M_S}{M_{Sb}}) \qquad (2.46)$$

Each of the parameters A, B, D and E are given in Appendix A.

Figure 2.4 shows how the composition of the liquid phase varies as a function of temperature under typical lower stratospheric conditions according to Equations 2.45 and 2.46. The solubility of HNO_3 (and other gases e.g. HCl) is low at temperatures above 200 K and the aerosol may be considered a binary H_2SO_4/H_2O aerosol. This situation changes dramatically as the temperature is lowered until, at around 192 K, HNO_3 forms the major solute in the aerosol and it is substantially depleted from the gas phase.

2.5.3 Nucleation of solid particles

The formation of solid particles may occur either through the homogeneous freezing of liquid aerosols or heterogeneous nucleation. Ice particle formation in the stratosphere is well characterised. Experimental studies by *Koop et al.* [2000] show that ice nucleates directly from the background ternary aerosol and is dependent only on water activity. An expression for the homogeneous nucleation rate coefficient as a function of water activity and pressure is also derived.
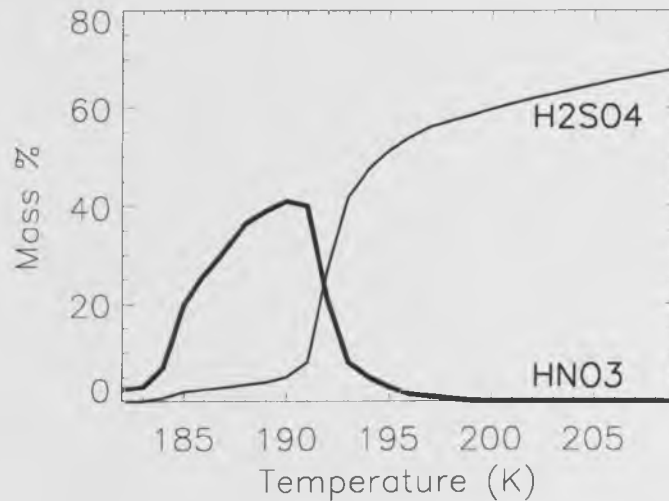
Figure 2.4: The partitioning of HNO$_3$ and H$_2$SO$_4$ as a function of temperature in STS aerosol. Reproduced from *Carslaw et al.*, [1997].

The nucleation mechanism of NAT in the stratosphere remains uncertain. *Tabazadeh et al.* [2001] have suggested that homogeneous nucleation of NAT may occur at a rate sufficient to denitrify the Arctic stratosphere based on extrapolation of laboratory data by *Salcedo et al.* [2001]. However, *Knopf et al.* [2002], have recently demonstrated using new laboratory experiments that homogeneous nucleation of NAT is too slow to account for the formation of NAT PSCs even at temperatures several K below T$_{NAT}$.

An alternative mechanism for NAT formation is through mountain wave temperature perturbations [*Meilinger et al.*, 1995; *Tabazadeh et al.*, 1996; *Carslaw et al.*, 1998, 1999]. Observations show that solid HNO$_3$ particles are produced by mountain wave ice clouds. Recent modelling studies by *Fueglistaler* [2002] have used a microphysical model to show that the widely distributed very large NAT particles at low number densities observed by *Fahey et al.* [2001] may be produced below a "mother cloud" composed of NAT, downwind of an ice cloud. *Dhaniyala et al.* [2001] have used a simple 2-D particle model to show that the formation of high number densities of NAT particles in lee waves may also produce large NAT particles at low number densities throughout cold regions of the vortex.

2.6 Denitrification and ozone loss

Denitrification may be defined as the permanent removal of NO_y from an airmass by the gravitational sedimentation of NO_y-containing particles. Denitrification reduces the formation rate of NO_x (Reactions 2.19 and 2.19) and slows the rate of ClO_x deactivation to $ClONO_2$, extending the O_3 loss period. For dynamical reasons, the Arctic vortex is warmer and more disturbed than the Antarctic vortex. Denitrification of the wintertime Arctic lower stratosphere is less intense and more sporadic than the Antarctic due to the lower frequency of formation of PSCs.

Extensive early denitrification may reduce halogen activation as an airmass depleted in HNO_3 has a reduced potential for forming the PSCs which catalyse the heterogeneous activation reactions. The PSC formation threshold is sensitive to gas-phase HNO_3 and H_2O concentrations and early denitrification may reduce the formation of PSCs and suppress the heterogeneous activation of halogens. This is discussed further in Chapter 3. Model studies of polar O_3 loss vary considerably in their complexity, from simple photochemical box models to global 3-D CTMs and coupled climate-chemistry GCMs. These models frequently ignore denitrification entirely or contain very simple thermodynamic equilibrium schemes which may be inappropriate for accurately simulating the re-distribution of HNO_3 by the sedimentation of PSCs. Several modelling studies [e.g. *Chipperfield and Pyle*, 1998; Waibel *et al.*, 1999; Tabazadeh et al., 2000, 2001], have indicated that denitrification may be important for enhancing springtime O_3 loss in the Arctic. This effect may become enhanced in the future with predicted radiatively-induced cooling of the lower stratosphere due to the increased burden of greenhouse gases in the atmosphere [*WMO*, 1999].

2.6.1 Observations of denitrification and ozone loss

Widespread and intense denitrification is a ubiquitous feature of the wintertime Antarctic stratosphere due to the persistently low temperatures of the vortex. In-situ observations of denitrification in the Antarctic stratosphere were reported by *Fahey et al.*, [1989] during AAOE. Frequent in-situ aircraft observations like these are precluded due to the remoteness of the Antarctic vortex.

Remote observations of HNO_3 from the Microwave Limb Sounder (MLS) instrument aboard the Upper Atmosphere Research Satellite (UARS) satellite have revealed that denitrification of the Antarctic lower stratosphere is essentially complete [*Santee et al.*, 1995, 1999]. *Tabazadeh et al.*, [2000], have used MLS observations of HNO_3 and H_2O together with aerosol extinction from the Cryogenic Limb Array Etalon Spectrometer (CLAES) aboard the same satellite in early winter to examine the timing of denitrification. They observed that denitrification of the Antarctic lower stratosphere occurs before the onset of temperatures low enough for the widespread formation of ice PSCs.

Cold winters are also associated with significant stratospheric O_3 depletion in the Arctic. Denitrification is more sporadic and less intensive than the Antarctic, although observations of this exist from both in-situ and remote instruments for the cold Arctic winters of 1988/89, 1994/95, 1995/96, 1996/97 and 1999/2000. In-situ measurements of NO_y made during the Airborne Arctic Stratospheric Experiment (AASE) were made by chemiluminescence during the winter of 1988/89 aboard the NASA ER-2 high altitude research aircraft. These observations revealed significant denitrification without accompanying dehydration at altitudes between 17 and 19 km [*Fahey et al.*, 1990]. Evidence for sedimentary redistribution of NO_y during this winter was supported by in situ-observations of NO_y between 10 and 12 km aboard the NASA DC-8 which indicated elevated levels of NO_y consistent with nitrification [*Hubler et al.*, 1990]. *Arnold et al.* [1989] also observed denitrification between 18 and 20 km and nitrification around 14 km during an in-vortex balloon flight carrying a mass spectrometer. They also observed denitrification during a similar balloon flight during 1992 [*Spreng and Arnold*, 1994].

During the Arctic winter of 1994/95, denitrification was observed between 18 and 20 km by an in-situ balloon-borne NO_y instrument [*Sugita et al.*, 1998]. *Fischer et al.* [1997] observed simultaneous enhancements in NO_y and HNO_3 at altitudes around 12 km. The use of separate methods of analysis for these components precluded the likelihood of instrumental effects as the cause of the enhancements which are attributed to nitrification. Further evidence of denitrification during this winter was obtained during an in-vortex flight of the Michelson Interferometer for Passive Atmospheric Sounding (MIPAS-B2) in February 1995. Strong denitrification was observed between 19 and 21 km with weaker nitrification around 13 km [*Wetzel et al.*, 1997; *Waibel et*

al., 1999].

The ER-2 made one flight into the polar vortex during the Stratospheric Tracers of Atmospheric Transport (STRAT) field campaign in 1996. Denitrification of 50% accompanied by dehydration of 0.5 ppmv at altitudes between 18.5 and 19.5 km were observed together with nitrification at 14 km. Back trajectories indicated that the sampled airmass had previously encountered temperatures below T_{ice} and selective ice-based nucleation was proposed [*Hintsa et al.*, 1998]. Significant cumulative O_3 losses (2.4 ppmv, 64%) in denitrified air were reported during the 1995/96 winter [*Rex et al.*, 1997]. Observations of continued O_3 loss in airmasses long after vortex temperatures rose above the PSC formation temperature were attributed to denitrification.

High latitude profiles of HNO_3 were recorded by the Improved Limb Atmospheric Spectrometer (ILAS) aboard the Advanced Earth Observing Satellite (ADEOS) during 1996/97. Denitrification exceeding 40% was observed in approximately 10% of profiles obtained between 18 and 23 km in late February. A region of nitrification between 13 and 15 km was also observed. Back trajectory analysis demonstrated that denitrification in airmasses was closely correlated with exposure to temperatures below T_{ice} [*Kondo et al.*, 2000]. One balloon flight in support of the ILAS instrument carrying a chemiluminescent NO_y detector also indicated moderate denitrification [*Kondo et al.*, 1999].

Dessler et al. [1999] have used MLS HNO_3 and CLAES aerosol observations combined with 4-day trajectories to examine temporary and permanent depletion of gas-phase HNO_3 during several Arctic winters. Reversible sequestration of HNO_3 by PSCs was best explained by uptake into ternary aerosols at temperatures below 196 K. Significant denitrification (of up to 17%) was only found when airmasses were exposed to minimum temperatures below 190 K during the four day trajectory. They conclude that extensive denitrification of the Arctic requires several cycles below 190 K.

The joint SOLVE/THESEO-2000 field campaign during the Arctic winter of 1999/2000 provided unprecedented observations of denitrification in the Arctic lower stratosphere by the ER-2 between January and March [*Fahey et al.*, 2001; *Popp et al.*, 2001]. All airmasses encountered over this entire period with $[N_2O] > 125$ ppbv were denitrified with maximal denitrification exceeding 80%. Remote observations from the Airborne

Submillimeter Radiometer (ASUR) during December 1999 and January – March 2000 aboard the DC-8 support the ER-2 observations. The timescale of these observations indicate that substantial denitrification had occurred between the two deployments [*Kleinbohl et al.*, 2002].

ASUR observations in January indicated the absence of a detectable signal of denitrification close to the edge of the vortex although the limited vertical resolution of the instrument in the lower stratosphere (6 – 8 km) restricts the detailed conclusions about the vertical distribution of HNO_3 which may be drawn. The MLS instrument was operated for two brief periods in February and March 2000 with restricted spatial coverage. Regions of low HNO_3 (4 ppbv) within the Arctic vortex at 465 K in February were attributed primarily to sequestration in PSCs at low temperatures. Depressed values of HNO_3 on the same isentropic surface in late March, after temperatures had risen above the PSC formation threshold, were considered to be due to a combination of photolysis, enhanced mixing from lower latitudes and denitrification. Levels of HNO_3 in plar regions recovered to similar values implying that there is no "memory" of denitrification from one year to the next [*Santee et al.*, 1999].

Richard et al. [2001] used in-situ observations from the ER-2 to quantify cumulative polar O_3 loss rates for 1999/2000. The cumulative loss by mid-March at 450 K was found to be 58%. *Gao et al.* [2001] have used the ER-2 NO_y and O_3 observations to quantify the effect of denitrification on O_3. Airmasses which were denitrified by 71% with residual NO_y (rNO_y) of 3 ppbv $\leq rNO_y \leq$ 5 ppbv were found to have an O_3 loss rate of 63 ppbv per day in late February and early March. Less severe denitrification was found to be associated with lower O_3 losses of 49 and 43 ppbv per day for airmasses with 5 ppbv $\leq rNO_y \leq$ 7 ppbv and 7 ppbv $\leq rNO_y \leq$ 9 ppbv respectively at the same time.

Significant chemical O_3 loss has been observed during several cold winters in the Arctic during the 1990s [for example, *von der Gathen et al.*, 1995; *Manney et al.*, 1996, 1997; *Bregman et al.*, 1997; *Rex et al.*, 1998]. Ozone loss rates in the Arctic were often comparable with the Antarctic but cumulative losses were lower due to the shorter loss period [*Rex et al.*, 1997]. The winters of 1995/96 and 1996/97 were characterised by unusually cold and stable polar vortices with the O_3 loss persisting into springtime [*Manney et al.*, 1997].

2.6.2 Modelling denitrification and ozone loss

Brasseur et al. [1997] used a semi-Lagrangian, 3-D off-line CTM to evaluate the effect of denitrification on O_3 depletion in the Antarctic. The model contained detailed gas-phase and heterogeneous chemistry schemes. Denitrification was parameterised using an equilibrium scheme based on the sedimentation of NAT-containing ice, which is adequate for the Antarctic where wintertime temperatures are sufficiently low for widespread ice formation. In their model, denitrification was found to delay ClO_x deactivation by two weeks and was responsible for an additional 20% O_3 depletion. *Chipperfield and Pyle* [1998] also found that denitrification tended to enhance Arctic polar O_3 loss, but they also found that very severe, early denitrification may decrease ozone loss by promoting deactivation of ClO_x to HCl, which is less efficiently re-activated.

Other modelling studies suggest that denitrification may play a more important role in the Arctic than the Antarctic, where continued springtime activation on PSCs is more effective at re-activating ClO_x. *Portmann et al.* [1996] used a 2-D model to show that denitrification is not a prerequisite for large Antarctic ozone losses. In their model, continuous heterogeneous processing at low temperatures on sulphate aerosols was sufficient to depress NO_x and maintain elevated ClO_x in spring.

Considine et al. [2000] have used a thermodynamic equilibrium parameterisation in the NASA Global Modelling Initiative (GMI) chemical transport model (CTM) which differs in key aspects from the more common approach used in the SLIMCAT (and REPROBUS) CTMs described in Chapter 3. Type I PSCs are assumed to have a ternary aerosol composition and Type II PSCs are assumed to be composed of ice with co-condensed NAT. PSC formation is only assumed when supersaturations of 10 and 1.6 over the thermodynamic equilibrium partial pressure of HNO_3 (Equation 2.39) and H_2O (Equation 2.38) respectively are achieved. A log-normal size distribution is used to determine particle radii based on an integrated number density of 10 particles cm^{-3} for the ternary aerosol and 0.01 particles cm^{-3} for ice with a standard deviation of 1.6. In common with other CTMs, denitrification only occurs by the gravitational sedimentation of ice particles containing the thermodynamic equilibrium concentration of NAT.

A photochemical box model study of the contribution of denitrification to Arctic O_3

loss in 1994/95 [*Waibel et al.*, 1999] showed that denitrification may cause an additional local 55% ozone loss by mid-April. A microphysical denitrification model was used to simulate the MIPAS-B observed NO_y in this winter. Three different denitrification schemes based on the condensation of the thermodynamic equilibrium concentration of NAT either directly or heterogeneously on ice were used. Particle number densities were prescribed to provide a best fit to observations.

No horizontal advection scheme was used in the denitrification model. Horizontal transport was achieved by homogeneous distribution with no cross-vortex mixing. This scheme does not retain horizontal gradients in tracers or particles which could be important if denitrification is a result of localised factors or its impact on O_3 is non-linear. The potential impact on O_3 loss of enhanced denitrification in a future colder Arctic stratosphere was also considered. They concluded that increased denitrification is likely to delay recovery of Arctic O_3 due to reductions in halogen loading and model simulations of future Arctic O_3 depletion are likely to require a realistic treatment of denitrification if a quantitative description of the process is to be achieved.

Tabazadeh et al. [2000] have used a photochemical box model with a comprehensive heterogeneous chemistry scheme to examine the role of denitrification in enhancing Arctic O_3 loss during the cold winters of 1994/95 and 1995/96. The magnitude of denitrification in model trajectories was modulated by varying the fall velocity of NAT particles. This simplistic approach indicted that complete denitrification of air parcels could produce a maximum additional 25% ozone loss. Denitrification of 50% was required to have a measurable impact on ozone loss. Additional model runs based on future halogen loading scenarios and a 4 K reduction in temperature indicated that the effect of denitrification would be limited to 30%.

Ozone loss during the 1999/2000 winter has been modelled by *Groß et al.*, [2002] using the Chemical Lagrangian Model of the Stratosphere (CLaMS). Hemispheric simulations were performed from mid-February to mid-March on four isentropic levels in the lower stratosphere based on an initialisation from observations and the Mainz 2-D chemical model. In order to overcome the absence of mixing normally associated with Lagrangian transport models, CLaMS used a complex physical mixing scheme based on the combination of air parcels or formation of new parcels as determined by the trajectory distribution if critical maximum and minimum trajectory separations were

exceeded.

CLaMS contained a detailed gas-phase and heterogeneous chemistry scheme with 36 species and 114 reactions. The denitrification scheme was based on a parameterisation of particle settling velocities derived from ER-2 NO_y in-situ particle observations. No nitrification was included in the model. The Lagrangian approach allows small-scale features such as filaments to be identified which are often unresolved in Eulerian models. CLaMS accurately reproduced observed O_3 loss at 425 – 450 K but underestimated loss at 475 K when compared to ER-2 observations. The model is not suitable for seasonal simulations without periodic re-initialisation because the trajectories do not descend diabatically.

Jensen et al. [2002] have used a 1-D column model to explore the sensitivity of denitrification by NAT particles to a number of factors including temperature history, number density and competition with liquid aerosols. They found that longer growth times led to larger particles and increased denitrification whilst particle concentrations were below 0.01 cm^{-3}, a factor of 100 higher than observed by *Fahey et al.* [2001] during 1999/2000. This study was limited by the use of a 1-D column as wind shear within the vortex would be expected to produce significant horizontal distributions of NAT particle trajectories as they sediment.

2.7   GCM studies of future Arctic ozone loss

There have been many GCM studies of the likely impact of the increased atmospheric burden of radiatively active gases on the future composition of the atmosphere. Particular emphasis has been placed on the potential impact of climate change on stratospheric O_3. Chapter 12 of *WMO* [1999] describes in detail seven coupled chemistry and climate models used for these studies. These models differ in their representation of many chemical and dynamical features. For example, significant variations in halogen loading, gas-phase chemistry, heterogeneous chemistry and the temperature response to greenhouse gas forcing makes direct comparison of climate models difficult. There follows a brief discussion of some of the more recent work in this area in an attempt to elucidate general trends for the future.

Shindell et al. [1998] used the Goddard Institute for Space Studies (GISS) GCM with a very simple O_3 chemistry scheme to predict future Arctic ozone depletion. Maximum ozone losses were predicted in the 2010-2020 decade based upon expected chlorine loadings and a decrease in stratospheric temperatures of around 10 K causing enhanced chlorine activation. The model did not explicitly include PSCs and related processes, though the study illustrates the potential for climate change to affect polar ozone depletion. In addition, the simplified treatment of planetary wave propagation in this study may bias the Arctic vortex towards unrealistically cold conditions not unlike the current Antarctic situation where the absence of upward wave propogation leads to an extremely cold, stable and persistent vortex.

Dameris et al. [1998] investigated the impact of predicted greenhouse gas and CFC emissions (using the IPCC IS92a scenario) on stratospheric O_3 in 2015 in an off-line coupled climate-chemistry model ECHAM3/CHEM i.e. the model had no feedback between O_3 and the GCM stratospheric temperatures which were derived using a climatology of O_3. The model used a simplified stratospheric heterogeneous chemistry scheme without denitrification. The model upper boundary is 10 hPa which is a severe limitation to meridional transport in the simulated upper atmosphere. In the northern polar region, the radiative cooling signal due to increased tropospheric GHG emissions was found to be small compared to the interannual variability. In the Antarctic, no significant recovery of springtime stratospheric O_3 was noticed despite the reduction in halogen loading. Their model predicted that Antarctic ozone recovery will be delayed by climate change.

An updated version of this model [*Schnadt et al.*, 2002] was able to reproduce the observed total O_3 trend and the springtime Antarctic O_3 losses but underestimated Arctic springtime losses between 1980 and 1990. For 2015, the model predicts a 10% decrease in total O_3 over the Antarctic in springtime (compared to 1990) due to enhanced chlorine activation at lower temperature. In the Arctic, springtime O_3 lossses were predicted to decrease by around 10% in the same period. This was attributed to enhanced deactivation of ClO_x due to in part to increased aircraft NO_x emissions in the Arctic lower stratosphere. Significantly, an increase in planetary wave activity in a warmer future troposphere led to a less stable and warmer Arctic vortex.

Most recently, Grewe *et al.* [2003] have used an updated version of the ECHAM3/CHEM

model to examine the composition of the future atmosphere based on predictions of direct GHG emissions and climate change. The overall impact was an increase in atmospheric NO_y and total O_3 (due to increased NO_x emissions) but a delay in the recovery of polar O_3 due primarily to changes in precipitation, cloud formation and circulation. They found that predictions of changes in the atmospheric composition due to temperature and water vapour changes were more reliable than those due to circulatory and precipitation changes.

There have been several studies of the potential impact of increased greenhouse gas emissions on stratospheric O_3 using the United Kingdom Meteorological Office (UKMO) Unified Model (UM) with stratospheric chemistry. *Austin et al.* [2000] have performed simulations of the period 1979 – 2015 using an extended version of the model with a full chemistry scheme including thermodynamic parameterisations of heterogeneous reactions but without denitrification. The modelled O_3 depletion was compared with observations in 1979 – 80 and 1994 – 95 and demonstrated good agreement. Antarctic O_3 depletion and total global O_3 were predicted to reach a peak in 2005. In the Arctic stratosphere, the O_3 trend was dominated by considerable interannual variation although a minimum was predicted for 2010.

An updated version of the coupled chemistry and climate UM featuring an increased upper boundary, updated rate constants and denitrification has been used by *Austin* [2002] to examine past trends in stratospheric O_3. The denitrification scheme assumes thermodynamic equilibrium formation of NAT and ice with sedimentation speeds of 0.14 and 13 mm s^{-1} respectively. It concludes that the typical interannual variability in O_3 is reproducible although discrepancies in absolute O_3 levels exist in polar regions. In the Antarctic, the model reproduces the magnitude of the O_3 loss but underestimates the area of loss and overestimates the duration of the loss with excessive interannual variation. Arctic O_3 losses are under-predicted compared to observations. Their conclusion is that coupled climate - chemistry GCMs are not yet capable of reliably predicting the future atmospheric composition.

Austin et al. [2003] have assessed GCM predictions of future polar stratopsheric O_3. The first signs of O_3 recovery (defined as the date when decadally averaged minimum O_3 starts to increase) are predicted to occur between 2001 and 2008 in the Antarctic. In the Arctic, recovery is predicted to occur slightly later (2004–2019) due to a combination of

radiative forcing and detection due to interannual variability. The ability of GCMs to accurately reproduce the dynamical processes in the current and future polar regions was identified as the dominant uncertainty.

Many of the dynamical interactions between the stratosphere and troposphere are not fully understood. Realistic quantification of the many feedbacks between dynamics and chemistry is also important. A major factor in this uncertainty is the limited model representation of planetary wave propogation, or the resultant heat flux-temperature relationship, which results in a significant cold bias in polar regions in many GCMs. The inclusion of non-orographic gravity wave drag and an increased resolution may improve model representation of these processes. Many GCM studies of the impact of increased emissions of GHG indicate a radiatively induced delay in the recovery of stratospheric O_3, especially in the Antarctic. The situation in the Arctic is less certain as any trend is masked by the considerable interannual variability in the meteorology of the Arctic polar vortex. The study by *Shindell et al.* [1998] stands out as predicting considerably enhanced O_3 losses for the Arctic region whereas other studies indicate that whilst severe O_3-loss events are possible, radiatively forced dynamical changes are more likely to reduce the severity of Arctic O_3 loss due to increased planetary wave activity. It is likely that the simplified dynamics in the *Shindell et al.* study is the cause of this discrepancy.

The inability of models to accurately reproduce the observed increase in stratospheric water vapour [*Oltmans et al.*, 2000] may also be a significant factor in the prediction of the future stratosphere. The temperature of formation of PSCs and resultant heterogeneous chlorine activation is sensitive to the prevailing water vapour concentration. Perturbations to the aerosol loading and hence, the heterogeneous activation of chlorine in the lower stratosphere due to volcanic emissions are another uncertainty. Significant volcanic events could increase stratospheric O_3 loss for a period of several years. Most of these studies have neglected the role of denitrification in their assessment of future changes to stratospheric O_3.

2.8 Summary

Tremendous progress has been made in our understanding of the dynamical, chemical and microphysical processes responsible for the observed distribution of stratospheric O_3. Despite this, a full quantitative understanding of the O_3-loss process at middle latitudes and the Arctic region have yet to be obtained. Considerable uncertainties still exist in our understanding of the formation and properties of PSCs, the rates of several key chemical reactions and the factors governing the underlying meteorology. The situation in the Arctic is considerably more uncertain than the Antarctic as interhemispheric differences in the prevailing meteorology mean that a more detailed understanding of these processes is imperative.

Model predictions of the future stratospheric O_3 layer are hampered by the complex interactions between chemistry and climate and the computational requirements of detailed model simulations. Despite the complexity of most recent models, many processes which may impact upon stratospheric O_3 are poorly represented or not included at all. One such process is denitrification. Stratospheric chemistry models and a few GCMs use thermodynamic equilibrium ice-based denitrification schemes which recent observations by *Fahey et al.* [2001] suggest are inappropriate for the current Arctic stratosphere. This thesis discusses the development of a more realistic microphysical NAT-based denitrification scheme based on new observations and an investigation of the impact of denitrification on Arctic O_3 loss.

Chapter 3

Description of the SLIMCAT model

3.1 Introduction

Atmospheric modelling aims to simulate the physical and chemical processes which occur in the atmosphere by solving the governing equations which represent these processes. A fully interactive solution describing each of these dynamic, thermodynamic and kinetic processes and their interdependencies is not feasible and suitable approximations are required in order to represent the system of interest. This study of Arctic denitrification, and its subsequent impact on stratospheric ozone depletion, utilises the SLIMCAT 3-D off-line CTM. SLIMCAT was developed by Martyn Chipperfield and Pascal Simon for the study of stratospheric processes and now forms one member of a suite of models used to simulate the chemistry of the atmosphere within the U.K.

This chapter describes the basic physical principles involved in numerical modelling of stratospheric chemistry and transport and describes the essential features of the SLIM-CAT CTM. Section 3.2 briefly describes the principles governing the transport and physical behaviour of atmospheric constituents while the subsequent section describes the essential chemical processes of relevance to this study. Finally, the detailed formulation of the SLIMCAT model is described, with particular emphasis on the default

thermodynamic (equilibrium) denitrification parameterisation used to represent the vertical redistribution of mass in polar regions due to the gravitational sedimentation of PSCs.

3.2 General theory of stratospheric modelling

3.2.1 The equation of state

For any ideal gas in the atmosphere, its equation of state may be defined in terms of temperature, pressure and density:

$$p = \rho RT \tag{3.1}$$

where p is the pressure in Pascals (Pa), T is the absolute temperature in Kelvin, ρ is the density in kg m^{-3} and R the gas constant for dry air in J kg^{-1} K^{-1}. A gas may behave as an ideal gas if the intermolecular forces are sufficiently small. The error associated with this approximation under typical atmospheric conditions for dry air is $< 0.2\%$ [*Pruppacher and Klett, 1997*].

3.2.2 The first law of thermodynamics

The first law of thermodynamics is an expression of the conservation of energy within a system:

$$dQ = dU + pdV \tag{3.2}$$

where dQ is an incremental change in the total energy transferred between an air parcel and its surroundings, dU is the change in internal energy and pd$V$ is the work done on (or by) the parcel. If the gas is considered to be ideal then combining Equations 3.1 and 3.2 for a dry atmosphere:

$$dQ = c_p dT - \frac{1}{\rho} dp \tag{3.3}$$

where c_p is the specific heat capacity of dry air (in J kg^{-1} K^{-1}). For adiabatic vertical motion $dQ = 0$, Equations 3.1 and 3.3 can be used to obtain the potential temperature

(θ) of the air parcel in K:

$$\theta = T \left(\frac{p_0}{p} \right)^{\frac{R}{c_p}}$$ (3.4)

3.2.3 Equations of motion

The law of conservation of momentum (Newton's second law of motion) relates the response of a fluid to the sum of the forces acting upon it. This may be expressed in an inertial frame of reference as:

$$\mathbf{a} = \frac{1}{m} \sum \mathbf{F}$$ (3.5)

where $\mathbf{a}$ is the inertial acceleration, m is the mass of the air parcel and $\mathbf{F}$ is the resultant force acting on it.

For a rotating frame of reference like the Earth's atmosphere, following *Jacobson* [2000], it can be shown that:

$$\mathbf{a} = \frac{d\mathbf{v}}{dt} + 2\mathbf{\Omega} \times \mathbf{v} + \mathbf{\Omega} \times (\mathbf{\Omega} \times \mathbf{R_e})$$ (3.6)

where $\mathbf{v}$ is the absolute velocity, Ω is the angular velocity of the air parcel (in radians s^{-1}) and R_e is the radius of the earth. The local acceleration ($\mathbf{a}_l$), Coriolis acceleration ($\mathbf{a}_c$) and centripetal acceleration ($\mathbf{a}_r$) are given respectively by:

$$\mathbf{a}_l = \frac{d\mathbf{v}}{dt} \qquad \mathbf{a}_c = 2\mathbf{\Omega} \times \mathbf{v} \qquad \mathbf{a}_r = \mathbf{\Omega} \times (\mathbf{\Omega} \times \mathbf{R}_e)$$ (3.7)

In the atmosphere, the air parcel is affected by the gravitational force ($\mathbf{F}_g^*$), the pressure-gradient force ($\mathbf{F}_p$), and the viscous force ($\mathbf{F}_v$). Since the Earth is rotating, the centripetal force ($-\mathbf{F}_r$) and Coriolis force ($\mathbf{F}_c$) per unit mass must be included in Equation 3.5 to give the total inertial momentum equation:

$$\mathbf{a}_l = \frac{1}{m} \left(\mathbf{F}_g^* + \mathbf{F}_p + \mathbf{F}_v - \mathbf{F}_c + \mathbf{F}_r \right).$$ (3.8)

The Coriolis force is given by:

$$\frac{\mathbf{F}_c}{m} = 2\mathbf{\Omega} \times \mathbf{v}$$ (3.9)

and the pressure-gradient force per unit area:

$$\frac{\mathbf{F}_p}{\mathrm{m}} = -\frac{1}{\rho}\nabla\mathbf{p} \tag{3.10}$$

In the absence of wind shear, $F_v = 0$ and with wind shear:

$$\frac{\mathbf{F}_v}{\mathrm{m}} = \eta\nabla^2\mathbf{v} \tag{3.11}$$

where η is the kinematic viscosity. The centripetal force may be combined with the true gravitational force to produce an effective gravitational force ($\mathbf{F}_g$):

$$\mathbf{F}_g = \mathbf{F}_g^* + \mathbf{F}_r \tag{3.12}$$

where $\mathbf{g}$ is the effective gravitational force and:

$$\mathbf{g} = \frac{\mathbf{F}_g}{\mathrm{m}} \tag{3.13}$$

Excluding turbulent effects, which is a reasonable approximation for the stratosphere, the momentum equation may be given as:

$$\frac{d\mathbf{v}}{dt} = 2\Omega \times \mathbf{v} - \frac{1}{\rho}\nabla\mathbf{p} + \eta\nabla^2\mathbf{v} + \mathbf{g} \tag{3.14}$$

3.2.4   The continuity equation

The rate of change of an atmospheric constituent, X, with time may be expressed at a fixed point or in a frame of reference which moves with X. The total derivative (dX/dt) may be expressed in 3-D as:

$$\frac{dX}{dt} = \frac{\partial X}{\partial t} + u\frac{\partial X}{\partial x} + v\frac{\partial X}{\partial y} + w\frac{\partial X}{\partial z} \tag{3.15}$$

where u, v, w are the 3-D components of the wind speed corresponding to the x, y, z directions and $\frac{\partial X}{\partial t}$ is the local derivative at a fixed point. The left side of Equation 3.15 is the total time derivative of X expressed with respect to a Lagrangian frame of reference whilst the time derivative on the right side is expressed with respect to an Eulerian frame of reference. Inclusion of the gradient operator (∇) into Equation 3.15 gives the flux divergence form of the total derivative:

$$\frac{dX}{dt} = \frac{\partial X}{\partial t} + u\frac{\partial X}{\partial x} + v\frac{\partial X}{\partial y} + w\frac{\partial X}{\partial z} = \frac{\partial X}{\partial t} + (\mathbf{v}.\nabla)X. \tag{3.16}$$

The continuity equation expresses the conservation of mass for a fluid. In the absence of internal sources of production or loss, and ignoring non-advective processes, then for the advection of an air parcel, the continuity equation may be expressed in terms of density as:

$$\frac{1}{\rho}\frac{\partial \rho}{\partial t} = -\nabla . \mathbf{v}$$ (3.17)

where $\nabla . \mathbf{v}$ is the velocity divergence and $\frac{1}{\rho}\frac{\partial \rho}{\partial t}$ is the fractional rate of increase of density.

Including photochemical production (P) and loss (L) terms into Equation 3.17 gives:

$$\frac{\partial [X]}{\partial t} = P - L[X] - \nabla . \mathbf{v}[X]$$ (3.18)

where [X] is the concentration of species X.

The choice of modelling framework is determined by the nature of the processes to be studied. Lagrangian models assume that there is no horizontal mixing (dispersion) between the model box and the surrounding air although emissions may enter through the top or bottom of the box. The air parcel is assumed to behave like a point source which is advected with the wind and typically has a resolution from a few metres to several km. Although this approach produces detailed structure, global 3-D Lagrangian models can require enormous computational resources and the Eulerian approach is generally used. In the Eulerian framework, the atmosphere is divided into a number of cells with a typical horizontal resolution of tens – hundreds of km. Vertical mixing processes in the stratosphere are generally weak due to the strong stability and weak turbulence. Horizontal mixing occurs through the formation and shearing of 2-D filamentary structures which are eventually removed by molecular diffusion or localised turbulence. High resolution numerical studies by *Waugh et al.* [1997] indicate that the mixing timescale for the stratospheric surf zone is of the order of one month. Therefore, accurate seasonal studies of transport and chemistry require the inclusion of realistic mixing, whether implicit or explicit. Mixing in Eulerian models is a product of the resolution and the advection scheme. Eulerian models generally overestimate the extent of mixing compared to the real atmosphere even when advection schemes with low numerical diffusion are used due to the relatively coarse horizontal resolution.

3.3 Chemistry

3.3.1 Kinetics

The chemistry of the stratosphere is complex and involves many species, including molecules, radicals and ions of widely differing reactivities. Experimentally determined kinetic data for many stratospheric reactions are available, for example *Sander et al.* [2000] and *DeMore et al.* [1997], and are updated periodically. Educated extrapolation of experimental results to stratospheric conditions is often required.

Rate coefficients for chemical reactions can depend on both temperature and pressure. Experimental kinetic techniques are used to determine the temperature and pressure dependence of rate constants. The rate constants of many reactions are observed to demonstrate an exponential temperature relationship denoted by the Arrhenius equation:

$$k = A\exp\left(\frac{-E_a}{\text{RT}}\right) \tag{3.19}$$

where A is the experimentally determined pre-exponential factor and E_a is the experimentally derived activation energy. For some reactions, A may also exhibit a temperature dependence.

3.3.2 Photochemistry

Solar radiation in the visible and UV regions of the spectrum contain energy comparable to the bond energies of many atmospheric components. Molecular absorption of photons of specific wavelengths causes electronic excitation. For example, for O_3:

$$O_3 + h\nu \rightarrow O_3^* \tag{3.20}$$
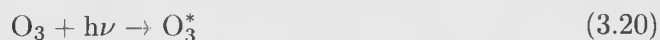
where * denotes an excited electronic state. Dissociation is one of the possible reaction pathways of the excited state(s). Other potential fates include ionisation, transfer of the energy to neighbouring molecules, quenching by molecular collision and fluorescence or chemical reaction with neighbouring molecules. The number of molecules which react along a given path per photon absorbed is the quantum yield (ϕ) for that pathway.

From the Beer-Lambert Law,

$$I_{abs} = I_0(1 - \exp(\sigma_c[X]l)) \tag{3.21}$$

where I_{abs} is the intensity of light absorbed by species X and I_0 is the intensity of the incident light (in photons cm^{-2} s^{-1}), l is the path length in cm and σ_c is the absorption cross section (cm^2 $molecule^{-1}$).

Equation 3.21 may be reduced to:

$$I_{abs} \approx I_0\sigma_c[X]l \tag{3.22}$$

if the absorption is weak in the atmosphere. Replacing I_0 with the actinic irradiance, $J(\lambda)$, which is the total irradiance at a wavelength λ in photons cm^{-2} s^{-1}. The photodissociation constant, (J) is given by:

$$J = \int \phi(\lambda)\sigma_c(\lambda)J(\lambda)d\lambda \tag{3.23}$$

and has units s^{-1}. In general, photolysis is considered to be a first order process. For example, the photolysis of ozone (Reaction 2.4) is given by:

$$Rate = J_{2.4}[O_3] \tag{3.24}$$

where $J_{2.4}$ is the photodissociation constant for Reaction 2.4.

In the atmosphere, the value of J for a chemical species is determined by its absorption spectrum. For all species at a given place the J values are affected by the overhead O_3 column, the surface albedo, and multiple scattering and absorption by atmospheric constituents (trace gases, aerosols and clouds).

3.4   SLIMCAT model formulation

SLIMCAT is an off-line Eulerian CTM which, therefore, does not solve the dynamical component of the continuity equation. Horizontal winds and temperatures are specified using meteorological analyses from either the UKMO or the European Centre for Medium-Range Weather Forecasts (ECMWF). In the strongly stable and stratified stratosphere, horizontal advection occurs mainly on isentropic levels (adiabatic

transport). The model may be run at a variety of horizontal and vertical resolutions. Typically, for polar studies, the horizontal resolution varies between 2.5° longitude × 2.5° latitude and 7.5° longitude × 5° latitude. SLIMCAT employs user-defined potential temperature levels in the range 330 K – 3000 K (approximately 10 km – 55 km) as the vertical coordinate. The vertical resolution typically varies from 18 – 36 isentropic levels with levels more closely spaced in the lower stratosphere. Vertical advection between isentropic levels is calculated from diabatic heating (cooling) rates using the MIDRAD radiation scheme [*Shine*, 1987]. Horizontal tracer advection is by conservation of second-order moments which is stable, accurate and has low numerical diffusivity [*Prather*, 1986].

3.4.1   Meteorological analyses

UKMO analyses

The UKMO analyses are based on the Unified Model and utilise a hybrid assimilation system which is terrain-following in the troposphere and follows pressure levels in the stratosphere. The model output of 3-D winds, temperature and geopotential height on a 3.75° longitude by 2.5° latitude grid are interpolated to 22 pressure levels corresponding to the UARS retrieval levels with an upper level at 0.3 hPa. The spacing between model levels produces a vertical resolution of approximately 1.5 km in the lower stratosphere [*Swinbank and O'Neill*, 1994].

No major changes were made to the analyses between December 1996 and April 2000 although there was an error in the model top level O_3 field during 1999/2000 which caused upper stratospheric temperatures to be too cold and could account for a systematic offset of ~1 K in the Arctic lower stratosphere [*R. Swinbank, pers. comm.*].

ECMWF analyses

The ECMWF analyses used in this study have changed considerably between 1996 and 2000 although the basic model remains a hybrid formulation which uses a terrain following vertical coordinate in the troposphere and a pressure coordinate in the

stratosphere. Model output is produced 6-hourly using variational assimilation (3-D VAR from January 1996 and 4-D VAR from November 1997). In 1996/1997, the model output was produced on 31 levels with stratospheric resolution of around 1.5 km in the lower stratosphere. The upper limit at 10 hPa imposes limitations on the use of these analyses for the upper stratospheric or long term studies. In 1999/2000, the vertical resolution of the model was increased to 60 levels with output at intervals of approximately 1 km in the lower stratosphere and an upper limit of 0.1 hPa.

In this thesis, the analyses were used on a 2.8° by 2.8° Gaussian grid associated with a T42 spectral resolution.

3.4.2 SLIMCAT chemistry

The model contains a detailed gas-phase stratospheric chemistry scheme which is described in more detail in Appendix B [see also *Chipperfield*, 1999]. Chemical rate constants are obtained from laboratory data [*DeMore et al.*, 1997] with updates of some NO_x reactions from *Brown et al.* [1999a, 1999b]. Photodissociation constants are calculated in the model using a 4-D look-up table of pressure, temperature, O_3 column and solar zenith angle based on [*Lary and Pyle*, 1991; *Lary*, 1991]. The effect of spherical geometry and multiple scattering are included. The model has a fixed albedo and contains no description of cloud effects. The model also contains a treatment of heterogeneous reactions on liquid aerosols, NAT and ice which is described in more detail below.

Chemical families

The high computational demands of integrating all the model chemical species separately is too great for contemporary 3-D CTMs. Furthermore, it is probably undesirable to advect short-lived species separately. To overcome this problem, SLIMCAT adopts the family approach to integrating the chemical continuity equations. In this approach, photochemical equilibrium between certain short-lived species listed in Table 3.1 is assumed.

Fixed	N_2, O_2, H_2, H_2SO_4
Long-lived	$CH_4, CO, H_2O, N_2O, CFC-11, CFC-12$
Steady-state	$HO_x(H, HO, HO_2)$
	$CH_yO_x(CH_3, CH_3O, CH_3O_2, CH_2O, HCO, CH_3COOH)$
Short-lived	$O_x(= O(^3P), O(^1D), O_3), H_2O_2,$
	$NO_x(= N, NO, NO_2), NO_3, N_2O_5, HNO_3, HNO_4,$
	$ClO_x(= Cl, ClO, Cl_2O_2), HCl, HOCl, OClO, ClONO_2,$
	$BrO_x(= Br, BrO), HBr, HOBr, BrCl, BrONO_2$

Table 3.1: Chemical species incorporated in the SLIMCAT equilibrium model. Sulphate aerosol loading is updated monthly from SAGE II satellite data.

An example of the family approach in SLIMCAT is provided by the Chapman chemistry of O_x (Reactions 2.2 – 2.4). Ignoring transport, the continuity equation for O_3 is given by:

$$\frac{\partial[O_3]}{\partial t} = k_{2.3}[O_2][O][M] - J_{2.4}[O_3] - k_{2.4}[O_3][O] \tag{3.25}$$

Similarly the continuity equation for O is:

$$\frac{\partial[O]}{\partial t} = J_{2.4}[O_3] + 2J_{2.2}[O_2] - k_{2.4}[O_3][O] - k_{2.3}[O_2][O][M] \tag{3.26}$$

Summing these equations gives the continuity equation for O_x:

$$\frac{\partial[O_x]}{\partial t} = 2J_{2.2}[O_2] - 2k_{2.4}[O_3][O] \tag{3.27}$$

Reactions 2.3 and 2.4 are not represented in the continuity equation for O_x as they represent the inter-conversion of O_x with no net change. The photochemical steady-state ratio of O_3 and O is given by:

$$\frac{[O]}{[O_3]} = \frac{J_{2.4}}{k_{2.3}[O_2][M]} \tag{3.28}$$

The assumption of photochemical steady-state may not be valid at night and species with long lifetimes in darkness (for example OClO) are not included in model families.

Heterogeneous chemistry

Chemical reactions on the surface of PSCs play a critical role in the halogen-catalysed depletion of polar ozone. The heterogeneous conversion of stable reservoir species to more active forms typically occurs in several steps. For example, the heterogeneous reaction of HCl and $ClONO_2$ (Reaction 2.22) begins with the adsorption of HCl on to the surface of the particle. The reaction occurs when a molecule of $ClONO_2$ with sufficient kinetic energy collides with the particle. Therefore, heterogeneous reactions may be treated as pseudo-first order. The rate of reaction is given by:

$$\frac{-d[ClONO_2]}{dt} = k'_{2.22}[ClONO_2] \tag{3.29}$$

where $k'_{2.22}$ is the equivalent first order rate constant. From kinetic theory:

$$k'_{2.22} = \frac{1}{4}\bar{\nu}_{ClONO_2}\gamma_{2.22}\bar{A} \tag{3.30}$$

where $\bar{\nu}_{ClONO_2}$ is the mean speed of $ClONO_2$ molecules, $\bar{A}$ is the available surface area of the particles and $\gamma_{2.22}$ is the experimentally derived reaction probability. $\bar{\nu}_{ClONO_2}$ is derived from kinetic theory.

SLIMCAT contains a detailed heterogeneous chemistry scheme. Reactions occur on the surface of frozen particles (ice and NAT) or liquid aerosols depending on the ambient temperature of the gridbox. Kinetic data is generally obtained from *DeMore et al.* [1997]. The reaction probabilities (γ) assumed for the different particles are given in Appendix B. The rates of heterogeneous reactions are parameterized following *Hanson and Ravishankara* [1994] using the HCl solubility of *Luo et al.* [1995]. The γ values for heterogeneous reactions on liquid aerosol is parameterized following the results of *Hanson et al.* [1996].

PSCs are assumed to be in thermodynamic equilibrium with the bulk gas-phase fields, with no modification of the model temperature to account for supersaturation. The composition of liquid aerosols (containing HNO_3, H_2SO_4, H_2O and HCl) is calculated analytically [*Carslaw et al.*, 1995a, 1995b].

The equilibrium saturation vapour pressure of H_2SO_4 is taken from *Ayers et al.* [1980]. The mass of condensed NAT formed in the model is as described by *Hanson and Mauersberger* [1988] and shown in Equation 2.39.

Pressure (hPa)	Ice saturation Temperature (K)	
	Murray [1967]	Hanson and Mauersberger [1988]
10	180.6	179.5
30	186.4	185.5
50	189.3	188.4
70	191.2	190.4
100	193.3	192.5
200	197.5	196.8

Table 3.2: Comparison of ice saturation temperatures from two parameterisations assuming 5 ppmv H_2O.

The presence of ice is tested using the following expression:

$$p^0_{H_2O} = 610.78 \exp \left(21.875 \frac{T - 273.16}{T - 7.66} \right) \quad (3.31)$$

where $p^0_{H_2O}$ is the saturation vapour pressure of water over ice in Pa and T is the temperature in Kelvin [*Murray*, 1967]. Ice is assumed to incorporate NAT as a co-condensate (though the heterogeneous chemical rates on the surface assume pure ice) and HNO_3 is removed from the gas phase according to the expression of *Hanson and Mauersberger* [1988].

Comparison of Ice Saturation Equations

Several alternative expressions exist to describe the saturation vapour pressure of water over ice. Assuming typical lower stratospheric water concentrations of 5 ppmv, the ice saturation temperature at varying pressures for the two expressions is given in Table 3.2.

The calculated temperature of ice formation under the conditions described show that the expression used in the SLIMCAT model (Equation 3.31) produces a greater region below the ice condensation temperature than the alternative expression from *Hanson and Mauersberger* [1988]. *Marti and Mauersberger* [1993] also describe an expression for the determination of the saturation vapour pressure of water over ice. Under the

conditions described in Table 3.2, calculated ice formation temperatures are within 0.2 K of those obtained from *Hanson and Mauersberger* [1988]. Available surface areas for heterogeneous chemistry are determined from the condensed masses assuming either a fixed number density or a fixed radius.

3.5 Summary

This chapter described the basic physical and chemical principles which underpin chemical modelling of the stratosphere. The SLIMCAT 3-D CTM used to perform thermodynamic equilibrium denitrification simulations for the Arctic 1999/2000 winter was also described. These simulations are discussed in detail in Chapters 4 and 8. The SLIMCAT CTM described here is also used for the advection of tracers when coupled to the Lagrangian microphysical denitrification model which is discussed further in Chapters 6 and 7.

Chapter 4

SLIMCAT thermodynamic equilibrium denitrification

4.1 Introduction

Full microphysical PSC schemes are complex and computationally extensive for inclusion into global 3-D models. The SLIMCAT CTM, in common with other CTMs and GCMs, uses simplified PSC schemes for the determination of heterogeneous chemistry and denitrification. These schemes are generally based on the assumption of thermodynamic equilibrium between the particles formed (whether liquid aerosol, NAT or ice) and the gas-phase. Denitrification is achieved by the application of a specific fall velocity to the particles. Such PSC schemes are easily implemented and are computationally efficient. This chapter examines whether thermodynamic equilibrium denitrification schemes are able to capture the observed Arctic denitrification during the winter of 1999/2000.

Before considering the implementation of NAT and ice-based denitrification schemes in SLIMCAT, the temperature structure of the polar vortex is considered. Temperature plays a crucial role in the calculation of denitrification in any model. The SLIMCAT 3-D CTM used for the modelling studies discussed in this chapter is forced with meteorological analyses from both the UKMO or ECMWF. All simulations using the new

microphysical model (Chapters 6 and 7) use only the ECMWF analyses. Model results from two cold Arctic winters (1999/2000 and 1996/97) are presented in this thesis, and this chapter discusses the prevailing meteorology of each.

4.2   The Arctic winter of 1999/2000

The Arctic winter of 1999/2000, following two relatively warm winters, was characterized by a cold and persistent vortex [*Manney and Sabutis*, 2000]. Temperatures remained below the nitric acid trihydrate (NAT) equilibrium temperature T_{NAT}, a nominal PSC formation temperature, from mid-December to early March (see Figure 4.1). These conditions caused widespread denitrification which, for the first time, was observed in the Arctic. Satellite observations of HNO_3 suggest that there was extensive denitrification around the 465 K potential temperature level which persisted long after temperatures rose above the PSC threshold in early March [*Santee et al.*, 2000].

4.2.1   Comparison of UKMO and ECMWF analyses

Buss et al. [2003] have compared the UKMO and ECMWF analyses with radiosondes and the NASA high-altitude research aircraft (ER-2) in-situ temperature data from the Meteorological Measurement System (MMS). This study found that the ECMWF analyses had lower scatter but UKMO reproduced the lowest temperatures better. The first in-vortex ER-2 flight was on 20th January 2000, at a time when vortex temperatures were increasing from the very low values in early January. In contrast, *Drdla et al.* [2002] used the UKMO analyses to simulate the formation of solid PSCs in a trajectory model. They found that the UKMO temperature minima were too cold by between 1 and 3 K in January. *Manney et al.* [2002] have compared six meteorological analyses during two cold Arctic winters (1995/96 and 1999/2000). They conclude that in January, the UKMO analyses were colder than other analyses, producing air parcel trajectories with significantly longer durations continuously below T_{NAT}.

Figure 4.1 shows the minimum temperature north of 50°N at 46 hPa from the UKMO analyses for the Arctic winters of 1994/95 to 1999/2000 and the minimum temperature

at 44 hPa for the ECMWF analyses of winter 1999/2000. In the UKMO analyses, winter 1999/2000 was one of the coldest of the past six years. As well as showing a long period below T_{NAT}, winter 1999/2000 also showed the longest period below the ice equilibrium point (T_{ice}). During the coldest period from mid-December 1999 to late January 2000, with temperatures well below the NAT point, temperature minima from the UKMO analyses were ∼1–3 K lower than the ECMWF analyses. This difference is also evident in comparisons of the UKMO analyses with the National Centers for Environmental Prediction (NCEP) analyses [*Manney and Sabutis*, 2000].
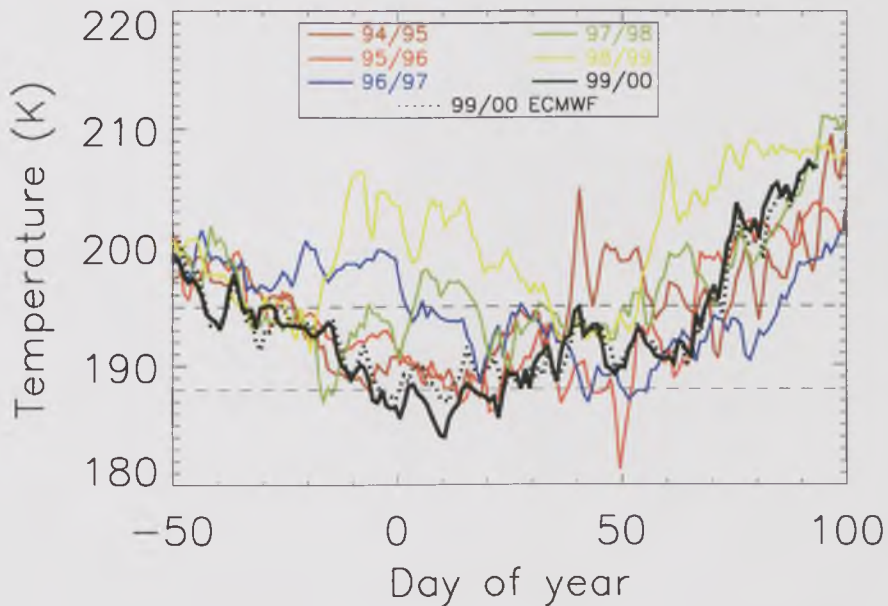
Figure 4.1: Minimum temperature in the UKMO analyses at 46 hPa poleward of 50°N for the Arctic winters 1994/1995 to 1999/2000 and ECMWF analyses at 44 hPa for 1999/2000.

The UKMO analyses produce a considerably greater area below T_{ice} than the ECMWF analyses in late December and January. Ice saturation covered an area of six million km² at its peak on January 10 using the UKMO analyses whereas the ECMWF analyses produced an area of only 1 million km² at the same time on the 460 K potential temperature surface.
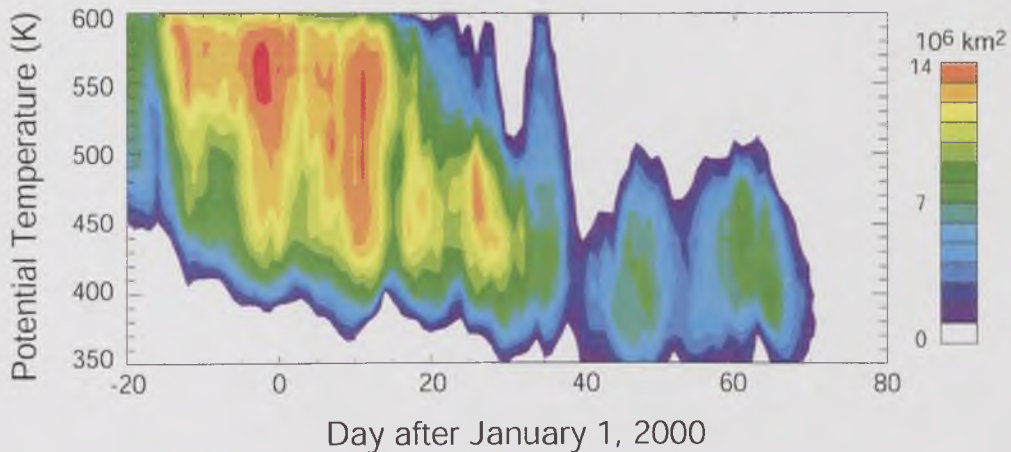
Figure 4.2: Modelled area of NAT supersaturation for 1999/2000 as a function of potential temperature from ECMWF analyses.

Figure 4.2 shows the evolution of the vertical distribution of the area of NAT supersaturation produced by the ECMWF analyses. Between late-December and mid-January, the analyses produce an extended area below T_{NAT} in a region from ~600 K to ~420 K. Vortex temperatures remained below T_{NAT} until early March although the extent of the NAT supersaturated region was significantly reduced after a warming event in February. The UKMO analyses produce a similar extent of NAT supersaturation. Figure 4.3 compares UKMO and ECMWF analyses inside the polar vortex at 460 K on the SLIMCAT model grid. At temperatures above 200 K the analyses agree well, but the UKMO analyses are consistently colder in the coldest regions of the lower stratospheric vortex, especially in mid-winter. Table 4.1 summarizes the differences at 460 K; between December 9, 1999 and January 7, 2000 the UKMO temperatures are significantly colder (-2.33 K, standard deviation 0.70 K) when the temperature is below 190 K and when $190 < T_{UKMO} < 195$ (-1.37 K ±0.73 K). Between January 8 and February 6, 2000 the UKMO analyses are also colder than the ECMWF analyses below 190 K (-2.46 K ±1.59), though the scatter is larger.

The UKMO and ECMWF analyses are clearly different in the 1999/2000 Arctic lower vortex. In order to determine which analyses are more realistic at high latitudes the
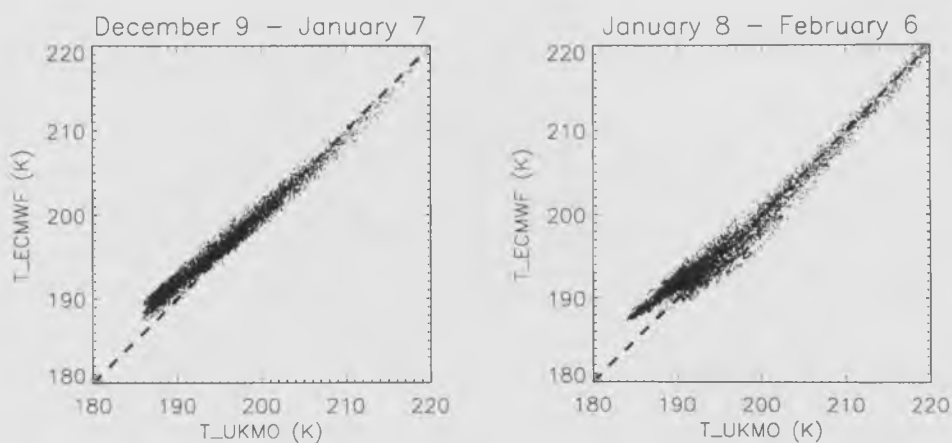
Figure 4.3: Scatter plot of in-vortex ECMWF and UKMO analyzed temperatures for the periods December 9, 1999 - January 7, 2000 and January 8, 2000 - February 6, 2000 interpolated to 460 K. The vortex is defined by UKMO potential vorticity > 30 PVU.

Date	T range (K)	Mean ΔT (K)	Standard Deviation (K)
Dec 9-Jan 7	< 190	-2.33	0.70
	190<T<195	-1.37	0.73
	> 195	-0.35	0.86
Jan 8-Feb 6	< 190	-2.46	1.59
	190<T<195	-0.77	1.18
	> 195	0.46	1.16
Feb 7-Mar 7	< 190	-	-
	190<T<195	0.24	0.68
	> 195	1.14	0.93

Table 4.1: Mean vortex UKMO - ECMWF temperature difference at 460 K.

analyses are compared with sonde data. Figure 4.4 compares the analyses with temperatures from ozone sonde launches at Ny Ålesund. (Note that these temperature observations are not routinely assimilated in the ECMWF analyses, though it is possible for launches before 1100 UT).

During the mid-winter period, where large UKMO-ECMWF temperature discrepancies exist in the lower stratosphere, the sondes show better agreement with the ECMWF analyses (Appendix C). Although this sonde comparison indicates the ECMWF temperatures are closer to independent observations, our comparisons with the in-situ ER-2 Meteorological Measurements System (MMS) [*Scott et al.*, 1990] temperature observations are not so clear. For example, on the flight of January 20, when temperatures below 191 K were observed by the ER-2, MMS temperature measurements were generally lower than both ECMWF and UKMO analyses at cruise altitudes. These results are not shown. Previous studies, using analyses for previous years, have shown that both the UKMO [*Pullen and Jones*, 1997] and the 31-level ECMWF (with a top boundary at 10 hPa) [*Knudsen*, 1996] analyses have tended to underestimate the possible extent of PSCs. In winter 1999/2000 the bias in the meteorological analyses during the coldest period is in the opposite sense to previous years with the UKMO analyses significantly colder than sondes. The new 60-level ECMWF analyses are in good agreement with observations.

The result of this analysis is supported by *Manney et al.* [2001] who found that the UKMO analyses were the coldest of the six analyses studied during December 1999 and January 2000 whilst the ECMWF analyses were coldest when temperatures were higher in February. The UKMO Unified Model contained an error in the top level O_3 field during this time which may have been a contributory factor. The ECMWF analyses have undergone considerable changes over the preceeding four years and are now produced by a 4-D variational analysis on 60 levels and appear to be the most realistic for this winter.
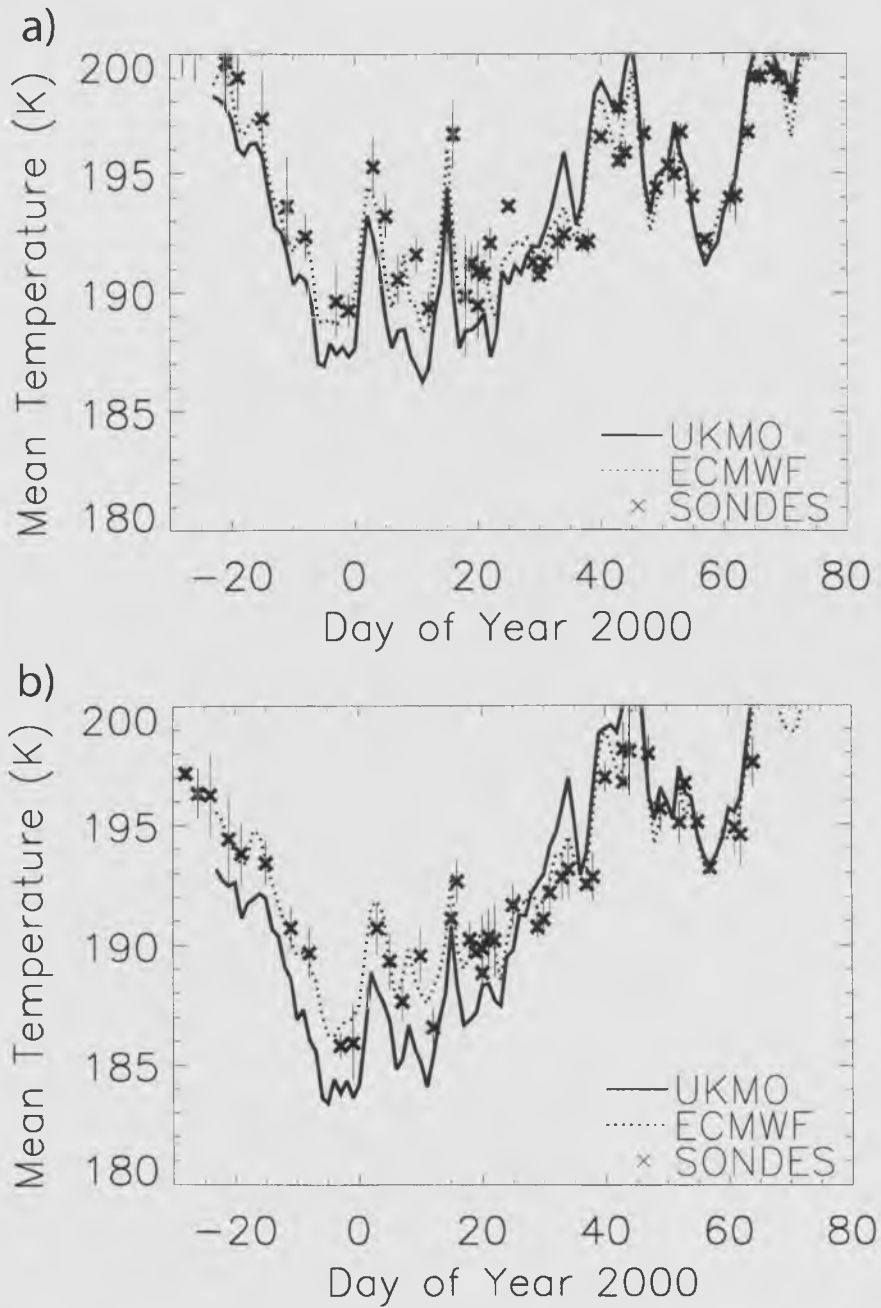
Figure 4.4: Comparison of UKMO and ECMWF temperature analyses with temperatures from ozone sonde flights from Ny Ålesund (79°N, 12°E) at (a) 460 K and (b) 506 K during winter 1999/2000. (Sonde temperatures are averaged over the model gridbox and vertical bars indicate 1 standard deviation.)
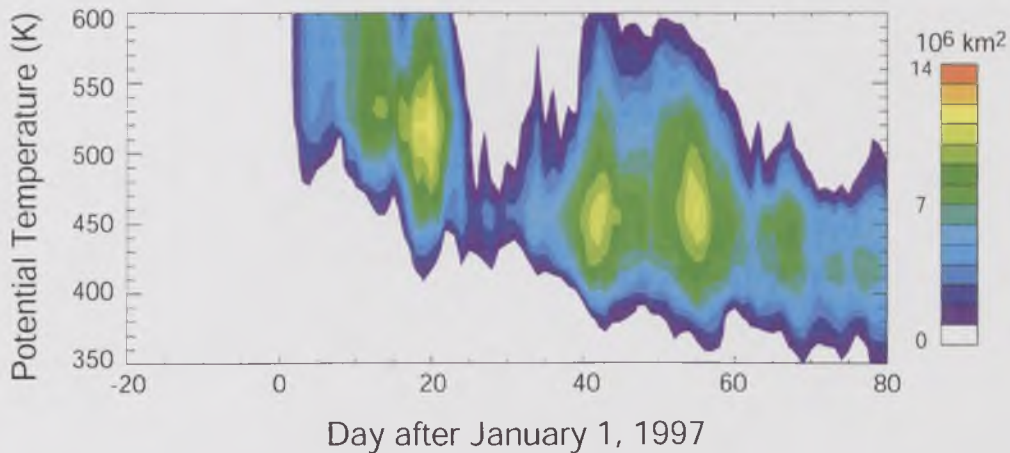
Figure 4.5: Modelled area of NAT supersaturation for 1996/97 as a function of potential temperature from ECMWF analyses.

4.3 The Arctic winter of 1996/97

The Arctic winter of 1996/97 was the third cold Arctic winter in a row. The early winter period (December 1996–January 1997) was characterised by a warm and disturbed vortex due to planetary wave activity reducing the intensity of the polar night jet. This was followed by a long period in February–April 1997 where wave activity was weak resulting in a strong and stable polar vortex. Figure 4.5 shows the area of the northern hemisphere where temperatures in the ECMWF 31-level operational analyses were below T_{NAT}. During the early winter period, the low temperatures were mostly confined to the region between 500 and 600 K and occupied a considerably smaller area than the corresponding period of 1999/2000. The polar vortex persisted until early May, over a month longer than the climatological mean for the Arctic vortex [*Pawson and Naujokat*, 1999].

4.4 Equilibrium model description

4.4.1 Model initialisation

A basic model run (using UKMO analyses) was initialized in October 1991 from a 2-D latitude – height model and integrated until December 1999 using UKMO analyses. Then eight 120-day experiments were initialized from this basic run. These experiments are described in the following paragraphs and a summary of these experiments is given in Table 4.2.

Both 24-hourly, 22-level UKMO [*Swinbank and O'Neill*, 1994] and 6-hourly 60-level ECMWF analyses have been used to force the model used in this Chapter. The model resolution was $7.5°$ longitude $\times$ $5°$ latitude $\times$ 18 isentropic levels from 330 to 3000 K (approximately 10 to 55 km). In all comparisons, model output is at 12 UT and is not temporally interpolated to observations.

A modelled passive ozone tracer was initialized from the model ozone field on December 1, 1999 and was used to diagnose chemical ozone loss. Despite the lower resolution, our results are in agreement with those obtained from the higher resolution simulation of this winter [*Sinnhuber et al.*, 2000].

4.4.2 Model denitrification schemes

Two different denitrification schemes have been used in the SLIMCAT model; one in which denitrification is driven by sedimentation of ice on which NAT has condensed; and one in which denitrification is based on sedimentation of NAT alone. In both schemes only liquid aerosol particles exist above T_{NAT} and NAT is assumed to form at T_{NAT}. The schemes differ in their treatment of NAT and ice. In the first scheme ice is assumed to form at the ice frost point and to remove gas phase HNO_3 as co-condensed NAT. In this scheme, ice particles are assumed to have a radius of 10 μm and a fall velocity of approximately 1500 m/day and NAT particles, released upon ice evaporation, are assumed to have a radius of 1 μm [*Larsen*, 1991]. Denitrification in this scheme is effectively due only to ice particles containing co-condensed HNO_3. For

Run	Analyses	Het. Chem.	Surface Area	Denitrification
UKICE	UKMO	LA/NAT/ice	10 cm^{-3} NAT, 10 μm ice	10 μm NAT/ice
UKNOD	UKMO	LA/NAT/ice	10 cm^{-3} NAT, 10 μm ice	none
ECICE	ECMWF	LA/NAT/ice	10 cm^{-3} NAT, 10 μm ice	10 μm NAT/ice
ECNOD	ECMWF	LA/NAT/ice	10 cm^{-3} NAT, 10 μm ice	none
UKNAT	UKMO	LA/NAT	0.5 μm (max. 1 cm^{-3}) NAT	6.5 μm NAT
UKNND	UKMO	LA/NAT	0.5 μm NAT	none
ECNAT	ECMWF	LA/NAT	0.5 μm (max. 1 cm^{-3}) NAT	6.5 μm NAT
ECNND	ECMWF	LA/NAT	0.5 μm NAT	none

Table 4.2: SLIMCAT 3-D equilibrium denitrification model runs

non-denitrified model runs, particle sedimentation is switched off. This scheme is the default denitrification scheme in SLIMCAT and is used in many CTMs.

In the second scheme no ice forms in the model. NAT particles are represented by a bimodal distribution (radii 0.5 μm and 6.5 μm) based on observations of *Fahey et al.* [2001]. Fall velocities of 1 m/day and 1100 m/day, respectively, are used for the two modes. In this scheme, denitrification occurs by the sedimentation of the large NAT particles, while heterogeneous chemical reactions are calculated on the small NAT mode, which has the greatest surface area density. The number density of the small mode is set to be 1 cm^{-3} and the condensed HNO$_3$ mass is assigned to this mode to produce particles with a mode radius of 0.5 μm. Any additional condensed HNO$_3$ is assigned to the large mode. For non-denitrified model runs using this scheme, the number density is not fixed and all the condensed mass is assumed to be in the small mode. Particles are assumed to reach the equilibrium size instantaneously in model runs, a process which may not be representative of the real atmosphere, especially for the large particles [*Carslaw et al.*, 2001]. The equilibrium liquid aerosol/NAT/ICE model chemistry scheme assumes that liquid aerosol exists only for T > T$_{NAT}$, NAT exists only for T$_{ice}$ < T < T$_{NAT}$, and ice exists only for T < T$_{ice}$.

The different model runs are listed in Table 4.2. Model runs UKNAT and ECNAT have a bimodal distribution of NAT with radii of 0.5 μm and 6.5 μm with a maximum number density for the small mode of 1.0 cm^{-3} with the remaining condensed mass

redistributed to the large mode [*Fahey et al*, 2001]. Model runs UKNND and ECNND have all the condensed mass in 0.5 μm NAT particles. For sedimentation NAT particles have a radius of 1 μm and ice particles have a radius of 10 μm with fall velocities of 40 m/day and 1500 m/day for UKICE and ECICE. Model runs UKNAT and ECNAT have a NAT fall velocity of 1 m/day and 1100 m/day for the 0.5 μm and 6.5 μm modes, respectively [*Larsen*, 1991]. These eight model runs cover the combinations of different analyses and different denitrification schemes with the corresponding non-denitrified runs.

4.5 Model results and comparison with observations

In this section modelled denitrification and dehydration are compared with in-situ and remote observations using a variety of instruments during the SOLVE/THESEO-2000 field campaign.

4.5.1 Modelled denitrification

Figure 4.6 shows the extent of modelled denitrification in ppbv of HNO_3 for the runs UKICE, ECICE, UKNAT and ECNAT on 5 days from late December to mid-January at 460 K diagnosed by comparison with their non-denitrified model runs (UKICE-UKNOD, ECICE-ECNOD, UKNAT-UKNND and ECNAT-ECNND).

Using the ice denitrification scheme, which was the default scheme in previous SLIM-CAT studies, the UKMO analyses produce strong, extensive denitrification in the lower stratosphere, which develops between late December and early January. The calculated vortex mean denitrification for UKICE for March, 2000 at 460 K is 65% (diagnosed from UKICE - UKNOD). This is the first Arctic winter since initialization in 1991 that this version of the model has produced denitrification, although observations have indicated that denitrification has occurred in previous winters. The magnitude of denitrification is significantly smaller when ECMWF analyses are used in conjunction with the ice scheme (16% at 460 K as a vortex mean, diagnosed from ECICE - ECNOD) as expected based on the limited period below T_{ice}.
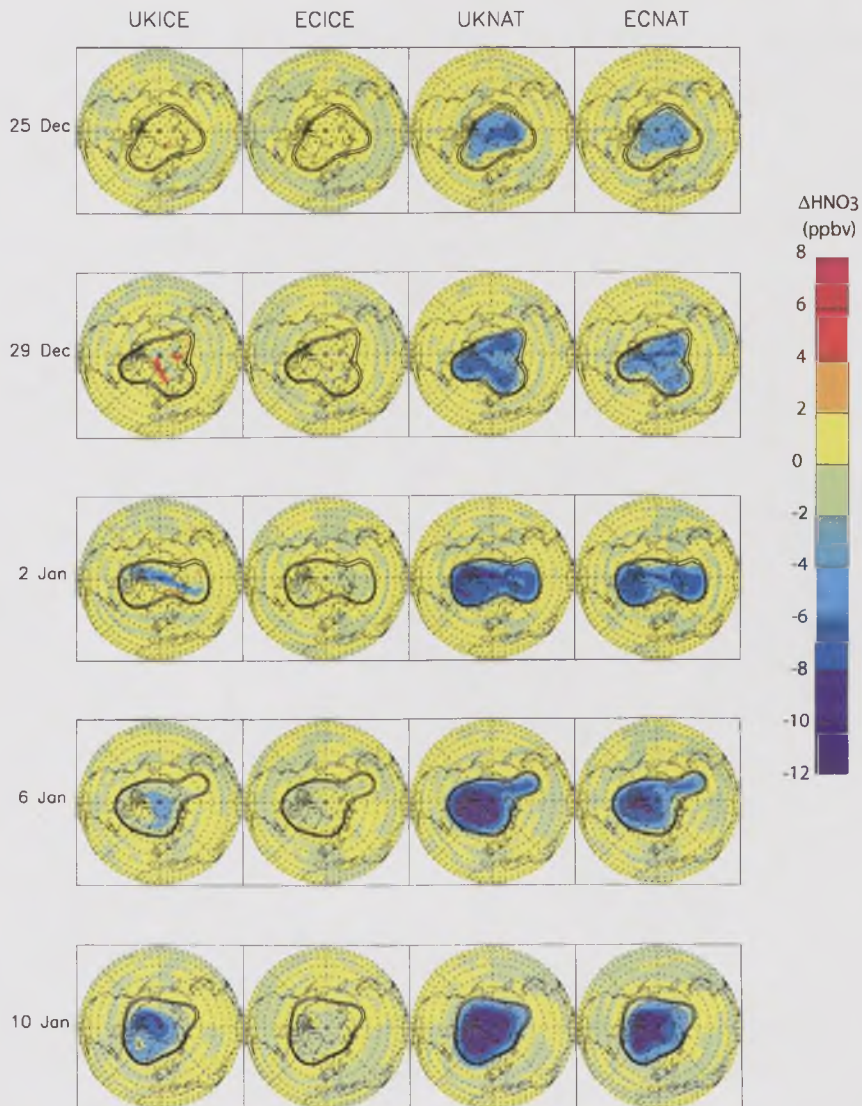
Figure 4.6: Modelled denitrification (in ppbv of HNO_3) on 5 days for winter 1999/2000 at 460 K. Also shown are the 28 and 30 PVU UKMO potential vorticity contours.

In the model, sedimentation of large NAT particles causes greater denitrification than the equivalent ice-based schemes. This difference is especially pronounced for the ECMWF analyses. Denitrification in NAT-based model runs starts earlier and is more extensive relative to the ice-based model runs. Although the denitrification starts

slightly earlier in the UKNAT run, both UKMO and ECMWF analyses give similar extents of denitrification at this level by early January. Using the colder UKMO analyses and the NAT scheme, vortex mean denitrification at 460 K for March, 2000 (from UKNAT - UKNND) is 77% whilst the modelled vortex mean denitrification using ECMWF analyses (ECNAT - ECNND) is 60%.

4.5.2 Comparison of modelled and observed NO_y

The different model runs are now compared with NO_y observations obtained during SOLVE/THESEO-2000 with the aim of evaluating the different schemes. Although the 3-D model denitrification schemes are relatively simple, their ability to capture the extent and timing of the observed denitrification in winter 1999/2000 is crucial when conclusions on the chemical effect of denitrification on chlorine chemistry and ozone depletion are to be drawn. Details of the NO_y instrument are given in Appendix D.

Figure 4.7 compares modelled NO_y with ER-2 observations [*Fahey et al.*, 2001] for four in-vortex flights on (a) January 20, 2000, (b) February 3, 2000, (c) March 7, 2000 and (d) March 12, 2000; chosen to represent the temporal evolution of the denitrification profile. Also shown are comparisons of SLIMCAT denitrification (UKICE-UKNOD, ECICE-ECNOD, UKNAT-UKNND and ECNAT-ECNND) and ER-2 denitrification (NO_y-NO_y^*) against θ for the same four flights (panels (e)-(h)). NO_y^* was obtained using data from the Mark IV balloon flight of December 3, 1999 using the relation $NO_y^* = 17.0959 - 0.02046[N_2O] - 0.000105[N_2O]^2$ (following *Fahey et al.* [1990]) and using Argus tunable diode laser N_2O [*Jost et al.*, 1998]. Experimental uncertainties for NO_y and N_2O are reported to be 20% and 10% respectively.

Figure 4.8 compares the profiles of mean denitrification inside the polar vortex from all ER-2 flights from January 14, 2000 to March 12, 2000. Modelled denitrification is diagnosed from the difference between the denitrified and non-denitrified pairs of model runs and ER-2 denitrification is calculated from NO_y - NO_y^*. This approach is used as the model NO_y^* (N_2O) is systematically low in the vortex. The data have been averaged in 10 K potential temperature bins and the vortex was defined as PV > 19 PVU at 420 K. The error bars show $\pm$ 1 standard deviation. ER-2 NO_y^* for January 23 uses ALIAS N_2O with an estimated accuracy 2-10%. For air masses with T < T_{NAT}, small particles

are oversampled by the NO_y instrument, thus enhancing the NO_y signal. Therefore, the magnitude of denitrification inferred from these data is a lower limit.

The observations clearly show regions of strong denitrification (up to 12 ppbv) at 460 K and evidence for nitrification below 400 K. Model run UKICE underestimates the magnitude of the observed denitrification and nitrification (as diagnosed from the NO_y^* correlation) by approximately 2-3 ppbv and the denitrification is displaced upwards by around 20 K potential temperature (Figure 4.8). Note that there is considerable fine horizontal structure in the observed NO_y which the coarse grid model and equilibrium denitrification scheme is unable to reproduce.

Forcing the ice model with the warmer, but more realistic, ECMWF analyses (run ECICE) produces considerably less denitrification (around 2 ppbv at 460 K) due to the very short time that air masses are exposed to temperatures below T_{ice}. This model run strongly underestimates the observed extent of denitrification.

Replacing the ice scheme with the denitrification scheme based solely on NAT (runs UKNAT and ECNAT) produces NO_y fields that are in better agreement with observations than either ECICE or UKICE. The mean difference between modelled and observed NO_y is generally smaller for ECNAT compared to UKNAT, which tends to overestimate NO_y at ER-2 altitudes in January and underestimate NO_y in March.

Runs ECNAT and UKNAT are also in better agreement with the vertical distribution of denitrification and nitrification. This is especially evident in the "stack" flight (flight consisting of a series of legs at increasing altitudes over Kiruna) of February 3 (Figures 4.7b and 4.7f) where the ice denitrification scheme shows NO_y increasing along the flight track, while observations show that the sampled air was generally denitrified above 380 K.

4.5.3   Comparison of modelled and observed dehydration

Ice-based denitrification schemes may produce significant dehydration if the synoptic temperature falls sufficiently low. By contrast, any denitrification scheme based solely on NAT will be limited to a dehydration of $3\times[HNO_3]$ or approximately 30 ppbv. This provides additional evidence to discriminate between an Arctic denitrification
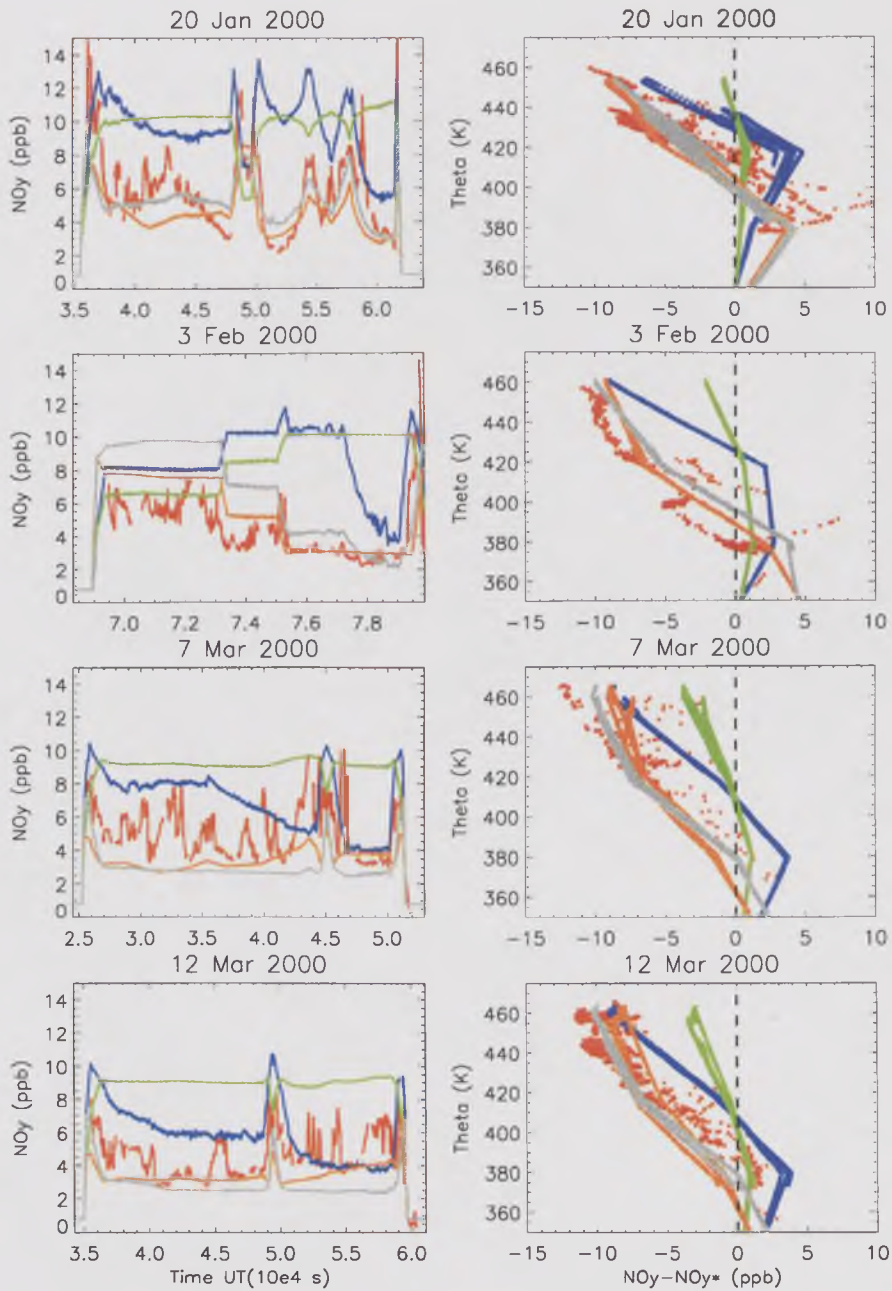
Figure 4.7: Comparison of SLIMCAT NO_y for four model runs (UKICE blue, ECICE green, UKNAT grey and ECNAT orange) and NASA ER-2 NO_y (brown) for four in-vortex flights.
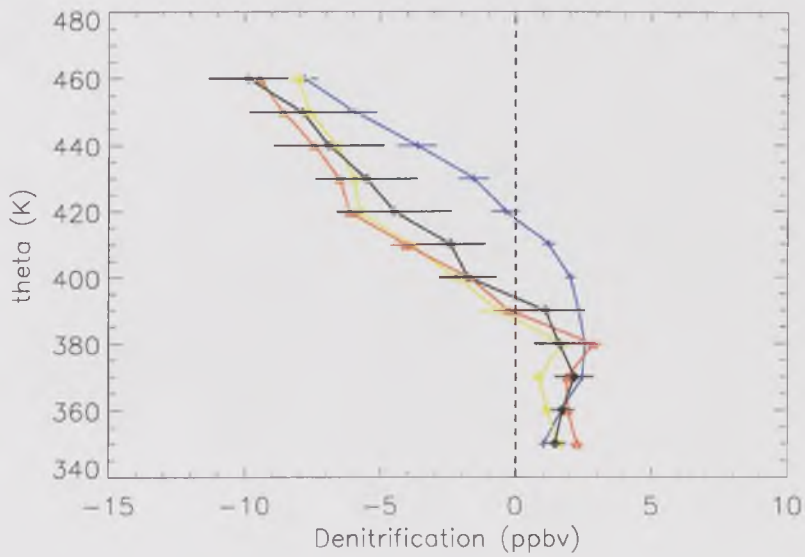
Figure 4.8: Profiles of mean denitrification inside the polar vortex from 11 ER-2 flights from January 14, 2000 - March 12, 2000 for ER-2 observations (black), UKICE (blue), ECNAT (yellow) and UKNAT (red).

mechanism based on the sedimentation of synoptic scale ice and a scheme based on sedimentation of large NAT particles. *Hermann et al.* [2002] has quantified dehydration in the Arctic winter of 1999/2000 using in-situ observations of total hydrogen ($H_{tot} = H_2O + 2\ CH_4 + H_2$) and equivalent water ($H_2O_{eq} = H_2O + 2\ CH_4$) aboard the ER-2. The mean value of H_2O_{eq} is 7.38 ± 0.11 ppmv within the vortex and 7.32 ± 0.13 in the extra-vortex regions sampled by the ER-2. In the model, H_2O_{eq} should be conserved in the absence of dehydration as oxidation of CH_4 yields two H_2O molecules. It is not necessary to assume that they are well mixed due to the compactness of the correlation between them.

Isolated occurrences of dehydration were observed during three flights, most notably January 27, 2000 when a 400-kilometre long region of the flight track near the vortex edge exhibited dehydration of up to 0.63 ppmv. This was attributed to the airmass experiencing temperatures below the ice-frost point eighteen days earlier. Figure 4.9 shows the modelled dehydration (diagnosed from UKICE-UKNOD) is in good agreement with the observations during this flight but, in general, the model exhibits much more extensive dehydration, especially at altitudes above the ER-2 (over 1 ppmv at 500 – 550 K in late January). This dehydrated air then descends diabatically until it is sampled by the ER-2 during the third deployment (February 26 – March 12). In-vortex dehydration at 440 – 460 K is around 0.6 ppmv in the model at this time. The absence of widespread dehydration from in-situ ER-2 observations indicates that the observed denitrification of the Arctic vortex during 1999/2000 occurred without large scale ice sedimentation.

4.6 Summary

Observations show that in the winter 1999/2000 widespread denitrification occurred in the Arctic vortex. Two of the NAT-based model simulations (UKNAT and ECNAT) were able to reproduce this widespread denitrification leading to modelled NO_y in good agreement with the ER-2 observations.

The ice denitrification scheme forced with UKMO analyses produces strong denitrification but the NO_y profile is displaced vertically upwards by around 20 K compared to
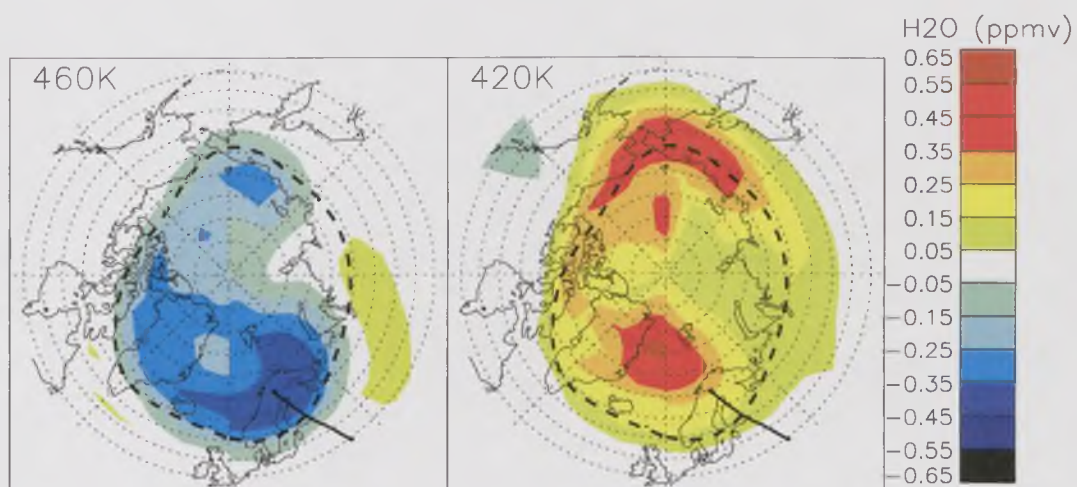
Figure 4.9: Model dehydration at 460 K and 420 K as diagnosed from UKICE-UKNOD on January 27, 2000. The ER-2 flight track (solid line) and MPV=30 PVU contour (dotted line) are also shown.

observations (Figures 4.7 and 4.8). Forcing the ice denitrification scheme with ECMWF analyses produces very little denitrification due to the very limited ice formation that occurs in the warmer ECMWF analyses. This difference illustrates the sensitivity of the ice-based denitrification scheme to relatively small temperature variations below 190 K.

The ECMWF-forced NAT scheme produces earlier and more widespread denitrification than the ice-based schemes. It captures the magnitude of denitrification well at all but the highest altitudes, where it underestimates the NO_y deficit by around 2 ppbv. This result is important because observed NO_y is an upper limit. The UKMO-forced NAT-based denitrification results are similar to the ECMWF NAT scheme but with better agreement at the highest (and lowest) altitudes.

This chapter described the chemical transport model used to perform equilibrium denitrification simulations for the Arctic 1999/2000 winter. Results were presented for both ice-based and NAT-based denitrification using UKMO and ECMWF analyses. Comparison of these analyses indicated that those from the UKMO were considerably colder than those from the ECMWF in the core of the vortex during December and January.

Although the NAT-based PSC scheme used in this chapter is simple, the NO_y fields produced with both the UKMO or ECMWF analyses are sufficiently realistic for use in chemical models. This scheme is based on specified particle radii for sedimentation which are obtained from observations. This scheme is therefore not useful for prognostic studies. Observations of large NAT particles with their long growth times and rapid sedimentation mean that thermodynamic equilibrium between the particles and the surrounding atmosphere cannot be assumed. For the first time, in-situ evidence of widespread and severe denitrification in the Arctic and the discovery of large NAT-particles at low number densities means that a full microphysical treatment of NAT in PSCs may be required. The following three chapters of this thesis describe the DLAPSE model, examine the sensitivity of microphysical denitrification to various meteorological factors and present results for simulations of denitrification in two recent cold winters.

Chapter 5

Principles of the new microphysical denitrification model

5.1 Introduction

PSCs have been observed in the Arctic winter vortex for a number of years. The SOLVE/THESEO-2000 field campaign has considerably improved our knowledge of the composition and size distribution of PSC particles although a complete understanding of the nucleation process remains outstanding. *Voigt et al.* [2000] have confirmed the presence of NAT in lee-wave PSCs by in-situ mass spectrometry. Observations by *Fahey et al.* [2001] revealed that PSC particles could have radii of up to 10 μm with integrated number densities of around 10^{-4} cm^{-3}. These particles are significantly larger and present at much lower abundances than previously reported. Microphysical calculations [*Carslaw et al.*, 2002] have revealed that under typical lower stratospheric conditions, a 10 μm radius NAT particle takes around 8 days to grow and has a terminal fall velocity of over 1500 m/day. Previous model PSC schemes based on parameterisations of the thermodynamic equilibrium between particles (usually ice) and their surroundings may, therefore, be invalid if a detailed simulation of Arctic denitrification is required.

Temperature (K)	Pressure (mb)	$\bar{\lambda}$ (10^{-6}m)
298	1000	0.065
200	100	0.5
185	50	0.6

Table 5.1: Mean free path of air at typical lower stratospheric temperatures and pressures

In this chapter, the microphysical foundations governing the non-equilibrium (kinetic) growth and sedimentation of particles are discussed. The major features of the new DLAPSE model are then described.

5.2   Continuum and non-continuum dynamics

The growth and sedimentation of individual aerosol particles are processes determined by the interaction between the particle and the surrounding atmosphere. The relative length scales of the particle and the molecular separation, the mean free path $(\bar{\lambda})$, determine the mode of transfer of mass and momentum between the particle and the surrounding atmosphere.

The Knudsen number (Kn) is used to express the relationship between particle size and molecular mean free path:

$$\text{Kn} = \frac{\bar{\lambda}}{r_\text{p}} \tag{5.1}$$

Representative values for the mean free path of air under typical stratospheric conditions are listed in Table 5.1. When $\bar{\lambda} \ll r_\text{p}$, Kn $\to$ 0 and the particle "views" the surrounding atmosphere as a continuous fluid – the continuum regime. If $\bar{\lambda} \gg r_\text{p}$, Kn $\to \infty$ and the particle interacts with the fluid as if it were a collection of discrete molecules – the non-continuum (kinetic) regime. At values of Kn $\approx$ 1, characteristic of PSCs in the lower stratosphere, particles are considered to be in the transition regime and corrections must be applied to growth and sedimentation terms to account for these effects.

5.3 Growth of single aerosol particles

5.3.1 Particle growth by vapour diffusion in the continuum regime

Diffusion of a gaseous species X to the surface of a stationary particle (radius r_p) is given by *Seinfeld and Pandis* [1998]:

$$\frac{\partial c}{\partial t} = -\frac{1}{r_p^2}\frac{\partial}{\partial r}(r_p^2 \tilde{J}_{X,r}) \tag{5.2}$$

where $c(r,t)$ is the concentration of X, and $\tilde{J}_{X,r}(r,t)$ is the molar flux of X at any distance r (m).

Fick's Law [e.g. *Bird et al., 1960*] describes the molar flux ($\tilde{J}_{X,r}$) to (from) the particle if the air is stationary relative to the particle:

$$\tilde{J}_{X,r} = -D_g \frac{\partial c}{\partial r} \tag{5.3}$$

where D_g is the diffusivity of X in air.

Using Fick's Law and assuming X is present in low concentrations, Equation 5.2 becomes:

$$\frac{\partial c}{\partial t} = D_g \left(\frac{\partial^2 c}{\partial r^2} + \frac{2}{r}\frac{\partial c}{\partial r} \right) \tag{5.4}$$

If c_∞ is the concentration of X in the uniform free atmosphere and c_s the concentration of X at the surface of the particle, then

$$c(r,0) = c_\infty \tag{5.5}$$

$$c(\infty,t) = c_\infty \tag{5.6}$$

$$c(r_p,t) = c_s \tag{5.7}$$

Using Equations 5.5 and 5.7 as boundary conditions, Equation 5.4 can be solved to give:

$$c(r,t) = c_\infty - \frac{r_p}{r}(c_\infty - c_s) + \frac{2r_p}{r\sqrt{\pi}}(c_\infty - c_s)\int_0^{(r-r_p)/2\sqrt{D_g t}} e^{-\chi^2}d\chi \tag{5.8}$$

where χ is the volume mixing ratio of X [*Seinfeld and Pandis*, 1998]. For large values of t:

$$(r - r_p)/2\sqrt{D_g t} \to 0 \tag{5.9}$$

and the concentration profile approaches steady-state:

$$c(r) = c_\infty - \frac{r_p}{r}(c_\infty - c_s) \tag{5.10}$$

The total flow of X (in moles per unit time) towards the particle (J_c) in the continuum regime is given by:

$$J_c = 4\pi r_p^2 (\bar{J}_X)_{r=r_p}, \quad \text{or} \tag{5.11}$$

$$J_c = 4\pi r_p D_g (c_\infty - c_s) \tag{5.12}$$

5.3.2 Particle growth in the kinetic regime

The derivation of mass flux does not include a correction for the kinetic effect when it is no longer appropriate to assume that $\bar{\lambda} \ll r_p$. For molecules in three-dimensional random motion the number of molecules striking a unit area per unit time (Z_N) is:

$$Z_N = \frac{1}{4}N\bar{c}_X \tag{5.13}$$

where N is the number of molecules per unit volume and $\bar{c}_X$ is the mean molecular speed:

$$\bar{c}_X = \left(\frac{8kT}{\pi m_X} \right)^{1/2} \tag{5.14}$$

where m_X is the molecular weight of X. The molar flux towards a particle of radius r_p per unit time (J_k) is:

$$J_k = \pi r_p^2 \bar{c}_X \alpha (c_\infty - c_s) \tag{5.15}$$

where α is the molecular accommodation coefficient.

The ratio of the kinetic regime flow to the continuum regime flow is given by:

$$\frac{J_k}{J_c} = \alpha \frac{\bar{c}_X r_p}{4D_g} \tag{5.16}$$

5.3.3 Model particle growth equation

In the model, the molecular flux (J_m) towards a particle of radius r_p is calculated in terms of molecular diffusion but using a modified diffusion coefficient (D_m) to account for non-continuum effects at the particle surface [*Pruppacher and Klett*, 1997]:

$$J_m = 4\pi r_p D_m (c_\infty - c_s) \tag{5.17}$$

where D_m is given by:

$$D_m = \frac{D_g}{1 + \frac{4D_g}{c_X r_p}} \tag{5.18}$$

From mass balance:

$$J_m = \frac{\rho_p}{m_X} \frac{d}{dt} \left(\frac{4}{3}\pi r_p^3 \right) \tag{5.19}$$

Combining Equation 5.17 and the above gives:

$$\frac{dr_p}{dt} = \frac{D_m m_X}{\rho_p} (c_\infty - c_s)\left(\frac{1}{r_p}\right) \tag{5.20}$$

where $c = \rho/RT$ and applying the equation to HNO_3 vapour over a NAT particle:

$$\frac{dr_p}{dt} = \frac{D_m m_{NAT}}{\rho_{NAT} RT} (p_{HNO_3} - p_{HNO_3}^{NAT}) \left(\frac{1}{r_p}\right) \tag{5.21}$$

where m_{NAT} is the molecular mass of NAT, p_{HNO_3} is the ambient partial pressure of HNO_3 and $p_{HNO_3}^{NAT}$ is the vapour pressure of HNO_3 over NAT.

Integrating Equation 5.21 gives:

$$r_p^2 = r_{p_0}^2 + 2Gt \tag{5.22}$$

where $G = \frac{D_m m_{NAT}}{\rho_{NAT} RT} (p_{HNO_3} - p_{HNO_3}^{NAT})$

5.3.4 The Kelvin effect

The saturation pressure of a gas over its condensed phase is not only a function of temperature but also the radius of the particle. This radius dependence is known as

the Kelvin effect and enhances the saturation vapour pressure over curved surfaces and is significant for small particles. The Kelvin effect may be defined as:

$$p_s^* = p_s \exp\left(\frac{2m_s\sigma}{RT\rho r_p}\right) \tag{5.23}$$

where p_s^* is the saturation vapour pressure over a curved surface of radius r_p, p_s is the saturation vapor pressure over a plane surface and σ is the surface viscosity. Figure 5.1 shows the Kelvin factor, $K = \left(\frac{2m\sigma}{RT\rho r_p}\right)$ as a function of radius for NAT and ice. For $r_p \geq 0.1$ μm, $K \rightarrow 1$ and, therefore, ignoring the Kelvin effect in the model growth equation has only a very small effect.
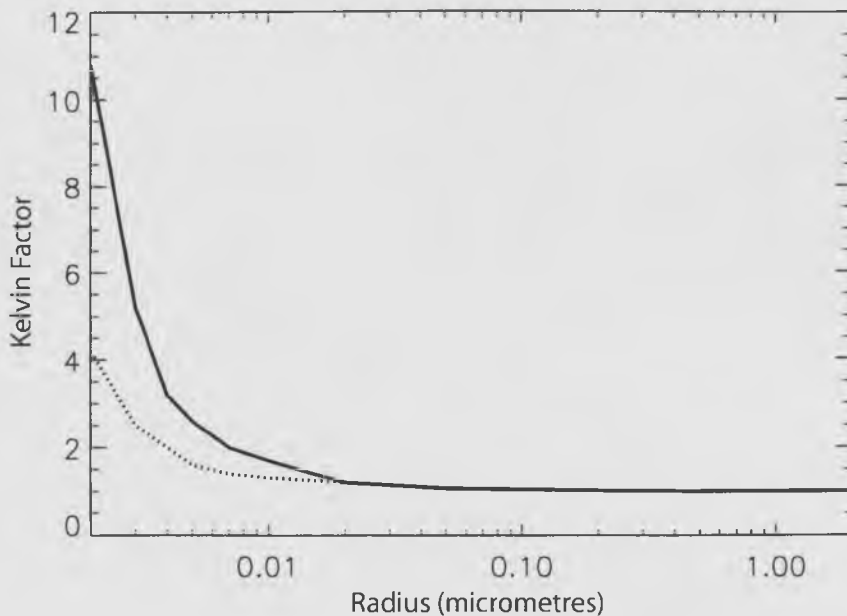
Figure 5.1: Kelvin factor for NAT (solid line) and ice (dotted line) as a function of particle size at 195 K and 187 K respectively.

5.4 Sedimentation

In order to examine the dynamical behaviour of NAT particles in the stratosphere, it is necessary to begin by considering idealised behaviour of a single spherical aerosol particle in a viscous fluid - the continuum regime. This discussion can then be ex-

tended to encompass non-continuum effects which may be relevant under stratospheric conditions.

5.4.1 Drag on a single spherical particle

Any particle moving with a velocity u_0, experiences a drag force, F_{drag}. In order to calculate F_{drag} for motion in an incompressible Newtonian fluid it is necessary to solve the continuity equation and the Navier-Stokes momentum balance equations to determine both the velocity and pressure fields around the particle. F_{drag} is the sum of the normal and tangential components of the force acting on the spherical particle and is obtained from *Seinfeld and Pandis* [1998]:

$$F_{drag} = 6\pi\eta r_p u_0 \qquad (5.24)$$

where η is the viscosity of the fluid. This is known as Stokes' Law and is applicable for situations in which the Reynolds number, $R_e \ll 1$ and is equally applicable to the situation in which a particle is moving through a stationary fluid.

5.4.2 Slip flow correction

Stokes' Law is based around continuum dynamics ($Kn \to 0$). When the particle diameter approaches $\bar{\lambda}$ of the surrounding fluid, the non-slip assumption is no longer valid and the drag force exerted on a particle by the fluid is lower than expected.

From kinetic theory, the mean free path of a gas molecule is given by:

$$\bar{\lambda} = \frac{2\eta}{p\sqrt{(8m/\pi RT)}}. \qquad (5.25)$$

Table 5.1 shows that the mean free path for gas molecules under typical lower stratospheric conditions is similar to the diameter of NAT particles in a PSC and a slip flow correction must be applied to fall velocities. The Cunningham slip flow correction factor (C_c) is defined according to *Pruppacher and Klett* [1997] as:

$$C_c = 1 + \frac{\bar{\lambda}}{r_p}\left[1.257 + 0.4\exp\left(-\frac{1.1r_p}{\bar{\lambda}}\right)\right] \qquad (5.26)$$

This factor is incorporated into the Stokes' Law drag equation used to describe particle sedimentation to correct for non-continuum effects in the model:

$$F_{drag} = \frac{6\pi\eta r_p u_0}{C_c},$$ (5.27)

$$u_0 = \frac{F_{drag}C_c}{6\pi\eta r_p}$$ (5.28)

$$\text{and} \quad F_{drag} = \frac{4}{3}\pi r_p^3 \rho g$$ (5.29)

Substituting for F_{drag} in Equation 5.28 and applying to sedimentation time (t) and distance (z):

$$\frac{dz}{dt} = -Sr_p^2 \quad \text{where} \quad S = \frac{2\rho g C_c}{9\eta}$$ (5.30)

5.4.3 Combined growth and sedimentation

The model growth and sedimentation terms may be combined (Equations 5.22 and 5.30) by substituting for r_p to give the coupled time-dependent growth and sedimentation equation used in the model for individual particles:

$$\frac{dz}{dt} = -S\,r_{p_0}^2 - 2GS\,t$$ (5.31)

where r_{p_0} is the particle radius at t_0.

Integration of Equation 5.31 gives:

$$z = z_0 - Sr_{p_0}^2 t - GSt^2$$ (5.32)

In the model, this is expressed as:

$$z(t + \Delta t) = z(t) - Sr_p(t)^2\Delta t - GS\Delta t^2$$ (5.33)

where Δt is the model timestep, $z(t)$ is the vertical position at time t, and $z(t + \Delta t)$ is the altitude at time $t + \Delta t$.

Model NAT particles are assumed to be spherical for the calculation of sedimentation velocity. In reality, NAT crystals may have a hexagonal cylindrical structure with an aspect ratio of $\sim$0.8 [Luo et al., pers. comm.], therefore the spherical assumption may overestimate NAT-particle fall velocities by approximately 10%.

5.5 DLAPSE Model description

In the DLAPSE model, the analytic term (Equation 5.33) is used to describe the 3-D time-dependent growth and sedimentation of a large number of NAT particles using a domain-filling Lagrangian approach [*Carslaw et al.*, 2002]. The essential features of this model are described in the following section.

5.5.1 Particle initialisation

For all simulations undertaken with the DLAPSE model, particles are initialised with a radius of 0.1 μm on a cosine-weighted latitude grid between 50° and 90°N wherever $T < T_{NAT}$ at a controlled rate to ensure a uniform spatial distribution of particles. New particles are initialised every 6 hours throughout the period of the simulation at random vertical positions between 350 and 600K to ensure that coherent structures in the particle fields are smoothed. This time-averaged nucleation rate makes no assumptions about potential nucleation mechanisms for NAT particles in the lower stratosphere which, as discussed in Chapter 2, are poorly understood. Our purpose in this study is not to examine the validity of potential nucleation mechanisms but to simulate whether large NAT particle-induced denitrification is capable of reproducing the observed denitrification in cold Arctic winters. The results presented are unlikely to be especially sensitive to the precise nature of the nucleation mechanism so long as they are eventually distributed widely throughout the vortex as shown in *Fueglistaler et al.* [2002]. The intention of this study is to examine the particle distributions and denitrification several days after the particle fields are generated.

5.5.2 Timestep

The analytic solution to particle growth and sedimentation works because the low number density of particles means that the gas phase and particle growth are essentially decoupled over a single timestep. The timestep needs to be short enough to minimise errors in the calculation of Δz and Δr without increasing the computational cost unacceptably. In practice, a timestep of 30 minutes is used.

5.5.3 Nucleation barrier

The model volume-averaged nucleation scheme has no barrier to the formation of NAT from the gas-phase. In the model, NAT is initialised wherever $T < T_{NAT}$. It has been suggested that the nucleation of NAT in the stratosphere may require significant supersaturation of the atmosphere, reducing the rate of particle formation [e.g. *Peter et al.*, 1991]. If a nucleation barrier does exist, the model will tend to overestimate particle formation. The effect on denitrification would depend on available HNO_3.

5.5.4 Horizontal and vertical advection

Particles are advected in the horizontal direction using a fourth-order Runge-Kutta scheme and utilising linear interpolation of the ECMWF 2.5° latitude × 2.5° longitude analysed winds to the particle position. Vertical transport of individual particles in the model is calculated at each timestep from Equation 5.33.

5.5.5 Coupling of the Lagrangian particle denitrification model with SLIMCAT

In order to simulate the 3-D impact of NAT particle growth and sedimentation on the seasonal evolution of gas-phase HNO_3 in a realistic manner, DLAPSE has been coupled to the Eulerian SLIMCAT CTM (as described in Chapter 3).

The initial coupling of the Lagrangian particle model and the SLIMCAT CTM was carried out by Jamie Kettleborough at the Rutherford Appleton Laboratory, Didcot, Oxfordshire in 2000/01. SLIMCAT is written in FORTRAN whilst the Lagrangian particle denitrification model is written in IDL. The models run in parallel and exchange information at each timestep. SLIMCAT gas-phase HNO_3 is passed to the Lagrangian particle model through a UNIX named pipe. In the particle model, gridded HNO_3 is interpolated to the position of each particle for the calculation of growth and sedimentation. This change in HNO_3 for each particle is converted to a gas-phase ΔHNO_3 on the SLIMCAT 3-D model grid and the field is passed back via the named pipe to the SLIMCAT model. SLIMCAT 3-D gas-phase HNO_3 is adjusted by ΔHNO_3 prior to the

DENITRIFICATION MODEL

Output to file

SLIMCAT CTM

Initialise gas phase

Grid ΔHNO3

Advection

Sedimentation

Growth

Aerosol Uptake

Horizontal Advection

Interpolate HNO3
to particles

Output to file

Initialise particles
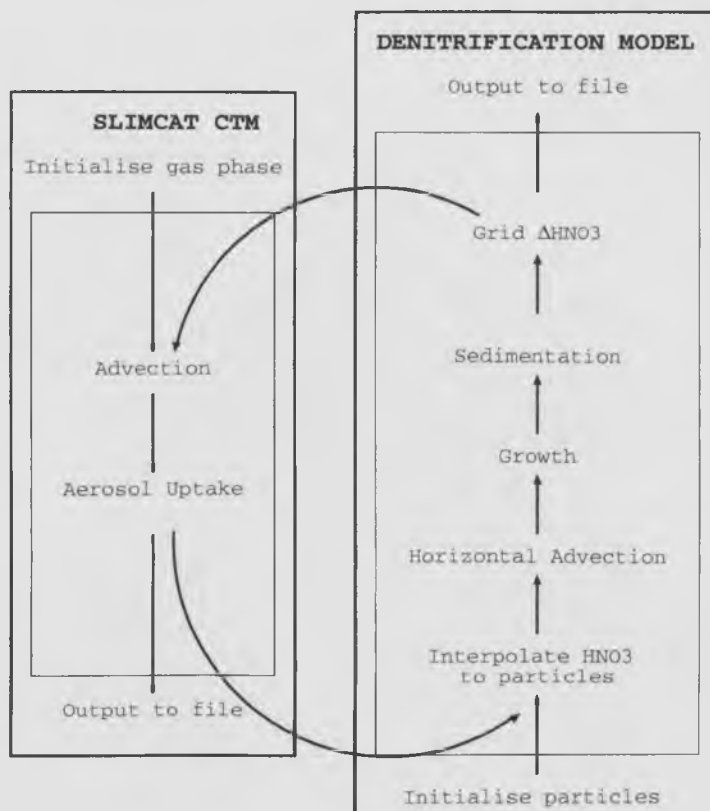
Figure 5.2: Schematic diagram of the coupled model.

advection step. The updated HNO_3 field is fed back to the Lagrangian particle model where localised changes in gas-phase HNO_3 alter particle growth rates. Figure 5.2 is a schematic representation of the coupled model.

This scheme was chosen over the more traditional method of advecting a series of particle number density and size distribution bins in an Eulerian model for a number of reasons, despite the computational cost involved in advecting up to 150 000 individual particles. The Lagrangian approach allows the tracking of individual particles throughout their lifetime without the numerical diffusion associated with bin-resolved Eulerian methods. The Lagrangian approach also allows the compilation of particle age, size and sedimentation statistics at any location, which provide valuable information about the most suitable meteorological conditions for denitrification. A full 3-D Lagrangian approach to modelling particle trajectories also overcomes the major drawback of col-

umn models, in which simplifying assumptions about particle temperature histories or gas-phase HNO_3 are usually required.

5.6 Summary

This chapter described in detail the microphysical concepts used in the DLAPSE model and its coupling with the SLIMCAT CTM. An analytic combined growth and sedimentation equation used in the DLAPSE model was derived. This novel approach provides the significant benefit of computational efficiency over the alternative method of Eulerian advection of particle size bins. A Lagrangian approach means that the model is not affected by the numerical diffusion often associated with Eulerian advection of particle sizes. In addition, this approach produces useful diagnostics about particle histories which enhance the understanding of the denitrification process. The following chapter explores the sensitivity of the denitrification in the coupled model to the nucleation rate and various meteorological factors. Results from the DLAPSE coupled to SLIMCAT are compared to SLIMCAT with an equivalent equilibrium denitrification scheme.

Chapter 6

Sensitivity study of microphysical denitrification

6.1 Introduction

A series of 10-day simulations were used to examine the sensitivity of denitrification in DLAPSE to the particle nucleation rate and meteorological conditions. Where appropriate, comparisons were made with the two thermodynamic equilibrium denitrification scheme to identify the impact of a full microphysical simulation on modelled denitrification. The aim of this chapter is to understand some of the factors controlling denitrification in the atmosphere before simulating denitrification with the full meteorological complexities of a specific Arctic winter.

6.2 SLIMCAT model formulation

The SLIMCAT CTM coupled to DLAPSE for this study is a simplified version of that described in detail in Chapter 3, but with several key modifications which are detailed below. Resolution of the SLIMCAT model is higher at $5.6°$ longitude $\times$ $5.6°$ latitude with 36 isentropic levels between 350 and 3000 K. (The resolution of SLIMCAT for equilibrium denitrification studies was $7.5°$ longitude by $5°$ latitude with 18 isentropic

levels.) Increasing the vertical resolution allows model isentropic levels to be spaced at 10 K (300 – 400 m) intervals in the lower stratosphere where this high resolution is useful for the accurate diagnosis of denitrification in the polar vortex.

This version of SLIMCAT contains no chemistry and advects two tracers - HNO_3 and a non-sedimented (passive) HNO_3. Two additional non-advected tracers are also output for diagnostic purposes - the cumulative change in gas phase HNO_3 (ΔHNO_3) and solid phase HNO_3 as determined by DLAPSE.

At low temperatures, the background sulphate aerosol sequesters gas-phase HNO_3, thereby reducing the rate of growth of NAT particles. The model used for these comparisons does not account for this process and is, therefore, likely to overestimate the rate of denitrification in regions where the temperature is low enough for substantial uptake of HNO_3 into liquid aerosol (4 K or more below T_{NAT}). This section examines the sensitivity of the coupled model denitrification fields to changes in vortex meteorology. The temperature field used is marginally above the threshold at which HNO_3 uptake into the background sulphate aerosol occurs. Neglect of liquid aerosols therefore has a minor effect in the calculation of denitrification from available HNO_3 in this case.

The meteorology used for the model studies of Arctic denitrification were carefully controlled in order to separate the influence of changing meteorological conditions from other factors. In order to achieve this separation, the temperatures, pressures and winds were fixed at the ECMWF analyses for 0 UT on December 23, 1999. These conditions were chosen for two reasons. Firstly, the temperatures in the polar lower stratosphere were below T_{NAT} but not so low that synoptic-scale ice or liquid aerosol formation was significant. Secondly, the region of NAT supersaturation (hereafter, the cold pool) and the polar vortex were concentric resulting in potentially long particle growth times.

For all model simulations in this chapter, the initial model HNO_3 and H_2O fields were set to representative stratospheric values (8 ppbv and 5 ppmv respectively). The 10-day time period of these simulations is sufficient to allow growing particles formed in the uppermost isentropic layer of the nucleation region (700 K) to descend to the lowermost model level (350 K). Use of a fixed meteorological analyses produces particle fields which are in a quasi-steady state. The constant particle nucleation rate when

$T < T_{NAT}$ creates spatial variations in particle number densities which may be attributed to advection, sedimentation and the atmospheric volume where the particles were nucleated.

6.2.1 Equilibrium model formulation

The equilibrium denitrification scheme used in this chapter is a simplified version of the SLIMCAT model used in Chapter 3. This model contains no chemistry and advects only gas-phase and passive HNO_3. The resolution of the equilibrium SLIMCAT model is identical to that used in the coupled SLIMCAT/DLAPSE model described above. Denitrification in this version of SLIMCAT is based on sedimentation of the thermodynamic equilibrium concentration of condensed HNO_3 [*Hanson and Mauersberger*, 1988]. A NAT particle radius of 2 μm was assumed for NAT in order to produce denitrification of a comparable magnitude to the microphysical simulation. As with the coupled model, initial model gas-phase HNO_3 and H_2O where set to 8 ppbv and 5 ppmv respectively and the fixed ECMWF analysis used. Denitrification of a comparable magnitude to that produced in the microphysical model is required to prevent complicating effects (e.g. unrealistic fall velocities leading to overly rapid denitrification) from occurring.

6.3 Sensitivity to NAT nucleation rate

The first of the idealised simulations examines the sensitivity of the denitrification produced in the DLAPSE model to the volume averaged nucleation rate. The downward mass flux ($\bar{J}_{HNO_3}$) for a particle distribution is the sum of the downward fluxes for each particle, which can be derived from the equations in Sections 5.3 and 5.4:

$$\bar{J}_{HNO_3} \propto \Sigma \; n_{NAT} \; r_{NAT}^5 \qquad (6.1)$$

The rate of denitrification at any point in space is equal to the divergence of the downward flux at that point and the cumulative denitrification is the sum of these divergences. Table 6.1 lists the nucleation rate used for each model run in this study.

Figure 6.1 shows the daily vortex mean HNO_3 (gas-phase and condensed phase) as a function of potential temperature for each model run (the vortex is defined as the region

Simulation	NR1	NR2	NR3	NR4	NR5	NR6
Nucleation rate ($\times 10^{-11}$ cm^{-3} s^{-1})	3.0	15.0	30.0	150.0	300.0	1500.

Table 6.1: Table showing nucleation rate used for each model run

poleward of the MPV = 30 PVU). The magnitude of the vortex mean denitrification is sensitive to the nucleation rate with peak denitrification increasing from 0.07 ppbv to 2.85 ppbv when the nucleation rate increases from 3.0×10^{-11} cm^{-3} s^{-1} to 1.5×10^{-8} cm^{-3} s^{-1}. At the lowest nucleation rates the modelled peak denitrification (at 565 K) increases almost linearly with the nucleation rate as there is sufficient condensable HNO$_3$ available to support the additional particles. Denitrification at the highest nucleation rates is limited by the available of HNO$_3$, as discussed above. The peak nitrification is around 50% of the corresponding peak denitrification mixing ratio due to the increased atmospheric pressure at nitrification altitudes. Figure 6.2 shows how the vortex mean cumulative denitrification at 565 K on Day 10 varies as a function of the nucleation rate. At very low number densities, denitrification by NAT particles is very inefficient.

The short model spin-up period is apparent before Day 3 of the simulation where the initial denitrification rate is low. This may be attributed to the small size of model NAT particles and their low abundance early in the simulation. There is around a 2 day time lag between the rates of peak denitrification at 565 K and nitrification at 425 K which is closely related to the transit time for the largest NAT particles between these two regions.

Figures 6.3 and 6.4 show the model particle size distributions at four 10 K deep isentropic layers between 450 and 410 K, close to the lower limit of the region of NAT supersaturation where the particles are largest. There is a striking decrease in the size of NAT particles between model runs NR1 and NR6. The modal radius at 420 K decreases from 7 μm at the lowest nucleation rate (3.0×10^{-11} cm^{-3} s^{-1}) to 2.5 μm at the highest nucleation rate (1.5×10^{-8} cm^{-3} s^{-1}). The mean particle radius over the entire model domain decrease from 4.3 μm to 1.8 μm between these model runs. Higher nucleation rates give rise to higher number densities of particles, which restrict
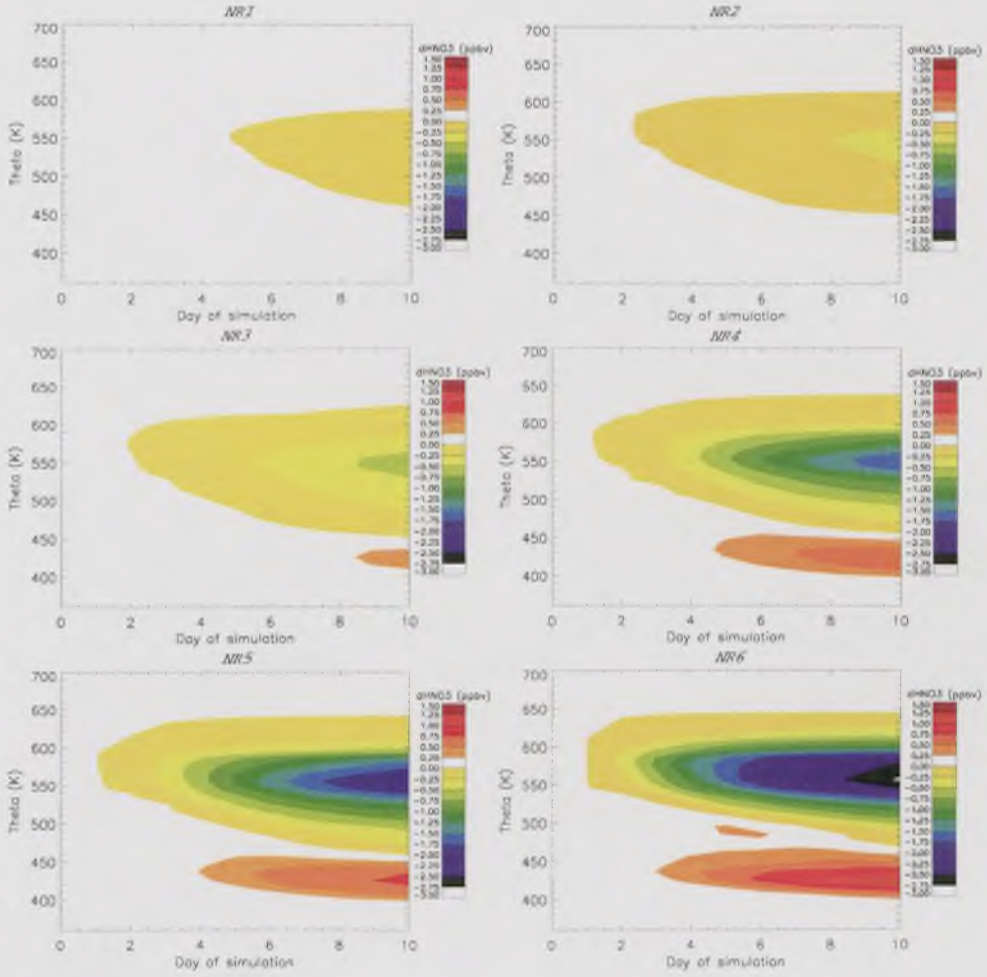
Figure 6.1: Vortex mean denitrification profiles for model runs NR1 – NR6.

their maximum size due to the availability of gas-phase HNO_3.

Denitrification at high nucleation rates is limited by the very small number of NAT particles. The maximum radius of each particle is limited to $\sim$10 μm, which can be achieved by falling through the full depth of the NAT-supersaturated region. Increases in the number density lead initially to increased denitrification due to the increased number of particles carrying HNO_3 downward [*Carslaw et al.*, 2002]. At very high nucleation rates denitrification would be expected to reach a maximum then, eventually, to decrease once more. This decrease occurs once increased number density is offset by a decrease in particle size and sedimentation speed as particles compete for the available
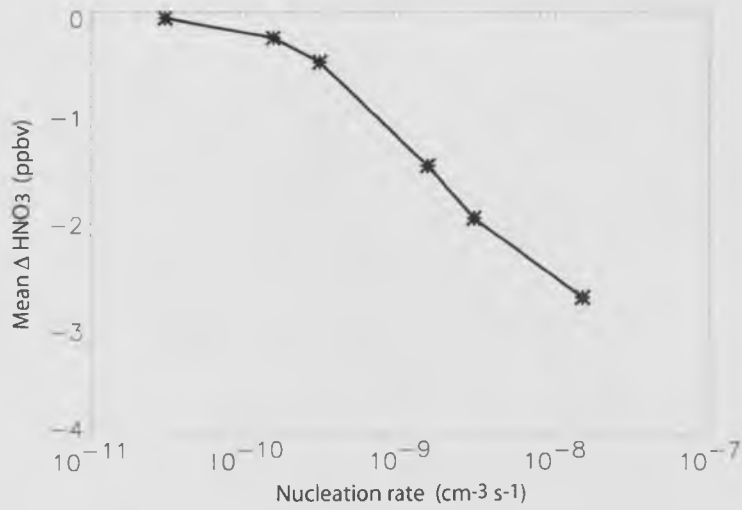
Figure 6.2: Vortex mean denitrification at 565 K on Day 10 as a function of nucleation rate for model runs NR1 – NR6.
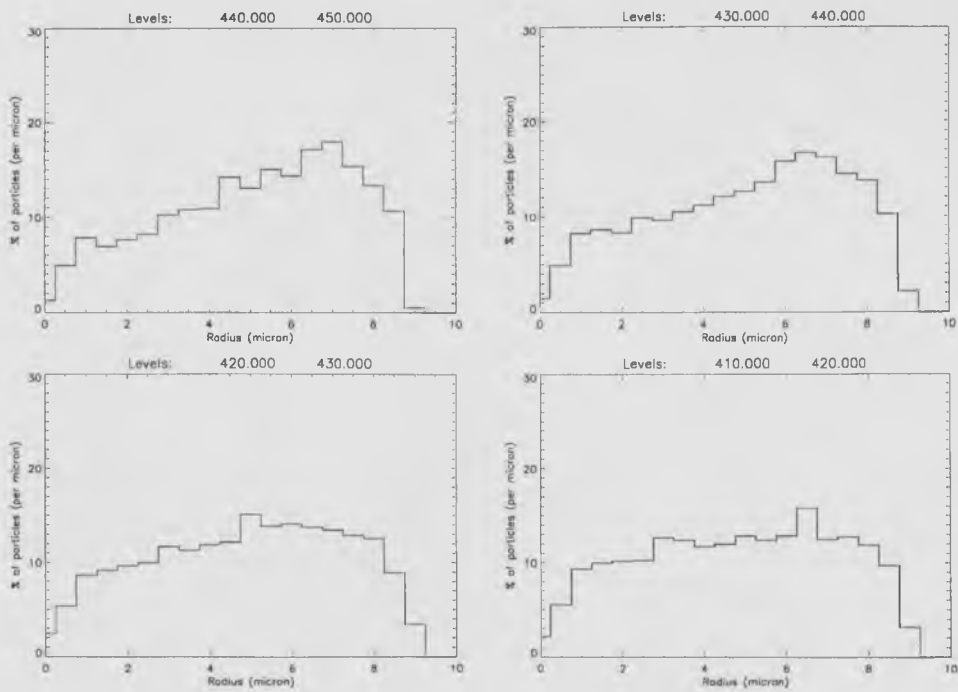
Figure 6.3: Particle size distributions at four isentropic levels on day 10 of the simulation for model run NR1.
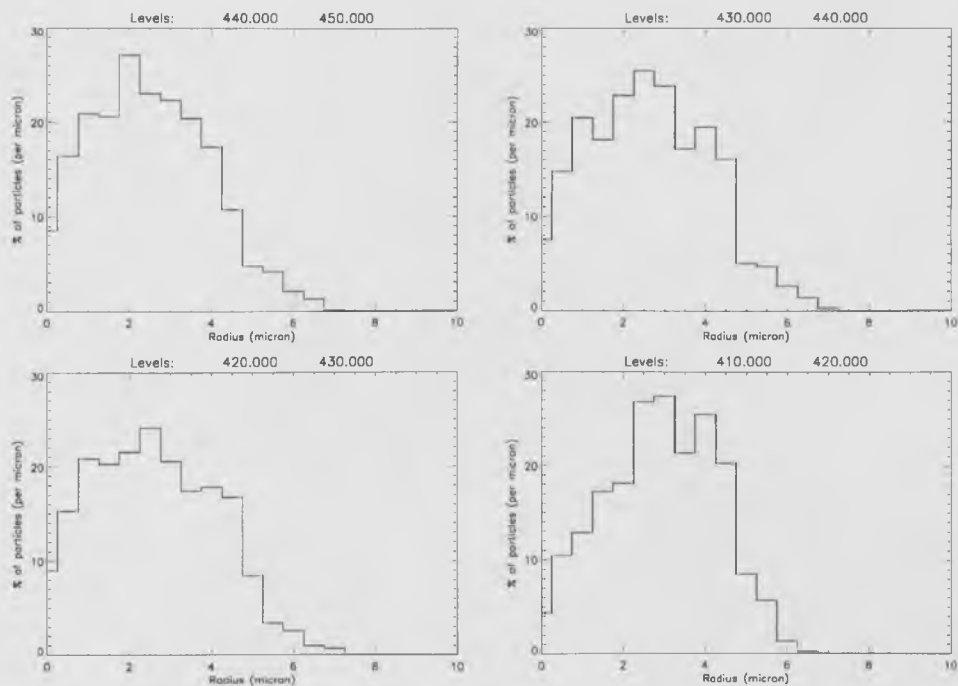
Figure 6.4: Particle size distributions at 4 isentropic levels on day 10 of the simulation for model run NR6.

HNO$_3$. This regime has not been simulated because the model is not optimised to simulate the short timescale processes occurring with rapid particle growth.

For all the subsequent sensitivity studies in this chapter a nucleation rate corresponding to 3.0×10^{-10} particles cm^{-3} s^{-1} is used, corresponding to NR3. This nucleation rate produces NAT-particle number densities comparable to those observed by the NO$_y$ instrument aboard the ER-2 on January 20, 2000 when the model is initialised 10 days earlier.

6.4 Temperature

The ambient temperature is expected to exert an important influence on the growth of NAT particles and denitrification. Particle growth is affected directly via the temperature dependence of Equation 5.21. Particle growth times and hence sizes are also

Equilibrium model run	EF1	EF2	EF3	EF4
Microphysical model run	MF1	MF2	MF3	MF4
Fractional T offset (*Frac*)	-0.50	-0.25	+0.25	+0.50
Offset at T_{min} (K)	-3.0	-1.5	1.5	3.0

Table 6.2: Table showing the temperature offsets applied to T-T_{NAT} for each model run.

affected because a global reduction in the ambient temperature will increase the volume of the region of NAT supersaturation. In this sensitivity study the temperature field is modified in two ways. Firstly, for each run the volume below T_{NAT} is kept constant whilst the temperature within the region of NAT supersaturation is altered. In the second series of runs, temperature offsets were applied globally to the temperature field in model run NR3, altering both the area and depth of the region of NAT supersaturation. In both cases, the fields from DLAPSE are compared to the equilibrium NAT scheme. The modified temperature fields were provided by Graham Mann (University of Leeds).

6.4.1 Temperature offset with constant area of NAT supersaturation

Table 6.2 lists the offsets applied to the model temperatures in the region of NAT supersaturation as a fraction of T-T_{NAT} with negative values indicating a decrease in temperature. A fractional temperature offset of *Frac* results in a new temperature in the T-T_{NAT} region of the vortex:

$$T_{new} = T_{old} - Frac(T_{old} - T_{NAT}) \tag{6.2}$$

Averaged across the cold pool, a fractional temperature offset of, for example, -0.5 corresponds to a 1.85 K reduction in temperature. Figure 6.5 shows the temperature profile at the location of the coldest temperatures within the NAT-saturated region applied to the model runs listed in Table 6.2. The indicated T_{NAT}, determined assuming 8 ppb HNO_3 and 5 ppm H_2O, is also shown. It can be seen that in addition to a constant area, the depth of the cold pool also remains approximately constant, restricting any changes in particle size, population or denitrification to the effect of temperature on particle growth.
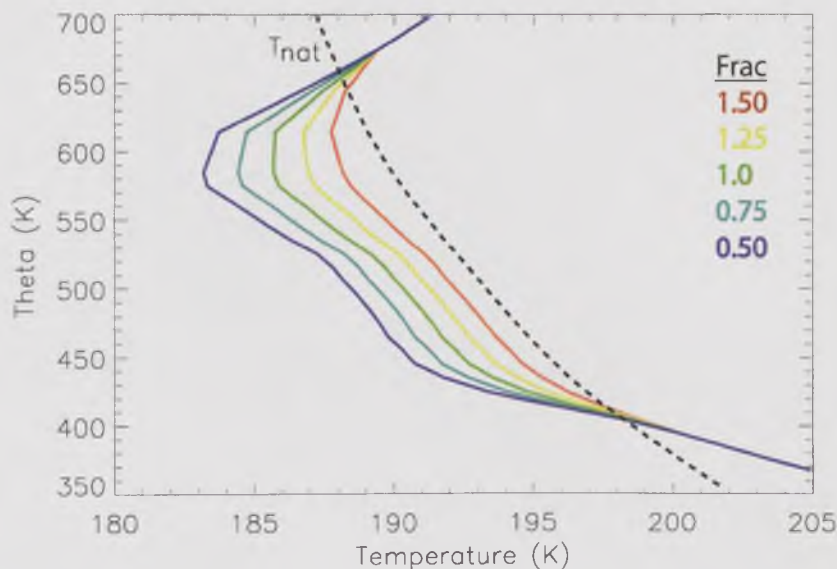
Figure 6.5: Temperature profiles of the fractional offset applied to the centre of the NAT supersaturation region.

Figure 6.6 shows the temporal development of denitrification as a function of potential temperature for two microphysical model runs (MF1 and MF4) and the corresponding equilibrium model runs (EF1 and EF4). In both cases denitrification is stronger in the colder model runs despite the approximately constant area and depth of the cold pool. The vertical extent of denitrification also appears to increase with a decrease in temperature in both sets of model runs although there are considerable differences in the overall structure of the denitrification produced by the microphysical and equilibrium schemes. Equilibrium denitrification in these idealised model runs is effectively a function of $T-T_{NAT}$ (which determines the condensed mass) and the period of the model run as the fall speed is prescribed until the redistributed mass approaches thermodynamic equilibrium. Microphysical denitrification has a longer "spin-up" time as the model requires around two days to produce sufficient large particles that can sediment.

Denitrification generally occurs at lower altitudes in DLAPSE than the thermodynamic equilibrium model. Peak denitrification in the equilibrium model occurs at 595 K. At the highest altitudes in the microphysical model, the particles must be small because they have not sedimented significantly and, therefore, redistribute little mass. The magnitude of denitrification is not directly comparable because the fall speed of NAT
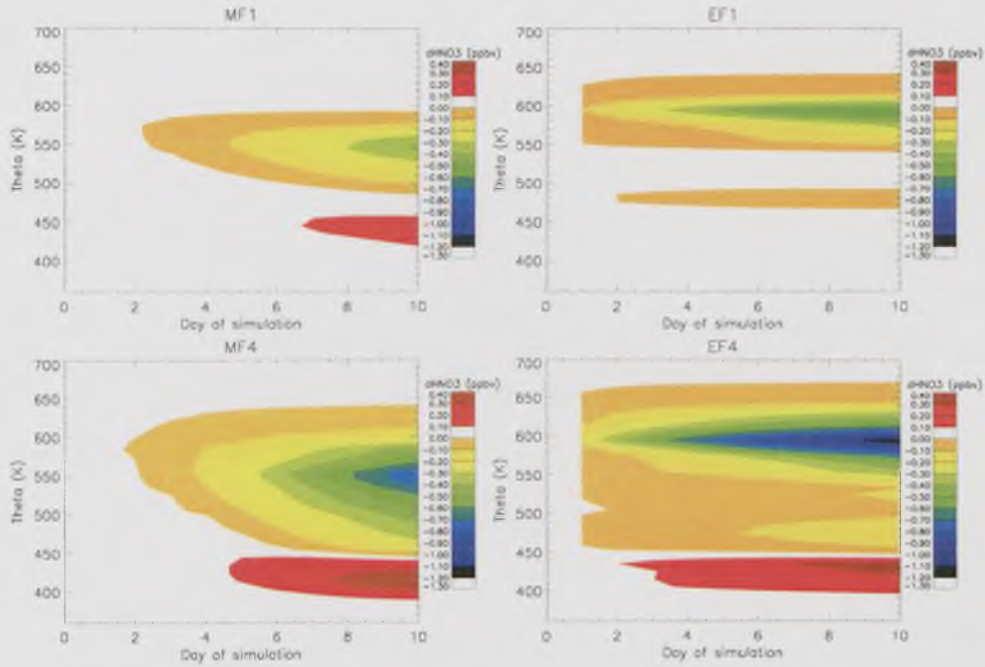
Figure 6.6: Vortex mean denitrification as a function of potential temperature and time for model runs MF1 and MF4, EF1 and EF4.

in the equilibrium scheme was adjusted to produce denitrification comparable to the DLAPSE model at 565 K.
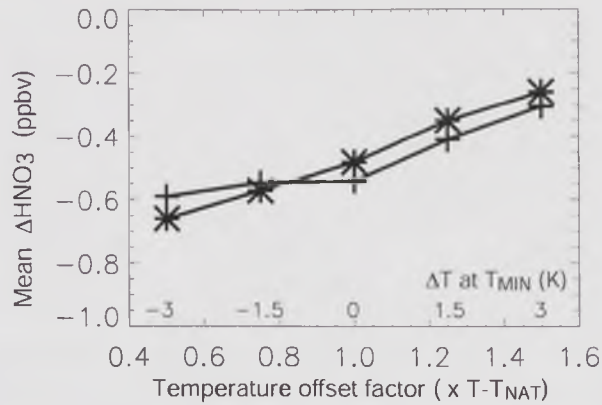
Figure 6.7: Vortex mean denitrification as a function of the cold pool fractional temperature offset from the microphysical model run (*) at 565 K and equilibrium model run × 0.5 (+) at 595 K on Day 10 of the simulations.

DLAPSE demonstrates an almost linear increase in vortex mean denitrification at 565 K with decreased temperature (Figure 6.7). At this altitude, a 2.3 K (50% of T-T_{NAT}) additional cooling is responsible for a further 0.19 ppbv (39%) denitrification. The relationship between these two variables is initially similar in the equilibrium model but at the lowest temperatures, the rate of denitrification is initially very rapid but slows as the available HNO_3 in the cold pool is diminished.
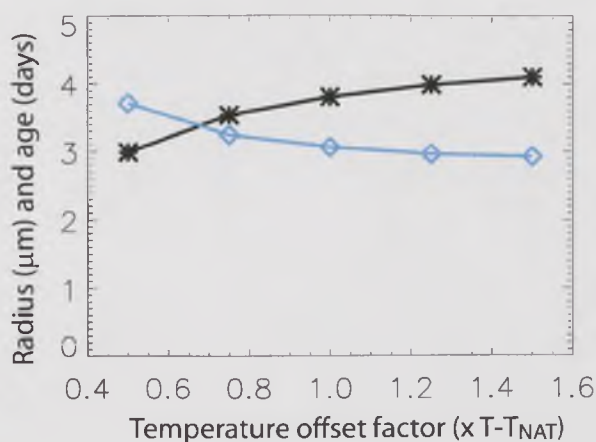
Figure 6.8: Vortex mean particle radius (black) and mean particle age (blue) on Day 10 for microphysical model runs MF1 – MF4.

Figure 6.8 shows how the vortex mean particle radius and particle age vary with the fractional temperature offset by Day 10 of the simulation. Particle radius decreases with increased temperature which is consistent with slower growth at higher temperatures due to decreased availability of condensable HNO_3. The age of particles has an inverse relationship with radius consistent with more rapid sedimentation of larger particles resulting in lower modelled mean ages.

6.4.2   Absolute temperature offsets

The absolute temperature offsets applied to each model equilibrium and microphysical model run are listed in Table 6.3. Also listed is the percentage change in that area of NAT supersaturation compared to model run NR3. Temperature profiles at the centre of the region of NAT supersaturation corresponding to each model run are shown in

Equilibrium model run	EO1	EO2	EO3	EO4
Microphysical model run	MO1	MO2	MO3	MO4
Temperature offset	-2.0	-1.0	+1.0	+2.0
% ΔA_{NAT} 565 K (NR3=13.3×10^6 km^2)	13.5	9.0	-28.5	-44.4

Table 6.3: Table showing the temperature offsets applied to each model run.

Figure 6.9. Unlike the sensitivity study above, the global temperature offset applied to each model run will also alter both the area and the depth of the cold pool in addition to the NAT-supersaturation. A 4 K decrease in temperature increases the area of NAT-supersaturation by 67% (from 11.5 to 19.2 million km^2). The depth of the NAT-supersaturated region increases from 440 – 620 K to 400 – 660 K with a 4 K decrease in temperature.
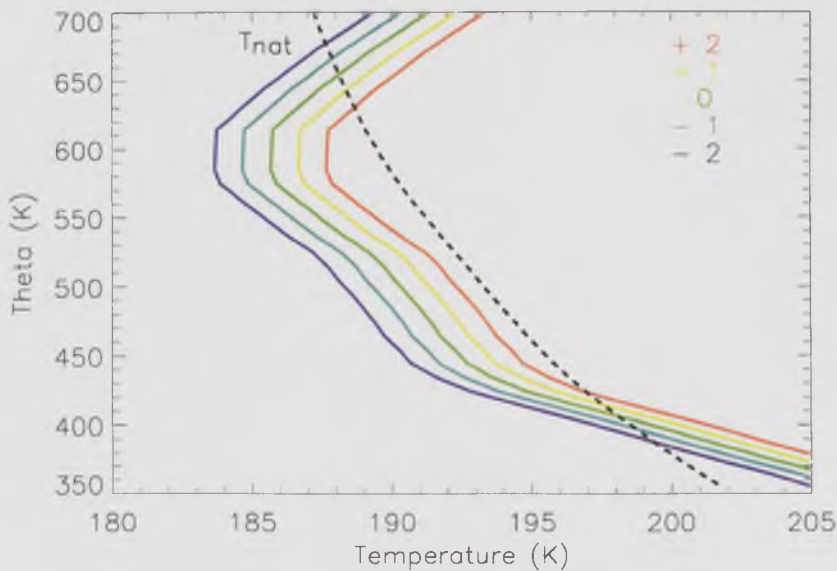
Figure 6.9: Profiles of the global temperature offsets applied at the centre cold pool

Figure 6.10 shows the vortex mean denitrification from both the microphysical and equilibrium models as a function of temperature offset on Day 10. Denitrification at 565 K in the microphysical model increases approximately linearly with decreased temperature. A 2 K decrease in temperature from the base model run causes an additional 0.43 ppbv (94%) increase in vortex mean denitrification. Equilibrium denitrification
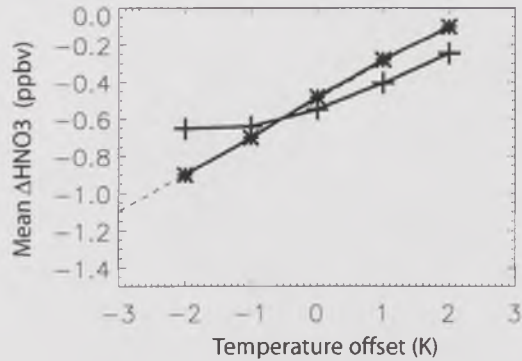
Figure 6.10: Vortex mean denitrification as a function of the temperature offset from the microphysical model run (*) at 565 K and equilibrium model run × 0.5 (+) at 595 K on Day 10 of the simulations.

demonstrates a linear initial response at 595 K to decreasing temperature. Denitrification for model runs EO1 and EO2 is around twice the magnitude of the denitrification in the equivalent microphysical model runs (MO1 and MO2). At the lowest temperatures, the rate of denitrification in the equilibrium scheme is slowed by saturation effects (model runs EO3 and EO4). In both models, decreasing the global temperature causes stronger denitrification than reducing the temperature within the cold pool alone.

Figure 6.11 shows the temporal development of vortex mean denitrification as a function of potential temperature for microphysical model runs, MO1 and MO4; and the corresponding equilibrium model runs, EO1 and EO4. A reduction of 4 K in the global temperature significantly increases both the magnitude and extent of denitrification in both models. At the highest temperatures, the microphysical model (MO1) produces weak denitrification in a narrow range between 560 and 585 K. The re-distribution of HNO_3 is more complicated in the equivalent equilibrium model run (EO1). There is a region of denitrification between 640 and 550 K with a narrow region of weak nitrification immediately below. A further region of denitrification is located between 460 and 440 K. This denitrification profile may be explained by Figure 6.9. The regions of denitrification and nitrification correspond to the location of maxima and minima in T-T_{NAT}.

Model run MO4 is strongly denitrified between 585 and 450 K whilst in the equivalent

equilibrium model run (EO4), denitrification is more localised between 620 and 550 K. Differences in the vertical location of nitrification also exist. Nitrification in model run MO4 is located between 420 and 360 K whereas model run EO4 is nitrified 20 K lower. Enhanced vortex mean denitrification at lower temperatures is due to increased NAT-supersaturation and larger vortex area below T_{NAT}. In common with the results in Section 6.4.1, peak denitrification in the microphysical model runs occurs at lower altitudes (565 K) than the equilibrium model (595 K). The initial development of denitrification is delayed in the microphysical model due to the initial spin-up period.
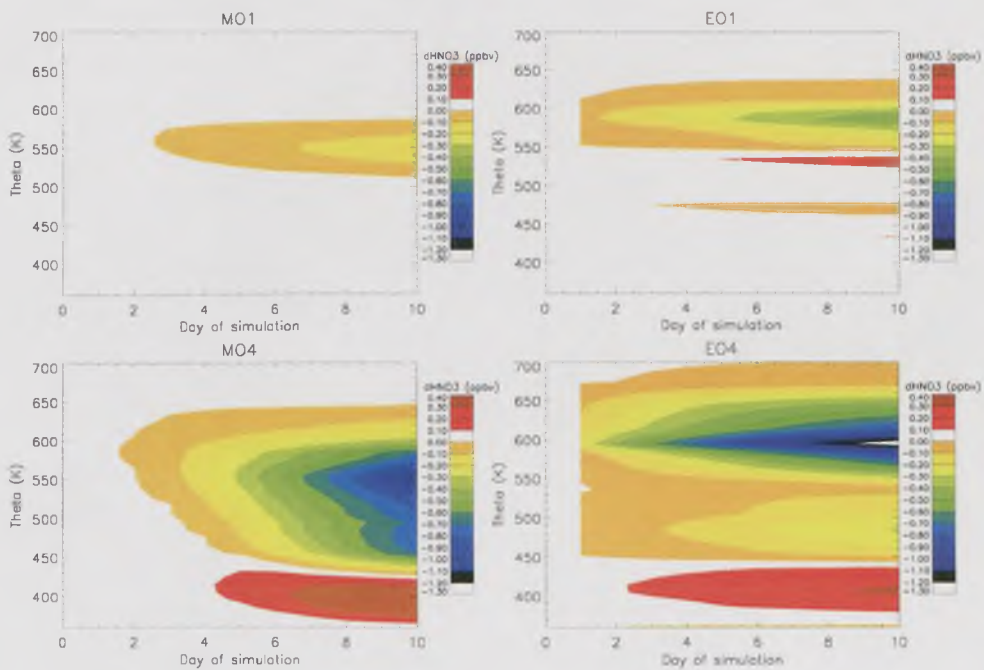
Figure 6.11: Daily vortex mean denitrification as a function of potential temperature for microphysical model runs (MO1, MO4) and equilibrium runs (EO1 and EO4).

Vortex mean radius and mean age of model particles for runs MO1 – MO4 are plotted in Figure 6.12. The mean radius increases from 2.3 μm to 4.5 μm with a decrease of 4 K in temperature. The mean particle age initially increases from 2.2 days to 2.95 days as temperatures are reduced then remains almost constant despite further reductions. Additional loss of larger particles through faster gravitational sedimentation at lower temperatures is offset by the increased volume of the cold pool, which reduces particle loss by horizontal advection out of the cold pool. This is in contrast to Figure 6.8
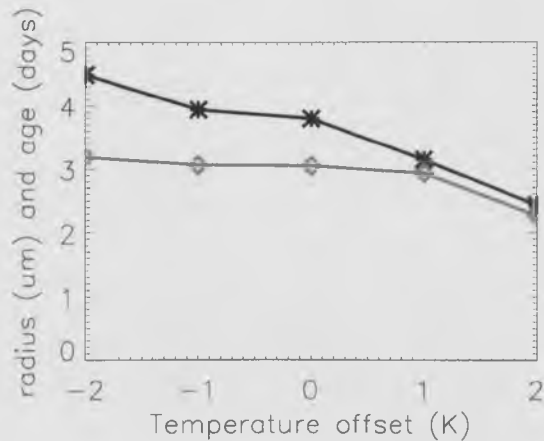
Figure 6.12: Vortex mean particle radius (black) and mean particle age (blue) on Day 10 for microphysical model runs MO1 – MO4.

where the fixed area of the cold pool results in a reduction in particle age at lower temperatures consistent with increased sedimentary losses.

The relative contributions of the increased area of NAT-supersaturation and lower temperatures within the NAT-supersaturated region to increased denitrification can be estimated. From Figure 6.7, a fractional offset of -0.5 $\times$(T-T_{NAT}) is equivalent to an additional 0.19 ppbv vortex mean denitrification compared to the baseline run (NR3). It can be shown that this fractional offset is equivalent to a mean reduction in temperature of 1.53 K in the NAT-supersaturated region at 565 K. From Figure 6.10, 1.53 K global cooling corresponds to 0.33 ppbv additional vortex mean denitrification compared to NR3. Increased particle growth contributes around 0.19 ppbv (58%) of this additional global denitrification and the remainder of the additional loss (0.14 ppbv, 42%) is due to the increased area of NAT-supersaturation. With a 0.77 K cooling, the contributions are 56% and 44% from enhanced growth and increased NAT-supersaturation, respectively.

Overall, the main effects of decreasing temperature are extension of particle lifetimes by increasing the volume of the vortex which is NAT-supersaturated. Increased particle growth rates through more rapid condensation of HNO_3 are also important. These processes are not decoupled as the lifetime of a growing particle is ultimately limited by the time taken to sediment through the NAT-supersaturated region.

6.5 Vortex concentricity

In the Antarctic vortex, the wind and temperature fields are normally concentric around the pole. In the Arctic, however, the wind and temperature fields are frequently offset [*Pawson et al.*, 1995]. The underlying meteorological causes of this offset (baroclinic) vortex state in the Northern Hemisphere have been discussed in Chapter 4. In a baroclinic vortex, NAT particles are more likely to be advected out of the cold pool, reducing the time available for growth. This situation would be expected to reduce the size of NAT particles and, therefore, their sedimentation velocity and denitrification potential.

The sensitivity of denitrification to the concentricity of the cold pool and vortex is explored by progressively increasing the offset between the centroids of the vortex and cold pool. The cold pool is rotated relative to the vortex from the baseline analysis used for the runs above. These rotated temperature fields were produced by performing solid body rotations of increasing magnitude ($0°$, $5°$, $10°$, $15°$ and $20°$) on the temperature field about an axis through the centre of the sphere connecting the latitude/longitude points $[0°,0°]$ and $[0°,180°]$ and were provided by Graham Mann. This approach has the advantage of retaining the cold pool area and shape which allows direct comparison of the effect of an increasingly baroclinic cold pool and vortex on particle growth and denitrification. These rotated temperatures mean that the model meteorological fields are not in thermal wind balance and may not be totally representative of baroclinic polar vortices. Nevertheless, the rotated fields are useful for investigating the sensitivity of denitrification to the degree of baroclinicity of the vortex and cold pool.

Figure 6.13 shows the temperature fields on the 565 K potential temperature level for cold pool rotations of $0°$ and $20°$. T_{NAT} is diagnosed from the expression of *Hanson and Mauersberger*, [1988] (Equation 2.39) for $[HNO_3] = 8$ ppbv and $[H_2O] = 5$ ppmv. At a rotation of less than $10°$ the entire cold pool is located within the vortex and at $20°$, the centroid of the cold pool is located close to the edge of the vortex (normalised centroid separation $= 1$). Figure 6.14 shows how the centroid separation of the vortex and cold pool normalised by the radius of the cold pool is determined. The vortex and cold pool are considered to be circles with centroids X and Y respectively. The centroid separation, $C = X\text{-}Y$, is normalised by the radius of the cold pool (R). Values of nor-
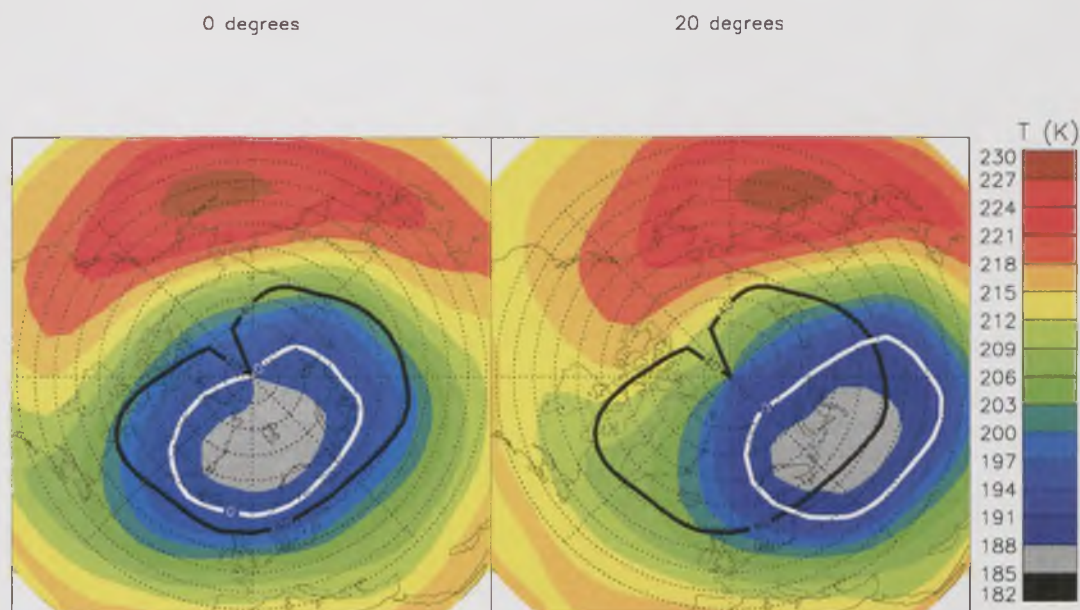
Figure 6.13: Temperature contour plot at 565 K for cold pool rotations of 0° and 20°. The 40 PVU MPV contour (black) and $T = T_{NAT}$ contour (white) are also shown.

malised centroid separation > 1 indicate the absence of "closed" flow conditions as all the vortex air is likely to experience excursions above T_{NAT}, considerably reducing the time available for particle growth and the potential for denitrification. This approximation is not useful when either the cold pool or vortex are considerably distorted. Nevertheless, it is an indicator of the extent of closed flow in this study as neither the cold pool or vortex are significantly distorted (Figure 6.13).

Figures 6.15 shows the denitrification produced in the microphysical and equilibrium schemes at 565 K (the altitude of coldest temperatures and close to peak denitrification). At rotations of 0° both the equilibrium and microphysical model runs produce denitrification of around 3 ppbv close to the centre of the vortex on Day 10. Increasing the rotation of the cold pool relative to the vortex affects the denitrification produced by the microphysical model in a very different way to that produced by the equilibrium scheme. Increasing the offset of the cold pool has much less effect in the equilibrium
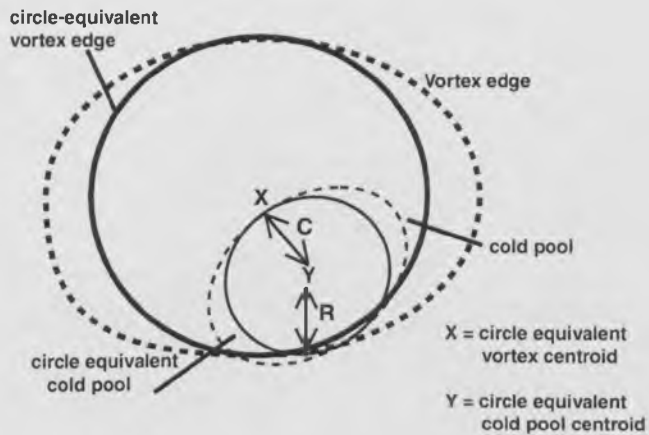
Figure 6.14: Determination of centroids of vortex and cold pool. Centroid separation normalised by cold pool radius = C/R.

scheme, indicating that denitrification is equally efficient wherever $T < T_{NAT}$. Maximum denitrification is reduced in the equilibrium scheme because it is spread over a wider area of the vortex. The denitrification produced by the microphysical model decreases rapidly as the separation of the vortex and cold pool centroids increases, as the lifetime of NAT particles and their denitrification potential is reduced.

The microphysical factors causing the decreased denitrification with increased cold pool and vortex offset are illustrated in Figure 6.16. The mean age of particles declines rapidly from 3 days (0° offset) to 0.8 days (20° offset) due to increased advection of particles out of the cold pool. This has a direct impact on denitrification by reducing the mean radius of particles and the mean number density, reducing vortex mean denitrification at 565 K from 0.48 ppbv with no offset to 0.03 ppbv with an offset of 20°. In contrast, the equilibrium model denitrification is less confined to the region close to the centre of the vortex and is much less affected by the offset between vortex and cold pool until a considerable fraction of the cold pool lies outside the vortex [*Mann et al.*, 2002].
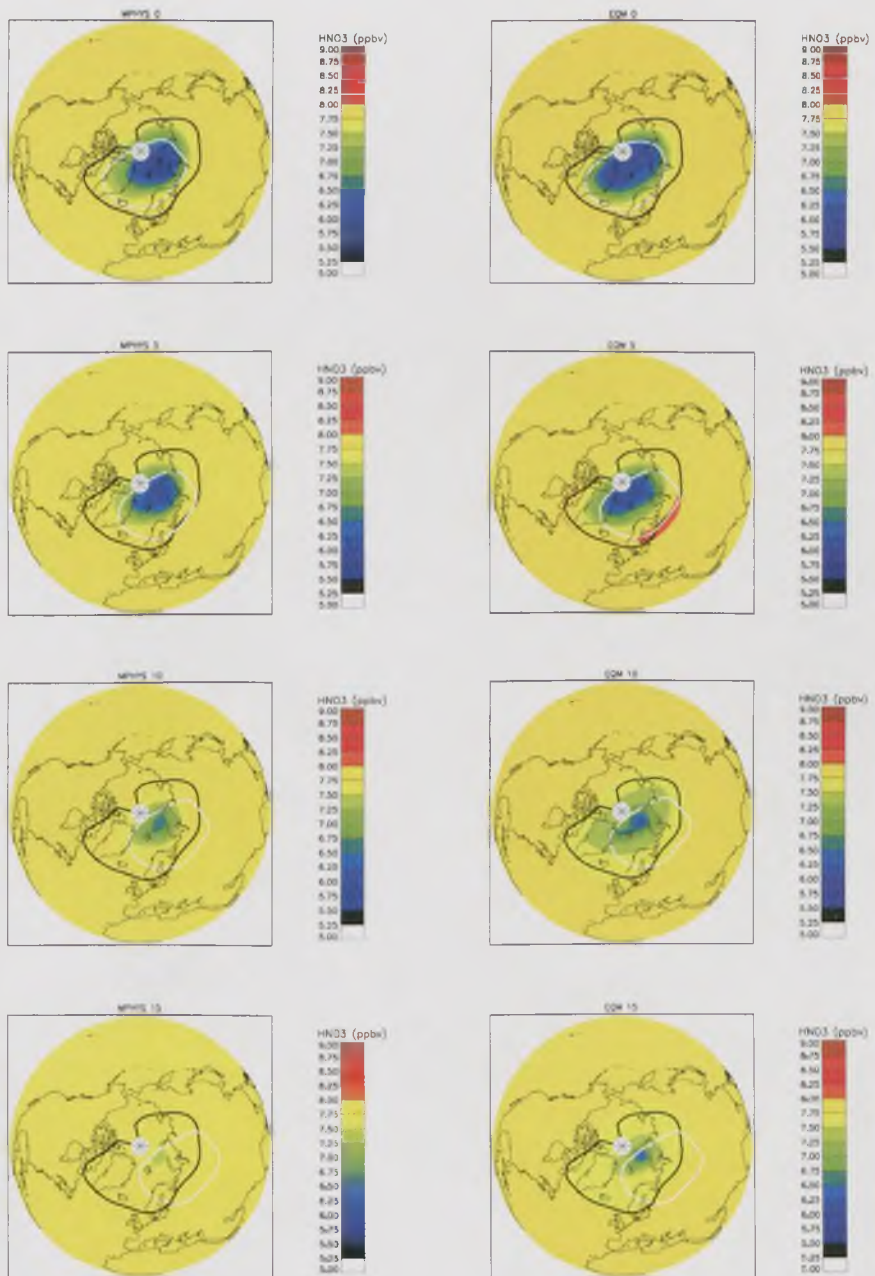
Figure 6.15: NO$_y$ field at 565 K on Day 10 for cold pool rotations of 0°, 5°, 10° and 15° for DLAPSE model (left) and the thermodynamic equilibrium scheme (right).
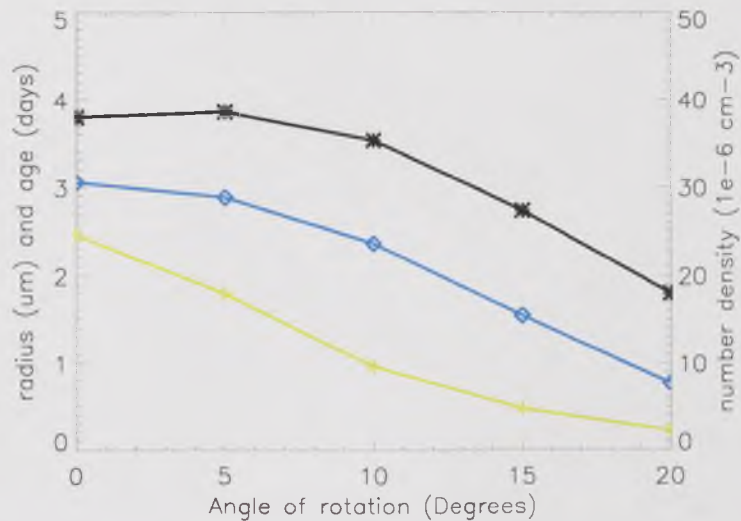
Figure 6.16: Vortex mean particle radius (black), mean age (blue) and mean number density (yellow) as a function of cold pool rotation for microphysical model runs.

6.6 Summary

This chapter has examined the sensitivity of the DLPASE model to changes in the model nucleation rate, vortex temperature and the relative orientation of the vortex and cold pool. At very low nucleation rates the particles grow to a maximum diameter of approximately 20 μm, which is an upper limit determined by continuous growth through the full depth of the NAT-supersaturated region. However, low nucleation rates result in very low total condensed mass, therefore, denitrification is small. The rate of denitrification increases with increasing nucleation rate until an upper limit is reached where particles are so numerous that competition for available HNO_3 limits their size and fall speed.

Decreasing the temperature increases the extent and magnitude of denitrification in the model. There are two contributory factors. A lower temperature increases the mass of HNO_3 available for condensation (by increasing the NAT-supersaturation) and increases the area of the cold pool available for particle growth. A 1.5 K decrease in temperature causes an additional 0.33 ppbv denitrification as a vortex average with enhanced particle

growth accounting for around 58% of the additional loss. Increases in the area of NAT-supersaturation accounting for the remaining 42% of this loss. The equilibrium denitrification scheme exhibits broadly similar sensitivity to changes in temperature as DLAPSE although the vertical distribution of denitrification is significantly different.

Increasing the offset between the cold pool and vortex has a dramatic effect on the magnitude of denitrification. The shift from "closed flow" conditions when the vortex flow and cold pools are aligned to "through flow" conditions reduces the lifetime and size of particles and therefore their denitrification potential. A rotation of $10°$ of the cold pool relative to the vortex is sufficient to reduce the vortex mean denitrification by 62% in the DLAPSE model. The equilibrium denitrification scheme is much less sensitive to the offset between the vortex and cold pool, decreasing by 16% for a $10°$ rotation because of the instantaneous particle growth assumption.

The following chapter uses a modified version of SLIMCAT coupled to DLAPSE to simulate the redistribution of HNO_3 during two previous cold winters. Comparisons are made with observations of denitrification from a variety of sources.

Chapter 7

Modelled denitrification in cold Arctic winters of the 1990s

7.1 Introduction

This chapter describes the modelled evolution of denitrification of the Arctic lower stratosphere during four recent cold winters - 1994/95, 1995/96, 1996/97 and 1999/2000. Detailed results are presented for seasonal simulations of two of these winters (1999/2000 and 1996/97) using the coupled SLIMCAT and DLAPSE model described in Chapter 5. Comparisons are made with observations of NO_y and HNO_3 from the SOLVE/THESEO-2000 field campaign during 1999/2000 and the ILAS instrument aboard the ADEOS satellite during 1996/97.

7.2 Specific model description

The model used in this chapter is similar to that described in Chapter 6 but with the modifications detailed below. Water and sulphuric acid are included as additional advected tracers in SLIMCAT to allow the inclusion of an equilibrium analytical liquid aerosol scheme for the sequestration of gas-phase HNO_3 [*Carslaw et al.*, 1995]. Uptake of HNO_3 into the background sulphate aerosol to produce a liquid PSC may

dramatically reduce the available gas-phase HNO_3 for NAT growth at low temperatures (typically ~ 3 K below the NAT equilibrium temperature). The model assumes a number density of 10 cm^{-3} for the background aerosol and the equilibrium mass of sequestered HNO_3 is calculated. The residual gas-phase HNO_3 volume mixing ratio is passed to the particle growth and sedimentation model. Water volume mixing ratios are also passed from the SLIMCAT advective model to DLAPSE for growth calculations. All simulations were run for a period of 100 days from a point in early winter prior to the onset of temperatures below T_{NAT}.

7.3 Modelled denitrification

Figures 7.1 – 7.4 show height-time slices of the calculated denitrification for 1994/95, 1995/96, 1996/97 and 1999/2000. Also shown is the area of the polar vortex where PSC formation is possible and the normalised separation of the centroids of the polar vortex and NAT-supersaturation area. The centroids of the polar vortex and cold pool are determined by considering each region as a uniform geometric structure (no weighting given to temperature or PV). The centroid separation is then normalised by the cold pool circle-equivalent radius (Figure 6.14).

Centroids are used to determine approximately the "concentricity" of the vortex and cold pool in order to indicate whether the vortex is in closed-flow or through-flow conditions. Large centroid separations are indicative of a highly baroclinic vortex dominated by through-flow conditions and short particle growth times. Low centroid separations indicate that the vortex and cold pool are concentric with a region of closed-flow leading to long particle growth times and significant denitrification potential. This simple approximation is useful for large periods of the winter although it may not accurately represent the flow when the Arctic vortex is highly distorted [*Mann et al.*, 2002].

Each of the winters studied were colder than the climatological average for the Arctic over the period 1965 – 1998 and featured extended periods of temperatures below the threshold for the formation of PSCs [*Pawson and Naujokat*, 1999]. Although each of these winters was cold, considerable dynamical differences exist between them. The Arctic winter of 1994/95 was characterised by a smaller cold pool in terms of both area
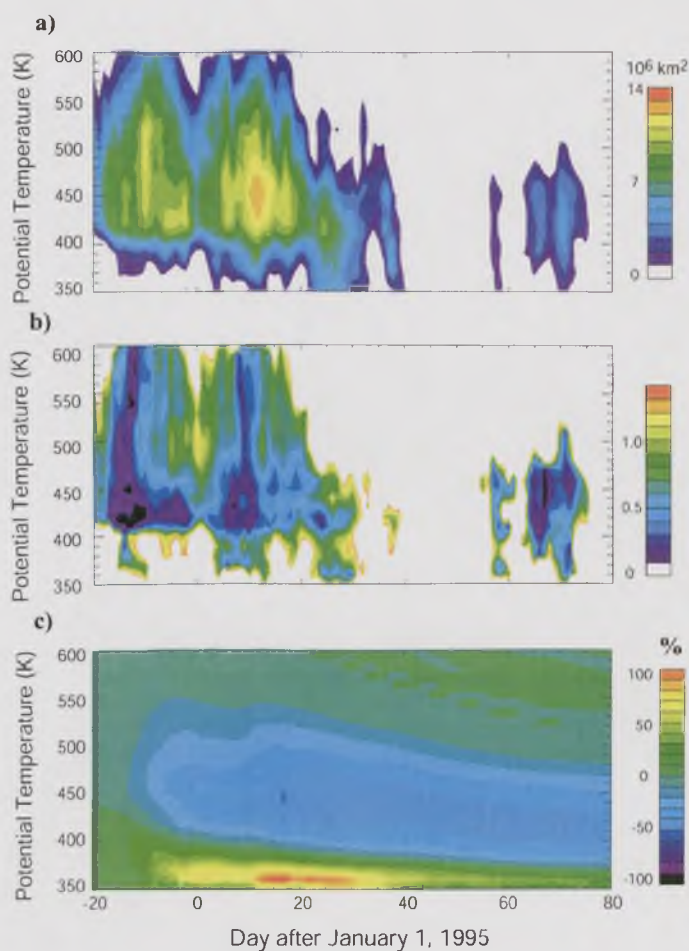
Figure 7.1: Contour plots showing the temporal evolution of a) vortex area; b) normalised separation of cold pool and vortex centroids; and c) % denitrification as a function of potential temperature for winter 1994/95.

and vertical extent compared to 1999/2000. In addition, the vortex and cold pool were generally less concentric (more baroclinic) in 1994/95. There were two short periods during 1994/95 (December 13 – 20 and January 10 – 15) when the centroid separation between the vortex and cold pool were low. This resulted in longer particle growth times and significant denitrification. Vortex-mean denitrification reached a maximum of 6 ppbv (35% of NO_y at 500 K) by mid-January 1995.

The early winter of 1995/96 was characterised by a cold and concentric vortex and cold
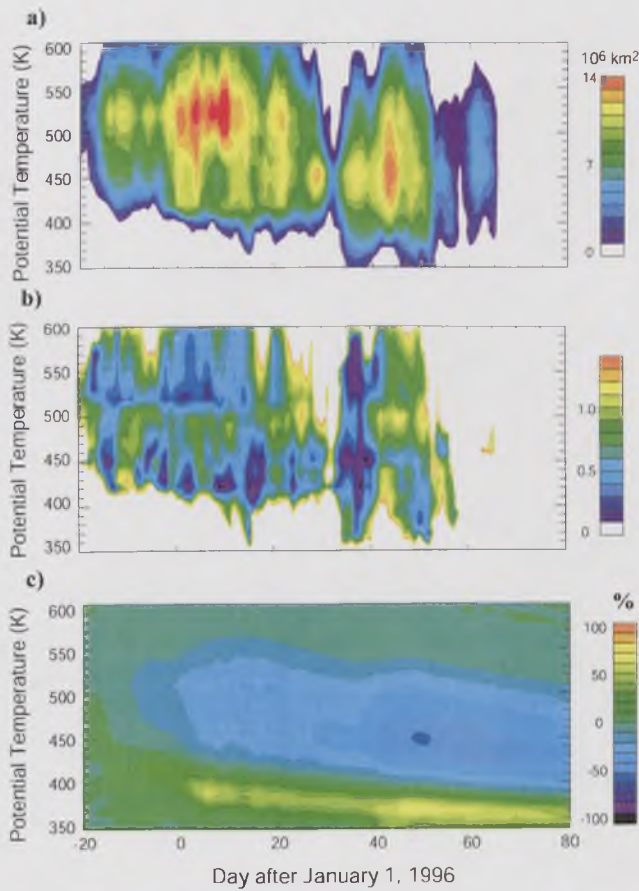
Figure 7.2: As Figure 7.1 but for 1995/96.

pool at altitudes above 500 K. This would be expected to produce intense denitrification, but Figure 7.2 reveals the existence of a region with a high centroid separation between 450 – 500 K. The impact of this dynamical feature on the magnitude of denitrification at this time is clearly demonstrated as the large centroid separation decreases the particle growth times. At around day 40 the vortex and cold pool become concentric and the rate of denitrification increases to give a maximum vortex-mean denitrification of 8 ppbv (50% of NO_y at 450 K).

In 1996/97, the polar vortex was too warm for the formation of PSCs until early January. The period between mid-January and early February was characterised by a shallow and disturbed region below NAT-supersaturation above 500 K with short par-
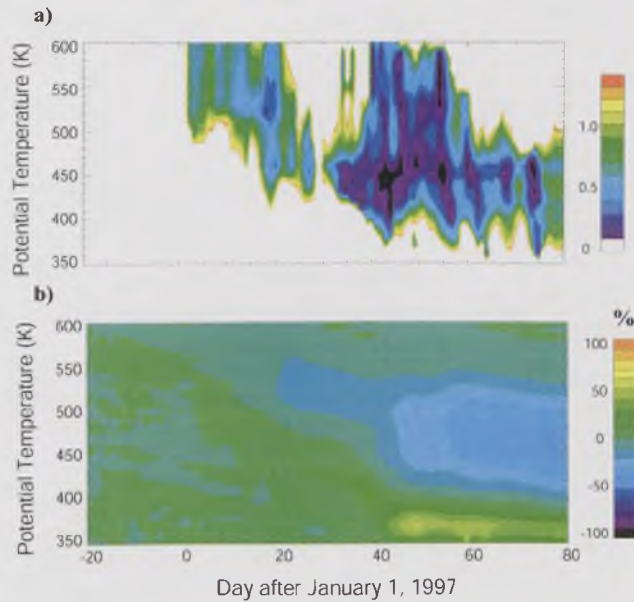
Figure 7.3: Contour plots showing the temporal evolution of a) normalised separation of cold pool and vortex centroids; and b) % denitrification as a function of potential temperature for winter 1996/97.

ticle lifetimes and minimal denitrification. From mid-February onwards, the situation was radically different with a deep cold pool of moderately large area and very low centroid separations. This allowed the formation of large NAT particles at significant number densities in the model causing moderately strong denitrification over a relatively small area of the vortex. The vortex mean denitrification at 450 K reached 30% by the end of February 1997.

The Arctic winter of 1999/2000 was characterised by an exceptionally cold and concentric vortex and cold pool between mid-December 1999 and late-January 2000, producing the ideal conditions for denitrification. Vortex-mean denitrification reached a peak of 55% by mid-February 2000 between 400 and 450 K. The vortex was also more than 40% denitrified between 550 and 380 K at this time.
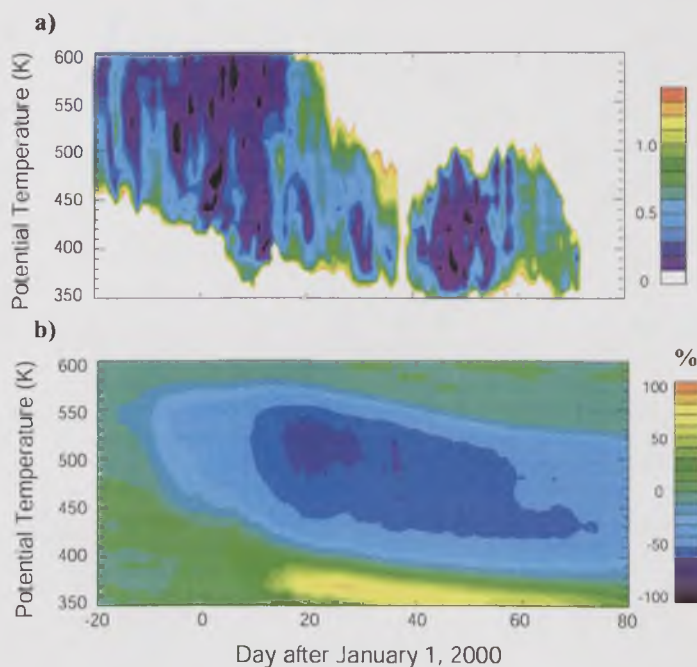
Figure 7.4: Contour plots showing the temporal evolution of a) normalised separation of cold pool and vortex centroids; and b) % denitrification as a function of potential temperature for winter 1999/2000.

7.4 Comparison of modelled denitrification with observations during winter 1999/2000

Model HNO_3 tracer fields are compared with in-situ NO_y observations from the ER-2 and the limited HNO_3 observations from the MLS instrument to evaluate the performance of the microphysical denitrification scheme. Modelled particle size distributions are also compared with in-situ particle observations from the NO_y instruments aboard the ER-2.

7.4.1 Model initialisation

Tracers for winter 1999/2000 were initialised from a full-chemistry, multi-annual SLIM-CAT model run [e.g. *Chipperfield*, 1999]. Model NO_y was scaled to observations from

the JPL Mark IV interferometer on December 3, 1999, within the polar vortex as the model produces excess NO_y at altitudes above 25 km. Diabatic descent within the vortex during the winter would bring this air into the denitrified region by the end of the winter making meaningful comparison difficult.

The baseline volume-averaged nucleation rate used in the model (8.0×10^{-9} cm^{-3} s^{-1}) was derived from ER-2 NAT-particle observations by *Northway et al.* [2002]. Integrated number densities from forward inlet on the NO_y instrument were approximately 10^{-4} cm^{-3} for particles greater than 2 μm diameter for long periods of this flight. A series of model runs were carried out with the nucleation rate adjusted each time to produce model particle number densities of $\sim 10^{-4}$ cm^{-3} in a sampling volume corresponding to the gridboxes containing the ER-2 flight track (latitude: 69.3°N to 85.6°N, longitude: 16.9°E to 22.5°E and altitude: 420 K to 440 K).

Figure 7.5 shows the sensitivity of the modelled denitrification to the volume-averaged nucleation rate for the entire winter rather than a 10 day period with fixed meteorology as discussed in Chapter 5. Increasing the rate of NAT particle nucleation has the expected effect of increasing the initial rate of denitrification at all levels within the NAT region, resulting in approximately 0.7 ppbv (10%) extra denitrification with a nucleation rate of 8.0×10^{-10} cm^{-3} s^{-1}, increasing to approximately 1.5 ppbv (20%) when the nucleation rate is increased further to 8.0×10^{-9} s^{-1}. The vortex is defined as the region poleward of the modified potential vorticity contour relative to the EPV at 460 K (MPV$_{460}$) greater than 36 PVU. The magnitude of denitrification may be determined by comparison with observations but is relatively insensitive to small changes in the nucleation rate. A nucleation rate of 8.0×10^{-10} cm^{-3} s^{-1} is used in all model runs in the remainder of this chapter and all particels are nucleated with a radius of 0.1 μm.

7.4.2 Comparison with ER-2 NO_y observations

Single flight comparisons

Comparisons of the model NO_y output at 12 UT when interpolated to the ER-2 flight track are generally very good, as illustrated by Figure 7.6. The yellow and green shaded regions indicate the range of model values obtained for NO_y and NO_y^*, respectively,
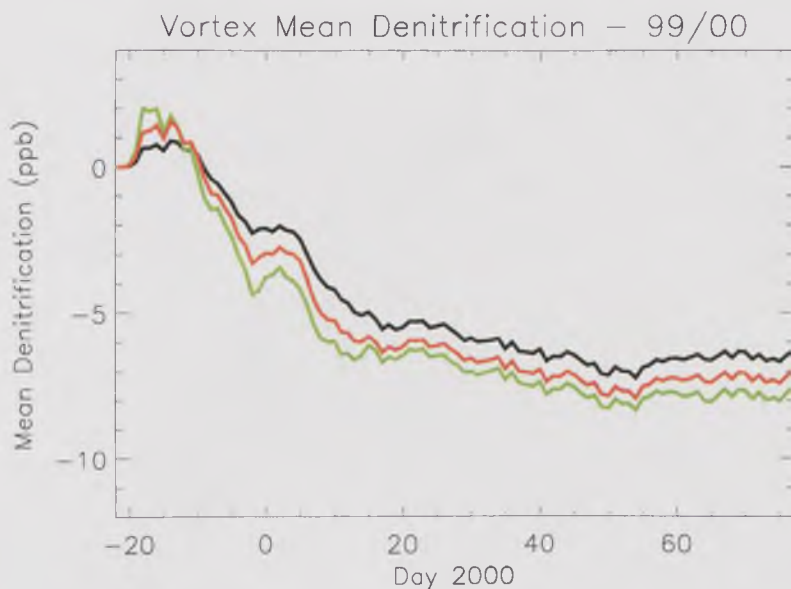
Figure 7.5: Modelled vortex mean denitrification at 455 K for the Arctic winter 1999/2000 at particle nucleation rates of 8.0×10^{-10} (black), 2.4×10^{-9} (red) and 8.0×10^{-9} (green) cm^{-3} s^{-1}.

when the eight neighbouring horizontal gridboxes are sampled (at latitude $\pm$ 5.6° and longitude $\pm$ 5.6° from the point of observation). This range is examined because a point-by-point comparison may be significantly affected by a small mis-match between the model 3-D fields and observations for reasons other than inherent model error. This problem is compounded when large spatial gradients in a tracer, such as NO_y, exist.

Figure 7.6 shows observed and modelled NO_y and NO_y^* for two ER-2 flights on January 20 and March 11, respectively. On both flights the observed NO_y^* and model passive NO_y are in good agreement, apart from the region between 3.7 and 4.2×10^4 s UT on January 20 and around the vortex edge (3.2–3.5×10^4 s UT and 4.2–4.6×10^4 s UT) on March 11. On January 20 the model reproduces the large spikes in observed NO_y at 3.6, 4.7, 5.0 and 6.2×10^4 UT which are associated with ascent and descent through layers of strongly nitrified air around 15 km. The model also reproduces the very low NO_y values of around 2 ppbv at 5.2×10^4 UT when the aircraft is at 20 km near the pole.
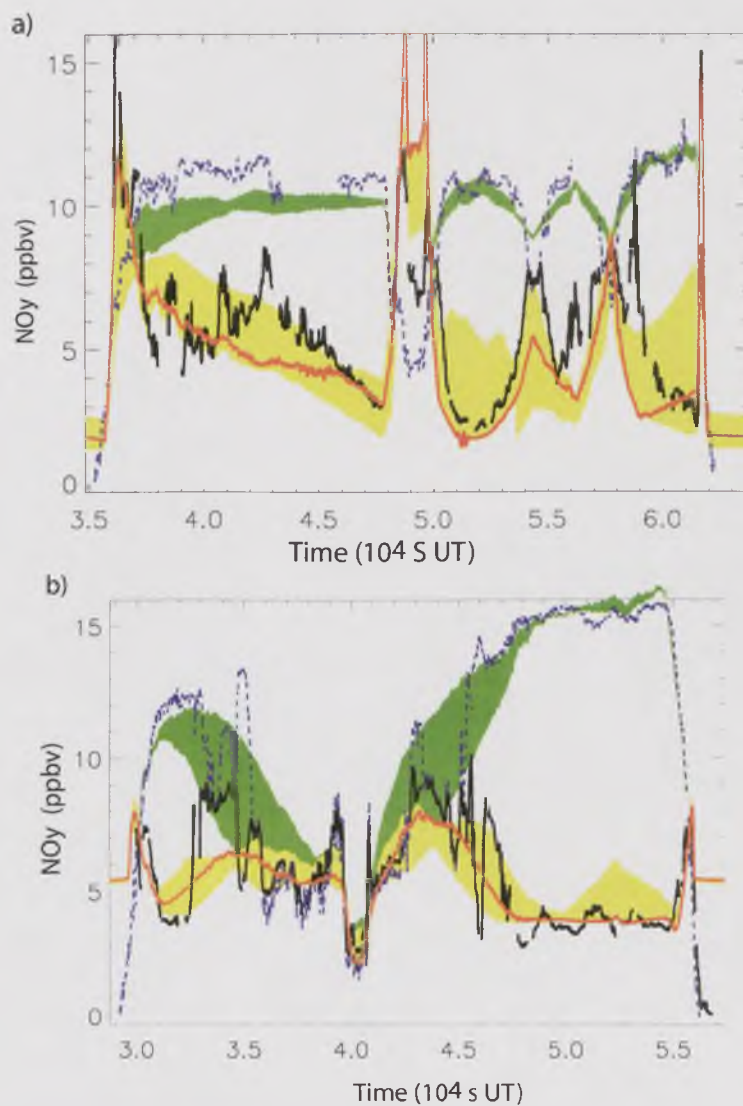
Figure 7.6: Comparisons of model and ER-2 NO_y for a) January 20 and b) March 11, 2000. Key : ER-2 NO_y (black), model NO_y (red) and ER-2 NO_y^* (blue), model NO_y range (yellow shading) and model passive NO_y range (green shading).

There are two regions of significant discrepancy between the observed and modelled NO_y. A large region between 4.0 and 4.5×10^4 UT and small regions later in the flight between 5.5 and 6.0×10^4 UT. The former discrepancy may be due to the

aircraft encountering a large PSC with significant numbers of small particles which are oversampled by the aircraft. The latter regions may be too small to be reproduced in a global model (see Appendix D for details of the NO_y instrument). The cross-vortex flight on March 11 demonstrates the excellent agreement between observed and modelled NO_y. Around the edge of the vortex (between $3.2 - 3.5 \times 10^4$ s UT and $4.2 - 4.6 \times 10^4$ s UT) the model does not fully capture the small-scale spatial variability in the observed NO_y. The minimum NO_y encountered on the flight of March 11, 2000 is ~4 ppbv at 460 K.

Figure 7.7 indicates that the region between $450 - 550$ K (directly above the ER-2) was almost totally denitrified on January 20. By mid-March these airmasses had descended to altitudes where they could be sampled by the ER-2. Denitrification had been essentially complete for over a month by this time and the very low NO_y concentrations found during the January flights have increased due to mixing within the vortex and across the vortex edge in the model. The ER-2 observations within the polar vortex during March indicate minimum gas-phase NO_y concentrations of ~4 ppbv, in excellent agreement with the model. There is no evidence of NO_y values significantly lower than this value during any of the ER-2 flights in March. Observations at higher altitudes in January would have provided additional constraints in order to evaluate the performance of the new model denitrification scheme.

In general, the model is able to reproduce the observed in-vortex NO_y for the majority of flights although certain flights show considerable regions of disagreement with the observed NO_y. Figure 7.8 shows the model and observed NO_y for the ER-2 stack flight of February 3, 2000. Here, for clarity, each of the model outputs is plotted as a line rather than the contours used in Figure 7.6. Modelled passive NO_y and ER-2 NO_y^* show very good agreement but the NO_y shows a considerable discrepancy between 6.9 $\times 10^4$ and 7.4 $\times 10^4$ UT.

NO_y normally exhibits a large vertical gradient which can be considerably enhanced in a strongly denitrified vortex, increasing the difficulty of exactly reproducing the observed denitrification. The apparent disagreement between the model and ER-2 NO_y during the early leg of the flight can be explained by Figure 7.9. This figure shows the model NO_y profile interpolated to the aircraft position. At the lowest altitudes, where the model discrepancy is greatest, it can be seen that the apparent disagreement is in
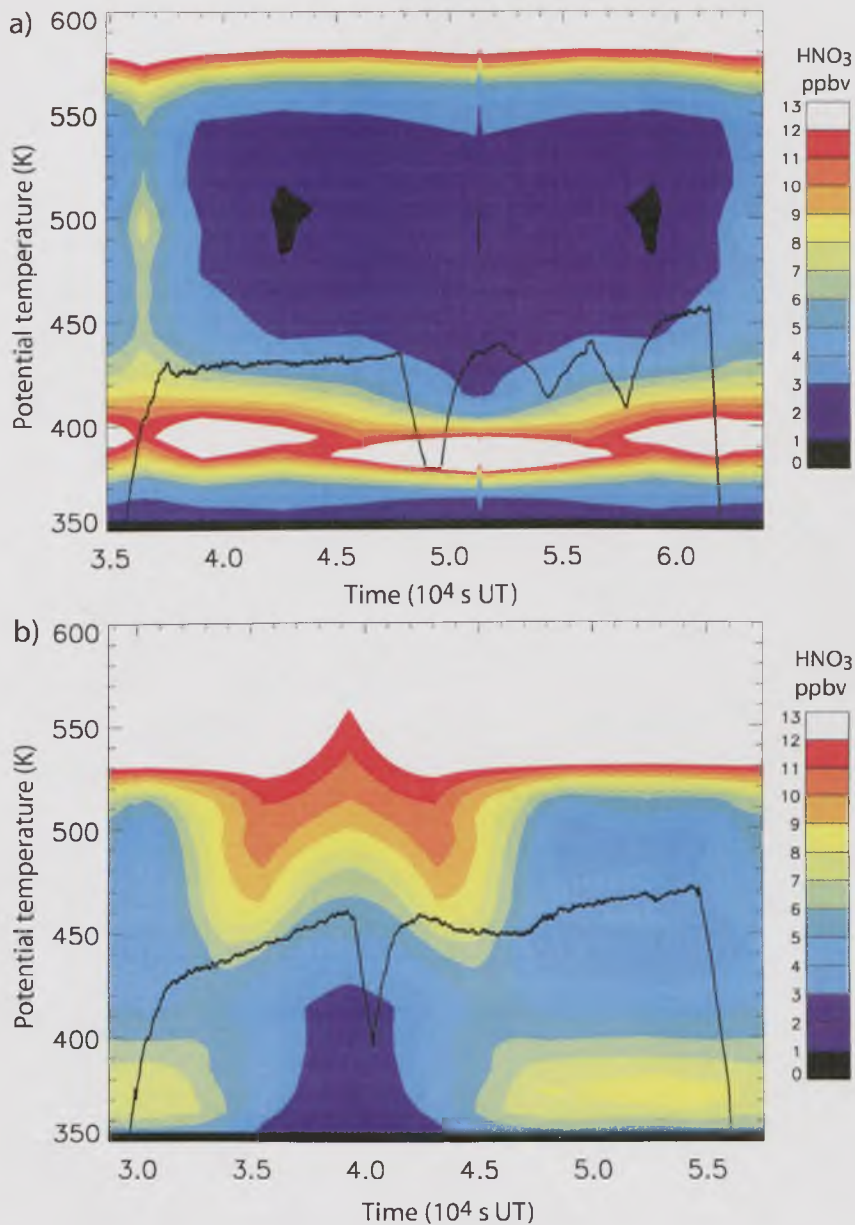
Figure 7.7: Comparisons of model and ER-2 NO_y for a) January 20 and b) March 11, 2000.

a region where the vertical NO_y gradient is particularly large - NO_y changes by 12 ppbv over a narrow vertical distance. This region is also close to the model bottom boundary at 350 K which also increases the difficulty of obtaining the correct vertical NO_y distribution in the lowest model isentropic levels. In addition, there is a region of
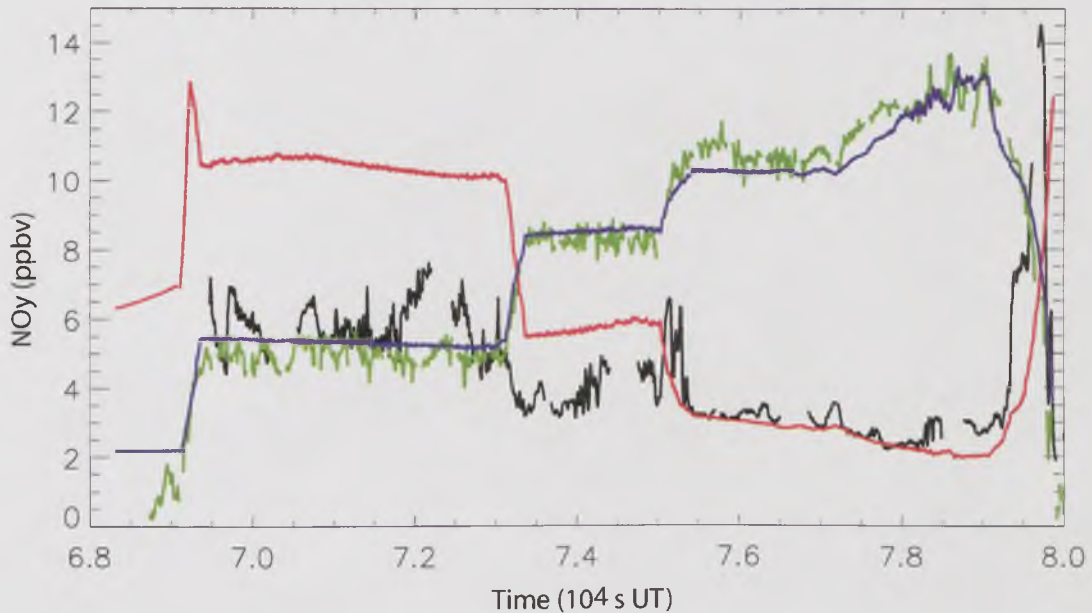
Figure 7.8: Comparisons of model and ER-2 NO$_y$ for February 3, 2000. Key : ER-2 NO$_y$ (black), model NO$_y$ (red), ER-2 NO$_y^*$ (blue) and model passive NO$_y$ (green).

highly denitrified air with NO$_y$ below 2 ppbv between 500 – 530 K, above the aircraft flight track.

Denitrification and nitrification are driven by the vertical temperature structure of the vortex. Accurately modelling the region of nitrification is especially difficult as it occurs in a very narrow vertical region of the vortex immediately below the region of NAT supersaturation. The model has a high vertical resolution in the lower stratosphere with isentropic levels at 10 K intervals corresponding to a vertical resolution of approximately 300 m but it is the resolution of the temperature field from the meteorological analysis ($\sim$800 m) used to force the model which governs the location of the region of nitrification.

Multi-flight NO$_y$ profiles

Figure 7.10 shows the probability distribution of modelled and observed denitrification as a function of potential temperature for all 12 ER-2 flights between January 14
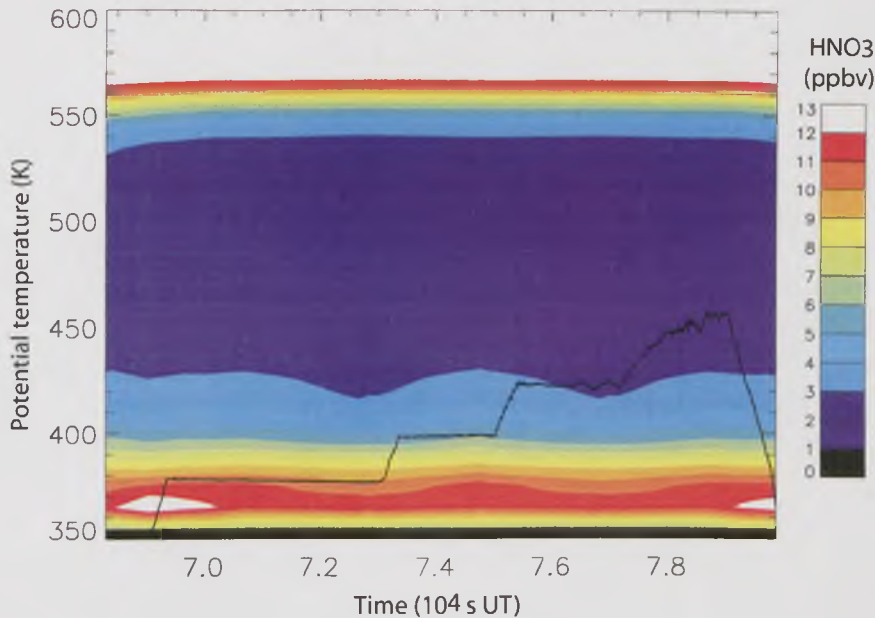
Figure 7.9: Model NO$_y$ profile along ER-2 flight track for February 3, 2000.

and March 12, 2000. The ER-2 data used in this comparison were 10-second running averages obtained from the merge files provided by Ross Salawitch (Jet Propulsion Laboratory, Pasadena). The model was interpolated to the ER-2 position at each of these times. The denitrification calculated at each data point was binned into 1 ppbv, 10 K bins and normalised by the total number of points.

Figure 7.10a shows the probability distribution for all points and Figure 7.10b shows only points where the temperature was above T_{NAT} (based on the in-situ data). This was done to avoid possible enhancement of the gas phase NO$_y$ by oversampling of NO$_y$-containing aerosol particles [*Popp et al.*, 2001]. Despite the rejection of the majority (over 80%) of data from the in-vortex fights during the first ER-2 deployment in January and early February, sufficient spread of points remain to allow a meaningful comparison. Comparing observed and modelled denitrification in this way removes some of the noise inherent in any point-by-point comparison between high resolution in-situ data and low resolution model fields due to the presence of sub-grid scale features in observations which are not reproduced in global 3-D models.

The majority of data were recorded at ER-2 cruise altitudes between 420 K and 460
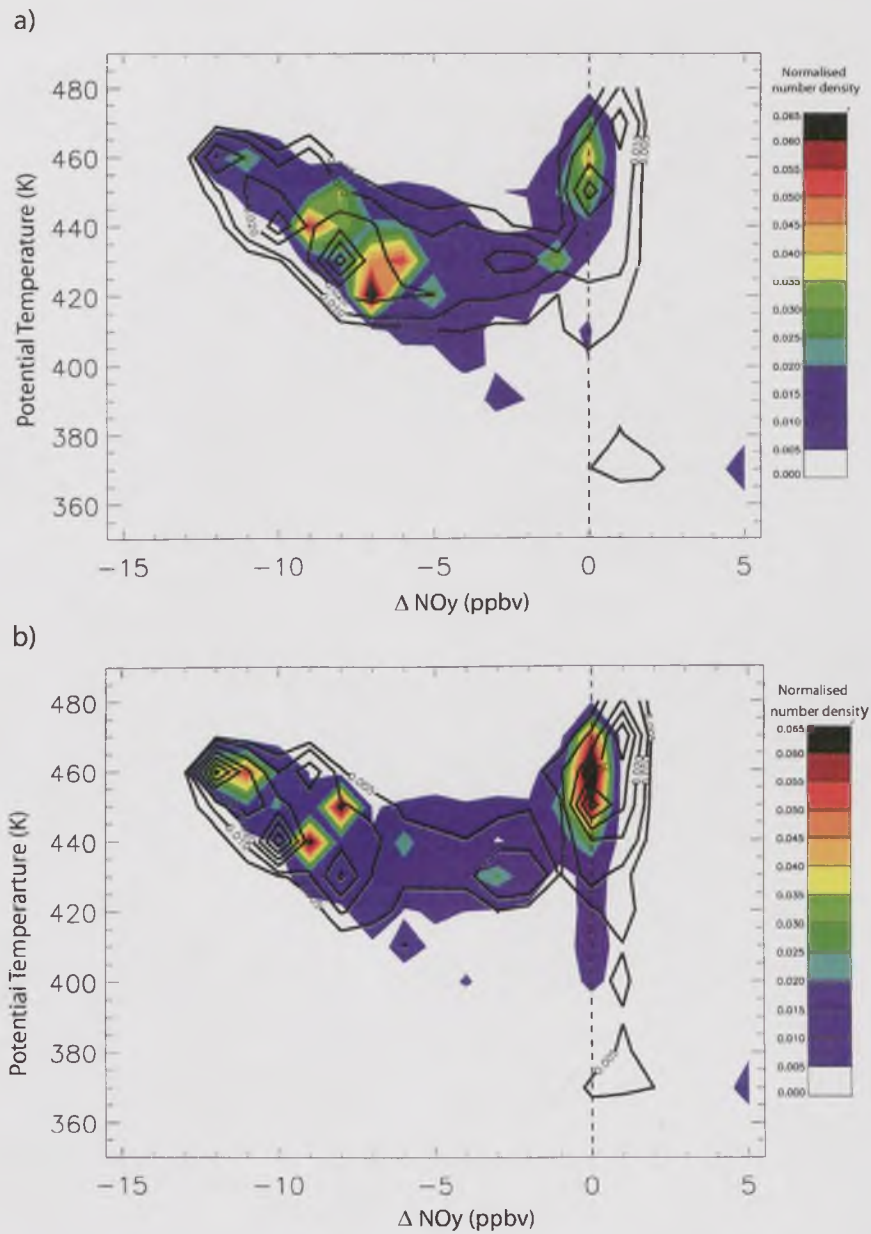
Figure 7.10: Normalised probability density distribution of model and ER-2 denitrification as a function of potential temperature for a) all points and b) points above T_{NAT} only. Coloured contours show model denitrification (NO_y minus passive NO_y) and black contour lines show ER-2 denitrification (NO_y minus NO_y^*) for all ER-2 flights to March 12, 2000.

K. The model captures the overall magnitude and vertical distribution of the observed denitrification. In both the observations and the model maximum denitrification of 13 ppbv occurs at 465 K, falling to around 8 ppbv at 415 K. There is a general 1 ppbv offset between modelled and observed denitrification in this region when the denitrification is greater than 8 ppbv. A small discrepancy like this is within the constraints of any comparison based on diagnosing denitrification from NO_y^*, which assumes the complete absence of mixing of in-vortex N_2O. This offset is also evident at 465 K in airmasses where there is little denitrification.

7.4.3 Microwave Limb Sounder comparisons

The MLS instrument aboard the UARS satellite has provided global observations of many key stratospheric species, including O_3, HNO_3 and ClO since its launch in 1991 [*Waters et al.*, 1999]. In recent years, the instrument has suffered a number of failures and its operation has been severely curtailed although it did provide gas-phase HNO_3 measurements over a restricted region of the Arctic for 3 periods during 1999/2000. The absence of significant denitrification in the MLS HNO_3 observations for the Arctic prior to 1999/2000 has been a major factor in support of the idea that denitrification was not a common phenomenon.

MLS instrument description

The MLS instrument measures microwave emissions in three regions – 63, 183 and 205 GHz with a vertical scan range between 15 and 85 km. Important advantages of this technique include the ability to observe profiles at night and the long wavelength is not degraded by the presence of stratospheric aerosols [*Santee et al.*, 1999]. HNO_3 is not a primary product of the MLS instrument but is routinely retrieved due to an emission line in the 205 GHz band. Latitudinal coverage interchanges between north-looking (80°N – 34°S) and south-looking (80°S – 34°N) periods every 36 days. The data used in this study are based on the Version 5 retrieval algorithm and have a quoted precision of 1 ppbv and have not been corrected for biases.

Figure 7.11 shows the MLS averaging kernel at the standard UARS pressure levels.
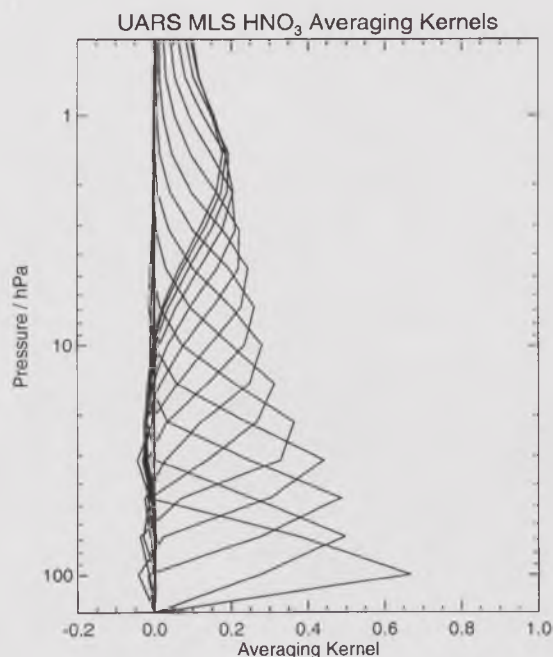
Figure 7.11: MLS HNO$_3$ averaging kernel as a function of pressure for the region 100–1 hPa.

The effective vertical resolution of the MLS instrument in the lower stratosphere is 6 km. This is a considerable disadvantage in the diagnosis of denitrification in the Arctic where HNO$_3$ is rarely removed from the stratosphere and the separation of the denitrified and nitrified air may be close to the resolution of the instrument.

The model is initialised with an NO$_y$ field from a scaled SLIMCAT model run whereas the MLS instrument measures only gas-phase HNO$_3$. Model NO$_y$ is assumed to be equal to HNO$_3$ in the Arctic lower stratosphere. In order to compare the model with the satellite observations the model fields were interpolated from their isentropic coordinates to the standard pressure coordinates. The model fields are further modified by the application of the MLS averaging kernel to degrade the model fields to the vertical resolution of the MLS instrument. Comparison between MLS HNO$_3$ and model NO$_y$ is restricted to the lower stratosphere where the assumption that NO$_y$ $\approx$ HNO$_3$ is valid.
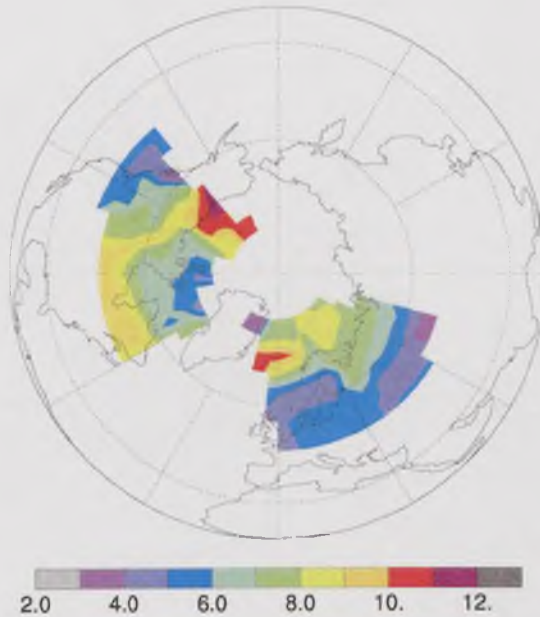
Figure 7.12: Contour plot of MLS HNO_3 at 68 hPa on February 9 – 11, 2000 (courtesy of Michelle Santee, NASA JPL).
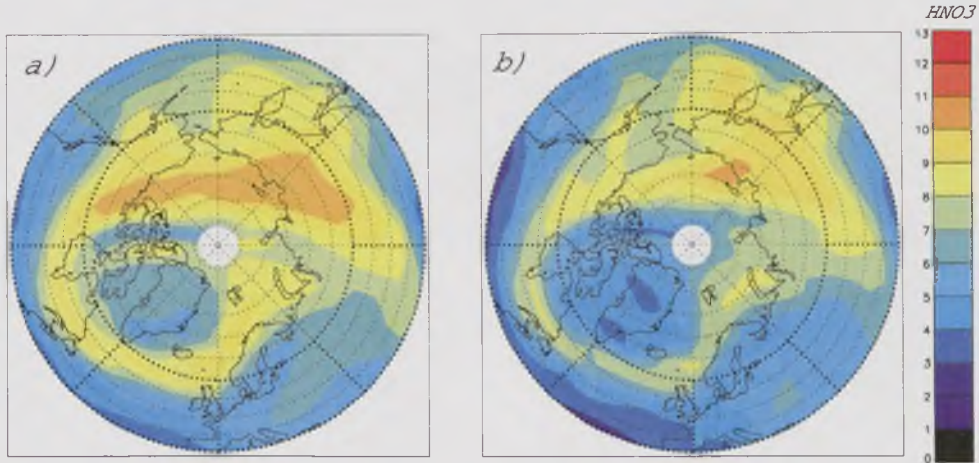
Figure 7.13: Model NO_y at 68 hPa on February 10, 2000 a) degraded to the MLS vertical resolution (~6 km) and b) without degradation (~1.5km).

February 9 – 11, 2000 observations

Observations of gas phase HNO_3 at 68 hPa on February 9 – 11, 2000 from the MLS instrument (Figure 7.12) indicate a region with mixing ratios as low as 5 ppbv in the

polar vortex over Greenland and Hudson Bay. The satellite observations also indicate a region with high HNO_3 mixing ratios (around 11 ppbv) located over the Alaska/Yukon coastline. Figure 7.13 shows the model NO_y interpolated to 68 hPa before and after the application of the MLS averaging kernel on February 10, 2000. Degrading the vertical resolution of the model increases the apparent gas-phase concentration by 2 – 4 ppbv within the polar vortex when the vortex is strongly denitrified. This may have contributed to the absence of an unambiguous denitrification signal in MLS observations of the Arctic in earlier winters [*Santee et al.*, 2000]. The degraded model field reproduces the overall magnitude and location of the observed high HNO_3 over the Alaskan coastline and the reduced HNO_3 over Greenland during 1999/2000.

7.4.4 Particle field comparisons

Figure 7.14 compares the modelled particle size distributions on January 20, 2000 with particle sizes derived from ER-2 NO_y observations by *Northway et al.* [2002]. The observed size distribution is obtained for a short period of the flight (46 – 47 ks UT) at altitudes of 420 – 440 K. Individual peaks in the forward facing inlet are assumed to be single particles which have a normal size distribution in the atmosphere. Model nucleation rates were scaled to produce integrated number densities which match the observations (around 10^{-4} particles cm^{-3}). The distribution of particle sizes is captured by the model with a sharp reduction in particle populations of particles with a diameter greater than 18 μm. No particles larger than 20 μm are observed which is consistent with the calculated upper limit of particle sizes based on microphysical theory [*Carslaw et al.*, 2002]. The modal particle size is greater in the model than observed (14 μm), especially when a small region of the model ($77° – 82°N$) is sampled.

Figure 7.15 shows the model particle size distributions on two isentropic levels corresponding to the upper and lower regions sampled by the ER-2 on January 20, 2000. The model indicates that the largest particles were located in a region 45 – 90°E, 70 – 80°N, to the east of the ER-2 flight track and close to the downwind edge of the cold pool. In contrast, at the upwind edge of the cold pool, modelled particles are considerably smaller. Model particles extend beyond the downwind edge of the indicated cold pool, consistent with the time required for evaporation of large particles. Particle size
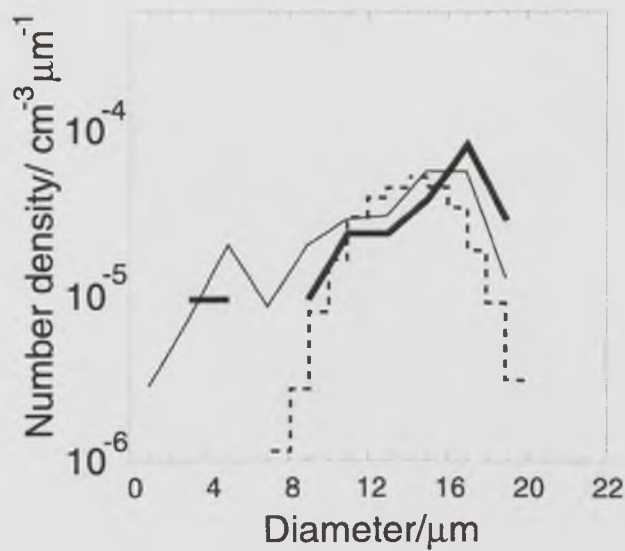
Figure 7.14: Comparison of ER-2 NO$_y$ instrument derived particle sizes with modelled particle sizes for January 20, 2000. The ER-2 size distribution (dashed line) was obtained for flight times between 46 and 47 ks UT at potential temperatures of 420 – 440 K. Two modelled particle size distributions corresponding to the flight track are shown: above 70°N (thin line) and 77 – 82°N (thick line). Reproduced from *Carslaw et al.* [2002].

distributions within the cold pool are dominated by sedimentation. The mean model particle size increases significantly with decreased altitude within the cold pool. This can clearly be seen in Figure 7.15, where the maximum mean modelled particle radius increases from ∼4.0 μm at 440 – 450 K to >5.5 μm at 410 – 420 K. In contrast, the model indicates that mean particle sizes at the upward edge of the cold pool are not significantly affected by changing altitude.

7.4.5 Summary

The microphysical model produces denitrification which is in good agreement with observations from the ER-2 during the winter of 1999/2000. However, the model suggests
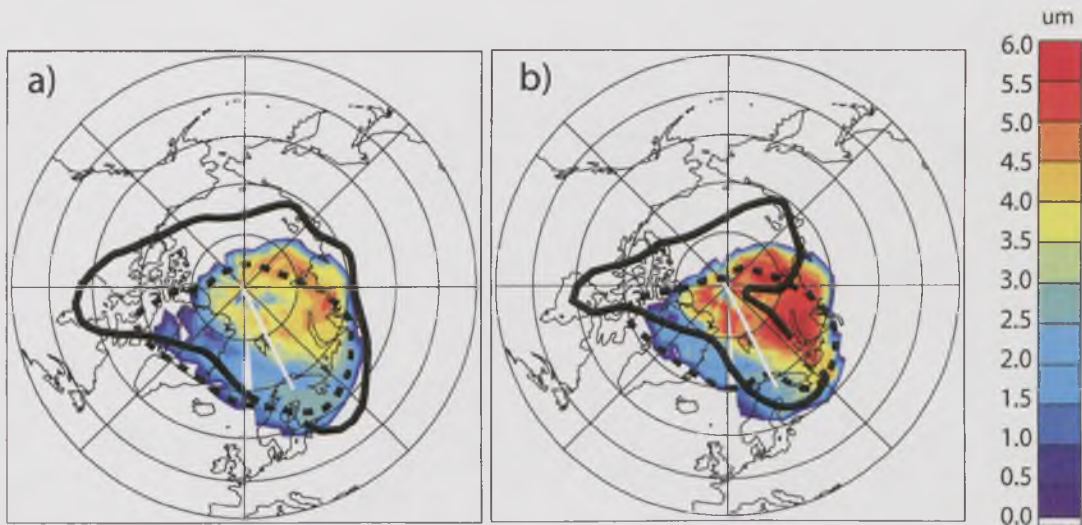
Figure 7.15: Model mean particle sizes at a) 450 – 440 K, and b) 420 – 410 K on January 20, 2000. Also shown is the MPV = 40 PVU contour (solid line), the region of NAT supersaturation (dashed line) and ER-2 flight track (white line)

that most of the denitrification had occurred before the first in-vortex flight on January 20, 2000, so there are no observations during the denitrifying phase. Observations during this period would have allowed additional constraints to be placed on the model nucleation rate as the rate of denitrification is sensitive to nucleation rate. In addition, the ER-2 vertical profiling of the vortex is limited to around 460 K, the region where different denitrification schemes exhibit the smallest differences. The most extensive denitrification in the models is to be found at higher altitudes (450 - 550 K).

In conclusion, although the observed and modelled denitrification are in agreement for this winter the lack of observations during the denitrifying phase and the limited vertical range of these observations limit their ability to fully constrain the microphysical denitrification model. In order to further evaluate the microphysical model denitrification scheme, model denitrification, results and observations for the Arctic winter of 1996/97 are now investigated.

7.5 Comparison of modelled denitrification with observations during winter 1996/97

The Arctic winter of 1996/97 was colder than the 1965 – 1998 average but characterised by a late onset of temperatures below the NAT equilibrium threshold. There was no full-scale scientific campaign during this winter although useful HNO_3 data is available from MLS and ILAS aboard ADEOS during this period [*Sasano et al.*, 1999].

7.5.1 Model initialisation

The model setup for this comparison was essentially as that used for the 1999/2000 winter (with a nucleation rate of 8.0×10^{-10} cm^{-3} s^{-1}). The 60-level ECMWF reanalyses were not yet available for the period of this study and, therefore, the 31-level analyses were used to force the model for the Arctic winter of 1996/97. This imposes limitations on the model transport as the uppermost level of these analyses is 10 hPa, considerably below the upper boundary of the model at 3000 K. Consequently, the model winds and temperatures are constant with height above the upper limit of the analyses. This linearity is likely to severely compromise long-term transport studies in the model when forced with these analyses. For the purposes of this seasonal study of the lower stratosphere the coarse vertical resolution of the 31-level analyses are likely to be a limiting factor.

In the absence of in-situ data for model initialisation, model NO_y, H_2O and H_2SO_4 were initialised from the latest multi-annual SLIMCAT model run (run 184) which contained the latest updates to gas-phase NO_y chemistry [*Brown et al*, 1999a; 1999b] and has more realistic in-vortex vertical NO_y profiles in the low to mid-stratosphere. This improvement is essential for comparisons in late winter when diabatic descent brings this air into the region where denitrification is possible (380 – 600 K).

Figure 7.3 shows the modelled vortex mean denitrification for 1996/97 as a function of potential temperature. During the first 25 days of this simulation there was a significant area between 500 and 650 K where temperatures were below T_{NAT} yet denitrification was only weak. This period was characterised by a distorted vortex with a large sepa-

ration of vortex and cold pool centroids resulting in short particle lifetimes and small particle radii. There is very little evidence of nitrification at lower levels during this period. In February and March 1997, there was an absence of dynamical activity [*Pawson and Naujokat*, 1999] which resulted in a stronger polar night jet, lower temperatures and moderate denitrification between 520 and 400 K. These results are consistent with the ILAS observations of *Kondo et al.* [2000], who attributed the observed denitrification during this February period to the sampled airmasses having experienced temperatures below T_{ice} 14 days earlier.

When compared to 1999/2000, the vortex-mean denitrification appears substantially lower (Figure 7.5). This may be attributed primarily to the much smaller area of denitrification in the modelled Arctic winter of 1996/97 compared to the unprecedented size in recent years of the cold denitrified region in 1999/2000. The core of the denitrified region has NO_y losses comparable to the denitrified regions of the vortex in 1999/2000 at 460 K (Figures 7.16 and 7.17) although the depth of the denitrified region is lower than 1999/2000.

7.5.2 Comparison of model with ILAS observations

Instrument description

The orbit of the ADEOS satellite was a sun-synchronous, subrecurrent polar orbit at an altitude of approximately 800 km. The ILAS sensor aboard this satellite was a solar occultation, visible and infra-red absorption spectrometer. Vertical distributions of measured atmospheric components (HNO_3, O_3, N_2O, CH_4, H_2O, NO_2, CFC-11, CFC-12 and aerosol extinction) were obtained by constant solar tracking. These factors in conjunction with an orbit period of approximately 100 minutes combine to produce around 14 profiles of the atmosphere in a narrow band at high latitude. There were no N_2O observations from ILAS after February 28, 1997, limiting the duration of this study although modelled denitrification had almost ceased by this date.

Comparisons of model and ILAS observations

In order to compare the model with ILAS observations within the polar vortex, the model output for each day is bilinearly interpolated to the co-ordinates of each satellite profile. The model was not temporally interpolated to the observations. Comparisons of model NO_y with ILAS HNO_3 have only been made using profiles in which the aerosol extinction is less than the background value plus 3 standard deviations. This method is in accordance with the method of *Kondo et al.* [2000] to avoid potential interference of PSCs on the retrieved profiles. ILAS N_2O profiles are used to derive NO_y^* following the method of *Sugita et al.* [1998].

$$[NO_y^*](\text{ppbv}) = 5.71 - 2.28\chi + 11.8\chi^2 - 2.14\chi^3 - 1.04\chi^4 \qquad (7.1)$$

where $\chi = \log_{10}([N_2O]\,(\text{ppbv}))$ and is valid in the range 20 ppbv $\leq [N_2O] \leq$ 220 ppbv. Comparisons of denitrification are limited to the region below 500 K where the assumption that observed $[HNO_3] \approx$ observed $[NO_y]$ within the polar vortex is valid.
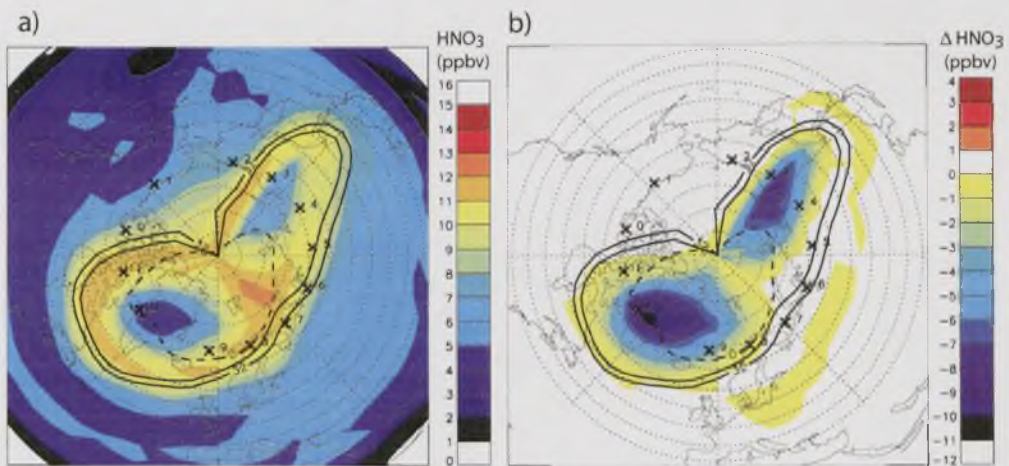
Figure 7.16: a) Modelled NO_y and b) modelled ΔNO_y at 465 K on February 21, 1997. Location of ILAS sampling points shown as numbered crosses. Solid lines indicate the MPV=32 and 36 PVU contours and the dashed line indicates the region of NAT-supersaturation.

Figures 7.16 and 7.17 show the model NO_y and denitrification on the 465 K isentropic level on February 21, and February 28, 1997. The location of the ILAS observations
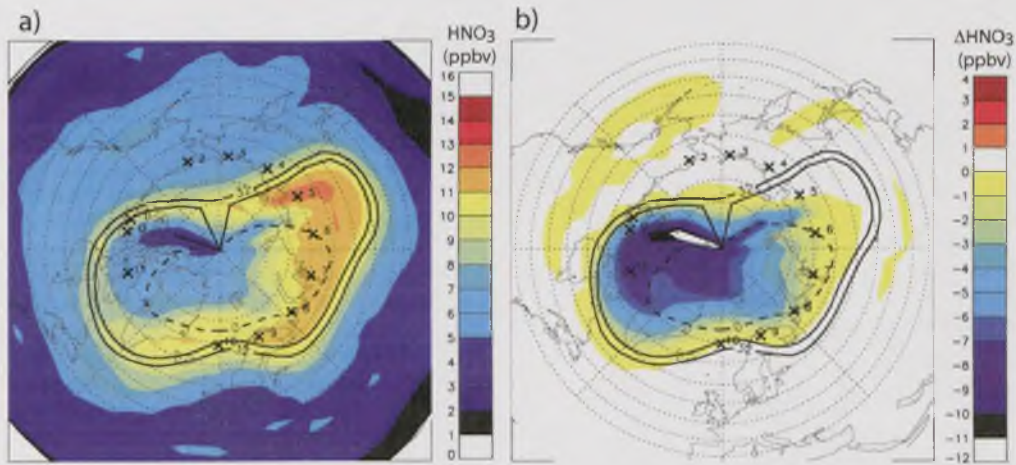
Figure 7.17: As Figure 7.16 but for February 28, 1997.
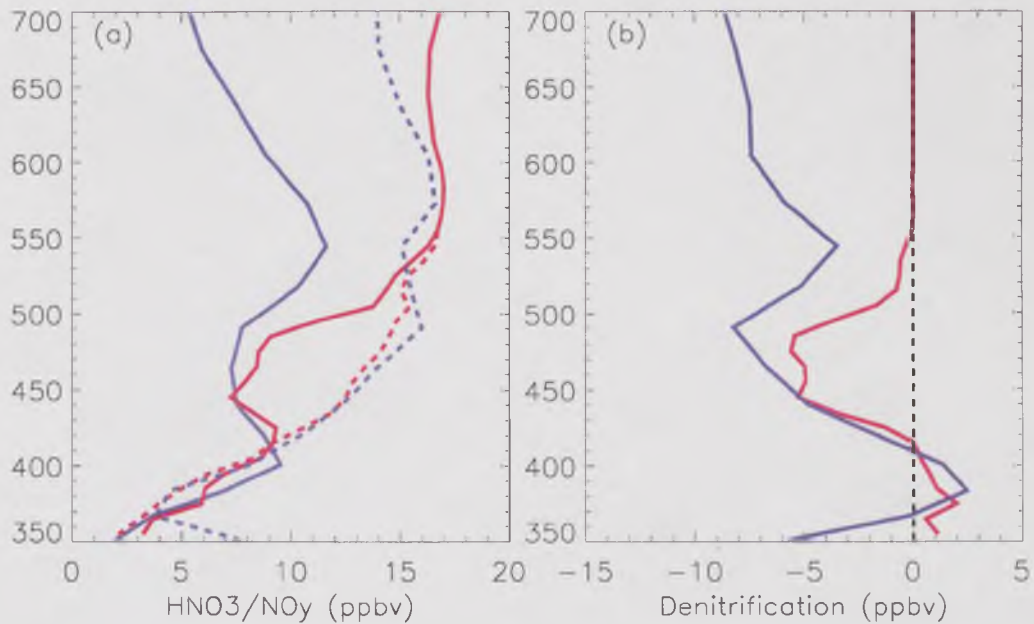
Figure 7.18: a) Model NO_y (solid red), model passive NO_y (dashed red), ILAS HNO_3 (solid blue) and ILAS NO_y^* (dashed blue) profiles. b) Model (red) and ILAS (blue) denitrification at Point 3 from Figure 7.16 on February 21, 1997.

is marked with numbered crosses. These plots are indicative of the frequency of ILAS observations sampling the denitrified region of the vortex, typically 1 or 2 profiles per day. Figures 7.18 – 7.21 compare model NO_y, and passive NO_y with ILAS HNO_3 and
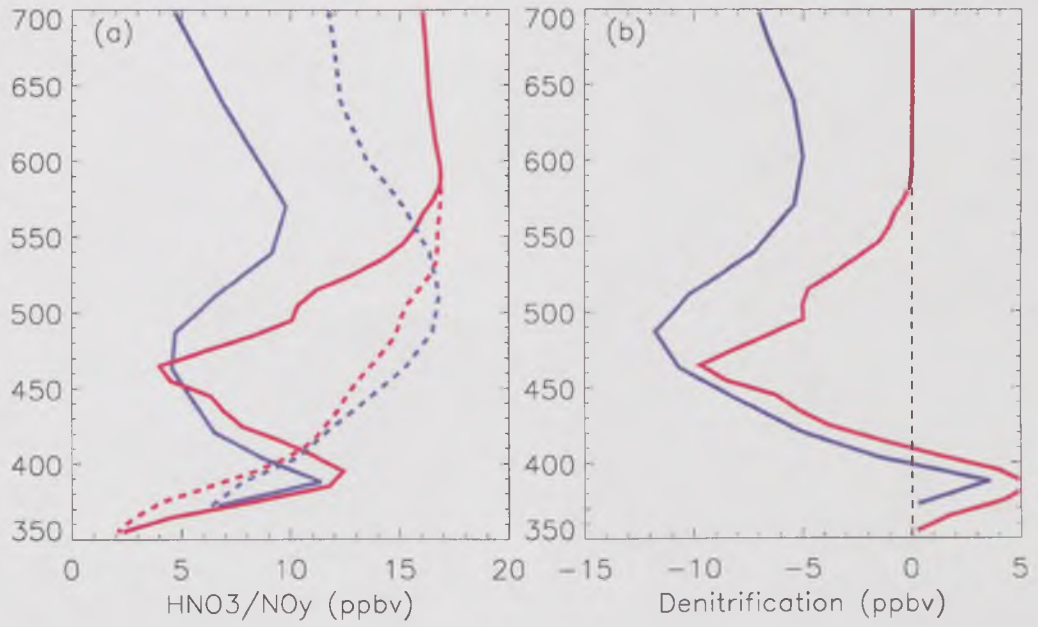
Figure 7.19: As Figure 7.18 but for Point 10 from Figure 7.16 on February 21, 1997.
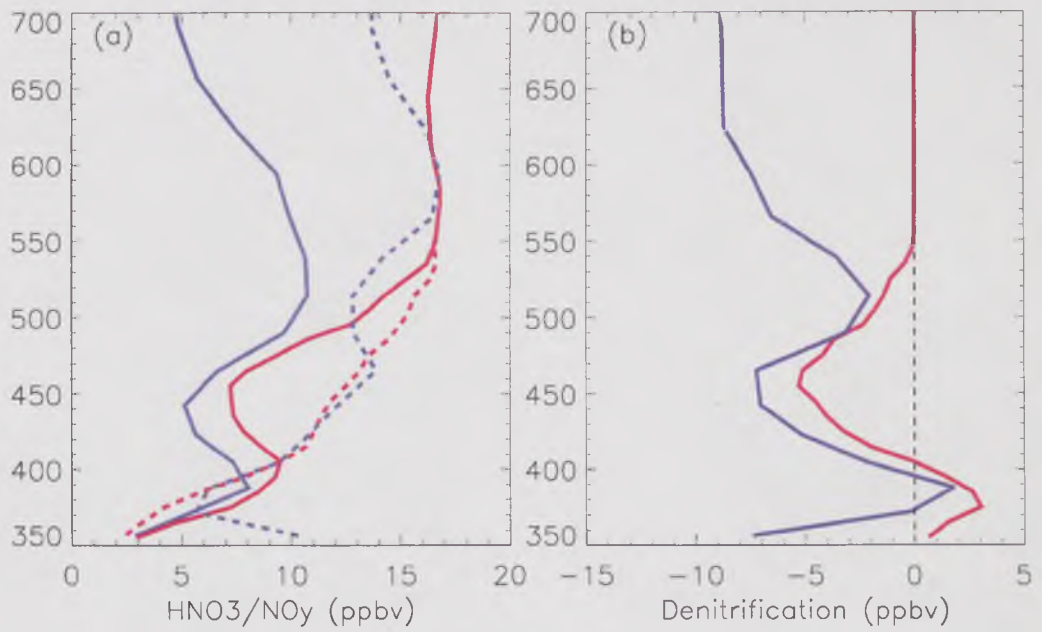
Figure 7.20: As Figure 7.18 but for Point 0 from Figure 7.17 on February 28, 1997.
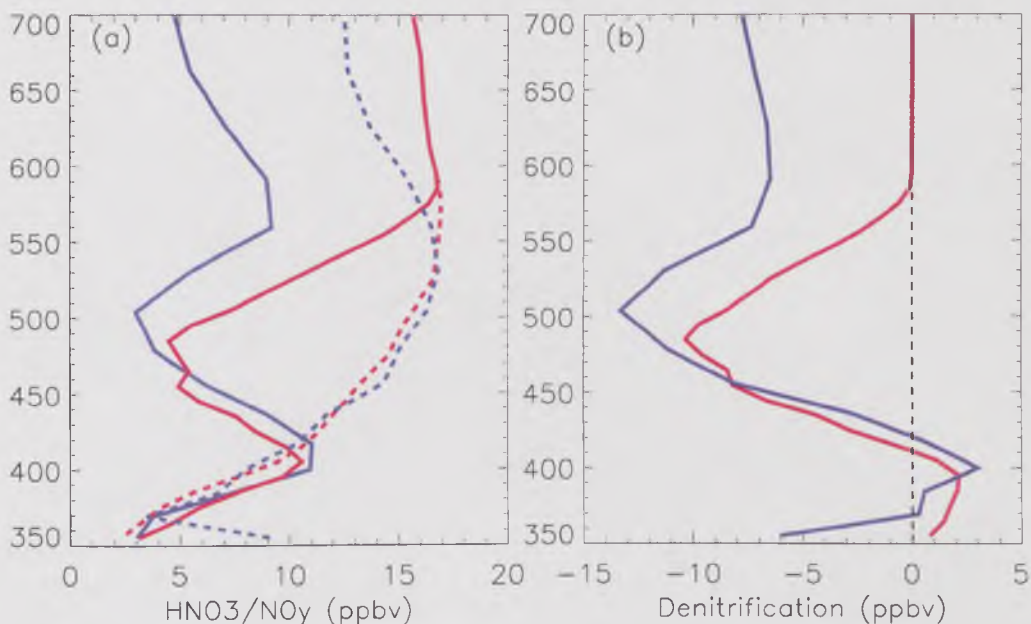
Figure 7.21: As Figure 7.18 but for Point 11 from Figure 7.17 on February 28, 1997.

NO_y^* on 2 days in late February. These observations have been selected to illustrate typical profiles obtained within the denitrified region for this period.

It can be seen that the model produces two separate and distinct regions of denitrification on February 21, 1997 (Figure 7.16); one located over central Greenland and the other over northern Siberia. Figure 7.18 shows the ILAS and model profiles at Point 3 over Siberia. The ILAS profile indicate significant denitrification between 420 and 500 K with modest nitrification at around 380 K, features which are reproduced in the model profile. Profile 10 from Figure 7.16 is shown in Figure 7.19. This point is located deep within the modelled denitrified zone. Modelled passive NO_y and observed NO_y^* are in excellent agreement below 475 K. The model also captures the altitude of the observed nitrification at 385 K and the vertical gradient of the denitrification. However, the model slightly underestimates the altitude and magnitude of the maximal denitrification.

Figures 7.20 and 7.21 show ILAS and modelled profiles at Points 0 and 11 from Figure 7.17. Profile 11 is located on the region of maximal modelled denitrification whereas profile 0 is located at the edge of this denitrified zone in a region of moderate deni-

trification. Profiles 0 and 11 on this day also demonstrate similar agreement between the model and ILAS observations as described for Profile 10 on February 21. Profile 0 with lower denitrification has better agreement between modelled and observed denitrification between 475 and 500 K.

In summary, the observed and modelled profiles demonstrate a remarkable agreement both in the vertical extent and the magnitude of the denitrification below 500 K. At higher altitudes the discrepancy between observed HNO_3 and NO_y^* does not indicate denitrification but is an illustration of the limitations of the assumption that $[HNO_3] = [NO_y]$.
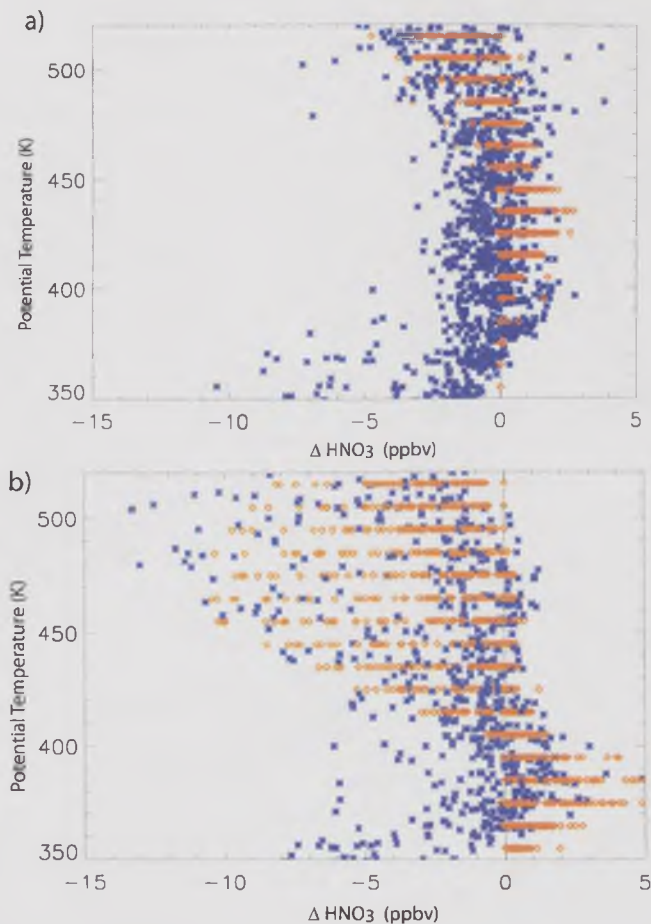
Figure 7.22: ILAS (blue) and model (red) denitrification for in-vortex profiles for the periods: a) January 21 - February 10, 1997 and b) February 20 - February 28, 1997.

Figure 7.22 shows scatter plots of ILAS and model in-vortex profiles for two periods during late winter 1997: Figure 7.22a) prior to the onset of extensive denitrification (January 21 - February 10, 1997) and Figure 7.22b) in the fully developed denitrified phase (February 20 - February 28, 1997) [*Kondo et al.*, 2000] for the 350–520 K region. In the model, denitrification is diagnosed as NO_y - passive NO_y whilst ILAS denitrification is obtained from HNO_3 - NO_y^*. The in-vortex profiles are identified using MPV ≥ 36 PVU on the 465 K isentropic level. It can be seen in Figure 7.22a that the HNO_3 - NO_y^* diagnostic has a tight correlation in the 370–500 K region during January 21 - February 10, 1997 but exhibits considerable scatter outside these altitudes. The discrepancy at higher altitudes in the ILAS diagnosed denitrification may be attributed to NO_y at these altitudes comprising significant concentrations of species other than HNO_3. At these altitudes during polar night N_2O_5, $ClONO_2$ and NO_3 may constitute a significant fraction of NO_y. At the lowest altitudes, the apparent denitrification in the ILAS data may be attributed to the breakdown in the NO_y^* relation at $[N_2O] > 220$ ppbv. The model profiles exhibit limited denitrification at higher altitudes (up to 3 ppbv at 500 K) and nitrification of up to 2 ppbv at 435 K.

Figure 7.22b shows the equivalent plot for the denitrified period. In contrast to Figure 7.22a, both the model and ILAS profiles exhibit considerable denitrification above 435 K for some profiles. Peak denitrification of over 10 ppbv is observed at higher altitudes in both the model and ILAS observations, although the model does not match the maximal observed denitrification at the highest altitudes. At lower altitudes (365 – 405 K) there is weak nitrification evident in both the model and ILAS profiles. There are no N_2O observations from ILAS after February 28, 1997, limiting the duration of denitrification comparisons for the purposes of this study.

7.5.3 Comparisons of model and MLS observations

The MLS instrument aboard the UARS satellite obtained Northern Hemisphere profiles to 80°N during the period February 19 – 28, 1997. This period coincides with the ILAS observed denitrification phase. Figure 7.23 shows the MLS-observed HNO_3 on the 68 hPa pressure level on February 26, 1997 and model gas-phase HNO_3 interpolated to the instrument pressure levels and sampled using the MLS instrument averaging kernel
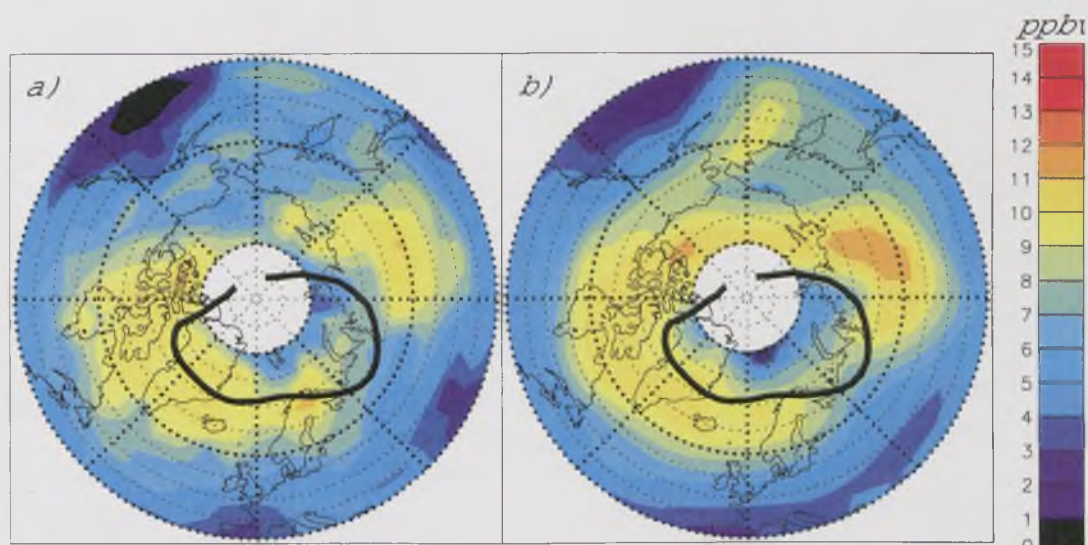
Figure 7.23: a) MLS HNO$_3$ and b) model NO$_y$ at MLS resolution on 68 hPa pressure level on February 26, 1997.

as described in Section 7.4. The model, when sampled according to the MLS averaging kernel, reproduces the observed region of reduced gas-phase HNO$_3$ between 70° – 80 °N and 0° – 90°E. This reduced gas-phase HNO$_3$ has been previously attributed to sequestration by PSCs and not denitrification [*Santee et al.*, 2000].

Figure 7.24a shows the modelled gas phase NO$_y$ minus passive NO$_y$ for February 26, 1997. Gas phase NO$_y$ is significantly reduced over an area poleward of 70°N between 0° and 90°E. The peak reduction in modelled gas phase NO$_y$ at 68 hPa is ∼6 ppbv in a region close to Spitzbergen. Figure 7.24b shows total NO$_y$ minus passive NO$_y$ which removes the effect of sequestration of NO$_y$ by liquid aerosol and NAT on gas phase NO$_y$. Denitrification of ∼3 ppbv is evident poleward of 70°N between 0° and 90°E. The model suggests that the reduced gas-phase HNO$_3$ observed by MLS is consistent with a combination of sequestration and denitrification. Comparisons with MLS data earlier in the north-viewing period show that the model is more denitrified than observations at 68 hPa although the MLS vertical resolution restricts detection of air which is not strongly denitrified.
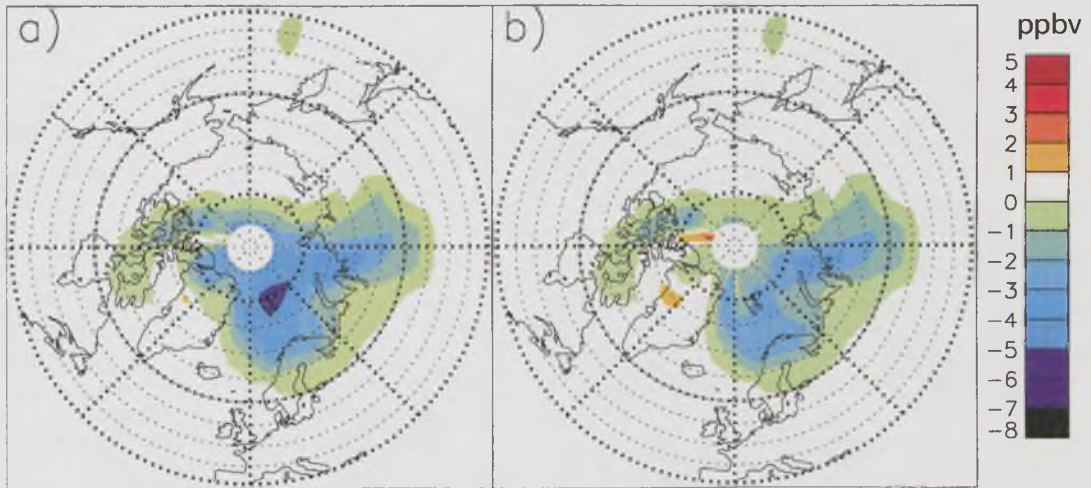
Figure 7.24: a) Modelled gas-phase NO_y minus passive NO_y and b) modelled total NO_y (= gas phase + condensed phase) minus passive NO_y at 68 hPa on February 26, 1997.

7.6 Summary

The microphysical model of denitrification by large NAT particles used for this study is capable of reproducing both the magnitude and extent of observed denitrification during both the winters included in this study. There are limitations to the extent to which the available datasets constrain the model for each of these winters. During 1999/2000 the in-situ observations from the ER-2 provided valuable information from mid-January to mid-March between 350 and 460 K but completely missed the crucial denitrifying phase in late December/early January. In-situ observations during the denitrifying phase would have provided an additional constraint on the nucleation rate used in the model as the model NO_y field is most sensitive to changes in nucleation rate in the early stages of denitrification. In addition, the upper altitude limit to the operation of the ER-2 was below the region where the model predicted maximal denitrification (500–550 K) during the first period of its deployment although this region had descended to ER-2 altitudes by the end of the second deployment in March. The MLS observations were severely limited during this winter both in the spatial extent of observations and the period of operation.

During the winter of 1996/97 observations from the ILAS instrument showed that

significant denitrification occurred during February within the Arctic polar vortex. However, the instrument produced only one or two profiles per day within the denitrified region. Despite the agreement between ILAS observations and modelled denitrification for this winter the frequency of observations limits the conclusions that may be drawn from such a comparison. Comparisons between model and MLS HNO_3 also demonstrate very good agreement in late February 1997 but less good in mid-February. The vertical resolution of the MLS instrument ($\sim$6 km at 68 hPa) significantly reduces its detection of denitrification and the instrument is limited to sampling regions equatorward of $80°$N. The most denitrified air is often located at the highest latitudes associated with the region of closed flow [*Mann et al.*, 2002]. Nevertheless, there is excellent agreement between the ILAS-observed and modelled denitrification during February 1997 using model nucleation rates based on observations from 1999/2000.

Observations of denitrification in the Arctic are currently either insufficient in number or compromised in resolution or vertical extent to fully constrain 3-D denitrification models. The forthcoming remote MIPAS global observations of HNO_3 and most of the constituents of NO_y aboard the ENVISAT satellite promise significantly increased vertical resolution (2 – 3 km in the lower stratosphere) coupled with high spatial resolution at high latitudes. This dataset should significantly improve our ability to constrain 3-D models of polar chemical and microphysical processes as current observations do not fully constrain the model.

Chapter 8

Impact of denitrification on Arctic ozone loss

8.1 Introduction

The aim of this chapter is to quantify the impact of denitrification on O_3 loss in the Arctic during the strongly denitrified winter of 1999/2000. Meteorological analyses from the UKMO and ECMWF are used in conjunction with ice and NAT-based thermodynamic equilibrium denitrification schemes to explore the sensitivity of O_3 loss to different parameterisations of denitrification. Sections 8.2 and 8.3 develop the study of denitrification for the model runs discussed in Chapter 4 and compare the modelled Cl_y and O_3 with observations from the SOLVE/THESEO-2000 campaign.

8.2 Effect of denitrification on Cl_y species

Denitrification can delay the deactivation of ClO_x at the end of the winter, which in turn can lead to increased ozone depletion [e.g. *Brasseur*, 1997; *Chipperfield and Pyle*, 1998; and *Tabazadeh et al.*, 2000]. Here, the effect of the different denitrification schemes on the behaviour of key Cl_y species is investigated. Comparison with ER-2 observations of ClO_x, $ClONO_2$ [*Stimpfle et al.*, 1999] and HCl [*Webster et al.*, 1994] is
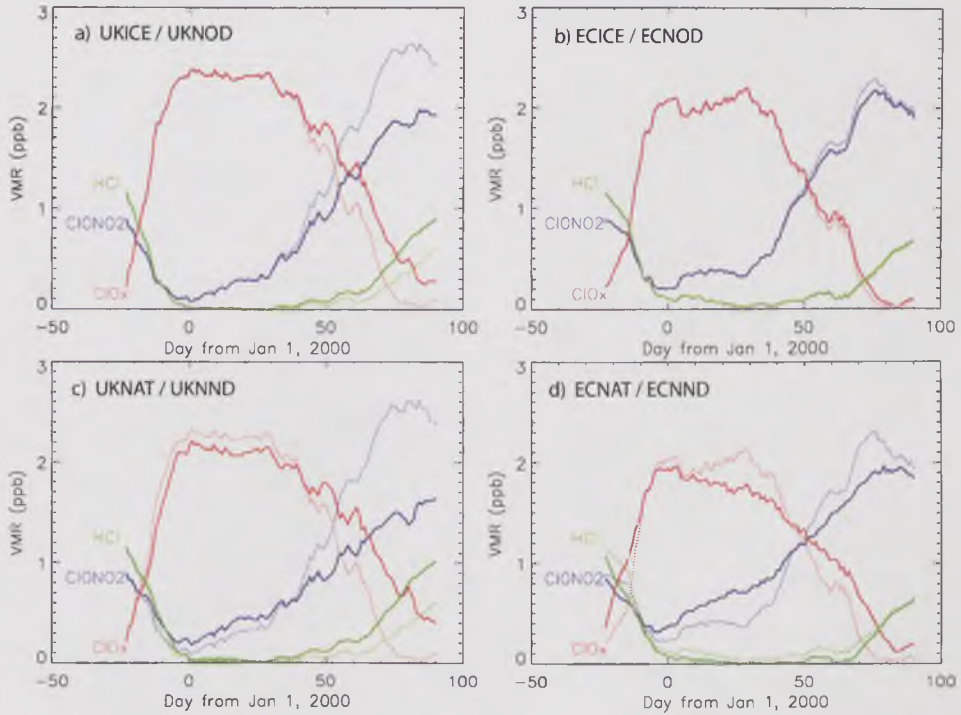
Figure 8.1: Model vortex mean ClONO$_2$ (blue), ClO$_x$ (red) and HCl (green) at 460 K for denitrified (solid lines) and non-denitrified model runs (dotted lines) for (a) UKICE and UKNOD; (b) ECICE and ECNOD; (c) UKNAT and UKNND; and (d) ECNAT and ECNND. The polar vortex is defined as the area at 460 K enclosed by the PV = 30 PVU contour.

used to investigate if these Cl$_y$ species can be used to evaluate indirectly the different denitrification schemes.

8.2.1 Activation

Figure 8.1a shows that the heterogeneous activation of reservoir species to ClO$_x$ on PSCs in early winter is identical in runs UKICE and UKNOD as this process occurs rapidly on NAT at temperatures below $\sim$195 K. (Table 4.2 in Chapter 4 lists the main features of these runs.) Similarly, for ECICE and ECNOD (Figure 8.1b) there is no difference between the denitrified and non-denitrified model runs during the activation phase.

Interestingly, for model runs based on NAT denitrification, the maximum mid-winter ClO_x mixing ratio is reduced in denitrified model runs (UKNAT and ECNAT) compared to their non-denitrified equivalents (UKNND and ECNND). In addition, the NAT-based model runs are less activated than their ice-based equivalents by 0.2 – 0.4 ppbv of ClO_x on January 1, 2000. This may be attributed to reductions in particle surface area available for heterogeneous reaction of halogen reservoirs in model runs UKNAT and ECNAT.

NAT-based model runs are strongly denitrified throughout the polar vortex (Figure 4.6) by early January, 2000, whereas, the ice-based runs show only weak denitrification over a small region of the vortex at this time. In addition there is reduced NAT surface area available for heterogeneous processing in model runs UKNAT and ECNAT, where the majority of the condensed NAT is in the large mode (which has a relatively low surface area) during this period in the denitrified models (see Figure 8.2). The area of the vortex below T_{NAT} at this time is not significantly different between the UKMO and ECMWF analyses although there are large differences in the area below T_{ice}.

8.2.2 Deactivation

For run UKICE, the diagnosed denitrification (65% as a vortex mean) has no effect on the vortex-averaged amount of active chlorine until early February, when a significant portion of the vortex is exposed to solar radiation and photochemical loss of HNO_3 reforms NO_x (Figure 8.1a). Denitrification slows the reconversion of ClO_x to $ClONO_2$ by around two weeks for run UKICE compared to run UKNOD by decreasing available NO_x. The relatively weak denitrification in run ECICE has a barely discernible effect on Cl_y chemistry. Deactivation of ClO_x to HCl is enhanced by denitrification due to low NO_x.

Delayed deactivation of ClO_x is also evident in model runs using the NAT denitrification scheme (UKNAT and ECNAT). Comparison of UKNAT with UKNND (Figure 8.1c) indicates that recovery of ClO_x to $ClONO_2$ is delayed by more than 20 days with a mean vortex denitrification of 8.1 ppbv (77%) at 460 K. The final $ClONO_2$ concentration is lower by $\sim$0.5 ppbv. Comparison of model runs ECNAT and ECNND (Figure 8.1d), with a mean vortex denitrification of 5.9 ppbv (60%) at the same potential temperature

demonstrates a reduced recovery time for Cl_y reservoirs of around 10 days in March.

8.2.3 Diagnosis of heterogeneous rates

In model runs ECICE, ECNOD, UKNAT, ECNND and, especially, run ECNAT, vortex-mean $ClONO_2$ remains significantly greater than zero throughout the winter. This is a result of incomplete activation due to slower heterogeneous processing rates at the higher temperatures in the ECMWF analyses and lower surface area in all NAT-based model runs. NAT denitrification runs are based on a bimodal NAT distribution with the large mode absorbing most of the HNO_3 at low temperature. Diagnosis of these rates over Ny Ålesund (Figure 8.2) shows that for the reaction of $ClONO_2$ with HCl, the heterogeneous rates on solid particles during the activation phase in mid-December are around 10^{-3} s^{-1} for the UKICE run and 10^{-4} s^{-1} for the ECICE run (expressed as the first-order loss rate of $ClONO_2$).

The denitrified NAT model runs UKNAT and ECNAT show significantly lower rates of around $3.0 - 7.0 \times 10^{-5}$ s^{-1} whilst their non-denitrified equivalents (UKNND and ECNND) exhibit more rapid processing, with rates around 10^{-4} s^{-1}. Reaction 2.20 also processes $ClONO_2$, and this reaction is much more rapid in the UKICE model run as the heterogeneous rates are considerably enhanced on ice particles (1×10^{-3} s^{-1}) compared with the ECICE run (1×10^{-7} s^{-1}) where there is very limited ice formation and most of the processing occurs on NAT.

8.2.4 ER-2 Comparisons

ER-2 observations of key Cl_y species are compared to model results from the ice schemes in Figure 8.3 and the NAT schemes in Figure 8.4 for January 20, March 5, March 7 and March 12. These dates include the ER-2 flights late in the winter where the effects of denitrification on Cl_y are expected to be the largest. No ER-2 HCl data were available for the flight on February 26, 2000. ClO data for all flights were adjusted according to Equation 8.1 to account for the formation of ClO_2 from reaction of Cl with O_2 at low
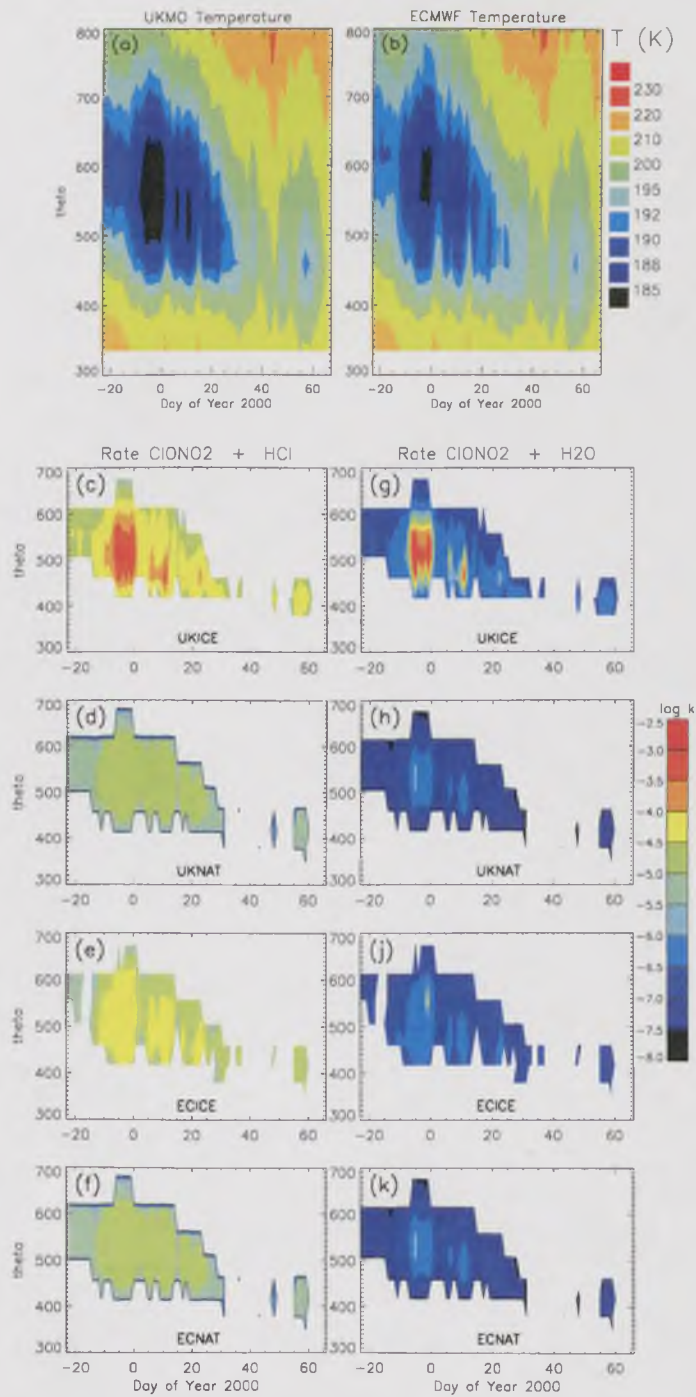
Figure 8.2: Time-height cross sections of temperature for a) UKMO and b) ECMWF analyses at Ny Ålesund (79°N, 12°E) and model heterogeneous reaction rates on solid PSCs for the 4 denitrified runs c)–k).

ambient temperatures within the instrument [*R. Stimpfle, pers. comm.*]

$$ClO_{adjusted} = ClO \times (3.0 - (0.00924 \times T_{MMS})) \tag{8.1}$$

where T_{MMS} is the in-situ temperature recorded by the MMS instrument.

All flights were within the polar vortex and uncertainties in the observations were quoted as HCl 2 – 10% [*Webster, pers. comm.*], ClO_x 17%, Cl_2O_2 20% and $ClONO_2$ 20% [*R. Stimpfle, pers. comm.*].

UKMO model runs overestimate ClO_x by between 0.2 and 0.6 ppbv in mid-winter when the model has essentially full activation, most likely due to the effect of unrealistically low temperatures on heterogeneous rates. It is only during late February and March that the effect of denitrification on ClO_x becomes apparent. During this period the denitrified UKMO runs (UKICE and UKNAT) have ClO_x values that exceed observations by around 0.2 – 0.5 and 0.2 – 0.6 ppbv respectively. The non-denitrified UKMO run UKNOD appears to agree better with the observations yet underestimate ClO_x by 0.2 – 0.4 ppbv in mid-March. In mid-March, the run UKNND underestimates ClO_x by around 0.5 ppbv.

The runs forced by ECMWF analyses overestimate the observed ClO_x in mid-winter by around 0.4 ppbv on many flights but underestimate ClO_x by a similar amount on January 27. In mid-March, runs ECICE and ECNOD both underestimate ClO_x by around 0.2 to 0.3 ppbv while model run ECNAT is in good agreement with observations while ECNND underestimates ClO_x by approximately 0.5 ppbv.

All model runs apart from UKNAT tend to overestimate $ClONO_2$ when compared with ER-2 observations. The strongly denitrified runs, especially UKNAT, but also UKICE and ECNAT, produce significantly smaller discrepancies in mid-March (< 0.4 ppbv). In fact, the observations of $ClONO_2$ inside the vortex on March 12 (Figures 8.3h) and 8.4h) give the clearest indication that the most strongly denitrified model runs (UKICE, UKNAT and ECNAT) are more realistic than the non-denitrified runs. Under the conditions of 1999/2000, observations of chlorine species even later in the winter would have been desirable to examine the deactivation of ClO_x to reservoir species under highly denitrified conditions.

The agreement between modelled and ALIAS HCl is poor during January and early
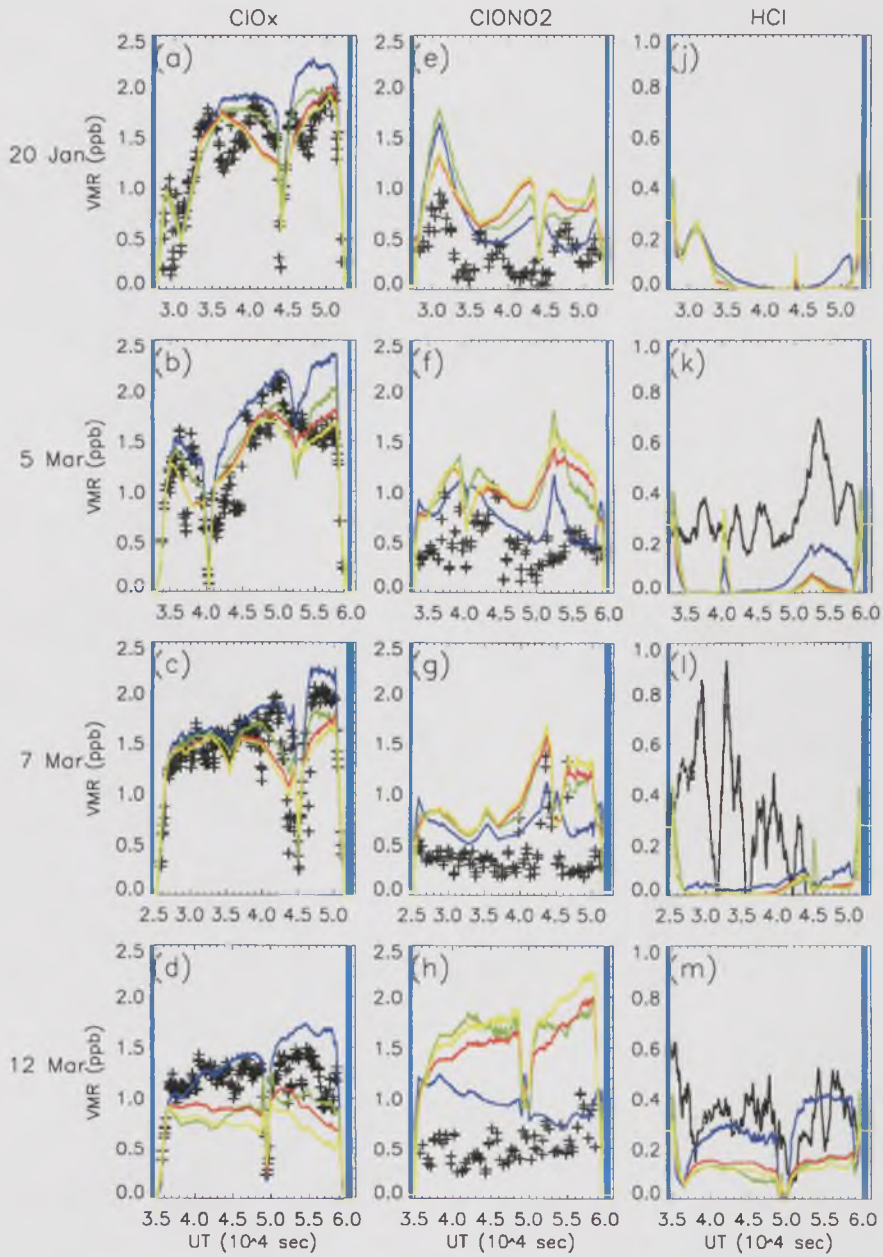
Figure 8.3: Comparison of ER-2 observations (black) with model results from runs UKICE (blue) and UKNOD (green), ECICE (red) and ECNOD (yellow) for ClO_x (a – d), $ClONO_2$ (e – h), and HCl (j – m) for January 20, March 5, March 7 and March 12, 2000.
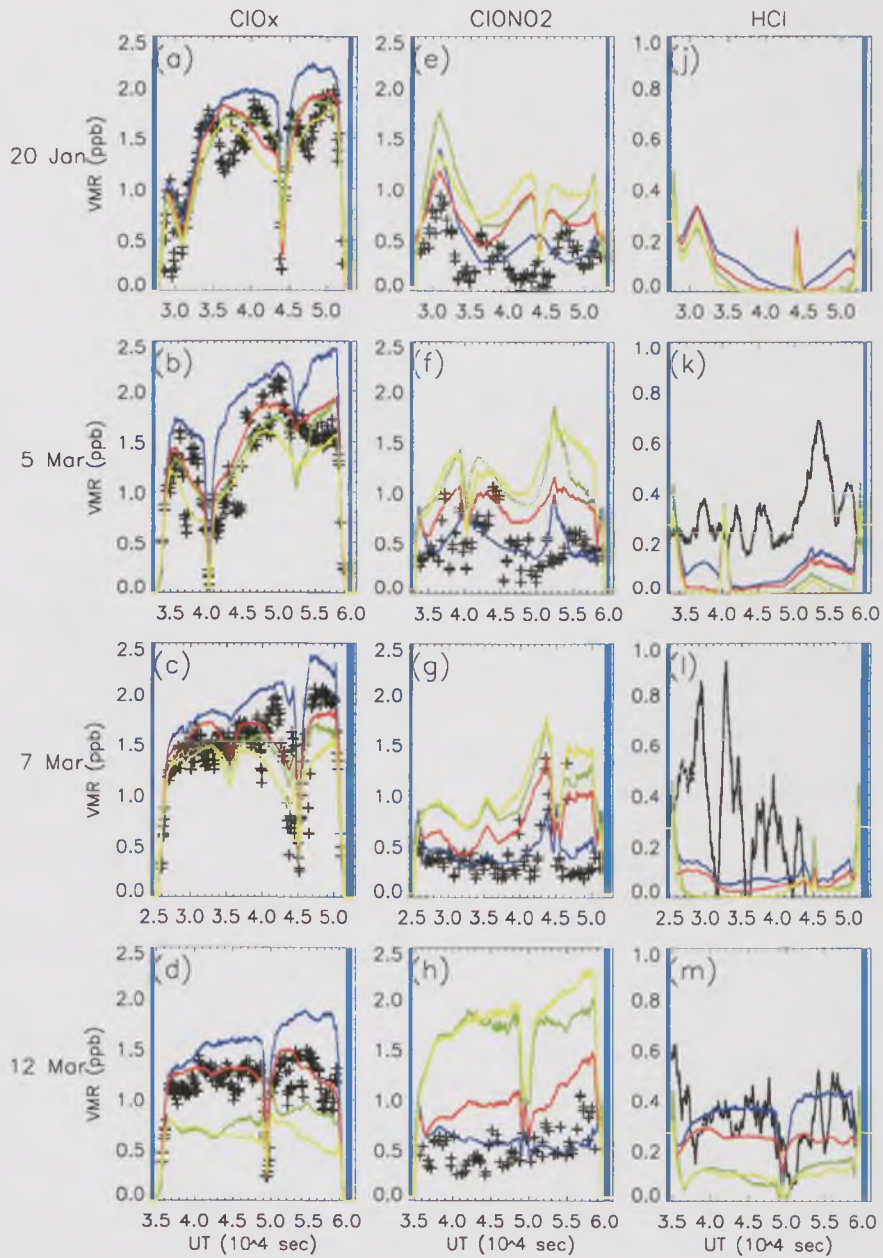
Figure 8.4: As Figure 8.3 but with model results from runs UKNAT (blue), UKNND (green), ECNAT (red) and ECNND (yellow).

February – the observations show much larger values than the model (not shown). In March the agreement is much better for the strongly denitrified model runs, and the larger HCl values of run UKNAT, UKICE, and ECNAT are in better agreement than the non-denitrified model runs due to enhanced recovery of ClO_x to HCl under denitrified conditions.

The comparison of the model with the ER-2 chlorine species observations is somewhat inconclusive. An important caveat to this comparison is that the sum of ER-2 HCl, $ClONO_2$ and ClO_x observations underestimates the expected Cl_y by an average of 20%. This discrepancy precludes any definitive statements about the performance of the different model schemes with the current data. In general, the denitrified model runs tend to give the best comparison with the HCl and $ClONO_2$ reservoirs in late winter. However, these denitrified runs tend to overestimate ClO_x in this period, especially for the runs forced by UKMO analyses.

8.3   Effect of denitrification on ozone loss

Denitrification slows the overall rate of deactivation of ClO_x to reservoir species in springtime. This section examines the effect of a decreased rate of ClO_x deactivation on ozone loss during 1999/2000. Comparisons are made with O_3 observations from the ER-2 and ozone sondes from Ny Ålesund.

Figure 8.5a) and b) show that there is generally excellent agreement between modelled and observed O_3 in the polar vortex on January 20 and February 3, 2000 before significant ozone depletion occurs. In early to mid-March the comparison with the model passive O_3 shows that significant O_3 depletion has occurred in UKICE and UKNAT (over 55% by March 12) and there is good agreement with observed O_3 values (Figures 8.5c), 8.5d) and 8.6a). Model run ECNAT (Figure 8.6b) gives smaller losses (around 40% by March 12) and overestimates observed ozone by around 0.6 ppmv.

ECMWF-forced runs and UKMO-forced runs show different features near the edge of the polar vortex (3.5×10^4 s - 4.5×10^4 s) on March 11. This difference is due to the higher temporal resolution of the ECMWF analyses which produces tighter horizontal gradients in modelled tracer fields at the edge of the vortex. Overall, these
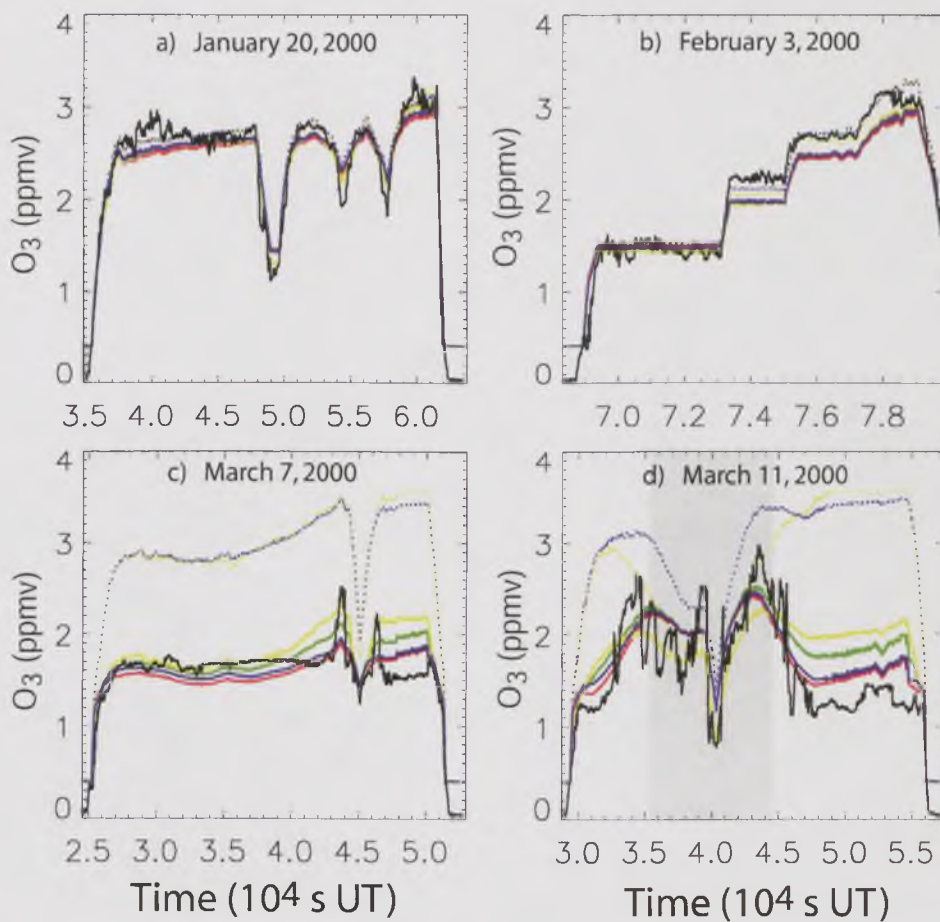
Figure 8.5: Comparison of ER-2 observed O_3 (black) with SLIMCAT model runs UKICE (blue), ECICE (yellow) and the passive O_3 tracers from UKICE (dashed blue) and ECICE (dashed yellow) on a) January 20, b) February 3, c) March 7 and d) March 11, 2000. Grey shaded region is extra-vortex air. Uncertainties in the ER-2 in-situ observations of O_3 are 3% [*Richard et al.*, 2001].
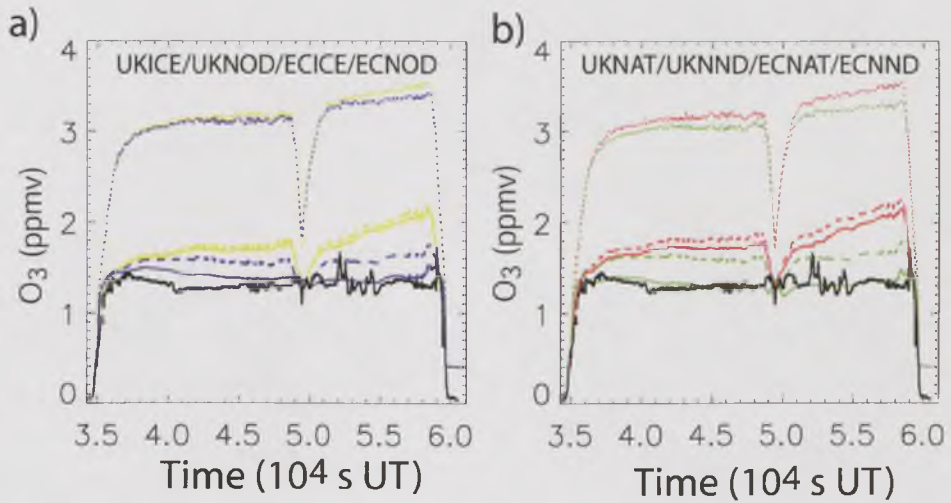
Figure 8.6: Comparison of ER-2 observed O_3 (black) with the SLIMCAT model for March 12, 2000. a) SLIMCAT ice-based model runs : UKICE (solid blue) ECICE (solid yellow), UKNOD (dashed blue), ECNOD (dashed yellow) and the passive O_3 tracers from UKICE (dotted blue) and ECICE (dotted yellow); b) SLIMCAT NAT-based model runs : UKNAT (solid green), ECNAT (solid red), UKNND (dashed green), ECNND (dashed red), and the passive O_3 tracers from UKNAT (dotted green) and ECNAT (dotted red).
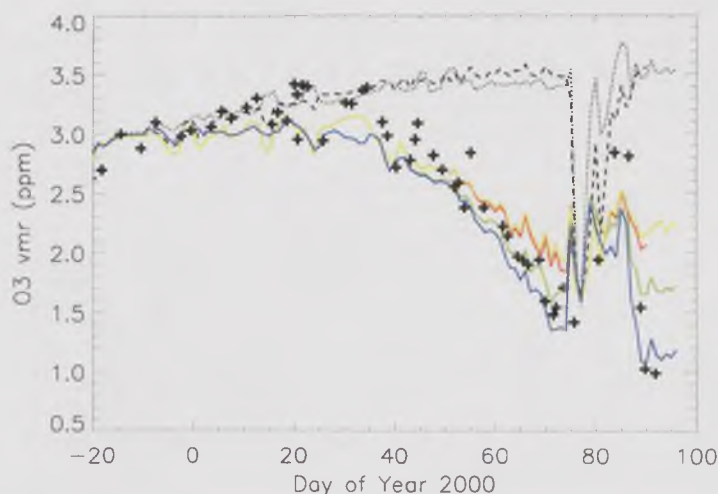
Figure 8.7: Comparison of O_3 sonde observations (+) at Ny Ålesund (79°N, 12°E) with model output from runs UKICE (blue), UKNOD (green), UKICE passive O_3 (dotted black), ECICE (red), ECNOD (yellow), ECICE passive O_3 (dashed black) at 460 K.

comparisons show that the concentrations of O_3 in the strongly denitrified model runs forced by the colder UKMO analyses (UKICE and UKNAT) are in good agreement with in-situ observations of O_3 in March when significant chemical depletion has occurred. Ozone mixing ratios in all ECMWF-forced model runs are significantly greater than observations due primarily to lower chemical depletion, although changes in vertical transport due to the different temperatures in UKMO and ECMWF analyses contribute up to 40% of the discrepancy.

Figure 8.7 compares the four ice-based model runs with sonde observations from Ny Ålesund at 460 K. Model run UKICE shows accumulated ozone loss by late March of 69%, with denitrification contributing around 30% of the loss (relative to non-denitrified UKNOD). Accumulated losses for the ECICE run peaks at 44% with denitrification responsible for only 6% of this loss. Figure 8.8 is similar to Figure 8.7 but for the 4 NAT-based model runs. The UKNAT model run shows accumulated losses reaching 74% by the same date with denitrification also contributing 30% of the loss (relative to UKNND). Accumulated losses for ECNAT is 48% and the effect of denitrification is smaller, contributing around 21% of the O_3 loss. The accumulated ozone loss in the
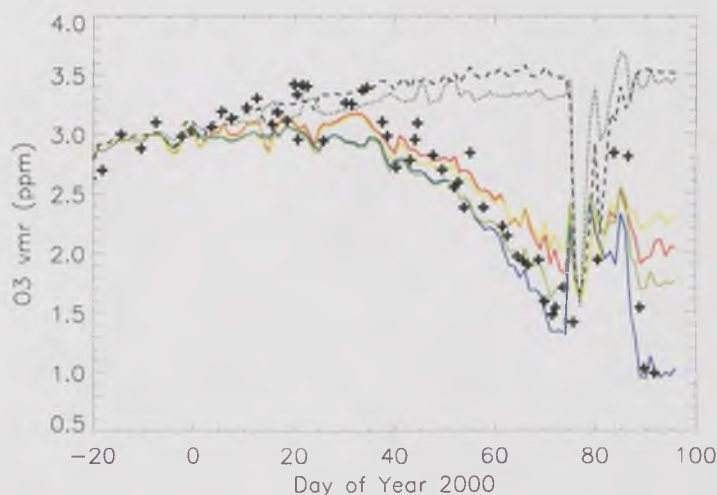
Figure 8.8: Comparison of O_3 sonde observations (+) at Ny Ålesund (79°N, 12°E) with model output from runs UKNAT (blue), UKNND (green), UKNAT passive O_3 (dotted black), ECNAT (red), ECNND (yellow), ECNAT passive O_3 (dashed black) at 460 K.

ECMWF runs at Ny Ålesund by late March is less than the UKMO runs.

The agreement between the different model runs and the observed O_3 is inconsistent with the NO_y and Cl_y comparisons in Chapter 4: ECNAT and UKNAT give the best simulation of the observed denitrification (compared with ER-2 NO_y observations); the ECMWF analyses appear to give more realistic stratospheric temperatures (compared with sondes) and ClO_x (compared with ER-2 observations) but ECNAT does not appear to reproduce the O_3 loss as well as run UKICE or UKNAT. However, ECNAT does appear to reproduce the ER-2 ClO_x observations better than the UKMO-forced runs. Based on these comparisons, it seems that the model with the realistic ClO_x evolution underestimates O_3 loss. Other modelling studies, for example, *Guirlet et al.* [2000]; *Hansen and Chipperfield* [1999] and *Becker et al.* [1998] have reported similar findings.

In-vortex chemical O_3 loss rates for the period February 26 - March 12, 2000 for the UKMO-forced model runs are comparable to the losses calculated by *Gao et al.*, [2002], from ER-2 observations. O_3 loss rates derived by *Gao et al.* [2002] are 63 ppbv/day for 71% denitrified air parcels and 43 ppbv/day for 43% denitrified air parcels. Losses

averaged 59 ppbv/day over this period for the 77% denitrified UKNAT model run and 56 ppbv/day for the 65% denitrified UKICE model run. The non-denitrified UKMO-forced model runs UKNOD and UKNND have loss rates of 42 ppbv/day and 39 ppbv/day, respectively. All ECMWF-forced models have O_3 loss rates that are considerably lower than their UKMO-forced equivalents. Figures 8.7 and 8.8 indicate that O_3 loss in even the most denitrified model runs had effectively stopped by late March, prior to the break-up of the polar vortex.

8.4 Summary

The uncertainties in the ER-2 observations of ClO_x, $ClONO_2$ and HCl mean that it is not possible to unambiguously determine which model simulation is the most realistic. All non-denitrified model runs have too much $ClONO_2$ and too little HCl in mid-March compared with ER-2 observations. Three strongly denitrified model runs show delayed recovery of ClO_x into $ClONO_2$ by between 10 to 20 days and enhanced recovery to HCl compared with the equivalent non-denitrified model runs, in better agreement with observations from the ER-2. The most denitrified model run (the UKMO-forced NAT scheme) gives the best agreement with observed $ClONO_2$ and HCl at this time but the UKMO-forced denitrified schemes appear to have too much ClO_x due to the low in-vortex temperatures in these analyses during December and January.

The modelled O_3 loss inside the vortex is sensitive to the analyses used. Losses reach 69% at 460 K by late March in UKMO-forced ice denitrification model run and 74% with the UKMO-forced NAT denitrification scheme, in excellent agreement with the sondes from Ny Ålesund, although in these runs ClO_x is apparently too large. O_3 losses are considerably smaller when the ECMWF analyses are used, reaching around 49% with the ice scheme and 56% with the NAT denitrification scheme at 460 K. This difference is due to reduced levels of ClO_x in the critical March period when vortex airmasses receive significant sunlight. Incomplete initial heterogeneous activation of Cl_y and smaller denitrification (resulting in faster deactivation of ClO_x) both contribute to this difference with the UKMO runs, though the ClO_x was in better agreement with the ER-2 data. UKMO-forced model O_3 loss rates for the period February 26 to March 12 show that extensive denitrification results in O_3 loss rates of $\sim$60 ppbv/day

(UKICE and UKNAT) and $\sim$40 ppbv/day for non-denitrified model runs (UKNOD and UKNND). O_3 loss rates were lower for ECMWF-forced runs at $\sim$25 ppbv/day for the extensively denitrified ECNAT run and $\sim$20 ppbv/day for non-denitrifed runs (ECNOD and ECNND).

The SLIMCAT model shows that widespread and severe denitrification of the Arctic lower stratosphere during the cold winter of 1999/2000 can account for an additional 30% O_3 loss at 460 K when the UKMO analyses are used with either the ice or NAT denitrification schemes, or an additional 21% loss when the ECMWF analyses are used with the NAT scheme. Despite the considerable denitrification in several model runs, the extent of denitrification was insufficient to prevent the deactivation of ClO_x and consequent O_3 loss beyond late March.

Chapter 9

Sensitivity of Arctic ozone depletion to denitrification in 1999/2000

9.1   Introduction

In the previous chapter, the impact of denitrification on Arctic ozone loss during the winter 1999/2000 was discussed. Ozone loss was found to be sensitive to the magnitude of denitrification produced with different meteorological analyses. Here, the sensitivity of Arctic ozone loss to denitrification is explored in a different way. Meteorological analyses from the ECMWF are used, but the magnitude of modelled denitrification is varied and its impact on chemical ozone depletion is examined in a series of winter-long simulations.

The denitrification scheme used in the SLIMCAT CTM for this study is the thermo-dynamic equilibrium bimodal NAT scheme previously described in Chapters 3, 4 and 8 (model run ECNAT). The magnitude of denitrification is controlled by varying a combination of the fall velocity of the large NAT-particle mode and adjusting the mass of HNO_3 contained in the large mode. Adjustments to the condensed mass in the large mode are achieved through reducing the temperature of the model calculation of the

equilibrium concentration of condensed HNO_3 (Equation 2.39) and reducing the mass retained in the non-sedimenting small NAT-particle mode (with a corresponding increase in particle number density to retain equivalent particle surface areas to prevent affecting heterogeneous chemistry calculations). The equilibrium denitrification scheme is chosen for this study for reasons of computational efficiency and simplicity.

9.2   Model description

The thermodynamic equilibrium concentration of condensed HNO_3 is partitioned between the small and large particle modes. The small NAT particle mode is initially assumed to have a radius of 0.25 μm and a maximum number density of 10 cm^{-3}. The fraction of condensed NAT in the small mode is assumed not to sediment. Denitrification occurs by the sedimentation of the large NAT-particle mode at pre-determined fall velocities as described in Chapters 3 and 4.

A series of model runs was performed with the magnitude of denitrification controlled by adjusting the fall velocity of the condensed NAT in the large mode. The magnitude of denitrification increases with increased fall velocity until the remaining gas-phase HNO_3 is no longer sufficient to allow further NAT formation. Subsequent reductions in gas-phase HNO_3 can then be achieved by reducing the temperature. A series of model runs were undertaken in which the temperature passed to the model thermodynamic equilibrium calculation (Equation 2.39) was reduced in increments of 1 K to further reduce p_{HNO_3} and increase modelled denitrification. To further increase model denitrification, the fraction of condensed HNO_3 retained in the small NAT-particle mode was reduced by decreasing their radius. Total particle number densities were adjusted to retain particle surface area used for model heterogeneous chemistry calculations. Table 9.1 lists the fall velocity and temperature offset applied to the NAT equilibrium calculation for each of these runs. The temperatures used in the chemical and advective model routines were not changed in order to maintain consistency of homogeneous and heterogeneous reaction rates with earlier model runs. These runs should be viewed as a straightforward means of adjusting the change in denitrification during the winter.

Finally, two model runs were undertaken where the temperature was reduced by 4

Model run	Fall velocity $(\mathrm{ms^{-1}})$	Equivalent particle radius $(\mu\mathrm{m})$	$\Delta\mathrm{T}$ to $\mathrm{T_{NAT}}$	Small NAT mode radius $(\mu\mathrm{m})$
ECN0	0.0	0.0	0	0.25
ECN1	0.0001	0.6	0	0.25
ECN2	0.001	2.1	0	0.25
ECN3	0.005	4.6	0	0.25
ECN4	0.01	6.4	0	0.25
ECN5	0.05	14	0	0.25
ECN6	0.1	19	0	0.25
ECN7	0.1	19	-4	0.25
ECN8	0.1	19	-8	0.25
ECN9	0.1	19	-8	0.125
ECN10	0.1	19	-8	0.031

Table 9.1: Fall velocity and temperature offsets used for SLIMCAT 3-D equilibrium sensitivity model runs ECN0 – ECN10.

K to i) model calculation of NAT PSCs and ii) NAT heterogeneous chemistry rate calculations and vertical transport subroutines. Temperatures were not reduced in either run for the calculation of ice supersaturation (Equation 3.31). The ECMWF analyses used for this study are not sufficiently cold to produce widespread ice formation and, therefore, ice-induced denitrification (Figure 4.6) is small. Quantification of the impact of NAT-induced denitrification on O_3 loss is therefore possible.

Estimated fall velocities for the large NAT particles observed during the 1999/2000 winter (3 – 10 μm radii) are 0.005 – 0.03 ms^{-1}. Observations of the small particle mode indicate a modal radius of ~0.5 – 1 μm. Model run ECN0 has a fall velocity of zero for the large mode of NAT particles and forms the control case with no denitrification.

Figure 9.1 shows the temporal change in vortex mean NO_y at 460 K over the course of the winter for model runs ECN0 – ECN10. Increasing the fall speed of NAT has a significant impact on the rate and magnitude of denitrification at this level in mid-December. However, recall that the impact of denitrification on O_3 loss in the model has been shown to be unimportant for the Arctic winter of 1999/2000 until February. The
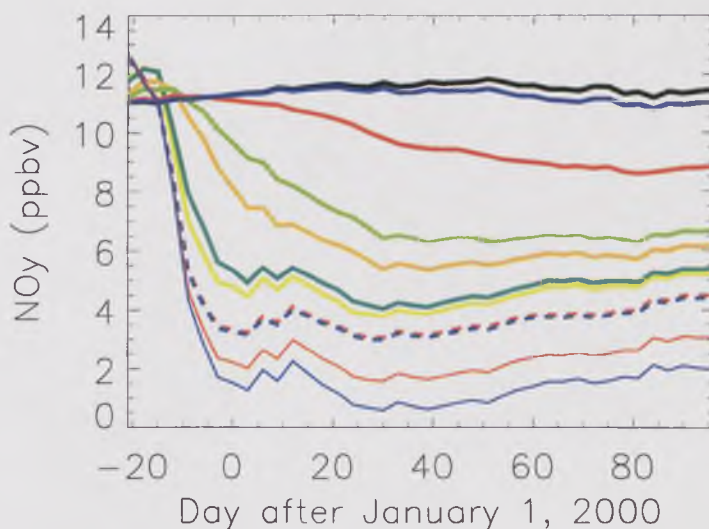
Figure 9.1: Daily vortex-mean NO$_y$ at 460 K for model runs ECN0 – ECN6 (thick lines), ECN7 – ECN8 (dashed lines) and ECN9 – ECN10 (thin lines).

minimum vortex-mean HNO$_3$ at 460 K for model runs with denitrification controlled by the fall speed of NAT alone (ECN1 – ECN6) is 3.8 ppbv in late January, which corresponds to a denitrification of 7.8 ppb (67%). Reducing the temperature in the NAT-equilibrium calculation further decreases the vortex-mean HNO$_3$ to 3.1 ppb (73% denitrification). Reducing the radius of the small NAT mode allows a greater fraction of the condensed mass to be sedimented, further decreasing vortex-mean HNO$_3$ at 460 K to 10.6 ppbv (91% denitrification). In addition, the absolute minimum in HNO$_3$ occurs earlier. The slow recovery evident in the vortex-mean HNO$_3$ from Day 30 may be attributed to the increased area enclosed by the MPV = 36 PVU contour. MPV scales linearly with height and diabatic descent increases the area enclosed by a given MPV contour over the course of the winter. Transport of less-denitrified air into the vortex may also contribute to the modelled NO$_y$ recovery. The range of modelled denitrification used in this simulation covers the typical ranges of denitrification which would be expected to occur in Arctic airmasses [*Mann et al.*, 2003].

9.3 Sensitivity of Cl_y to denitrification

The response of ClO_x to varying denitrification is shown in Figure 9.2a for the model runs ECN0 – ECN10. The rates of heterogeneous reactions on NAT are sufficiently rapid at these low temperatures that activation is almost complete in all model runs, leading to a vortex-mean ClO_x of around 2.1 ppbv by Day 30. Figure 9.2b shows that $ClONO_2$ reaches a minimum in all model runs of 0.2 ppbv on January 1 before recovering to a plateau of 0.4 – 0.5 ppbv for the following four weeks. Concentrations of $ClONO_2$ remain at approximately 1 ppb in a sunlit "collar" region close to the vortex edge, which is responsible for the vortex-mean value reaching a plateau significantly above zero. Figure 9.2c shows that HCl is completely removed in all model runs until at least Day 45, followed by a slow recovery. The most denitrified model runs (ECN9 – ECN10) are activated most rapidly although the difference in minimum HCl is small ($\sim$0.1 ppbv) by January 1.

After Day 35, denitrification delays the deactivation of ClO_x to $ClONO_2$ whilst recovery to HCl is enhanced. ClO_x is fully deactivated in the non-denitrified model run ECN0 by Day 75 whereas complete deactivation of model runs ECN9 – ECN10 has not occurred by the end of the simulation on Day 96. Deactivation of ClO_x in this winter occurs in two phases separated by a short period of reduced deactivation around Day 60.

Between Day 35 and Day 55, the deactivation of ClO_x occurs predominantly to $ClONO_2$ and is sensitive to the magnitude of denitrification. The 91% denitrified model run, ECN10, has 1.5 ppbv ClO_x remaining by Day 55, whereas the non-denitrified model run, ECN0, has only 0.7 ppbv ClO_x remaining by the same time. During this period, HCl recovery is very slow in all model runs although HCl recovery is slightly enhanced by strong denitrification. In model run ECN10, HCl recovers to 0.4 ppbv by Day 55, double the level in model run ECN0 by the same time. The 10.6 ppbv denitrification in model run ECN10 is equivalent to a 20 day delay in ClO_x deactivation compared to ECN0 at this time.

The "plateau" between Day 55 and Day 65 in all species can be attributed to an increase in the area of the cold pool during this period, enhancing rates of reactivation of reservoir species to ClO_x and compensating for the on-going deactivation reactions.
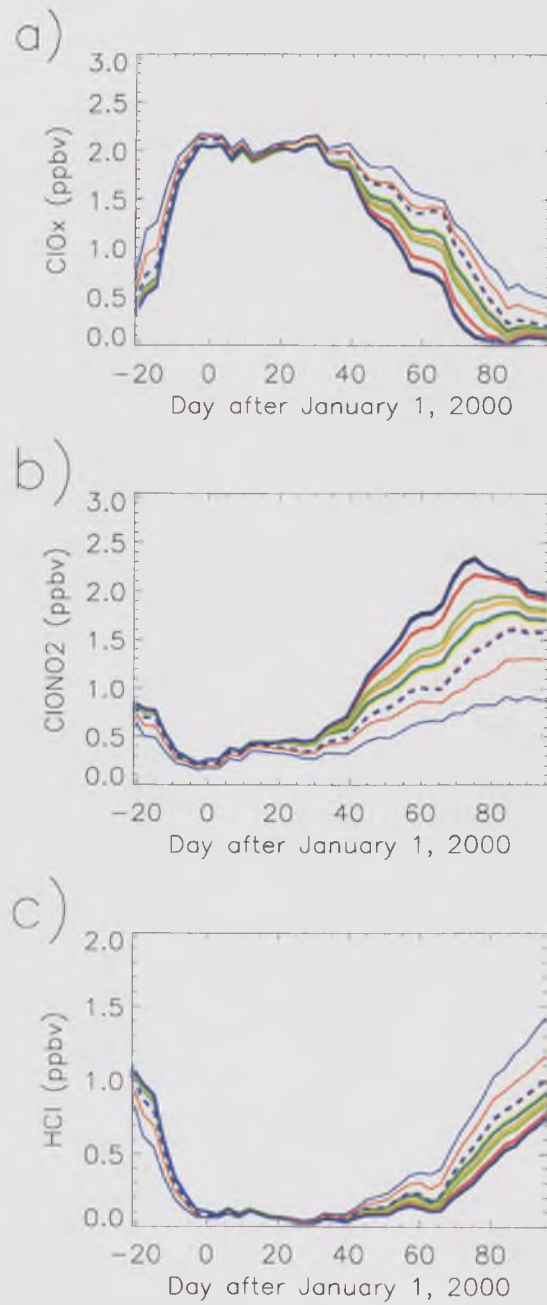
Figure 9.2: Daily vortex-means at 460 K for a) ClO$_x$, b) ClONO$_2$, and c) HCl, for model runs ECN0 – ECN6 (thick lines), ECN7 – ECN8 (dashed lines) and ECN9 – ECN10 (thin lines).
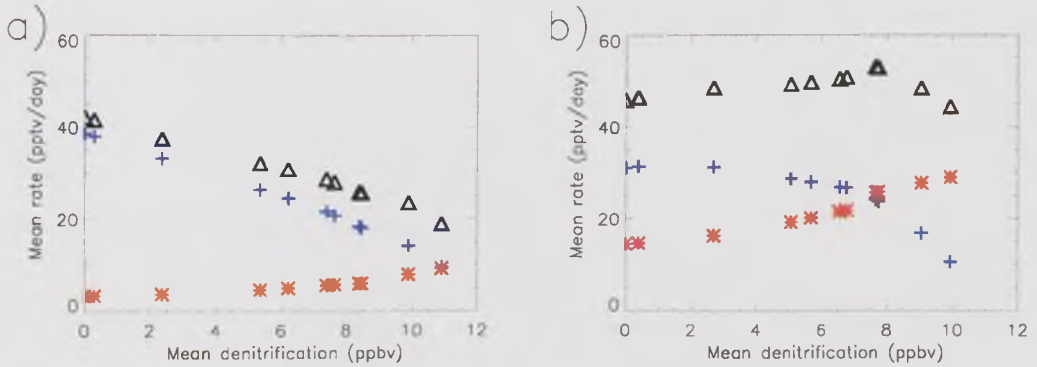
Figure 9.3: Vortex-mean ClO$_x$ deactivation rate (black triangles), ClONO$_2$ formation rate (blue crosses) and HCl formation rate (red stars) for model runs ECN0–ECN10 for a) Days 35–56 and b) Days 60–78.

Between Day 65 and the end of the simulation, deactivation of ClO$_x$ occurs to both ClONO$_2$ and HCl. Enhanced recovery to HCl in the most denitrified model runs compensates for the decreased rate of recovery to ClONO$_2$ in this period, such that the rate of deactivation of all model runs is similar during this time.

Figure 9.3 shows the average rate of deactivation of ClO$_x$ at 460 K as a function of mean denitrification for the same two periods: a) February 6 to February 22, 2000 and b) March 4 to March 19, 2000. During the February period (Figure 9.3a) the rate of deactivation of ClO$_x$ decreases almost linearly with increasing denitrification, from 42 pptv/day with no denitrification to 19 pptv/day with 10.6 ppbv denitrification. The rate of deactivation of ClO$_x$ to HCl increases from 3 pptv/day in the absence of denitrification (∼7% of the total deactivation) to a maximum of 8 pptv/day (∼47%). Figure 9.3b shows the equivalent situation for March. In this later period, the ClO$_x$ deactivation rate does not exhibit such a dependence to denitrification as in February. Here, the ClO$_x$ deactivation rate remains ∼45 pptv/day, reducing slightly for model runs with a vortex-mean denitrification greater than 9 ppbv. Decreased loss of ClO$_x$ to ClONO$_2$ due to decreased availability of NO$_x$ in strongly denitrified model runs is mitigated by increased ClOx deactivation to HCl. The non-linear trend in modelled ClONO$_2$ in this early spring period may be due to the almost complete deactivation of ClO$_x$ in model runs with weak or moderate denitrification, rather than the availability

of NO_x.

In the absence of severe denitrification, deactivation of ClO_x in the Arctic lower strato-
sphere occurs predominantly through reaction with NO_2 (formed from photolysis of
HNO_3) to form $ClONO_2$. Low HCl abundance means that springtime reactivation
of chlorine in periods with low temperatures occurs through the heterogeneous reac-
tion of $ClONO_2$ and water (Reaction 2.20). The more rapid heterogeneous reaction
of $ClONO_2$ and HCl (Reaction 2.22) is suppressed. However, intense denitrification
enhances deactivation of ClO_x to HCl. In this winter, model run ECN10 (91% deni-
trified) has approximately equal recovery of ClO_x to HCl and $ClONO_2$, increasing the
susceptibility of the springtime Arctic lower stratosphere to subsequent reactivation.
Suppression of PSC formation by low NO_y abundance would be expected to reduce the
rate of reactivation although the background sulphate aerosol alone may be sufficient
to catalyse the heterogeneous conversion of HCl and $ClONO_2$ to ClO_x and reactivate
the vortex.

9.4 Sensitivity of ozone loss to denitrification

Section 9.3 examined the impact of denitrification on the rate of deactivation of ClO_x.
During February 2000, the availability of ClO_x was sensitive to the magnitude of denitri-
fication due to delayed recovery of $ClONO_2$. Here the impact of denitrification-induced
delays in the recovery of ClO_x on ozone are explored.

Figure 9.4a shows the vortex-mean O_3 at 460 K for model runs ECN0 – ECN10. In the
absence of denitrification, comparison of model run ECN0 with the passive O_3 tracer
indicates that 1.2 ppbv of O_3 has been lost due to chemistry by Day 80. This corre-
sponds to 34% of the model-predicted passive O_3 at this level. Stronger denitrification
increases the rate of O_3 loss until, in model run ECN10, a vortex-mean denitrification
of 91% causes 1.0 ppbv (83%) additional loss compared to the non-denitrified model
run (ECN0) on Day 95. Figure 9.4b shows the average vortex-mean O_3-loss rate as
a function of average vortex-mean denitrification at 460 K for Day 60 – 80 for model
runs ECN0 – ECN10. In the absence of denitrification, the vortex-mean O_3 loss rate
during this period is ∼14 ppbv/day. The increase in the vortex-mean O_3 loss rate with
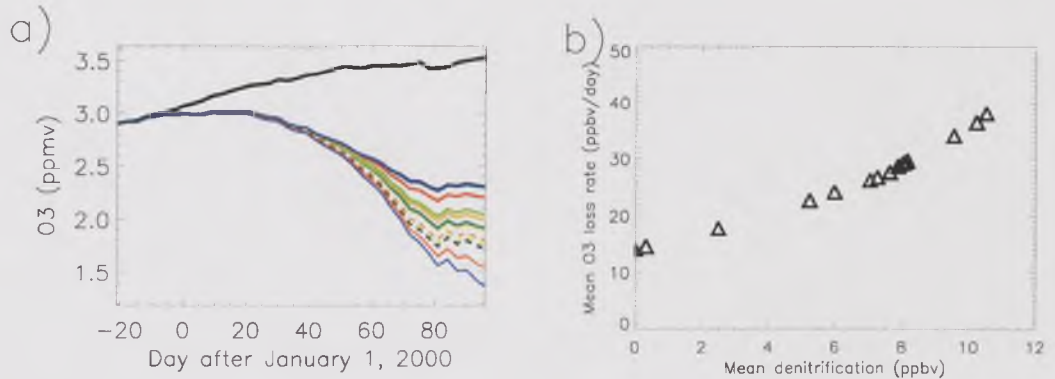
Figure 9.4: a) Daily vortex-mean O_3 at 460 K for model runs ECN0 – ECN6 (thick lines), ECN7 – ECN8 (dashed lines) and ECN9 – ECN10 (thin lines); b) vortex-mean O_3 loss rate as a function of vortex-mean denitrification between Day 60 – Day 80 for model runs ECN0 – ECN10.

additional denitrification is non-linear.
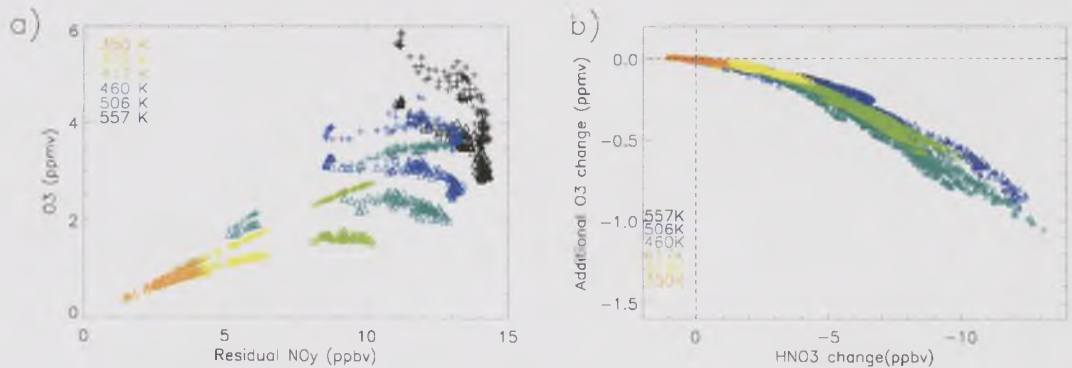
Figure 9.5: a) In-vortex O_3 (Δ) and passive O_3 (+) as a function of rNO_y for model run ECN0 on Day 80. b) Additional model O_3 loss as a function of denitrification for model runs ECN1 – ECN10 on Day 80. Colours denote the potential temperature of model points.

Figure 9.5a shows a correlation plot of in-vortex O_3 and passive O_3 from model run ECN0 as a function of residual NO_y on Day 80 (March 20) at 6 isentropic levels from 557 – 350 K. The vertical trend of increasing O_3 mixing ratios with altitude is clearly

155

evident in the modelled passive O_3. Modelled O_3 loss at the lowest isentropic levels (350 – 379 K) is <0.5 ppmv although this constitutes a significant fraction of the available O_3 at these altitudes. Modelled O_3 loss generally increases with increasing NO_y. Larger NO_y mixing ratios are related to greater Cl_y abundances as both have a positive vertical gradient in this altitude range, increasing the potential for chemical O_3 loss. At the higher altitudes, there is considerable chemical O_3 loss (up to ~1.7 ppmv) in the absence of denitrification.

Figure 9.5b shows a scatter plot of additional in-vortex O_3 loss (ΔO_3, diagnosed as model O_3 – non-denitrified O_3) on Day 80 as a function of denitrification at 6 model isentropic levels for model runs ECN0–ECN10. The maximum increase in O_3 loss due to denitrification in model run EC10 is 1.1 ppmv for airmasses denitrified by > 12 ppbv and occurs at the same altitude. This is equivalent to an additional 66% loss compared to non-denitrified air parcels. Additional loss is less than 0.2 ppmv for airmasses below 400 K where Cl_y is small.

Weak nitrification (~1 ppbv) is evident in a few model points at the lowermost isentropic levels although the impact of this weak nitrification on O_3 in the model is negligible. The absence of strong nitrification in the model by this time may be attributed to transport. Nitrification occurs in a relatively narrow region (~1 km) below the region of NAT supersaturation as sedimenting particles evaporate in their sub-saturated surroundings. During the winter of 1999/2000, the region of nitrification was at altitudes where the vortex is less isolated from mid-latitudes (Figure 7.4) and mixed away relatively rapidly. In addition, subsequent diabatic descent carried nitrified air close to (or below) the model bottom boundary.

The response of cumulative model O_3 loss to increasing denitrification is non-linear although there is no "runaway" O_3 depletion in the most denitrified air parcels. Recovery of ClO_x to HCl compensates for slower deactivation to $ClONO_2$.

Denitrification of this magnitude by the sedimentation of NAT particles in the real Arctic stratosphere is difficult to achieve. From Equation 5.21 the rate of increase of particle radius is given by:

$$\frac{dr_p}{dt} \propto (p_{HNO_3} - p_{HNO_3}^{NAT})\frac{1}{r_p} \tag{9.1}$$

At low temperature, $p_{HNO_3}^{NAT} \rightarrow 0$:

$$\frac{dM_{HNO_3}}{dt} \propto p_{HNO_3} r_p^2 \qquad (9.2)$$

where M_{HNO_3} is the mass of HNO_3 in the condensed phase. A factor of 10 reduction in p_{HNO_3} by denitrification leads to an equivalent reduction in the rate of growth of NAT particles. Reduced particle radius, as a consequence of reduced condensed HNO_3 in denitrified air, also reduces the rate of NAT particle growth (assuming a fixed number concentration) which further reduces NAT particle growth and denitrification. Removing the last 1 – 2 ppbv of HNO_3 is a slow process even at very low temperature (where $p_{HNO_3}^{NAT}$ is essentially 0). Growth times of 8 days or more are required to grow large NAT particles [*Carslaw et al.*, 2002] but this growth time will be increased by at least a factor of 10 under highly denitrified conditions.

9.5 The relative importance of denitrification for ozone loss in a colder stratosphere

Enhanced O_3 loss at lower temperatures may be attributed to a combination of factors. Stronger denitrification leads to delayed deactivation of ClO_x as described in the previous section. The increased volume of NAT supersaturation increases the proportion of the vortex in which activation and denitrification can occur. A reduction in temperature also increases the duration of possible PSC formation, potentially leading to increased springtime activation of Cl from reservoirs. In addition, the rates of heterogeneous reactions which activate ClO_x from their reservoir species increase at lower temperature.

Diabatic descent within the vortex is also affected; lower temperatures result in slower diabatic descent. This tends to reduce the overhead O_3 column. In addition, there is a positive feedback between low temperatures and a reduced O_3 column. Lower stratospheric O_3 means reduced absorption of solar UV radiation resulting in delayed temperature recovery and potentially greater O_3 loss through the processes identified above. Several GCM studies have indicated that enhanced atmospheric burdens of greenhouse gases may lead to a cooling of the lower stratosphere. However, there

Model run	Fall velocity (ms^{-1})	ΔT (K)	Small mode radius (μm)	Small mode number (cm^{-3})
ECNAT	0.014	0	0.5	10
ECNND	0.0	0	0.5	10
ECH4	0.0	-4	0.06	640
ECT4	0.014	-4	0.06	640

Table 9.2: Temperature offset and NAT fall velocity applied to SLIMCAT 3-D equilibrium sensitivity model runs ECH4 and ECT4.

is considerable uncertainty about the impact of a warmer future troposphere on the strength and duration of the Arctic polar vortex, which is critical for future O_3 loss.

Two additional model runs (ECH4 and ECT4) were undertaken in which the model temperature was reduced by 4 K to investigate the sensitivity of O_3 loss to temperature changes. Table 9.2 lists the fall velocity and temperature offset applied to these model runs and the equivalent runs without temperature modification from Chapter 4. In order to produce realistic denitrification in the colder model runs, the radius of the non-sedimenting small mode was reduced and the abundance of the small particle mode was adjusted to retain the equivalent particle surface area for heterogeneous chemistry calculations. The values used are unrepresentative of the real atmosphere but serve the purposes of this simulation which is to quantify the effect of enhanced denitrification at lower temperatures on O_3 loss. No changes to the calculation of ice PSCs was made in any of the model runs at reduced temperature.

Figure 9.6a shows the temporal evolution of vortex mean NO_y at 460 K for the model runs listed in Table 9.2. Vortex-mean denitrification is $\sim$6.5 ppbv in model run ECNAT by Day 40. A reduction in temperature of 4 K initially increases the rate of denitrification due to the earlier onset and increased volume of NAT-supersaturation where particle sedimentation can occur. Vortex-mean denitrification is increased by $\sim$4 ppbv relative to ECNAT. Small discrepancies between NO_y in non-denitrified model runs by spring are due to slight changes in diabatic descent and are negligible.

The temporal evolution of vortex-mean Cl_y species at 460 K for each of the 4 model runs is shown in Figure 9.6b – d. The impact of denitrification on Cl_y partitioning
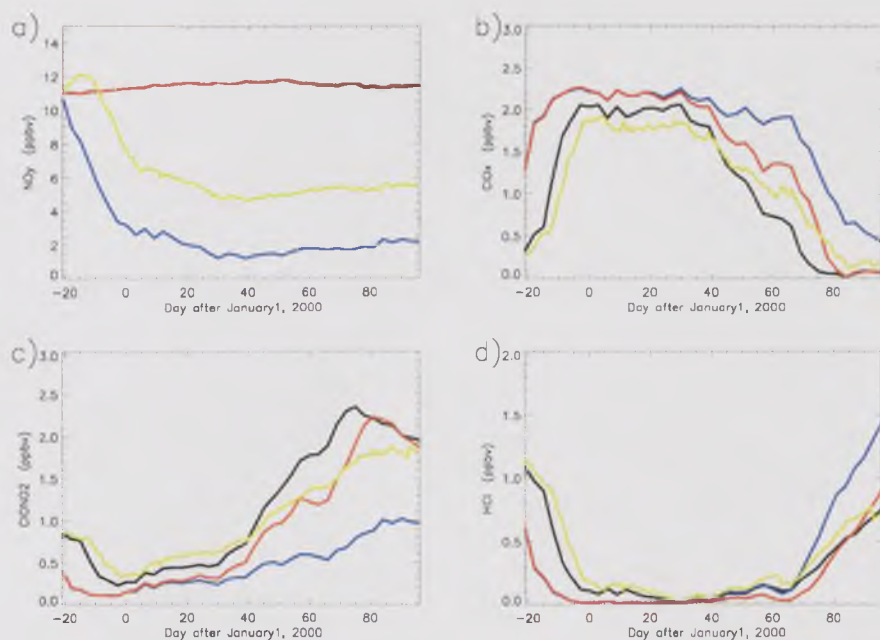
Figure 9.6: Temporal evolution of vortex-mean: a) NO_y; b) ClO_x; c) $ClONO_2$; and d) HCl for model runs ECNAT (yellow), ECNND (black), ECH4 (red) and ECT4 (blue) at 460 K.

in model runs ECNAT and ECNND has been discussed previously in this chapter. A reduction of 4 K causes activation to occur around 10 days earlier than model run ECNAT. A temperature reduction of 4 K produces mid-winter ClO_x values of 2.2 ppbv, an increase of ~0.4 ppbv in the colder model runs (compared to ECNAT). Levels of $ClONO_2$ and HCl at this time indicate almost complete activation of reservoir species.

Denitrification has no impact on levels of ClO_x in the low temperature runs until Day 20. Model runs ECNAT, ECNND and ECH4 show the characteristic "double dip" during deactivation identified in the previous section, with the earlier phase dominated by $ClONO_2$ recovery and the later phase in which deactivation produces both HCl and $ClONO_2$. The low-temperature, denitrified model run (ECT4) undergoes only slow recovery to $ClONO_2$ before Day 65. After this time, deactivation to HCl is rapid and ClO_x levels are reduced to <0.5 ppbv by the end of the simulation. The distribution of $ClONO_2$ and HCl produced from deactivation of ClO_x in ECT4 is affected in a similar manner to highly denitrified model runs in the previous section.
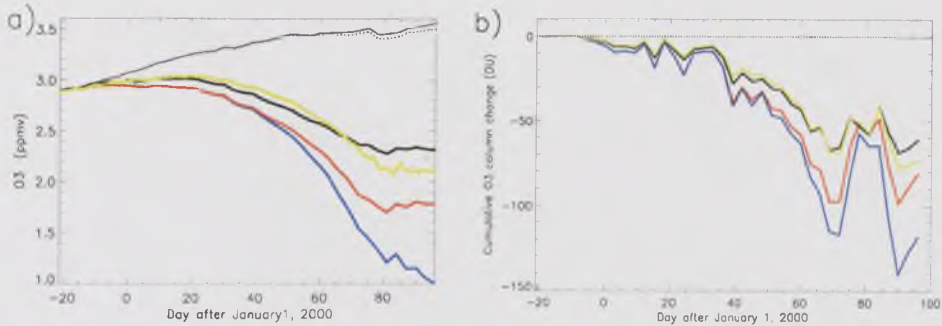
Figure 9.7: a) Daily vortex-mean O_3 at 460 K for model runs ECNAT (yellow line), ECNND (black line), ECH4 (red line) and ECT4 (blue line). Model passive O_3 for ECNAT (thin dotted line) and ECT4 (thin solid line) are also shown. b) Modelled cumulative total column O_3 loss in DU as a function of time above Ny Ålesund for model runs ECNAT, ECNND, ECH4, and ECT4.

Daily vortex-mean O_3 at 460 K for model runs ECNAT, ECNND, ECH4, ECT4 and two passive O_3 tracers (from ECNAT and ECT4) are shown in Figure 9.7a. Vortex-mean passive O_3 is fractionally higher in the -4 K run but the difference is not significant. Vortex-mean O_3 loss increases from 1.4 ppmv (40%) without temperature reduction (ECNAT) to 2.5 ppmv (71%) when the temperature is reduced by 4 K (ECT4), an 86% increase on ECNAT. Increased denitrification contributes 0.8 ppmv (32%) of the vortex-mean O_3 loss when the temperature is reduced by 4 K compared with 17% without temperature adjustment (0.2 ppmv out of a total loss of 1.2 ppmv).

The temporal evolution of modelled cumulative O_3 column loss above Ny Ålesund for model runs ECNND, ECNAT, ECH4 and ECT4 is shown in Figure 9.8. Decreased column losses between Day 65 and 75 above Ny Ålesund in all model runs are due to the vortex moving away from this location. Total column losses on Day 90 reach a peak of 68, 78, 97 and 143 DU respectively for each of these model runs. An overall reduction in temperature of 4 K in the model increases cumulative O_3 loss by 65 DU (83%) compared with the model run without temperature adjustment. Denitrification contributes 46 DU, 32% of the 143 DU total loss.

Figure 9.8a shows the evolution of cumulative O_3 loss in DU K^{-1} (Dobson Units per unit potential temperature) as a function of potential temperature at Ny Ålesund from
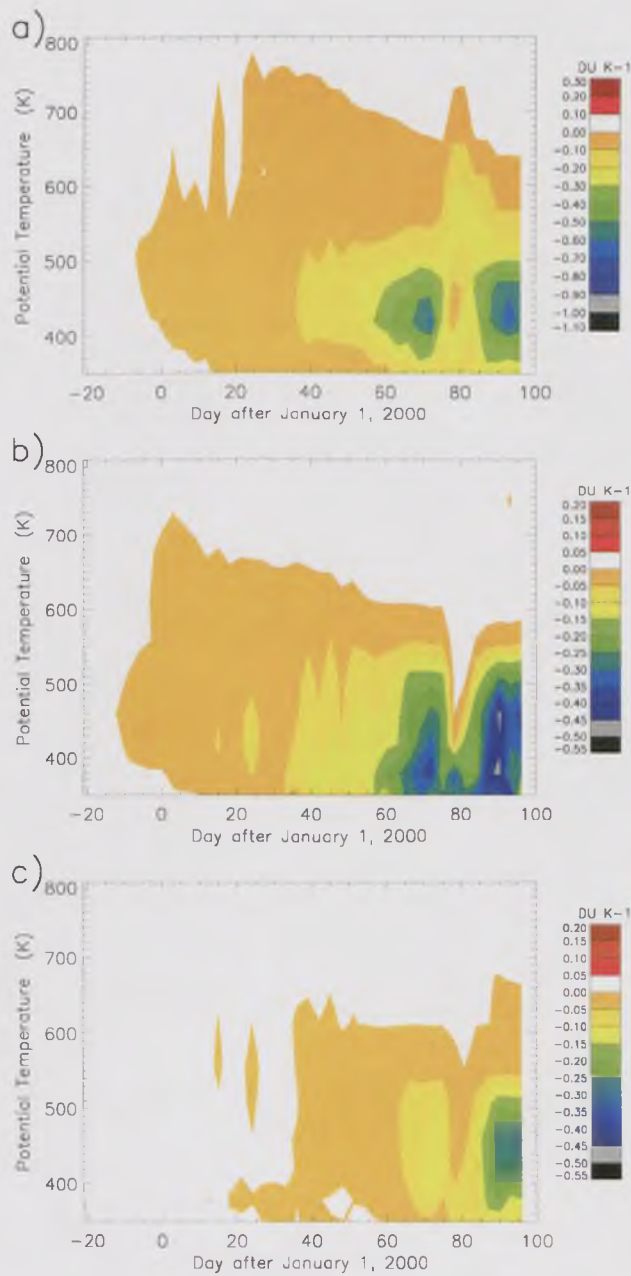
Figure 9.8: Daily cumulative ozone loss (DU K^{-1}) as a function of potential temperature at Ny Ålesund for model runs a) ECNAT b) ECT4 and, c) ECT4-ECH4.

model runs ECNAT. The vertical distribution of O$_3$ loss in March is restricted to the region between 550 and 350 K for model run ECNAT, with the largest losses between

380 – 480 K. The apparent reduction in cumulative losses between Day 65 and 75 is due to the vortex shifting away from Ny Ålesund. The cumulative column loss on any day may be obtained by integrating over potential temperature.

The cumulative O_3 loss due to a 4 K reduction in temperature is shown in Figure 9.8b. Lower temperatures have only a small effect until March. Thereafter, ECMWF-analysed temperatures (Figure 4.2) indicated a diminishing area below T_{NAT}. Both an extension to the duration and extent of NAT-supersaturation from the 4 K reduction in temperature and the increased denitrification contribute to increased O_3 loss. By Day 90 of the simulation, the additional contribution of lower temperature to O_3 loss is ~ 0.45 DU K^{-1} predominantly between 490 and 350 K. The contribution of stronger denitrification to cumulative O_3 depletion due to a 4 K temperature reduction is shown in Figure 9.8c. Additional O_3 losses due to denitrification are small until after Day 85 when ECNAT and ECH4 are fully deactivated. The impact of denitrification accelerates to around an additional 0.3 DU K^{-1} and denitrification-induced losses continue to the end of the simulation in the region between 400 and 500 K.

9.6   Summary

A series of model runs using SLIMCAT with the thermodynamic equilibrium denitrification scheme, and forced by ECMWF analyses, has been used to examine the sensitivity of Arctic O_3 loss to denitrification during the winter of 1999/2000. The rate of activation of ClO_x from HCl and $ClONO_2$ reservoirs was found to be effectively insensitive to the magnitude of denitrification. The rate of deactivation of ClO_x and the relative amounts of HCl and $ClONO_2$ formed were, in contrast, found to be very sensitive to the magnitude of denitrification.

Two separate phases were apparent in the conversion of ClO_x to reservoir species in late winter and early spring. Initially, deactivation of ClO_x was dominated by reaction with NO_2 (from photolysis of HNO_3) to form $ClONO_2$. The rate of ClO_x deactivation during this time was strongly dependent on the degree of denitrification, decreasing almost linearly from 42 ppbv/day in the absence of denitrification to 19 ppbv/day for 88% denitrified air. Denitrification delayed ClO_x deactivation by a maximum of 20

days.

During the later deactivation phase, the rate of ClO_x deactivation was found to be insensitive to denitrification with an overall loss rate of ~40 ppbv/day. Decreased deactivation to $ClONO_2$ with increased denitrification is mitigated by increased deactivation to HCl. Extensive denitrification deactivates ClO_x to approximately equimolar quantities of HCl and $ClONO_2$ by early March. This may increase the sensitivity of the lower stratosphere to subsequent re-activation as heterogeneous rate of HCl + $ClONO_2$ is significantly faster than the alternative heterogeneous activation reactions which occur in the absence of HCl.

Model simulations of the sensitivity of O_3 loss to a 4 K decrease in temperature were also carried out for the winter of 1999/2000 using the ECMWF analyses. In the baseline run, total column losses in the model attained a peak of 78 DU on Day 90 of the simulation with denitrification contributing 17% of the loss. A reduction in model temperatures of 4 K relative to the ECMWF analyses increased cumulative column O_3 loss by 65 DU (83%). Denitrification contributed 32% of the O_3 loss at lower temperature, with extended activation due to the extended region of NAT-supersaturation contributing most of the remainder. Therefore, the contribution of denitrification on O_3 loss is enhanced at low temperature.

Chapter 10

Overall summary and future work

10.1 Conclusions

A better understanding of key processes responsible for depletion of stratospheric ozone is required if accurate predictions of the future Arctic ozone layer are to be made. The gravitational sedimentation of HNO_3-containing PSC particles is one such process.

In the Antarctic, seasonal observations of denitrification were always accompanied by strong dehydration. The most plausible mechanism used to explain these observations involved the co-condensation of NAT into ice PSCs at the extremely low temperatures found in the wintertime Antarctic stratosphere [Peter et al., 1990; Wofsy et al., 1990]. The absence of strong denitrification in observations of the wintertime Arctic stratosphere was attributed to the higher temperatures and limited formation of ice PSCs. Seasonal suppression of gas-phase HNO_3 in MLS observations during cold Arctic winters was attributed to sequestration of HNO_3 in Type I PSCs and not viewed as evidence of significant denitrification. The 6 km vertical resolution of the MLS HNO_3 instrument in the lower stratosphere, combined with the instrument viewing restrictions at the highest latitudes has limited the potential for observations of Arctic denitrification in past winters. In addition, balloon-borne observations were often close to mountain ranges

where the local influence of lee-waves could dominate, restricting the conclusions which may be drawn from these observations about synoptic-scale features. However, recent observations from the MLS instrument have indicated that denitrification occurred before significant dehydration in the early winter Antarctic stratosphere. Therefore, denitrification may have initially occurred by the sedimentation of HNO_3-containing particles without ice early in the Antarctic winter [*Tabazadeh et al.*, 2000].

Observations of strong Arctic denitrification in the absence of significant dehydration [*Fahey et al.*, 2001; *Herman et al.*, 2002] together with very large NO_y-containing particles provided support for the Antarctic MLS observations discussed above by indicating that severe denitrification of the polar lower stratosphere by the gravitational sedimentation of particles other than ice was possible. Mass flux calculations indicated that the large NO_y-containing particles at observed integrated number densities (approximately 10^{-4} cm^{-3}) [*Fahey et al.*, 2001] were sufficiently numerous and large to denitrify the Arctic stratosphere. NAT particle growth times of up to 8 days were required to attain particle diameters comparable with observations ($14 - 20$ μm) based on kinetic calculations [*Carslaw et al.*, 2002]. Thermodynamic ice-based denitrification schemes used in most stratospheric models were not appropriate for accurately simulating denitrification by the large NO_y-containing particles in the 1999/2000 Arctic winter.

Most global models of stratospheric chemistry, including SLIMCAT, have used very simple thermodynamic denitrification schemes based on parameterisations of the formation and sedimentation of co-condensed NAT and ice either at or below T_{ice}. The magnitude of denitrification produced by the ice scheme in SLIMCAT has been shown here to be comparable to observations in the 1999/2000 Arctic winter but displaced vertically by 20 K when the unrealistically cold UKMO analyses were used. No significant denitrification was obtained using the ice denitrification scheme when the model was forced with the warmer ECMWF analyses. This is consistent with results from previous winters, in which SLIMCAT has failed to produce denitrification although observations clearly show that it has occurred. UKMO-analysed temperatures in all previous modelled winters have been too warm to re-distribute significant condensed NO_y when only sedimentation of ice particles has been assumed.

In this thesis, a simple denitrification scheme based on the sedimentation of a bimodal particle distribution of condensed NAT in equilibrium with the gas phase (designed to

represent the large particles observed during 1999/2000) produces denitrification in general agreement with observations from 1999/2000. However, modelled denitrification tended to be too great at the edge of the vortex. In Chapter 5, a full Lagrangian microphysical calculation of NAT growth and denitrification (DLAPSE) was incorporated in SLIMCAT. Results in Chapter 6 have shown that the microphysical denitrification in DLAPSE is more sensitive to the orientation of cold pool and vortex due to the reduction in particle growth times which occurs when particle trajectories are advected out of the cold pool in the baroclinic case. Although the vortex and cold pool were concentric for long periods during 1999/2000, there were also periods where the cold pool was offset sufficiently to reduce particle growth times and denitrification in the DLAPSE model without significantly affecting the equilibrium denitrification scheme.

Significant differences in the vertical distribution of denitrification also existed between thermodynamic equilibrium and microphysical denitrification at the highest altitudes. DLAPSE predicted significantly less denitrification at the top of the NAT-supersaturated region (Chapter 6). Comparisons with the balloon-borne ILAS instrument were unable to resolve this issue due to the limitations of the assumption that $HNO_3 = NO_y$ above 500 K. Outside the work in this thesis, the DLAPSE model has been coupled with the full SLIMCAT chemistry scheme, so this issue can now be revisited with more detailed comparisons.

The DLAPSE model captured both the magnitude and spatial distribution of denitrification compared to observations from the ER-2 during 1999/2000. By the time of the first ER-2 flight on January 20, 2000, the Arctic vortex was already extensively denitrified. Capturing the initial denitrification phase would have provided valuable information on particle size information and denitrification rates to further constrain the model. The model was also used to simulate denitrification during 1996/97 utilising nucleation rates based on observations of particle number densities from 1999/2000.

Remarkable agreement between modelled denitrification and observations from the ILAS instrument occurred below 500 K for the 1996/97 winter. Above this altitude range, the assumption that $HNO_3 = NO_y$ becomes invalid even in a cold and strongly activated vortex, limiting the effective vertical range of the comparison. The timing of denitrification was also consistent with observations from ILAS but not compared to MLS, which observed a later onset of denitrification. The absence of denitrification in

MLS HNO_3 can be attributed to the much lower vertical resolution compared to ILAS. Future high resolution HNO_3 data from the MIPAS instrument aboard ENVISAT will provide 3-D HNO_3 and aerosol data to further evaluate the model.

There was considerable O_3 loss during the 1999/2000 Arctic winter. Calculations based on in situ observations by *Richard et al.* [2001] showed record cumulative losses of 58% had occurred at 450 K by mid-March of that year. Total column losses reached 20-25% [*EORCU*, 2001], slightly lower than those recorded during the Arctic winter of 1995/96. SLIMCAT accurately reproduced the observed O_3 loss but appeared to overestimate ClOx for the winter of 1999/2000 when the colder UKMO analyses were used. Similar results were obtained with equilibrium denitrification schemes based on either NAT or ice.

Comparison of denitrified and non-denitrified model runs indicated that denitrification accounted for 30% of the cumulative O_3 loss at 450 K in the core of the vortex. Better agreement with observed ClO_x was obtained when the warmer but more realistic ECMWF analyses were used to force the model although the errors associated with the measurements of Cl_y species mean that drawing robust conclusions about activation is not possible. Significantly lower O_3 loss was produced when the model was forced with the ECMWF analyses. The contribution of denitrification to O_3 loss was also smaller at 21% due to the lower levels of ClO_x in spring as a result of incomplete activation in early winter. These results are consistent with the results of other modelling studies which indicate that, in order to reproduce the magnitude of chemical O_3 loss, levels of ClO_x in excess of observations are required [for example, *Becker et al.*, 1998; *Goutail et al.*, 1999].

Sensitivity studies of the impact of denitrification on O_3 loss in the Arctic lower stratosphere during 1999/2000 were undertaken with the SLIMCAT CTM in Chapter 9. Model denitrification was based on a bimodal NAT-equilibrium scheme and forced with the ECMWF analyses with the magnitude of denitrification controlled by adjusting a combination of NAT particle fall velocity, $p_{HNO_3}^{NAT}$ and the mass of the non-sedimenting small mode. Results from this study showed that denitrification the impact of denitrification on vortex-mean O_3 loss was slightly greater than linear, in contrast to *Tabazadeh et al.* [2000], who used a photochemical box model to determine that 50% denitrification was required for a measurable impact on O_3 loss. Recovery of ClO_x was delayed

by a maximum of 20 days, even for model runs with denitrification in excess of 90% due to enhanced recovery of HCl under extremely denitrified conditions.

Ozone loss increased almost linearly with increasing denitrification beyond the 5 ppbv threshold. 90% denitrification increased vortex-mean cumulative O_3 loss by 1.0 ppmv (83%) by late-March. There was no evidence of significant nitrification reducing the impact of chemical O_3 loss at lower altitudes during 1999/2000. Reduced O_3 loss due to nitrification did not compensate for enhanced O_3 loss due to denitrification at higher altitudes during 1999/2000.

The magnitude of cumulative O_3 loss during the 1999/2000 Arctic winter is sensitive to the synoptic temperature. Significant systematic temperature differences between the UKMO and ECMWF analyses were found in the Arctic stratosphere during 1999/2000. The UKMO analyses were found to be significantly colder than the ECMWF analyses, resulting in enhanced activation of reservoir species to ClO_x and significantly enhanced O_3 loss. A model sensitivity study based on the ECMWF analyses and denitrification by the sedimentation of NAT was carried out to explore the response of Arctic O_3 loss to reduced temperatures. A reduction of 4 K in the synoptic temperature resulted in an 86% increase in vortex-mean O_3 loss at 460 K compared to the base model run. Increased denitrification was responsible for $\sim$1/3 of the O_3 loss with the remainder attributable mainly to the increased duration and extent of PSC temperatures and faster heterogeneous halogen activation reactions. Changes due to diabatic descent in the polar vortex at lower temperatures were small. In other winters this may be more important because modelled passive O_3 had relatively small vertical gradients in the lower stratosphere during 1999/2000.

Ozone column losses in the model were significantly enhanced by a reduction in temperature. Total column losses increased by 83% (from 78 to 143 DU) when the temperature was reduced by 4 K. Increased denitrification once again accounted for $\sim$1/3 of this change. The additional O_3 loss at lower temperature occurred between 490 K and the model lower boundary at 350 K.

Significantly, the effect of increased denitrification on O_3 loss in the model is mitigated by enhanced recovery of ClO_x to HCl. Stronger denitrification leads to slower initial recovery of ClO_x to $ClONO_2$ which produces greater O_3 loss. The enhanced HCl

recovery limits the impact of denitrification to the equivalent of ~20 days additional loss. The resulting vortex contains approximately equimolar concentrations of HCl and ClONO$_2$ which pre-dispose the springtime vortex to re-activation as the most rapid heterogeneous reactivation reaction pathways require HCl.

Observations of Arctic stratospheric meteorology [*Pawson and Naujokat*, 1999] indicate a decrease in the temperature of the Arctic lower stratosphere and increased persistence of the polar vortex in spring during the last decade. These physical changes favour the formation of PSCs in the Arctic lower stratosphere, increasing the available surface area to catalyse the conversion of halogen reservoirs to ozone-destroying forms and aiding denitrification. The trend of increased stratospheric water vapour (~1% per annum since 1980) observed by *Oltmans et al.* [2000], if continued, would also promote the formation of PSCs. T_{NAT} and T_{ice} are increased by ~1 K per ppmv increase in water vapour under typical lower stratospheric conditions (10 ppbv HNO$_3$ and 5 ppmv H$_2$O).

GCM studies have shown that a combination of increased levels of greenhouse gases, ozone depletion and water vapour changes can explain much of the observed stratospheric temperature changes over the past 20 years [*WMO*, 2003]. The impact of a warmer troposphere on the future Arctic polar vortex in these models is considerably less certain. In particular, representation of planetary wave propogation from the troposphere to the polar lower stratosphere is a major source of uncertainty in GCMs. An increase in the frequency and intensity of sudden Arctic stratospheric warmings due to planetary wave propogation from a warmer troposphere could significantly reduce the severity of halogen-induced ozone loss in the Arctic [*Schnadt*, 2002].

Denitrification caused by the sedimentation of large NAT-containing particles was inefficient at denitrifying the outer regions of the vortex due to the relatively short time available for particle growth in this region. In 1999/2000, despite temperatures below T_{NAT} only around 50% of the vortex area was strongly denitrified. The optimal conditions for denitrification require long particle growth times, which is generally favoured by a concentric orientation of the cold pool and vortex. Equilibrium denitrification schemes tend to denitrify more evenly across the entire vortex and are capable of efficiently denitrifying the outer regions of the vortex. Such a mechanism based on the sedimentation of NAT is unrealistic due to the time required for the growth of NAT particles to sizes sufficient for appreciable sedimentation.
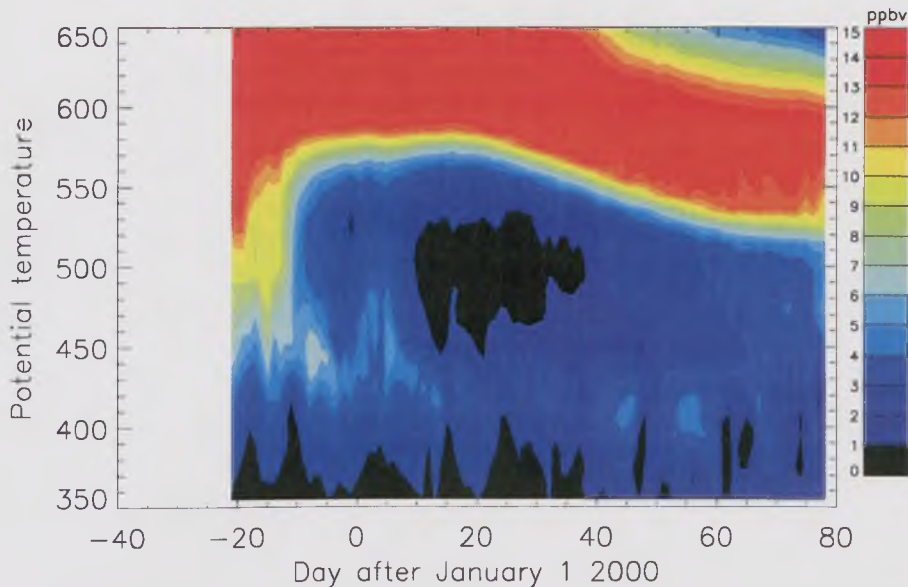
Figure 10.1: Temporal evolution of in-vortex minimum NO_y as a function of potential temperature during 1999/2000 from DLAPSE.

Figure 10.1 shows that the modelled minimum NO_y within the polar vortex (from the DLAPSE model) decreases between mid-December and mid-January between 580 and 430 K due to extensive and severe denitrification. From the end of January there is a steady erosion of the lowest NO_y mixing ratios associated with the earlier intense denitrification. This increase in minimum NO_y is due to mixing of non-denitrified air from non-denitrified regions of the vortex or across the vortex edge. Minimum NO_y increases from ∼1 ppbv over the innermost 50% of the vortex to 3 – 4 ppbv by mid-March. Observations from the ER-2 in March (Figure 7.7) demonstrate that the model reproduces the observed NO_y in the denitrified vortex, although no observations of NO_y are available to confirm the existence of almost totally denitrified air over a wide region of the vortex between 460 – 580K in late December and early January. In contrast, Figure 7.4 in Chapter 7 shows that modelled vortex mean denitrification is eroded much more slowly by transport across the vortex edge, supporting the supposition that mixing within the vortex rather than transport across the vortex edge is responsible for the majority of the observed increase in minimum NO_y during March.

These findings may have significant implications for the enhancement of O_3 depletion in

the Arctic due to denitrification by large NAT particles. If mixing from the edge of the vortex is sufficient to dilute intense denitrification over a time period of several weeks then it is likely that further denitrification events will be required in late winter/early spring to significantly enhance O_3 loss. Alternatively, the vortex would have to be strongly denitrified over its entire area. Such a situation is only likely to occur if the entire vortex is below T_{NAT} for a period of several weeks or an additional denitrification mechanism operates (such as synoptic scale ice formation). Currently in the Arctic, less than 50% of the vortex is below T_{NAT} in a cold winter. Under these conditions, denitrification by large NAT particles fails to denitrify the full area of the vortex.

The temperature of the polar vortex and chemical O_3 loss within the vortex are strongly coupled. Low temperatures in the vortex increase the rate of heterogeneous reactions which activate chlorine from reservoir species. The potential for severe denitrification to delay the deactivation of ClOx is also increased at low temperatures.

10.2 Suggested future work

The limitations of the assumption that $NO_y = HNO_3$ in the DLAPSE model presented here are particularly relevant for comparisons with observations made at higher altitudes within the polar vortex, as demonstrated in Chapter 7. The coupling of the full SLIMCAT chemistry code with DLAPSE removes the limitations of this assumption. Further comparisons are required between observations and the full-chemistry version of DLAPSE to validate the model denitrification scheme at higher altitudes where this assumption is invalid. The full chemistry DLAPSE model would also allow the effects of realistic denitrification by the growth and sedimentation of NAT on polar halogen activation and O_3 depletion to be evaluated. The inclusion of a full chemistry code, however, has significant computational costs.

Runs at higher resolution with a reduced timestep are needed to examine the effect of mixing and dilution on highly denitrified air over the course of a winter. Comparisons with Lagrangian transport models e.g. CLaMS [*Groß et al.*, 2002] would allow investigations of the effects of numerical and physical mixing to be compared. SLIMCAT, in common with all Eulerian models, experiences a degree of numerical diffusion between

gridboxes.

Considerable uncertainty still exists over the mechanism of selective nucleation of the background aerosol to form large NAT particles. The current volume-averaged nucleation rate used in the model for the determination of denitrification could be replaced by schemes which nucleate NAT on ice at temperatures below T_{ice}. Other schemes to test theories about the formation of NAT or ice in lee-waves could be included if a suitable parameterisation for lee-wave temperature effects within the polar vortex were used. However, at present there are no observations that allow a preferred nucleation mechanism to be identified.

The advent of a new generation of satellites from both the US (Earth Observing System and SAGE III), Europe (ENVISAT) and Japan (ADEOS-2) will provide unprecedented global observations of range of key species to further constrain the DLAPSE model and nucleation mechanisms. In particular, the high vertical resolution of MIPAS (aboard ENVISAT), ILAS-2 (aboard ADEOS-2), and EOS MLS should allow detailed comparisons of the magnitude and timing of model and observed denitrification.

The feasibility of incorporating the denitrification scheme in CTMs on an operational basis needs to be investigated. Currently this is too expensive but increased computational power and code optimisation could soon make this viable. Alternatively, a suitable parameterisation could be developed for inclusion in CTMs and GCMs although this may prove difficult due to the coupling of meteorology with particle growth, sedimentation and denitrification.

Appendix A

Analytic expression for liquid aerosol composition

From *Carslaw et al.*, [1995b] an analytical expression for the composition of aqueous ternary $HNO_3/H_2SO_4/H_2O$ solutions under stratospheric conditions is used both the SLIMCAT and DLAPSE models. The parameters A B, D and E used in Figure 2.45 are defined as follows:

$$A = \frac{ZH_{NNb}M_{Nb}^2 - ZH_{NSb}M_{Nb}M_{Sb}^2 p_N^0}{M_{Nb}^2 - M_{Nb}M_{Sb}}$$

$$B = \frac{M_{Sb}((-2ZH_{NNb}M_{Nb}) + (ZH_{NSb}M_{Sb}) + (M_{Nb}M_{Sb}) - (H_{NNb}M_{Sb}p_N^0))}{M_{Nb} - M_{Sb}}$$

$$C = \frac{ZH_{NNb}M_{Nb}M_{Sb}^2}{M_{Nb} - M_{Sb}}$$

$$D = atan\left(\frac{\sqrt{(4A^2 - 3B)^3 - (-2A^3 + 9AB - 27C)^2}}{-2A^3 + 9AB - 27C}\right)$$

$$E = 2sin(1.0)$$

where $Z = RT\ n_s$.

Appendix B

SLIMCAT heterogeneous reaction probabilities

Reaction	Reference number	Reaction Probability (γ)		
		Liquid Aerosol	NAT	ICE
$N_2O_5 + H_2O$	2.23	0.1	0.0003	0.01
$ClONO_2 + H_2O$	2.20	*1*	*3*	0.1
$ClONO_2 + HCl$	2.22	*1,2*	*3*	0.2
$HOCl + HCl$	2.24	*4*	0.1	0.3
$BrONO_2 + H_2O$	2.21	*5*	0.006	0.3
$N_2O_5 + HCl$			0.003	0.03
$HOBr + HBr$		*4*	0.1	0.1
$HOBr + HCl$		*4*	0.1	0.3
$HOCl + HBr$		*4*	0.1	0.3

1) Hanson and Ravishankara [1994].

2) HCl solubility from *Luo et al.* [1995].

3) Hanson and Ravishankara [1994].

4) Treated as bulk reaction.

5) Hanson et al. [1996].

Appendix C

Comparison of Ny Ålesund ozone sonde temperatures with UKMO and ECMWF analyses.

UKMO temperatures

Theta (K)	Dates	Temperature Range (K)	Temperature offset (K)	Standard Deviation	Number of observations
460	Dec 9–	< 195	-2.31	1.58	16
	Jan 27	> 195	-3.19	2.00	5
	Jan 28–	< 195	1.29	1.54	13
	Mar 31	> 195	0.41	1.88	22
506	Dec 9–	< 195	-2.29	1.06	21
	Jan 27	> 195	-	-	0
	Jan 28–	< 195	1.94	1.21	10
	Mar 31	> 195	0.28	2.18	22

ECMWF temperatures

Theta (K)	Dates	Temperature Range (K)	Temperature offset (K)	Standard Deviation	Number of observations
460	Dec 9–	< 195	-0.41	1.58	16
	Jan 27	> 195	-1.65	1.48	5
	Jan 28–	< 195	0.71	1.19	13
	Mar 31	> 195	-0.22	1.83	22
506	Dec 9–	< 195	0.12	1.09	21
	Jan 27	> 195	-	-	0
	Jan 28–	< 195	0.80	0.83	10
	Mar 31	> 195	-0.71	1.75	22

Appendix D

NO$_y$ instrument description

The NO$_y$ instrument aboard the NASA ER-2 first flew at high latitudes in 1987 during the Airborne Antarctic Ozone Experiment (AAOE) [*Fahey et al.*, 1989]. Detection of the multiple component NO$_y$ species is based on chemical conversion of NO$_y$ to NO at high temperature followed by the chemiluminescent detection by reaction with added O$_3$. The instrument (Figure D.1) comprises two sub-isokinetic sample inlets, one at the front facing forwards and the second, at the rear but also forward-facing. Condensed NO$_y$ in the sampled atmosphere are also detected by the instrument.

Aerodynamic studies [*Northway et al.*, 2002] show that the maximum diameter of aerosols detected in the rear inlet is 2 μm although the sub-isokinetic nature of this inlet results in oversampling of particles which is a function of the particle size. This indicates that NO$_y$ values within PSCs are subject to an enhancement whenever there are particles smaller than 2 μm diameter.

Attempts were made to use the Multiple Aerosol Scattering Probe (MASP) in-situ particle counter to reject only those data points recorded when the aircraft was flying in an enhanced aerosol region. In this approach, the MASP size distribution for particles up to 2 μm was calculated for each point and, in conjunction with the NO$_y$ instrument inlet enhancement factor, an enhanced condensed NO$_y$ mixing ratio (NO$_y$*enh*) was determined. Whenever NO$_y$*enh* exceeded 10 % of observed NO$_y$ then the point was rejected. This resulted in the rejection of most of the data from the first ER-2
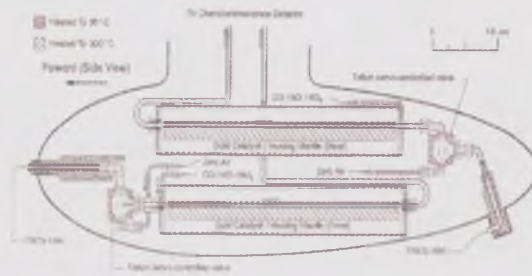
Figure D.1 Schematic diagram of ER-2 NO_y instrument. Courtesy of Megan Northway, NOAA.

deployment.

The MASP data indicated that large enhancements in NO_{rmy} should be observed by the rear inlet of the NO_y instrument over long periods of many flights during the first ER-2 deployment. Such enhancements were not observed by the NO_y instrument. The MASP data has recently been re-evaluated and there has been a reduction particle mass in the $1-2$ μm range [*Baumgardner, pers. comm.*]. Therefore, the magnitude of denitrification inferred from these data is a lower limit.

References

Andrady, A.L. *et al.*, 1998. Effects of increased solar ultraviolet radiation on materials. *J. Photochem. Photobio.*, **B46**, 96 103

Arnold, F. *et al.*, 1989. Evidence for stratospheric nitric acid condensation from balloon and rocket measurements in the Arctic. *Nature*, **342**, 493–497.

Arnold, F. *et al.*, 1998. Observations of nitric acid peturbations in the winter Arctic stratosphere: Evidence for PSC sedimentation. *J. Atmos. Chem.*, **30**, 49–59.

Austin, J., J. Knight and N. Butchart, 2000. Three-dimensional chemical model simulations of the ozone layer: 1979–2015. *Q. J. Roy. Meteor. Soc.*, **126**, 1533–1556.

Austin, J., 2002. A Three-Dimensional Coupled Chemistry-Climate Model Simulation of Past Stratospheric Trends. *J. Atmos. Sci.*, **59**, 218–232.

Austin, J. *et al.*, 2003. Uncertainties and assessments of chemistry-climate models of the stratosphere. *Atmos. Chem. Phys.*, **3**, 1–27.

Becker, G. *et al.*, 1998. Ozone loss rates in the Arctic stratosphere in the winter 1991/92: Model calculations compared with Match results. *Geophys. Res. Lett.*, **25**, 4325-4328.

Bird, R.B., W.E. Stewart, and E.N. Lightfoot, 1960. *Transport Phenomena*. Wiley, New York.

Bodhaine, B.A. *et al.*, 1997. UV measurements at Mauna Loa: July 1995 to July 1996. *J. Geophys. Res.*, **102**, 19265–19273.

Bojkov, R.D., 1986. The 1979-85 ozone decline in the Antarctic as reflected in ground based observations. *Geophys. Res. Lett.*, **13**, 1236–1239.

Brasseur, G.P., X. Tie, P.J. Rasch, and F. Lefevre, 1997. A three-dimensional simulation of the Antarctic ozone hole: Impact of anthropogenic chlorine on the lower stratosphere and upper troposphere. *J. Geophys. Res.*, **102**, 8909–8930.

Bregman, A. *et al.*, 1997. Ozone depletion in the late winter lower Arctic stratosphere: Observations and model results. *J. Geophys. Res.*, **102**, 10815–10828.

Brewer, A.W., 1949. Evidence for a world circulation provided by the measurements of helium and wa ter vapour distribution in the stratosphere. *Q. J. R. Meteorol. Soc.*, **75**, 351–363.

Browell, E.V. *et al.*, 1990. Airborne lidar observations in the wintertime Arctic stratosphere:polar stratospheric clouds. *Geophys. Res. Lett.*, **106**, 385–388.

Brown, S., R. Talukdar, and A. Ravishankara, 1999a. Reconsideration of the rate constant for the reaction of hydroxyl radicals with nitric acid. *J. Phys. Chem.*, **103**, 3031–3037.

Brown, S., R. Talukdar, and A. Ravishankara, 1999b. Rate constants for the reaction $OH + NO_2 + M \rightarrow HNO_3 + M$ under atmospheric conditions. *Chem. Phys. Lett.*, **299**, 277–284.

Buss, S. /em et al., 2003. Arctic stratospheric temperature in the winters in the winters 1999/2000 and 2000/2001: a quantatative assessment and microphysical implications. *J. Geophys. Res.*, submitted.

Carslaw, K.S. *et al.*, 1994. Stratospheric aerosol growth and HNO_3 gas phase depletion from coupled HNO_3 and water uptake by liquid particles. *Geophys. Res. Lett.*, **21**, 2479–2482.

Carslaw, K.S., S.L. Clegg and P. Brimblecome , 1995a A thermodynamic model of the system $HCl - HNO_3 - H_2SO_4 - H_2O$ including solubilities of HBr from <200 to 328K. *J. Phys. Chem.*, **99**, 11557-11574.

Carslaw, K.S., B.P. Luo and T. Peter, 1995b An analytic expression for the composition of aqueous HNO_3–H_2SO_4 stratospheric aerosols including gas phase removal of HNO_3. *Geophys. Res. Lett.*, **22**, 1877-1880.

Carslaw, K.S. *et al.*, 1997. Modeling the composition of liquid stratospheric aerosols. *Rev. Geophys.*, **35**, 125–154.

Carslaw, K.S. *et al.*, 1998. Increased stratospheric ozone depletion due to mountain-induced atmospheric waves. *Nature*, **391**, 675–678.

Carslaw, K.S. *et al.*, 2002. A vortex-scale simulation of of the growth and sedimentation of large nitric acid hydrate particles. *J. Geophys. Res.*, **107**, 10.1029/2001JD000467.

Caldwell, M.M. *et al.*, 1997. *J. Photochem. Photobiol.*, **46**, 40–52.

Chapman, S., 1930a. A theory of upper-atmosphere ozone. *Mem. R. Meteorol. Soc.*, **3**, 103–125.

Chapman, S., 1930b. On ozone and atomic oxygen in the upper atmosphere. *Phil. Mag.*, **10**, 369–383.

Chapman, S., 1931a. The absorption and dissociative or ionizing effect of monochromatic radiation in an atmosphere on a rotating earth. *Proc. Phys. Soc.*, **43**, 26–45.

Chapman, S., 1931b. The absorption and dissociative or ionizing effect of monochromatic radiation in an atmosphere on a rotating earth, Part II. Grazing incidence. *Proc. Phys. Soc.*, **43**, 483–501.

Chipperfield, M.P. and J.A. Pyle, 1998. Model sensitivity studies of Arctic ozone depletion. *J. Geophys. Res.*, **103**, 28389–28403

Chipperfield, M.P., 1999. Multiannual simulations with a three-dimensional chemical transport model, *J. Geophys. Res.*, **104**, 1781–1805.

Considine D. *et al.*, 2000. A polar stratospheric cloud parameterization for the global modeling initiative three-dimensional model and its response to stratospheric aircraft. *J. Geophys. Res.*, **105**, 3955–3973.

Craig, R.A., 1950. The observations and photochemistry of atmospheric ozone and their meteorological significance. *Meteorol. Monogr.*, **1**, ???

Crutzen, P.J. and F. Arnold, 1986. Nitric acid cloud formation in the cold Antarctic stratosphere – a major cause for the springtime ozone hole. *Nature*, **324**, 651–655.

Dameris, M. *et al.*, 1998. Assessment of the future development of the ozone layer.

Geophys. Res. Lett., **25**, 3579–3582.

DeMore, W.B. *et al.*, 1997. Chemical kinetics and photochemical data for use in stratospheric modelling, Evaluation 12. JPL Publ. 97–4.

Dessler, A.E. *et al.*, 1999. Satellite observations of of temprary and irreversible denitrification. *J. Geophys. Res.*, **104**, 13993–14002.

Dhaniyala, S., K.A. McKinney and P.O. Wennberg, 2002. Lee-wave clouds and denitrification of the polar stratosphere. *Geophys. Res. Lett.*, **29**, 10.1029/2001GL013900.

Dobson, G.M., A.W. Brewer and B.M. Cwilong, 1929. Measurements of the amount of ozone in the Earth's atmosphere and its relation to other geophysical conditions - Part III. *Proc. R. Soc. Lond., Ser. A*, **122**, 456–486.

Dobson, G.M., A. Brewer and B. Cwilong, 1943. Meteorology of the lower stratosphere. *Proc. Roy. Soc.*, **185**, 144–175.

Douglass, A.R. *et al.*, 1995. Interhemispheric differences in springtime production of HCl and ClONO$_2$ in the polar vortices. *jgr*, **100**, 13967–13978.

Drdla, K., M.R. Schoeberl and J. Rosenfeld, 2002. Microphysical modeling of the 1999/2000 Arctic winter, 1, Polar stratospheric clouds, denitrification and dehydration. *J. Geophys. Res.*, **107**, pp, doi:10.1029/2001JD/001159.

Dye, J.E. *et al.*, 1992. Particle size distributions in Arctic polar stratospheric clouds, growth and freezing of sulfuric acid droplets, and implications for cloud formation. *J. Geophys. Res.*, **97**, 8015–8034.

European Ozone Research Coordinating Unit, 2001. The Northern Hemisphere Stratosphere in the Winter and Spring of 1999/2000. Cambridge.

Fahey, D.W. *et al.*, 1989. Measurements of nitric oxide and total reactive nitrogen in the Antarctic stratosphere: Observations and chemical implications. *J. Geophys. Res.*, **94 (D14)**, 16665–16681.

Fahey, D.W. *et al.*, 1990. Observations of denitrification and dehydration in the winter polar stratospheres. *Nature*, **344**, 321-324.

Fahey , D.W. *et al.*, 2001. The detrection of large HNO$_3$-containing particles in the winter Arctic stratosphere and their role in denitrification. *Science*, **291**, 1026-1031.

Farman, J.C., B.G. Gardiner and J.D. Shanklin, 1985. Large losses of total ozone in Antarctica reveal seasonal ClO$_x$/NO$_x$ interaction. *Nature*, **315**, 207–210.

Fioletov, V.E., J.B. Kerr and D.I. Wardle, 1997. The relationship between total ozone and spectral UV irradiance from Brewer observations and its use for derivation of total ozone from UV measurements. *Geophys. Res. Lett.*, **24**, 2997–3000.

Fischer, H. *et al.*, 1997. Observations of high concentrations of total reactive nitrogen (NO$_y$) and nitric acid (HNO$_3$) in the lower Arctic stratosphere during the Stratosphere-Troposphere Experiment by Aircraft Measurements (STREAM) II campaign in February 1995. *J. Geophys. Res.*, **102**, 23559-23571.

Frederick, J.E., Z. Qu and C.R. Booth, 1998. Ultraviolet radiation at sites in the Antarctic coast. *J. Photochem. Photobiol.*, **68**, 183–190.

Fueglistaler, S. *et al.*, 2002. NAT-rock formation by mother clouds: a microphysical model study. *Atmos. Chem. Phys.*, **2**, 93–98.

Gao, R.S., *et al.*, 2001. Observational evidence for the role of denitrification in Arctic stratospheric loss. *Geophys. Res. Lett.*, **28**, 2879–2882.

Goutail, F. and J.P. Pommerau, 1997. Ozone loss: The northern polar picture, *Report on the Fourth European Symposium on Stratospheric Ozone Research*, Schliersee, 273–276.

Grewe, V. *et al.*, 2003. Future changes of the atmospheric composition and the impact of climate change. *Tellus accepted*

Groß, J.-U. em et al., 2002. Simulation of ozone depletion in spring 2000 with the Chemical Lagrangian Model of the Stratosphere (CLaMS). *J. Geophys. Res.*, **107**, pp, doi:10.1029/2001JD000456.

Guirlet, M. *et al.*, 2000. Modeled Arctic ozone depletion in winter 1997/1998 and comparison with previous winters. *J. Geophys. Res.*, **105**, 22185–22200.

Guyot, G., 1998. Physics of the Environment and Climate. John Wiley and Sons, New York.

Hansen, G. and M.P. Chipperfield, 1999. Ozone depletion at the edge of the Arctic polar vortex 1996/1997. *J. Geophys. Res.*, **104**, 1837–1845.

Hanson, D. and K. Mauersberger, 1988. Laboratory studies of nitric acid trihydrate: Implications for the south polar stratosphere. *Geophys. Res. Lett.*, **15**, 855–858.

Hanson, D.R., and A.R. Ravishankara, 1994. Reactive uptake of $ClONO_2$ onto sulfuric acid due to reaction with HCl and H_2O. *J. Phys. Chem.*, **98**, 5728–5735.

Hanson, D.R., A.R. Ravishankara, and E.R. Lovejoy, 1996. Reaction of $BrONO_2$ with H_2O on submicron sulfuric acid aerosol and the implications for the lower stratosphere. *J. Geophys. Res.*, **101**, 9063–9069.

Herman, J.R. *et al.*, 1996. UVB-B increases (1979–1992) from decreases in total ozone. *Geophys. Res. Lett.*, **23**, 2117–2120.

Hermann, R.L. *et al.*, 2002. Hydration, dehydration, and the total and the total hydrogen budget of the 1999/2000 winter Arctic stratosphere. *J. Geophys. Res.*, **107**, 10.1029/2001JD001257.

Hintsa, E.J. *et al.*, 1998. Dehydration and denitrification in the Arctic polar vortex during the 1995-1996 winter. *Geophys. Res. Lett.*, **25**, 501–504.

Hoffmann, D.J. *et al.*, 1997. Ten years of ozonesonde measurements at the South Pole: Implications for recovery of springtime Antarctic ozone. *J. Geophys. Res.*, **102**, 8931–8943.

Holton, J.R., 1992. An introduction to dynamic meteorology (3rd Edition). *Academic Press*, Cambridge.

Holton, J.R. *et al.*, 1995. Stratosphere-troposphere exchange. *Rev. Geophys.*, **33**, 403–439.

Hubler, G. *et al.*, 1990. Redistribution of reactive odd nitrogen in the lower Arctic stratosphere. *Geophys. Res. Lett.*, **17**, 453–465.

Jacobson, M.Z., 2000. *Fundamentals of Atmospheric Modeling.* Cambridge University Press, Cambridge.

Jensen, E.J., O.B. Toon, A. Tabazadeh and K. Drdla, 2002. Impact of polar stratospheric cloud particle composition, number density, and lifetime on denitrification. *J. Geophys. Res.*, **107**, 8284, doi:10.1029/2001JD000440.

Jost, H. *et al.*, 1998. Laminae in the tropical middle stratosphere: Origin and age estimation. *Geophys. Res. Lett..*, **25**, 4337–4340.

Juckes, M.N. and M.E. McIntyre, 1987. A high-resolution one-layer model of breaking planetary waves in the stratosphere. *Nature*, **328**, 590–596.

Kleinböhl *et al.*, 2002. Vortexwide denitrification of the Arctic polar stratosphere in winter 1999/2000 determined by remote observations. *J. Geophys. Res.*, bf 107, 10.129/2001JD001042.

Knopf, D.A. *et al.*, 2002. Homogeneous nucleation of NAD and NAT in liquid stratospheric aerosols: insufficient to explain denitrification. *Atmos. Chem. Phys.*, **2**, 207–214.

Knudsen, B.M., 1996. Accuracy of arctic stratospheric temperature analyses and the implications for the prediction of polar stratospheric clouds, *Geophys. Res. Lett..*, **23**, 3747–3750.

Kondo, Y. *et al.*, 1999. NO_y-N_2O correlation observed inside the Arctic vortex in February 1997: Dynamical and chemical effects. *J. Geophys. Res.*, **104**, 8215–8224.

Kondo, Y., H. Irie, M. Koike and G.E. Bodecker, 2000. Denitrification and nitrification in the Arctic stratosphere during the winter of 1996/97. *Geophys. Res. Lett.*, **27**, 337–340.

Koop, T., B.P. Luo, A. Tsias and T. Peter, 2000. Water activity s the determinant for homogeneous ice nucleation in aqueous solution. *Nature*, **406**, 611-614.

Lait, L.R., 1994. An Alternative Form for Potential Vorticity. *J. Atmos. Sci.*, **51**, 1754–1759.

Larsen, N., 1991. Polar Stratospheric Clouds: A Microphysical Simulation Model, *Sci Rep. 91-2* Danish Meteorological Institute, Copenhagen.

Lary, D.J. and J.A. Pyle, 1991. Diffuse radiation, twilight and photochemistry, *J. Atmos. Chem.*, **13**, 373–392.

Lary, D.J., 1991. Photochemical studies with a three-dimensional model of the atmosphere. PhD Thesis, Cambridge University, 1991.

Longstreth, J. *et al.*, 1998. Health risks. *J. Photochem. Photobiol.*, **B46**, 20–39.

Luo, B. *et al.*, 1995. Vapour pressures of $H_2SO_4/HNO_3/HCl/HBr/H_2O$ solutions to low stratospheric temperatures. *Geophys. Res. Lett.*, **22**, 247–250.

Mann, G.W *et al.*, 2002. Vortex concentricity as a controlling factor of Arctic denitrification. *J. Geophys. Res.*, ,

Marti, J. and K. Mauersberger. A survey and new measurements of ice vapor pressure at temperatures between 170 and 250 K. *Geophys. Res. Lett.*, **20**, 363–366.

Meilinger, S.K. *et al.*, 1995. Size-dependent stratospheric droplet composition in mesoscale temperature fluctuations and their potential role in PSC freezing. *Geophys. Res. Lett.*, **22**, 3031–3034.

Millard, G.A., A.M. Lee and J.A. Pyle, 2003. A model study of the connection between polar and mid-latitude ozone loss in the northern hemisphere lower stratosphere. *J. Geophys. Res.*

Moan, J. *et al.*, 1989. Ozone depletion and its consequences for the fluence of carcinogenic sunlight. *Cancer Res.*, **49**, 4247–4250.

Manney, G.L. *et al.*, 1996. Comparison of U.K. Meteorological Office and U.S. National Meteorological Center stratospheric analyses during northern and southern winter. *J. Geophys. Res.*, **101**, 10311–10334.

Manney, G.L. *et al.*, 1997. MLS observartions of Arctic ozone loss in 1996-97. *Geophys. Res. Lett.*, **24**, 2697–2700.

Manney, G.L. and J.L. Sabutis, 2000. Development of the polar vortex in the 1999-2000 Arctic winter stratosphere. *Geophys. Res. Lett.*, **27**, 2589–2592.

Manney, G.L. *et al.*, 2002. Lower stratospheric temperature differences between meteorological analyses in two cold Arctic winters and their impact on polar processing studies. *J. Geophys. Res.*, **108**, doi 10.1029/2001JD001149.

Middlebrook, A.M. *et al.*, 1996. Evaporation studies of model polar stratospheric cloud films. *Geophys. Res. Lett.*, **23**, 2145–2148.

Molina, L.T. and M.J. Molina, 1987. Production of Cl_2O_2 from the Self-Reaction of the ClO Radical. *J. Phys. Chem.*, **91**, 433–436.

Molina, M.J. and F.S. Rowland, 1974. Stratospheric sink for chlorofluoromethanes: Chlorine atom catalysed destruction of ozone *Nature*, **249**, 810–812.

Murray, F.W., 1967. On the computation of saturation vapour pressure, *J. Appl. Met.*, **6**, 203–204.

Nash, E.R. *et al.*, 1996. An objective determination of the polar vortex using Ertel's potential vorticity. *J. Geophys. Res.*, **101**, 9471–9478.

Newman, P.A., J.F. Gleason, R. McPeters and R.S. Stolarski, 1997. Anomalously low ozone over over the Arctic. *Geophys. Res. Lett.*, **24**, 2689–2692.

Northway, M.J. *et al.*, 2002. An analysis of large HNO_3-containing particels sampled in the Arctic stratosphere during the winter of 1999/2000. *J. Geophys. Res.*, **108**, 10.1029/2001JD001079.

Noxon, J.F., 1978. Stratospheric NO_2 in the Antarctic winter. *Geophys. Res. Lett.*, **5**, 1021-1022.

Oltmans, S.J. *et al.*, 2000. The Increase in Stratospheric Water Vapour from Balloonborne Frostpoint Hygrometer Measurements at Boulder, Colorado. *Geophys. Res. Lett.*, **27**, 3453–3457.

Pawson, S., B. Naujokat and K. Labitzke, 1995. On the polar stratospheric cloud formation potential of the northern stratosphere. *J. Geophys. Res.*, **100**, 23215–23225.

Pawson, S. and B. Naujokat, 1999. The cold winters of the middle 1990s in the northern lower stratosphere. *J. Geophys. Res.*, **104**, 14209–14222.

Peter, T. *et al.*, 1991. Increase in the PSC formation probability caused by high-flying aircraft. *Geophys. Res. Lett.*, **18**, 1465–1468.

Peter, T., 1997. Microphysics and Heterogeneous Chemistry of Polar Stratospheric Clouds. *Annu. Rev. Phys. Chem.*, **48**, 785-822.

Plumb, R.A. *et al.*, 1994. Intrusions into the lower stratospheric Arctic vortex during the winter of 1991-1992. *J. Geophys. Res.*, **99**, 13083–13089.

Popp, P.J. *et al.*, 2001. Severe and extensive denitrification in the 1999-2000 Arctic winter stratosphere. *Geophys. Res. Lett.*, bf 28, 2875–2878.

Portmann, R.W. *et al.*, 1996. Role of aerosol variations in anthropogenic ozone depletion in the polar regions, *J. Geophys. Res.*, **101**, 22991-23006.

Prather, M.J., 1986. Numerical advection by conservation of second-order moments. *J. Geophys. Res.*, **91**, 6671-6681.

Pruppacher, H.R. and J.D. Klett, 1997. Microphysics of Clouds and Precipitation, xnd Ed. D. Reidel, Dordecht.

Pullen, S. and R.L. Jones 1997. Accuracy of temperatures from UKMO analyses of 1994/95 in the Arctic winter stratosphere, *Geophys. Res. Lett.*,**24**, 845–848.

Rex, M. *et al.*, 1997. Prolonged stratospheric ozone loss in the 1995-96 Arctic winter. *Nature*, **389**, 835.

Rex, M. *et al.*, 1997. In-situ measurements of stratospheric ozone depletion rates in the Arctic winter 1991/92: a Lagrangian approach. *J. Geophys. Res.*, **103**, 5843–5853.

Rex, M. *et al.*, 1999. Subsidebce, mixing, and denitrification of Arctic polar vortex air measured during POLARIS. *J. Geophys. Res.*, **104**, 26611–26623.

Rex, M. *et al.*, 2002. Chemical loss of Arctic ozone in winter 1999/2000. *J. Geophys. Res.*, **107**, 8276, doi:10.1029/2001JD000533.

Richard, E.C. *et al.*, 2001. Severe chemical ozone loss inside the Arctic polar vortex during winter 1999/2000 inferred from in situ airborne measurements. *Geophys. Res. Lett.*, **28**, 2197–2200.

Salawitch, R.J., G.P. Gobbi, S.C. Wofsy and M.B. McElroy, 1989. Denitrification in the Antarctic stratosphere. *Nature*, **339**, 525–527.

Salcedo, D., L.T. Molina and M.J. Molina, 2001. Homogeneous freezing of concentrated aqueous nitric acid solutions at polar stratospheric temperatures. *J. Phys. Chem. A*, **105**, 1433–1439.

Sander, S.P. *et al.*, 2000. Chemical Kinetics and Photochemical Data for Use in Stratospheric Modeling. Evaluation 13. JPL Publ. 00–3.

Santee, M.L. *et al.*, 1999. UARS Microwave Limb Sounder HNO_3 observations: Implications for Antarctic polar stratospheric clouds. *J. Geophys. Res.*, **103**, 13285–13313.

Santee, M.L. *et al.*, 1999. Six years of Microwave Limb Sounder HNO_3 observations: Seasonal, interhemispheric, and interannual variations in the lower stratosphere. *J. Geophys. Res.*, **104**, 8255–8246 .

Santee, M.L., G.L. Manney, N.J. Livsey and J.W. Waters, 2000. UARS Microwave Limb Sounder observations of denitrification ond ozone loss in the 2000 Arctic late winter. *Geophys. Res. Lett.*, **27**, 2313–2316.

Sasano, Y., M. Suzuki, T. Yokota and H. Kanzawa, 1999. Improved Limb Atmospheric Spectrometer (ILAS) for stratospheric ozone layer measurements by solar occultation technique. *Geophys. Res. Lett.*, **26**, 197–200.

Schnadt, C., 2000. Poceedings of the Quadrennial Ozone Symposium. Sapporo 2000.

Schnadt, C. *et al.*, 2002. Interaction of atmospheric chemistry and climate and its impact on stratospheric ozone. *Clim. Dynam.*, **18**, 501–517.

Scott, S.G., T.P. Bui, K.R. Chan and S.W. Bowen, 1990. The meteorological measurement system on the NASA ER-2 aircraft. *J. Atmos. Oceanic Technol.*, **7**, 525–540.

Seinfeld, J.H. and S.N. Pandis, 1998. Atmospheric Chemistry and Physics. *Wiley-*

Interscience, New York.

Shindell, A.T., 1998. Increased polar stratospheric ozone losses and delayed eventual recovery owing to increased greenhouse-gas emissions. *Nature*, **392**, 589–592.

Shine, K.P., 1987. The middle atmosphere in the absence of dynamical heat fluxes, *Q. J. Roy. Met. Soc.*, **113**, 603-633.

Sinha, R.P. and D.P. Hader, 1998. Effect of ultraviolet-B radiation in three rice field cyanobacteria. *J. Plant Physiol.*, **153**, 763–769.

Sinnhuber, B.M., *et al.*, 2000. Large loss of total ozone during the Arctic winter of 1999/2000, *Geophys. Res. Lett.*, **27**, 3473–3476.

Solomon, S., 1999. Stratospheric Ozone Depletion: A Review of Concepts and History. *Rev. Geophys.*, **37**, 275–316.

Spreng, S. and F. Arnold, 1994. Balloon-borne mass-spectrometer measurements of HNO_3 and HCN in the winter Arctic stratosphere - evidence for HNO_3-processing by aerosols. *Geophys. Res. Lett.*, **21**, 1251–1254.

Stimpfle, R.M. *et al.*, 1999. The coupling of $ClONO_2$, ClO and NO_2 in the lower stratosphere from in-situ observations using the NASA ER-2 aircraft. *J. Geophys. Res.*, **104**, 26705–26714.

Sugita, T. *et al.*, 1998. Denitrification observed inside the Arctic vortex in February 1995. *J. Geophys. Res.*, **103**, 16221-16223.

Swinbank, R. and A. O'Neill, 1994. A stratosphere-troposphere data assimilation system, *Mon. Weather Rev.*, **122**, 686-702.

Tabazadeh, A., R.P. Turco, K. Drdla and M.Z. Jacobson, 1994. A study of type 1 polar stratospheric cloud formation. *Geophys. Res. Lett.*, **21**, 1619-1622.

Tabazadeh, A. *et al.*, 1996. Observational constraints on the formation of type 1a polar stratospheric clouds. *Geophys. Res. Lett.*, **23**, 2109–2112.

Tabazadeh, A. *et al.*, 2000. Quantifying denitrification and its effect on ozone recovery.

Science, **288**, 1407–1411.

Tabazadeh, A. *et al.*, 2001. Role of the stratospheric polar freezing belt in denitrification. *Science*, **291**, 2591–2594.

Tolbert, M.A. and A.M. Middlebrook, 1990. FTIR studies of model polar stratospheric cloud surfaces. *J. Geophys. Res.*, **95**, 22423-22431.

Toon, O.B., P. Hamil, R.P. Turco and J. Pinto, 1986. Condensation of HNO_3 and HCl in the winter polar stratospheres. *Geophys. Res. Lett.*, **23** 1284–1287.

Toon, O.B., R.P. Turco and P. Hammill, 1990. Denitrification mechanisms in the polar stratospheres. *Geophys. Res. Lett.*, **17**, 445–448.

United Nations Environment Programme (UNEP), 1995. *Envionmental Effects od Ozone Depletion: 1994 Update*, Nairobi, Kenya.

Voigt, C. *et al.*, 2000. Nitric acid trihydrate (NAT) in polar stratospheric clouds. *Science*, **290**, 1756–1758.

von der Gathen, P. *et al*, 1995. Observational evidence for chemical ozone depletion over the Arctic in winter 1991-92. *Nature*, bf 375, 131–134.

Waibel, A.E. *et al.*, 1999. Arctic ozone loss due to denitrification. *Science*, **283**, 1756–1758.

Waters, J.W. *et al.*, 1999. The UARS and EOS Microwave Limb Sounder (MLS) experiments. *J. Atmos. Sci.*, **56**, 194–218.

Waugh, D.W. *et al.*, 1997. Mixing of polar vortex air into middle latitudes as revealed by tracer-tracer scatterplots. *J. Geophys. Res.*, **102**, 13119–13134.

Webster, C.R. *et al.*, 1994. Aircraft (ER-2) laser infrared absorption spectrometer (ALIAS) for in-situ stratospheric measurements of HCl, N_2O, CH_4, NO_2, and HNO_3. *Applied Optics*, **33**, 454–472.

Wetzel, G. *et al.*, 1997. Vertical profiles of N_2O_5, HO_2NO_2 and NO_2 inside the Arctic vortex, retrieved from nocturnal MIPAS-B2 infrared limb emission measurements in

February 1995. *J. Geophys. Res.*, **102**, 19177–19186.

Wofsy, S.C. *et al.*, 1990. Condensation of HNO$_3$ on falling ice particles: Mechanism for denitrification of the polar stratosphere. *Geophys. Res. Lett.*, **17**, 449-452.

World Meteorological Organisation, 2003. Scientific Assessment of Ozone Depletion: 2002. Global Ozone Research and Monitoring Project Report No. 47, Geneva.

World Meteorological Organisation, 1999. Scientific Assessment of Ozone Depletion: 1998. Global Ozone Research and Monitoring Project Report No. 44, Geneva.

Worsnop, D.R., L.E. Fox, M.S. Zahniser and S.C. Wofsy, 1993. Vapor pressure of solid hydrates of nitric acid: Implications for polar stratospheric clouds. *Science*, **259**, 71–74.

Yung, Y.L., J.P. Pinto, R.T. Watson and S.P. Sander, 1980. Atmospheric bromine and ozone peturbations in the lower stratosphere. *J. Atmos. Sci.*. **37**, 339–353.